Analysis of multicomponent VSP data for shear-wave anisotropy

by

David A. Campden

(B.Sc. University of Edinburgh)

Thesis submitted for the degree of Doctor of Philosophy

Department of Geology and Geophysics

University of Edinburgh

November 1990

I declare that this thesis has been composed by myself and that the work described is entirely my own unless otherwise explicitly stated in the text.

David Campden

Abstract

The main aim of this thesis was to analyse three-component VSP data for shear-wave anisotropy. Two VSP data sets are presented and investigated for shear-wave splitting.

Propagation characteristics of split shear-waves are studied to gain an understanding of the effects of attenuation anisotropy. It is shown that compared to velocity anisotropy, attenuation anisotropy is a more difficult quantity to measure, being dependent on the attenuation of the faster split shear-wave and the velocity anisotropy. Measuring changes in attenuation anisotropy from repeated shear-wave experiments is also considered, with a view to monitoring EOR processes.

Three automatic methods for measuring shear-wave splitting parameters are developed and tested on a synthetic VSP data set contaminated with different amounts of random noise. Standard signal processing techniques are investigated using the synthetic data, to determine whether they distort or improve observations of shear-wave splitting.

The first of the real VSPs to be presented comes from a North Sea gas field. This consisted of four wide offset source locations, relying on *P*-waves being mode-converted to *SV*-waves at the top of the cap-rock overlying the gas saturated reservoir sands. Fast shear-wave polarizations and time delays are measured from shear-waves in the reservoir region using the three automatic techniques previously developed. Results suggest a predominant crack orientation of N47°W agreeing with maximum horizontal stress directions found from earthquake focal mechanisms and borehole breakout data. One of the main problems associated with these North Sea VSPs was that the source to borehole azimuths were very nearly parallel to the crack strike, resulting in poor observations of shear-wave splitting.

The second VSP was carried out at the Geysers geothermal zone, where the most reliable shear-wave observations were from a wide offset VSP using relatively shallow (maximum 640m) geophones. Two

shear-wave source polarizations were used, one in-line and the other cross-line. Shear-waves from the in-line source arrive about 0.1s ahead of shear-waves from the cross-line source polarization. This difference in arrival times was initially interpreted in terms of vertically aligned, parallel cracks/fractures striking in the source to well head direction, acting to slow down shear-waves from the cross-line source relative to those from the in-line source. A subsequent hammer seismic refraction experiment at the source location revealed the presence of a thin, very low velocity surface layer. This acts to mode-convert *P*-waves emitted from the in-line source to *SV*-waves at the base of the surface layer, giving an apparent shear-wave arrival time about 0.1s earlier than the directly travelling shear-waves from the cross-line source. Synthetic seismograms showing this effect are given and compare favourably with observations. However, the observations also show significant cross-component energy: the transverse component from the in-line source is almost twice the amplitude of the vertical component, and the vertical component from the cross-line source has a similar amplitude to the transverse component. This energy suggests complex, near surface anisotropy and as such, no good match between synthetics and observations is achieved.

Acknowledgements

None of this research would have been possible without the enthusiasm, support and guidance of my supervisor, Stuart Crampin. I am indebted to Stuart for his time, effort and the patience he showed when explaining anisotropy to me.

I gratefully acknowledge the financial support provided by Shell Expro throughout the three years of my research, allowing my travel to numerous conferences abroad and to visit the Geysers geothermal zone in California to collect valuable data. Special thanks must go to the Lawrence Berkeley Laboratories (Ernie Majer and Tom McEvilly) in Berkeley, California for providing the Geysers VSP data and thanks also to Conoco UK for allowing me access to the North Sea VSP data. I am very grateful to Tom Daley from the Lawrence Berkeley Laboratories and Gareth Yardley from BGS for the time and effort they gave in helping me with fieldwork at the Geysers VSP site.

The Global Seismology Research Group in the BGS provided a friendly, helpful working environment, and I would like to thank everyone for their help in my work. Members of the Edinburgh Anisotropy Project were a constant source of useful discussion and information for which I thank all concerned. Thanks to Gerhard Graham, Phil Wild and Gareth Yardley for proof reading some of the chapters in this thesis.

Last, but not least, thanks to my parents for feeding me and generally putting up with me as I was writing up.

LIST OF CONTENTS

Attached to back cover:

Campden, D.A., Crampin, S., Majer, E.L. and McEvilly, T.V., 1990. Modeling the Geysers VSP: A progress report, The Leading Edge, 9 (August), 36-39.

Chapter 1 - Introduction

1.1 About this thesis

Over the past few years, many observations of shear-wave splitting have been published compared to the occasional passing reference before. This explosion of interest in shear-waves has been prompted by the requirement for more *in situ* information about reservoir properties, such as porosity, permeability and preferential directions of fluid flow. Knowledge of shear-wave and *P*-wave velocities can yield estimates of the porosity of a particular reservoir rock, while observations of shear-wave splitting can give estimates of reservoir anisotropy, leading to better constrained reservoir models.

This thesis investigates some of the processing and automatic interpretation procedures applied to multicomponent shear-wave VSP data and uses the results to determine anisotropy parameters within a gas reservoir. Forward modelling, using the ANISEIS fullwave modelling package, is also used, in an attempt to match synthetic and observed shear-wave particle motions in a steam reservoir.

Chapter 2 is a detailed analysis of the propagation of shear-waves through an attenuating, anisotropic earth. In particular, differential shear-wave attenuation is looked at as a means of monitoring enhanced oil recovery processes. Development is made of

three automatic methods for measuring shear-wave splitting in terms of time delay separating the fast and slow shear-waves, and the polarization of the leading split shear-wave. These techniques are tested on a set of synthetic VSP data.

Chapter 3 investigates two basic processing procedures; deterministic source signature deconvolution and F-K filtering. A synthetic VSP data set is processed using these techniques to find out whether they distort or improve observations of shear-wave splitting. This is done by applying the three automatic measuring techniques, developed in Chapter 2, to the processed data and comparing the estimated values of time delay and leading shear-wave polarization to the theoretical values, calculated from the model parameters.

Chapter 4 is an interpretation of a suite of marine VSPs in a North Sea gas reservoir, to investigate anisotropy in a producing hydrocarbon reservoir. The unusual feature of this data set, is that the shear-waves analysed for anisotropy are generated by mode conversion at the top of the cap-rock overlying the reservoir rocks. This makes processing of shear-waves more difficult.

Chapter 5 makes use of the ANISEIS full wave, anisotropic modelling package to try and match synthetic shear-waves, generated from an anisotropic model, to shear-waves observed from a VSP in the Geysers geothermal field in California. The idea here is that when a good match between synthetics and observations has been found, an estimate of the anisotropic structure is obtained.

Chapter 6 gives the main conclusions of the thesis and makes some suggestions about future research topics related to shear-wave splitting.

The rest of this chapter is devoted to a brief overview of shear-wave splitting, and introduces some of the terms and concepts used in this thesis.

1.2 Frequently used abbreviations and notations

Symbols

α_1, α_2 - Absorption coefficients of the fast and slow shear-waves.

$\Delta\alpha$ - Difference between the fast and slow shear-wave absorptions.

c_1, c_2 - Group velocities of the fast and slow split shear-waves.

Δc - Difference between fast and slow split shear-wave velocities.

f - Frequency.

K_1, K_2 - Complex propagation constants of the two split shear-waves.

ΔK - Difference between fast and slow split shear-wave complex propagation constants.

r_1, r_2 - Total path lengths from source to receiver for the two split shear-waves.

Δr - Difference between r_1 and r_2.

$\delta\gamma$ - Differential shear-wave damping factor, measured in units of time.

t_1 - Arrival time of the faster split shear-wave.

δt - Time delay between split shear-waves.

Q - Attenuation quality factor.

Vp, Vs - Isotropic P- and shear-wave velocities.

ω - Circular frequency.

Abbreviations

CD - Crack density.

CDP - Common depth point, applied to a gather of geophone records in a reflection survey.

CO - Crack orientation, refers to the strike direction of vertical, parallel cracks relative to some reference direction.

EDA - Extensive-dilatancy anisotropy.

EOR - Enhanced oil recovery.

NMO - Normal moveout.

PD - Polarization diagram.

PTL - Periodic thin layer.

qS1, *qS2* - Fast and slow split shear-waves.

VSP - Vertical seismic profile.

1.3 Seismic anisotropy

The basic definition of anisotropy, applied to a homogeneous, uniform material, is the variation of physical properties with direction. Seismic anisotropy refers to the variation of seismic velocities in different directions. Seismic waves travelling through an anisotropic medium exhibit characteristics which are subtly different from waves in isotropic media. The general theory of wave motion in anisotropic, elastic solids is well documented (e.g. Love, 1944; Musgrave, 1954; Kraut, 1963; Dieulesaint and Royer, 1980) and comprehensive reviews have been written by Crampin (1977; 1981).

In an isotropic medium, there is one *P*-wave velocity and one shear-wave velocity, and both these velocities are defined by two independent elastic constants, λ and μ, otherwise known as Lame's parameters. In a general anisotropic medium, there can be up to 21 independent elastic constants.

Wave velocities in anisotropic media can be calculated from the elastic constants by means of the Christoffel equation (e.g. see Cerveny, 1972). Without delving into theoretical formulations, the Christoffel equation can be rewritten as a linear eigenvalue problem, which has three, real positive roots with corresponding orthogonal eigenvectors. These roots refer to a quasi *P*-wave and two quasi shear-wave (*qS1* and *qS2*) phase velocities, where *quasi* indicates that these waves have only superficial resemblence to the isotropic *P*- and shear-waves. The eigenvectors give the polarization directions of the phase velocities.

Hence, there are fundamental differences between isotropic and anisotropic propagation. In every direction of phase propagation in an anisotropic medium, there are three body waves propagating with velocities varying with direction and with orthogonal polarizations fixed for the particular direction of phase propagation. Thus, shear-waves passing through an anisotropic medium will be split into two separate phases, travelling at different velocities and with different polarizations. The most straightforward observations of shear-wave splitting can be interpreted in terms of a fast shear-wave polarization and a time delay separating the two shear-waves. Isotropy is a special case where the two eigenvalues corresponding to

the two quasi shear-wave velocities are degenerate, giving the same value, and the polarization of the single shear-wave is controlled by the source, rather than the (isotropic) medium through which it passes.

Propagation in anisotropic media is further complicated by the deviation of the group velocity direction from the phase velocity. In general, the deviation will mean that the polarizations of the group velocities belonging to the three body waves are no longer orthogonal, with the consequence that the two split shear-waves are not orthogonal. This can create problems with automatic techniques for measuring shear-wave splitting, discussed in Chapter 2. Yedlin (1980) gives a good geometrical explanation of the difference between phase and group velocity directions, bypassing the need for long, complicated equations!

Anisotropic structures in the earth

Out of all the different permutations and combinations of the 21 independent elastic constants, there are only 8 possible symmetry systems, including isotropy. Of the 7 anisotropic possibilities, only two symmetry systems are thought to be commonly present in the earth.

The first of these is hexagonal symmetry with five independent elastic constants. This form of anisotropy can be caused by two phenomena. Periodic thin layer (PTL) anisotropy (Postma, 1955; White and Angona, 1955; Backus, 1962) (there is some debate whether *periodic* is appropriate) is caused by a stratified section composed of alternating layers of different elastic materials, provided the wavelengths being propagated are large in comparison with the individual layer thicknesses. If this last assumption holds true, the

entire section can be described in terms of one set of five effective elastic constants producing a new medium which is hexagonally anisotropic, with a vertical axis of symmetry meaning that velocity does not vary azimuthally (i.e. velocity is constant for a particular incidence angle and any azimuthal propagation direction).

The extensive-dilatancy anisotropy (EDA) hypothesis (Crampin and Atkinson, 1985) states that the observed anisotropy is dominated by the effect of stress-aligned cracks or pores. At sufficiently great depths, the alignment of these cracks or pores (otherwise known as inclusions) is generally vertical, with the normal of the inclusions parallel to the minimum horizontal compressive stress. Like PTL anisotropy, EDA has hexagonal symmetry, but the axis of symmetry is horizontal, producing azimuthal variations of velocity. Near the surface, where anomalous stress conditions occur, the alignment of EDA inclusions may be severely altered (Crampin, 1990b). In the upper portion of the crust, the inclusions are filled with water, possibly highly mineralised (Kozlovsky, 1984). In hydrocarbon reservoirs the inclusions will contain a gas- or oil-water mixture. There are valid physical reasons why liquid filled microcracks are expected to be aligned by stress (Crampin and Atkinson, 1985), but there is currently a lot of debate about whether these inclusions will be realigned as stress directions change, such that measurements of seismic anisotropy represent the current state of stress or some palaeo stress direction.

Shear-waves passing through a medium containing PTL anisotropy or EDA will be split into two, orthogonal polarizations travelling at different velocities. In the special case of hexagonal anisotropy, the polarizations of the shear-waves relating to the group velocity directions will be orthogonal. Figure 1.1 is a schematic diagram showing how shear-waves propagate through a medium containing EDA. The leading split shear-wave is polarized parallel to the strike of the stress-induced cracks, providing a direct way of relating observations of shear-wave anisotropy to the internal strucure of a rock.

The second type of anisotropy commonly thought to be found in the earth is a combination of PTL anisotropy and EDA, forming an orthorhombic symmetry with nine independent elastic constants. A cyclic sequence of sedimentary layers containing vertical, stress-aligned inclusions would give rise to such an anisotropic structure. Propagation of shear-waves in the presence of this type of anisotropy is more complex compared to hexagonal anisotropy. The (group) polarizations of the shear-waves are unlikely to be orthogonal, the extent of the non-orthogonality depending on the degree of anisotropy. One of the characteristics of this type of anisotropy is that it contains point singularities, corresponding to directions where the two shear-wave have the same velocities. Bush (1990) successfully modelled a set of shear-wave VSP data in the Paris Basin in terms of an orthorhombic anisotropic structure, and used the locations of point singularities to define the relative amounts of EDA and PTL anisotropy present, which in combination formed the orthorhombic structure.

EXTENSIVE DILATANCY ANISOTROPY (EDA)

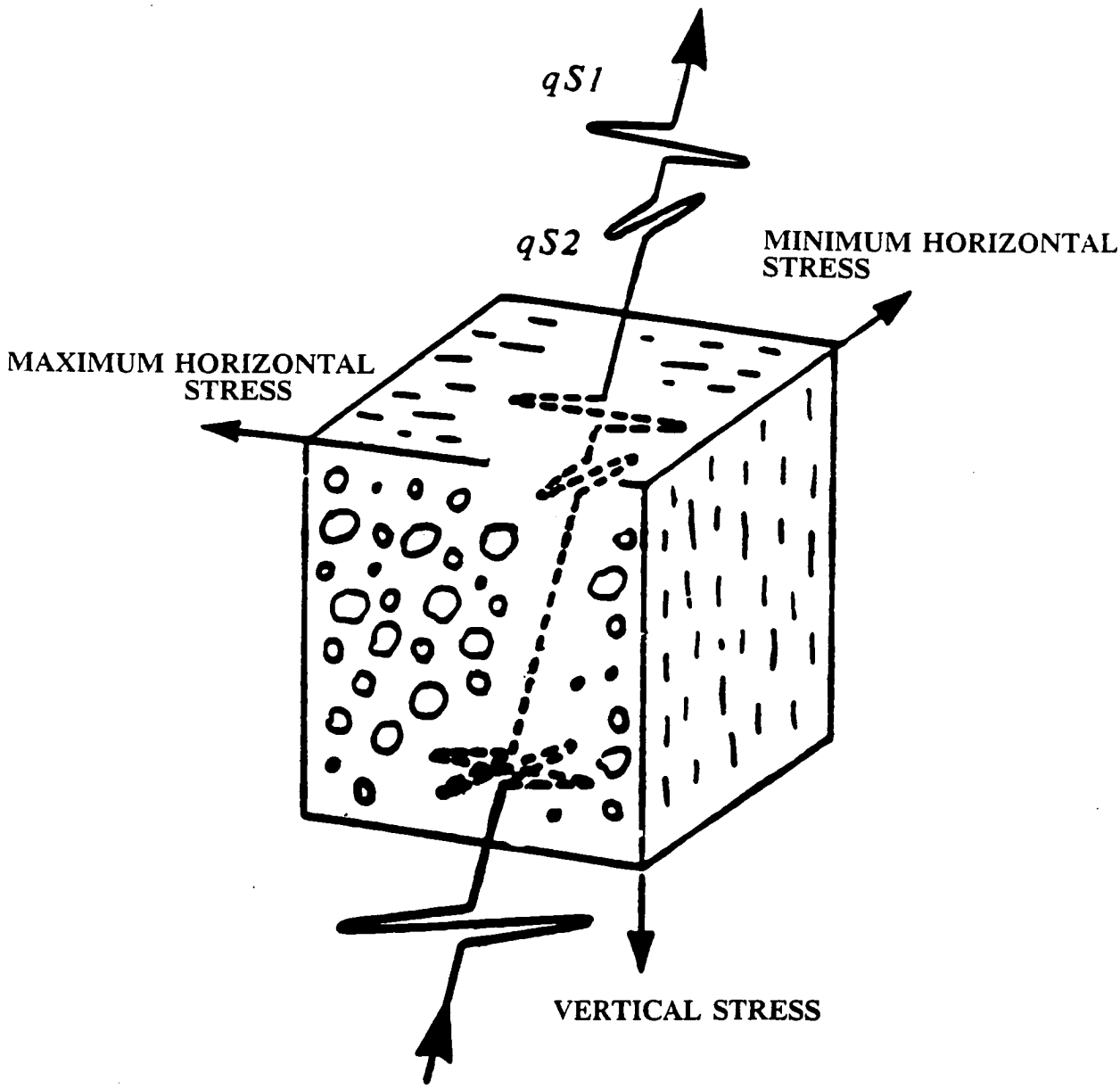

Figure 1.1. Schematic diagram showing how shear-waves are split into two polarizations, travelling with different velocities, while passing through an anisotropic medium containing parallel, vertical cracks. The leading split shear-wave is polarized parallel to the strike of the cracks.

1.4 Observations of seismic anisotropy

Early experimental studies were not very encouraging in demonstrating utilization of shear-waves to the exploration industry (Jolly, 1956). Ironically, a central focus of this discouragement was the problem of shear-wave velocity anisotropy! The primary aim of initial shear-wave experiments was to obtain a reflection section that could be compared to *P*-waves, or where *P*-wave data were poor, to replace *P*-wave reflection sections. In this context, the presence of anisotropy was looked upon as coherent noise which could not be removed by any amount of processing, and anyway, was not paricularly well understood. Other problems were encountered with the generation of shear-waves at the earth's surface. No suitable shear-wave sources were available at that time that could create shear-waves with enough energy to penetrate to useful depths.

At the time the experiments were carried out, very little practical theoretical work had been published on how to interpret observations of shear-wave anisotropy, resulting in no one being able to interpret the results properly. Further, theoretical developments were necessary to find ways of interpreting shear-wave anisotropy in terms of real earth structures by way of mathematical models. Development, too, of equipment had to be looked into.

Perhaps the first reliably interpreted observations of anisotropy from shear-waves, came from the three Turkish Dilatancy Projects (TDPs) (Booth et al., 1985; Crampin and Booth, 1984; Crampin, Evans and Ucer, 1984). These experiments recorded small earthquakes near the North Anatolian fault, in northern Turkey, with closely spaced networks of three-component seismometers. The polarizations of the shear wavetrains recorded immediately above the earthquake foci were

examined. Horizontal plane polarization diagrams (PDs) were used for this stage of analysis. Abrupt changes in the orientation and/or ellipticity of the shear-wave polarizations were almost always observed during the first few cycles following the initial shear-wave arrival on each seismogram which were manually interpreted in terms of a fast shear-wave polarization and a time delay. The fast shear-wave polarizations measured at any given station showed nearly parallel alignments with nearly the same orientations at each recording site. It was considered almost impossible that the uniform alignment could be explained by scattering at irregular surface topography or by earthquake focal mechanisms, and it was concluded that the observed shear-wave splitting was most likely the result of crack induced anisotropy in the region above the earthquake foci.

Since these observations were published, there have been many more experiments designed to look for shear-wave splitting, almost all of them giving some positive indication of shear-wave splitting. These experiments can be classified into two distinct groups: those relying on earthquakes as a source of shear-waves (these experiments are usually involved with earthquake prediction research), and those where man-made shear-wave sources are used (e.g. in an exploration or production environment, where knowledge of crack/fracture orientations can be very useful).

1.5 Theoretical developments in understanding seismic anisotropy

In section 1.3, reference was made to two different sources of seismic anisotropy, PTL anisotropy and EDA, which are thought to be the most common anisotropic structures in the earth. In the case of

PTL anisotropy, papers were published showing how to calculate anisotropic velocity variations given the isotropic velocities of a stack of layers, and the thicknesses of each layer (Postma, 1955; Uhrig and Melle, 1955; White and Angona, 1955; Backus, 1962).

Much development has also been made in determining velocity variations in a medium containing EDA cracks. Anisotropic velocities in a homogeneous, isotropic solid containing a random distribution of small (compared to seismic wavelengths) flat cracks were formulated by Garbin and Knopoff (1973, 1975a, 1975b). Hudson (1980, 1981) extended the theory to include cracks with aspect ratios up to about 0.1. Nishizawa (1982) developed a way of calculating velocities in an isotropic medium containing cracks with any aspect ratio (i.e. from flat to pencil shaped). Douma (1988) compared the velocity variations calculated from Hudson's and Nishizawa's formulations and concluded that the two methods were almost identical for aspect ratios up to 0.3, which is beyond the expected limits of Hudson's crack theory. Further developments were made by Hudson (1986), allowing cracks to be inserted into an anisotropic medium, such that the correct velocity variations could be calculated in a medium containing a combination of crack and PTL (orthorhombic) anisotropy. In the following text, the term *Hudson cracks* refers to cracks derived from Hudson's theoretical formulations for penny shaped cracks.

Although theoretical formulations for various anisotropic structures, described above, do help to understand the behaviour of shear-waves in homogeneous anisotropic media, they provide only part of the solution to the behaviour of shear-waves in an inhomogeneous, anisotropic earth structure. For more complex models, the computation

of synthetic seismograms is necessary for the interpretation of wave propagation. Numerical experimentation allows realistic interpretation of observations from complicated structures, that would have been quite impossible before the arrival of powerful digital computers.

Many software packages have been developed to generate synthetic seismograms from anisotropic earth models. These use reflectivity methods, ray theory, Fourier methods or finite difference solutions and have mostly been developed from isotropic modelling techniques, but invariably take up much more computer time than their isotropic predecessors. The relative limitations and strengths of the various software packages are presently being investigated through the Anisotropic Modelling Collaboration (AMC) project, initiated by Leon Thomsen of Amoco USA. This project compares synthetic seismograms from all the currently available anisotropic modelling packages using a common anisotropic model (see Wild and Crampin (1990) for a list of AMC members and the model parameters). The preliminary findings of the project are to be published by Thomsen et al. shortly.

Being able to produce synthetic seismograms showing shear-wave splitting is one thing, but trying to match the output from a modelling package to observed seismograms and PDs is a much more difficult task! There are two steps to achieve this:

1. The observations of shear-wave splitting must be correctly interpreted in terms of a leading split shear-wave direction and a

time delay between the two split shear-waves. A number of different automatic techniques have been developed to measure shear-wave splitting (see Chapter 2), but there are still problems with this stage of processing.

2. The measured polarizations and delays must then be related to an anisotropic structure. Depending on the number of different incidence angles and azimuths at which observations of shear-wave splitting are made, there may be more than one possible anisotropic structure that gives the correct polarizations and delays at all observation points. MacBeth (1990) has developed an inversion technique that compares observed *qS1* polarization directions alone with a large number of theoretical anisotropic structures stored in a data base. This is a relatively new procedure and is still undergoing tests.

After these two (non trivial) steps, the anisotropic structure(s) can be used in the modelling package to produce synthetic seismograms and PDs. Some "tweaking" of the initially interpreted anisotropic structure(s) may be required before the best match between synthetic and observations is found. To date, Bush (1990) is the only person to have published a successful account of modelling shear-waves in this way.

1.6 Equipment development

In the USSR, sources made from explosive charge patterns were described by Puzyrev et al. (1966) and Brodov et al. (1968). These descriptions relied on cancellation of *P*-waves by subtracting two signal traces rich in oppositely phased, polarized shear-waves that

were obtained by separately detonating charges on opposite sides of a cavity previously created by firing of a charge for the companion *P*-wave survey. Compagnie General de Geophysique commercially developed this shear-wave source with the trademark SYSLAP.

Another shear-wave source was made by striking a rectangular plate coupled to the ground surface alternately on opposite ends, giving two, opposite polarity shear-wave sections. This type of source has been used by many scientists in search of an inexpensive source of shear-waves. Commercial development of this source type by Institut Francaise du Petrol led to a very large hammer device known as MARTHOR.

The most recently developed shear-wave sources are OMNIPULSE (Bolt Technology, Tinkle et al., 1990) and ARIS (ARCo). OMNIPULSE uses compressed air to accelerate a mass upwards, while ARIS uses compressed air to drive a mass downwards. The travelpath of the mass in each case can be tilted from vertical (for engineering reasons, ARIS cannot be deployed in in a vertical orientation) to cause a component of horizontal displacement (shear motion) at the earth's surface. Similar *P*-wave signatures are generated regardless of tilt direction, although *P*-wave amplitudes do vary with the amount of tilt used, while oppositely polarized shear-wave are produced from opposite tilt directions. Tilt angles used are commonly between 30° and 45°. Consequently, shear-wave records can be obtained by subtracting individual records generated from opposite tilts. Similar to SYSLAP, two traces containing similarly polarized *P*-waves and oppositely polarized shear-waves can be subtracted, effectively removing the *P*-waves.

In addition to these impulsive sources, swept frequency shear-wave sources have been developed under the general VIBROSEIS patent by Conoco. A horizontal vibrator was developed along the lines of the conventional vertical vibrator, discussed by Cherry and Waters (1968) and Erickson et al. (1968). For horizontal vibrators, coupling with the ground can be a problem at high frequencies. The SHOVER system, developed by Prakla-Seismos GmbH, uses two vertical vibrators side-by-side and set 180 degrees out of phase with each other. This procedure has the feature of using two environmentally acceptable vertical vibrators instead of one environmentally harsh horizontal vibrator. Despite this, horizontal vibrators seem to be more popular.

Borehole three-component sondes have probably undergone more development than surface three-component geophones. In their original form, borehole three-component sondes consisted of a steel cylinder, about two metres long and about ten centimetres in diameter. This unit contained the vertical and two horizontal receivers, along with all the other electronics necessary for recording seismic signals. The whole (rather heavy) assembly is clamped to the side of the borehole during recording by one or two arms. Recent developments in instrument design have tended to place the three geophones in a small, light subassembly pressed into direct contact with the well casing. The geophones thus accurately monitor borehole motion in good acoustic isolation from the heavy body of the sonde containing the rest of the electronics (e.g. Horowicz, 1990).

The main problem associated with recording full wave-form data is with the horizontal receivers. These can operate incorrectly when

tilted more than a few degrees off horizontal. Most tool designs mean that the horizontals are more prone to resonances in the seismic band, although these are rarely at low enough frequencies to mess up shear-wave recordings.

1.7 The ANISEIS full waveform modelling package

In this thesis, the ANISEIS full waveform modelling package (Taylor, 1988) was used exclusively to model observed shear-wave splitting and investigate the properties of anisotropic media. The method for generating synthetic seismograms is described by Taylor (1987) and can use either a propagator matrix method (Keith and Crampin, 1977a, 1977b, 1977c) or an anisotropic reflectivity technique (Booth and Crampin, 1983; Fryer and Frazer, 1984, 1987).

An ANISEIS model is usually specified in the following way:

1. Velocity structure. Up to twenty anisotropic and/or isotropic layers can be defined to make up a model, with the restriction that the layers are plane and horizontal.
2. Source type. Three different point source types are available, these being explosive, vertical force or horizontal force. When modelling observed results, the source should be chosen to correspond to that actually used in the field. Since the modelling package was designed primarily as a commercial tool, there is no source type corresponding to a double couple earthquake, although the addition of such a source would not pose too many problems.
3. Geophone locations must be specified to produce the required geometry (e.g. reflection survey, VSP or cross-hole).
4. The calculation of synthetic seismograms requires an integration

over frequency, slowness and optionally azimuth if large deviations from the sagittal plane are expected. Thus, a frequency range must be given, usually corresponding to the bandwidth of the signal being modelled.

5. Attenuation may be added to each layer making up the velocity structure.

The source signature shape need not be given until the impulse response of the model has been calculated. This allows a number of different signatures to be tried, each being convolved with the impulse response. The effect of changing the source signature can be dramatic with regard to the shape of PDs. Figure 1.2 shows six shear-wave PDs, all with the same *qS1* polarization and time delay between faster and slower shear-waves, where different source shapes have been used. It is evident from this diagram that if observed shear-wave PDs are to be successfully modelled, the correct source signature must be chosen. It can also be seen that the source types with emergent first arrivals (i.e. Figures 1.2c and 1.2d) are much more difficult to interpret in terms of a fast shear-wave polarization direction than the impulsive source types in Figures 1.2a and 1.2b.

1.8 Recording shear-waves

In a commercial environment, there are three different experimental geometries for recording seismic waves: reflection profiles, VSPs and cross-hole experiments.

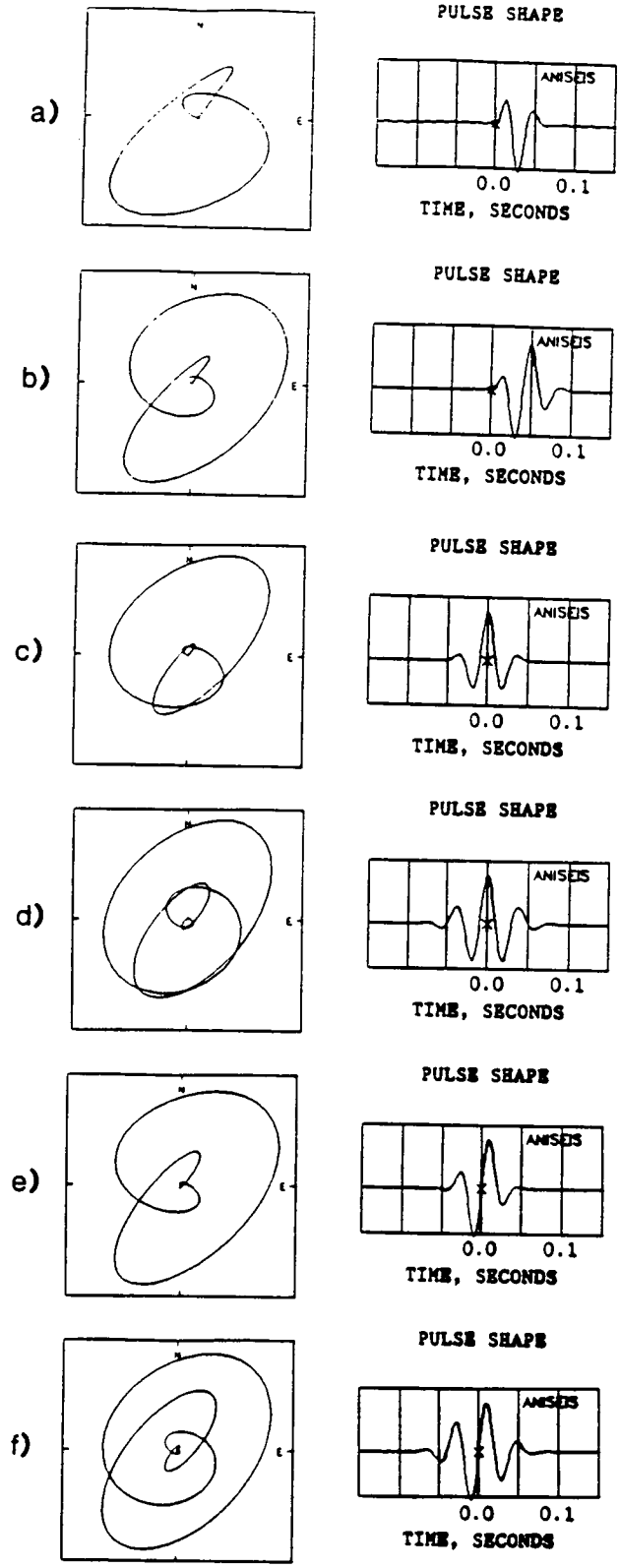

Figure 1.2 Example of how the shape of polarization diagrams depends on the shape of the source pulse. In all six PDs shown, exactly the same fast and slow shear-wave polarizations and time delay separating the two split shear-waves are used. Only in the first two PDs, where the source pulse is more impulsive, is the initial shear-wave polarization obvious, at 33° clockwise from North (N).

Reflection surveys

The most frequently used geometry is the reflection profile, where source and receivers are at or just below the surface. If this geometry could be reliably used for recording shear-wave splitting (only in land surveys), then lateral variations in anisotropy could be monitored, possibly indicating where the reflector of interest was more fractured. In these circumstances, shear-wave splitting could be used as an exploration tool, aiding the search for new hydrocarbon deposits. Mueller (1990) is currently the only person to have published successful results using shear-waves to locate a fractured area within a chalk oil reservoir in Texas. Subsequent drilling confirmed the presence of oil filled fractures.

The main problems with this type of geometry are associated with recording at the free surface, where the weathered layer and changing types of anisotropy have adverse effects on shear-wave polarizations. The polarizations of recorded shear-waves are controlled, to some extent, by the last anisotropic structure through which the shear-waves have passed (i.e. the medium in which the recording instrument is placed). Yardley and Crampin (1990b) have demonstrated, using ANISEIS, that near surface crack orientations that are significantly different from those at depth, where shear-waves are being reflected, can introduce significant distortions to shear-wave polarizations, making direct interpretation for the deep anisotropic structure impossible.

The free surface itself has degrading effects on shear-wave polarizations. Nuttli (1961) and Evans (1984) show that for plane shear-waves arriving at the surface of an isotropic medium with angles of incidence less than $\sin^{-1}(Vs/Vp)$, the motion at the surface

has approximately twice the amplitude of the motion at depth, but otherwise the free surface does not harm polarization information. At greater incidence angles, shear-waves suffer mode conversion at the surface and phase amplitude changes, effectively destroying any polarization information the shear-waves may have contained before arriving at the free surface. The incidence angle at which shear-wave polarization information becomes unreliable, $\sin^{-1}(Vs/Vp)$, defines the *shear-wave window* (Evans, 1984; Crampin, 1985) within which the incident shear-wave ray paths must lie if analysis for shear-wave splitting is to be made.

Example of free surface effects on shear-wave polarizations

Figure 1.3a shows the geometry of a simple synthetic experiment, where a receiver is on the surface with ten subsurface shots located 2km from the receiver but giving different incidence angles between vertical and 79°. An *SH*-source polarization was used. A homogeneous, anisotropic medium was used for the model, the anisotropy being caused by thin vertical Hudson cracks, striking 33° anticlockwise from the radial direction (the propagation direction). Figure 1.3b shows an equal area plot upon which the horizontal projections of the fast shear-wave polarizations have been displayed for the modelled anisotropic medium. The centre of the plot represents vertical propagation and the perimeter horizontal propagation. The inner circle marks the outer limit of the shear-wave window, beyond which the recorded shear-wave polarizations are expected to be distorted. The diagram here represents the correct *qSI* polarizations, without the distorting effect of the free surface. The boxed zone on the equal area plot shows the range of incidence angles covered by the

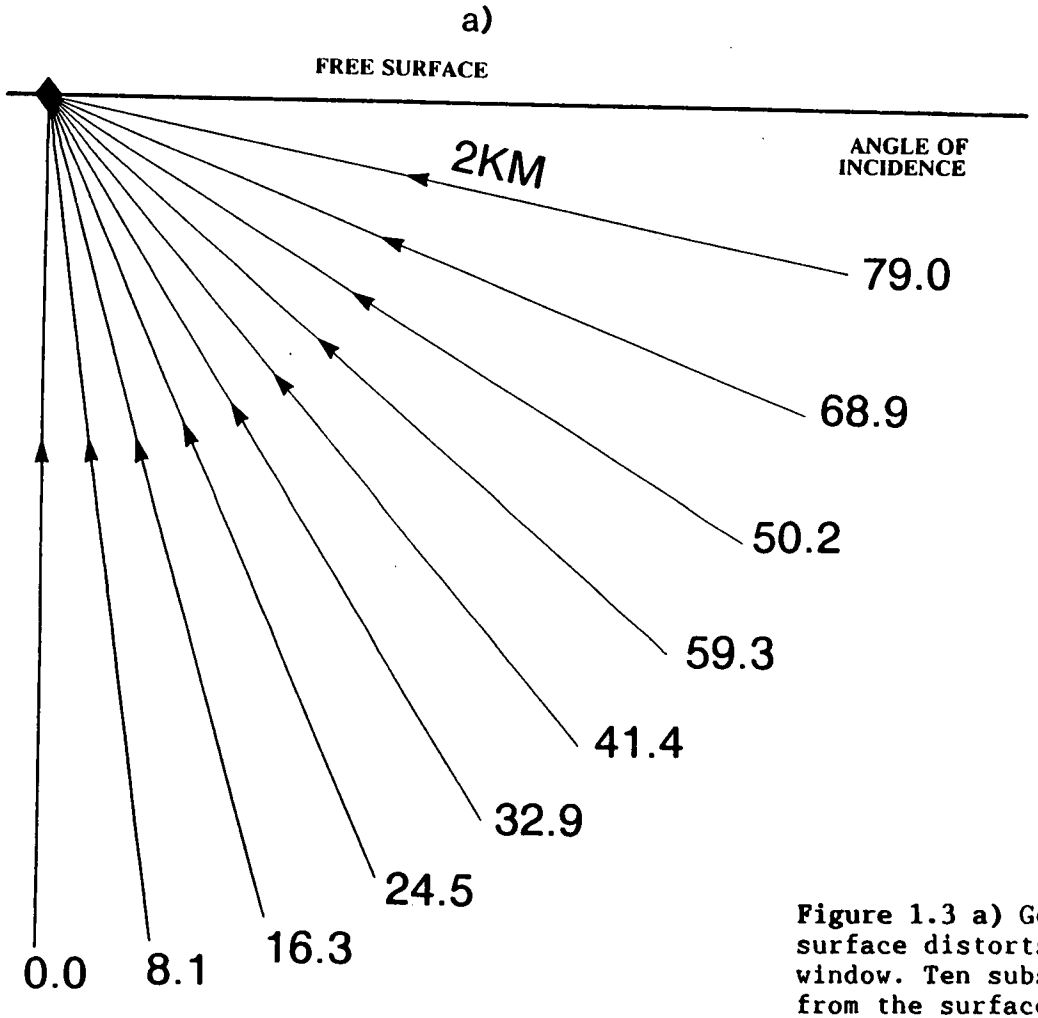

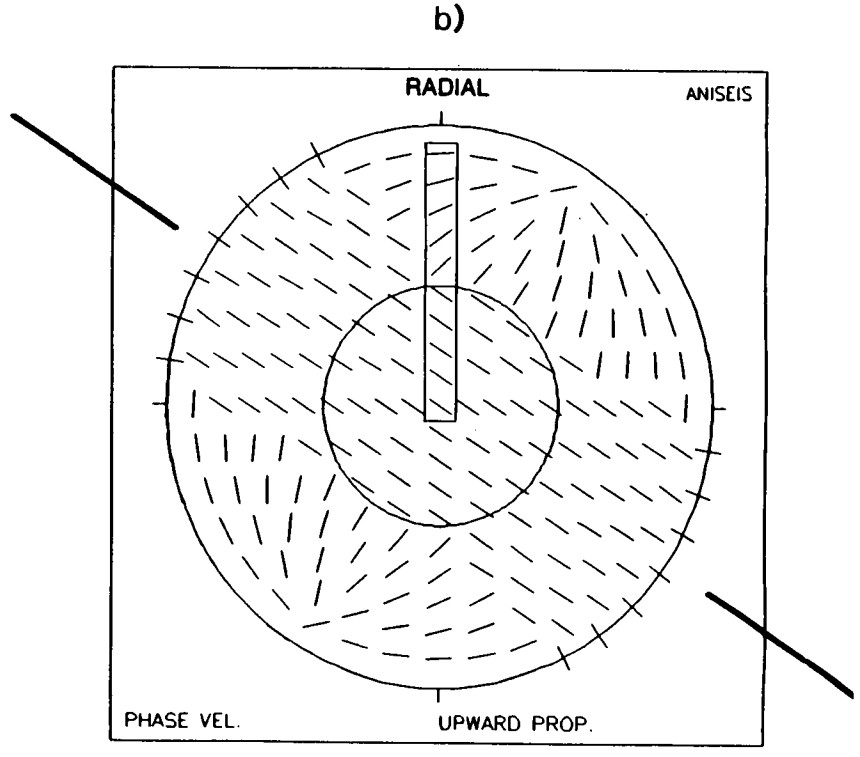

Figure 1.3 a) Geometry of anisotropic model to show how the free surface distorts shear-wave polarizations outside the shear-wave window. Ten subsurface source locations are used, all at 2km distance from the surface receiver, producing incidence angles from 0° to 79°. **b)** Equal area plot showing horizontal projections of the theoretical fast shear-wave polarizations for an anisotropic medium containing parallel, vertical Hudson cracks striking 33° anticlockwise from radial. The inner circle marks the shear-wave window and the boxed area indicates the range of incidences sampled by the model. The incidences marked in a) correspond exactly to the ten theoretical fast shear-waves polarizations given within the boxed area.

ray paths in Figure 1.3a. The abrupt change of *qS1* polarization within the box is not caused by the free surface, but is a result of the fast and slow shear-wave velocity surfaces (which have orthogonal polarizations) crossing over at an intersection singularity.

Figure 1.4a gives the synthetic radial and transverse component seismograms, showing similar arrival times from all source locations, but significantly different wavelet shapes. The PDs in Figure 1.4b represent the horizontal shear-wave motion between 0.8s and 1.0s. The boxed section of the equal area plot showing *qS1* polarizations in Figure 1.3b has been expanded and displayed next to the PDs, such that the ideal *qS1* polarizations can be compared directly to those from the PDs. It can clearly be seen that within the shear-wave window, the *qS1* polarization from the PDs is the same as the ideal *qS1* polarization, but outside the shear-wave window, the modelled shear-wave motion has been distorted, giving no distinct *qS1* polarization.

If the model is reversed (Figure 1.5a) such that there is one source at the surface and ten subsurface geophones, the effects of the free surface are removed from the modelled shear-waves polarizations. Figure 1.5b shows the shear-wave PDs for this reversed model, from which clear differences can be seen in the PDs beyond the shear-wave window compared with the PDs in Figure 1.4b. Where the receivers are away from the free surface, the correct shear-wave polarizations will be recorded at all incidence angles.

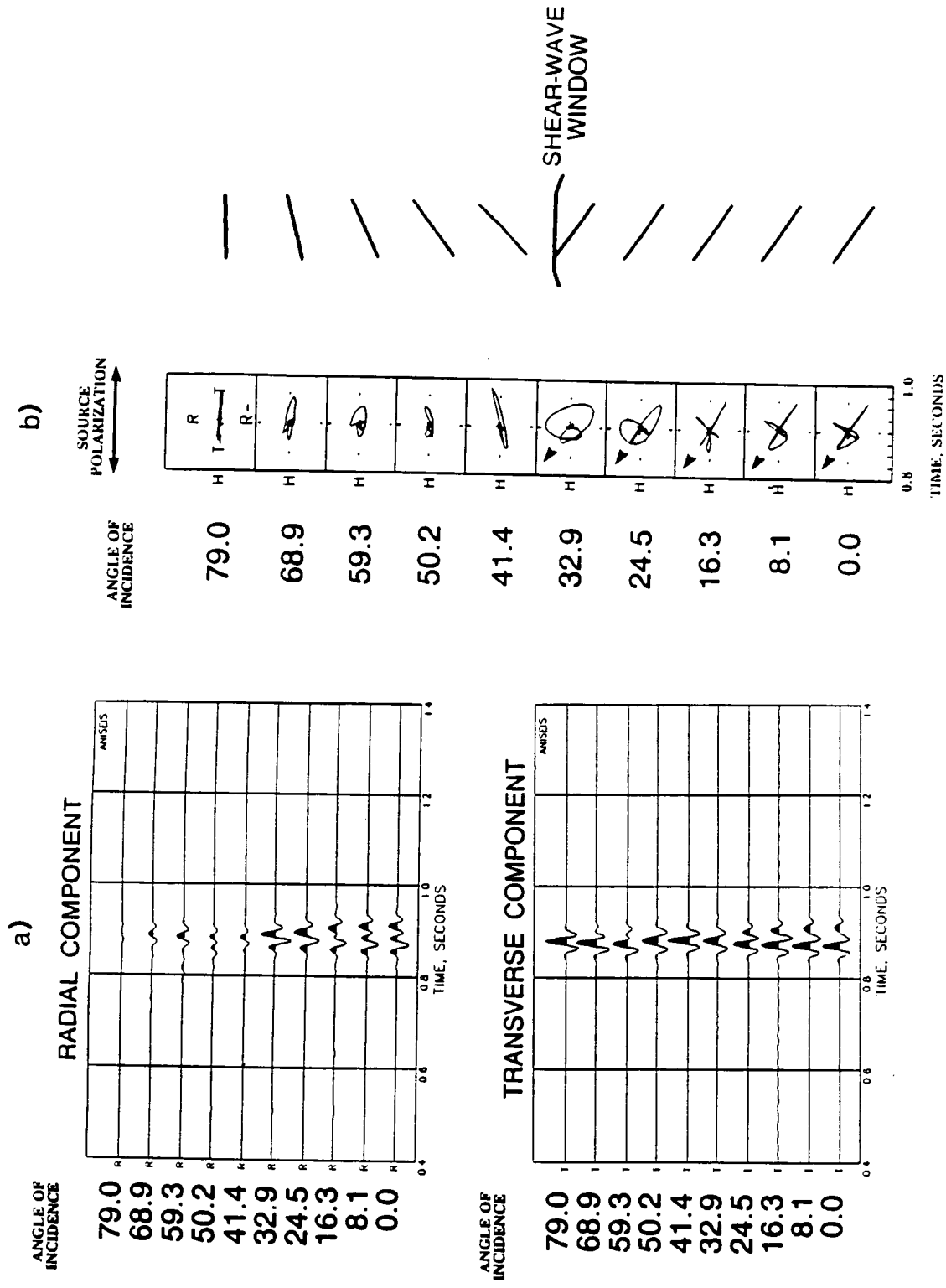

Figure 1.4 a) Radial and transverse component synthetic seismograms from the model in Figure 1.3. **b)** Synthetic, horizontal plane PDs for a time window between 0.8s and 1.0s with initial shear-wave polarizations marked by arrow heads. An expanded version of the theoretical fast shear-wave polarizations in the boxed part of Figure 1.3b is also given. Modelled and theoretical fast shear-wave polarizations agree within the shear-wave window, but beyond this, the modelled shear-waves polarizations are distorted by the free surface. The sudden change of theoretical fast shear-wave polarization at the shear-wave window is a result of the crossing over of the two shear-wave velocity surfaces and not due to the free surface.

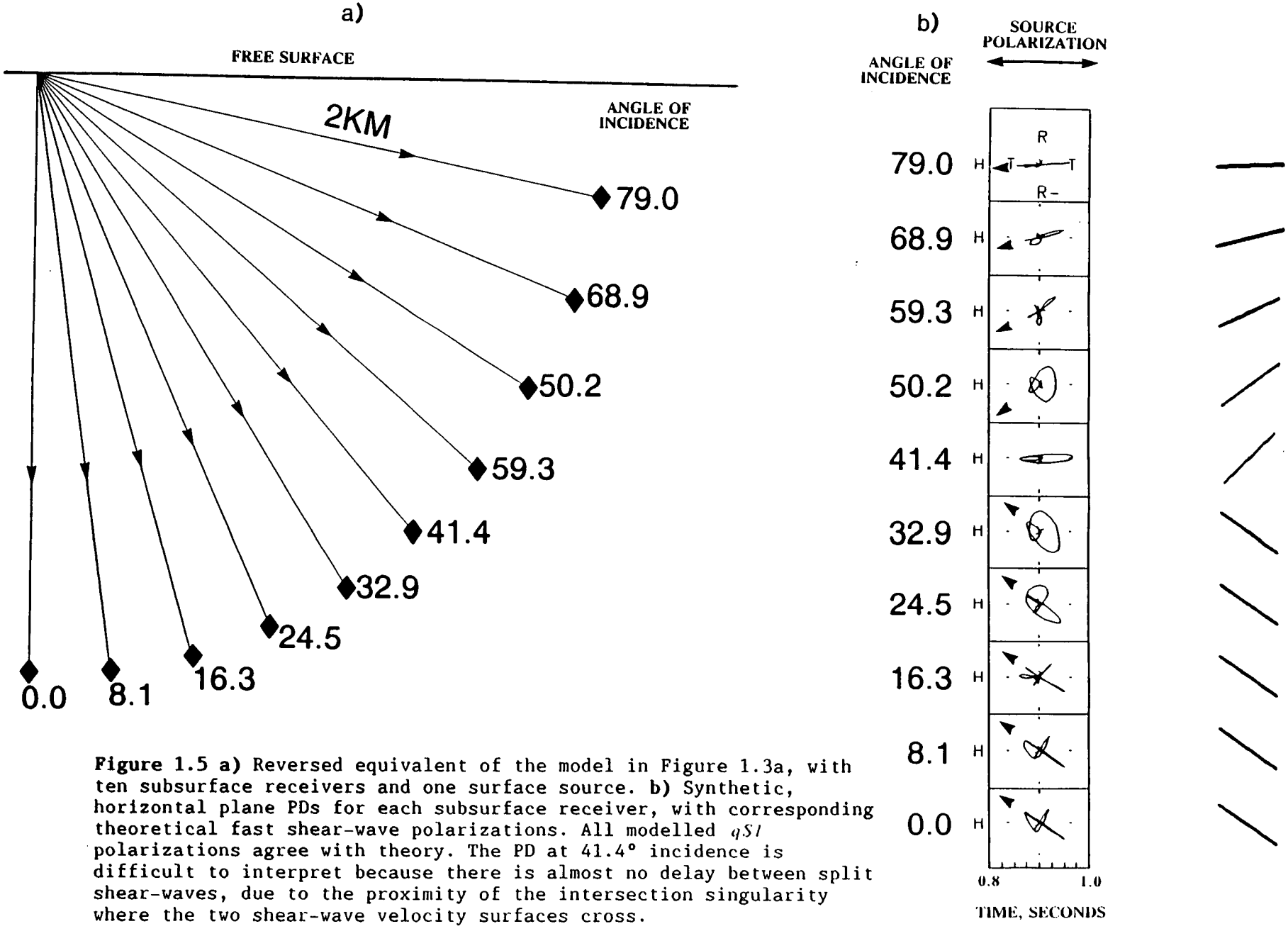

Figure 1.5 a) Reversed equivalent of the model in Figure 1.3a, with ten subsurface receivers and one surface source. **b)** Synthetic, horizontal plane PDs for each subsurface receiver, with corresponding theoretical fast shear-wave polarizations. All modelled *qS1* polarizations agree with theory. The PD at 41.4° incidence is difficult to interpret because there is almost no delay between split shear-waves, due to the proximity of the intersection singularity where the two shear-wave velocity surfaces cross.

Internal interfaces

Subsurface velocity interfaces, like the free surface, can have significant effects on shear-wave polarizations. Liu, Crampin and Yardley (1990) show that in a purely isotropic model, shear-waves with an intermediate polarization between *SV* and *SH* will suffer a distortion of polarization, similar to shear-wave splitting, after being reflected at a plane horizontal interface. In the presence of anisotropy, however, the initial shear-wave polarization is controlled by the anisotropy, such that the polarization distortion caused by reflection is less prominent.

Similar polarization disortions can occur in shear-waves transmitted through velocity interfaces, though the incidence angles involved are usually high. This led Liu and Crampin (1990) to define the *internal shear-wave window*, analogous to the shear-wave window previously defined for incidence at the free surface, except that the behaviour of shear-waves at internal interfaces is more complicated because of additional critical angles.

Cross-hole experiments

Cross-hole experiments, where the source and receivers are all downhole, are the most expensive, and consequently, most infrequently used geometry. They have the great advantage over surface seismic reflection surveys that both source and receivers are away from the free surface and all its associated problems.

Obviously, cross-hole surveys cannot be used as an exploration tool because at least two wells must already exist where the source and receivers can be placed. In a production environment, cross-hole

surveys can be used to provide multiple ray path information between two or more wells which can be used in a tomographic inversion scheme, giving a detailed picture of the velocity structure between the two wells (e.g. see Worthington, 1984).

Liu, Crampin and Booth (1989) have studied synthetic models of shear-wave splitting in cross-hole surveys, where the anisotropy was produced by parallel, vertical Hudson cracks. The theoretical and numerical examples presented in this paper indicate that information about the anisotropic structure causing shear-wave splitting is unlikely to be extracted easily from cross-hole experiments unless sufficient observations can be made at a range of azimuths. This is because shear-wave PDs from cross-hole surveys are difficult to interpret, with less easily recognised information about the crack parameters compared with near vertically propagating shear-waves.

Another problem with cross-hole surveys is that a practical, down hole shear-wave source has yet to be developed, although many attempts are being made (e.g. Aronstam, Kennedy and Wiggins, 1989; Angeleri et al., 1990; Omnes, 1990; Laurent et al., 1990; Safar, 1990).

Vertical seismic profiles

Some of the initial reasons for carrying out VSP surveys were looking ahead of the drill bit, looking around the borehole, estimating physical parameters of the rock, identifying primaries, multiples and *P*-to-*S* converted waves as well as deriving time-depth curves. Noble et al. (1987) give an example where offset VSP surveys were acquired during the initial phase of development drilling of a

new gas field. The VSPs were used to highlight any potential drilling hazards or structural complexities, not seen from surface seismics, which could have an impact on the location of later development wells.

For land-based VSPs, reliable shear-wave sources already exist, such as horizontal vibrators, SYSLAP and OMNIPULSE. Thus VSPs offer an ideal way for investigating shear-wave anisotropy, since the receiver is placed down a borehole, within the area of interest. Since shear-wave polarizations are controlled by the last anisotropic structure seen before arriving at a receiver, any shear-wave splitting recorded by a three-component VSP can be directly interpreted in terms of the anisotropy at depth, something which is not possible with surface recordings of shear-wave splitting. This fact was recognised by Crampin et al. (1986a), where three-component recordings from a shear-wave VSP in the Paris Basin were modelled using the ANISEIS software package, with an anisotropic structure of parallel, vertical Hudson cracks. Bush (1990) went on to refine the model by adding PTL anisotropy to the initial crack anisotropy, thus producing a better match between observed and modelled shear-wave PDs.

In an ideal VSP experiment, many different offsets and azimuths should be used in order that shear-waves sample as much of the anisotropic structure as possible, which helps to keep the number of interpreted anisotropic structures to a minimum. This can be done by placing the source at many different locations around a single borehole.

From the point of view of economics, data interpretation and available technology, VSPs appear to be the best way to record shear-wave splitting.

Chapter 2 - Measuring shear-wave splitting

2.1 Introduction

Until recently, most measurements of shear-wave splitting have been restricted to the visual interpretation of polarization diagrams and manual measurement of the polarization of the leading split shear-wave and the time delay separating the fast and slow shear-waves (e.g. Booth et al., 1985; Kaneshima et al., 1987; Kaneshima et al., 1988; Peacock et al., 1988; Booth et al., 1990; Bush, 1990; Gledhill, 1990). This assumes that both the fast and slow shear-wave arrivals can be correctly identified if both polarization and time delay are to be estimated. Such a method is not only time consuming, but is also subjective so measurements may be significantly different between different interpreters (note that such subjectivity can be minimised by using specified schemes for identifying parameters, as in Chen et al., 1987). Another problem arises when dealing with non-impulsive source shapes, such as VIBROSEIS which is ideally antisymmetric about its arrival time or deconvolved records which may contain symmetric pulse shapes with low amplitude side lobes. In these cases, it is not possible to define objectively a first break arrival time for the leading shear-wave (or slow shear-wave) due to the emergent nature of the pulse. Thus, for small time delays, it may not be possible to recognise the initial polarization direction of the leading split shear-wave. Some other analysis is required that does not rely on identification of first break energy.

Methods have been developed for measuring polarizations and time delays of signals recorded on two components. For example, Kanasewich (1981) uses a polarization analysis to look at the ellipticity of the motion and measure polarizations of the major and minor axes. This has a significant flaw with respect to measuring shear-wave splitting parameters in that the fast and slow shear-wave polarizations are normally unconnected to the polarizations of the major and minor axes of the non-linear shear-wave motion. However, the technique is particularly useful for aligning horizontal geophones from polarization analysis of *P*-wave arrivals.

Other developments have been made where changes in the shape of shear-waves recorded in (for example) the horizontal plane at different locations are attributed to anisotropy. These changes can be interpreted as a constant leading split shear-wave direction and a change in time delay between the two geophone locations which accounts for the difference in shape of the shear-wave motion. Naville (1986) uses a time domain technique where correlation is sought between two geophone levels, with the restriction that the fast and slow shear-wave polarizations must be the same at both geophone levels and the source functions must be similar. The output from this technique is the change in time delay between the two measuring positions. Nicoletis et al. (1988) present a propagator matrix method similar to Naville's, but working in the frequency domain. Here, a transfer function is found relating the shear-wave motion recorded at two depths. This method requires that two orthogonal source polarizations are present, which tends to be a limiting factor in some data sets where only one source polarization has been used. Both techniques are valid only for vertical and near vertical offsets where measurements are made along the same ray path.

A number of further techniques have been devised and published in recent years, some of which are reviewed by MacBeth and Crampin (1990a) and compared by applying them to a set of synthetic VSP data containing typical anisotropy. This Chapter develops three more automatic methods for measuring shear-wave splitting, two based on the spectral interference method working in the frequency domain (MacBeth and Crampin, 1990b), and the other in the time domain using a correlation technique. All methods are applied to synthetic VSP data with added noise to test the consistency of measurements between methods. When dealing with real data, as many different automatic methods as possible should be applied. This can help to determine the reliability of the output shear-wave splitting parameters.

Virtually all automatic methods have been designed primarily to find the polarization angle of the leading split shear-wave and the time delay between the split shear-waves. Crampin (1990a) has suggested that the effects of differential shear-wave attenuation could be used in repeated shear-wave experiments to monitor changes in the contents of the inclusions (such as pore spaces, fractures or stress aligned micro cracks) creating seismic anisotropy. This is particularly appropriate in enhanced oil recovery (EOR) processes where estimates of this quantity could have important implications for reservoir management. This suggests that a third parameter should be measured from shear-wave splitting, from which an estimate of attenuation anisotropy can be made. This Chapter also investigates if it is possible to measure attenuation anisotropy in a practical situation.

2.2 Propagation of split shear-waves

In this section, the differential propagation effects between the two split shear-waves are studied, with the aim of finding out whether it is possible to reliably measure attenuation anisotropy, $\Delta Q/Q$, from shear-wave splitting. The theory here also provides a starting point for understanding the spectral interference method (MacBeth and Crampin, 1990b), leading to two frequency domain techniques for automatically estimating shear-wave splitting.

Figure 2.1 shows the source and receiver orientations for a zero offset VSP (vertically propagating shear-waves). The polarization directions of the fast, *qS1*, and slow, *qS2*, shear-waves are also marked, with the assumption that the split shear-waves have orthogonal polarizations, which is generally true for propagation in nearly vertical directions in distributions of parallel, vertical cracks. In the example presented here, the *H1* geophone and the source polarization are parallel in the X-direction, which simplifies the following analysis.

Given that the angle from the source polarization direction to the polarization of *qS1* is θ (Figure 2.1), the projected amplitudes of the split shear-waves on the *H1* and *H2* geophones can be calulated:-

qS1 H1-component	$s(t)\cos^2\theta;$	(2.2a)
qS1 H2-component	$s(t)\cos\theta\sin\theta;$	(2.2b)
qS2 H1-component	$s(t-\delta t)\sin^2\theta;$	(2.2c)
qS2 H2-component	$-s(t-\delta t)\cos\theta\sin\theta;$	(2.2d)

where $s(t)$ is the source function, and δt is the time delay between the two split shear-waves.

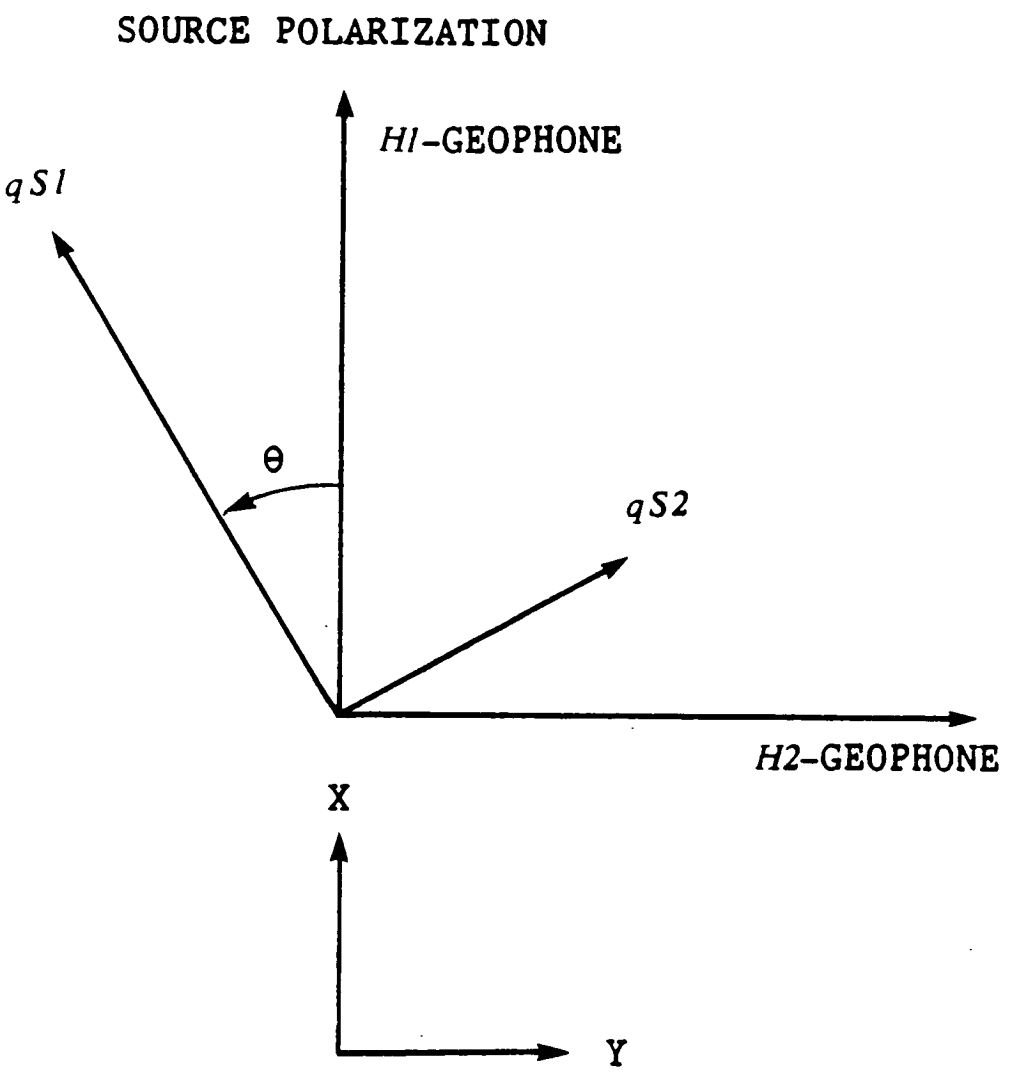

Figure 2.1 Source and receiver orientations for a zero offset VSP. Polarizations of the *qS1* and *qS2* split shear-waves are also marked, with an angle θ between the source and *qS1* directions.

Moving into the frequency domain (replacing $s(t)$ by $S(\omega)$) and including the earth filtering effects of dispersion and absorption and geometrical spreading, the total shear-wave signal recorded on the *H1* and *H2* geophones is the sum of the two split shear-waves:

$$H1(\omega) = S(\omega)\left[\frac{1}{r_1}\cos^2\theta\exp(-iK_1 r_1) \pm \frac{1}{r_2}\sin^2\theta\exp(-iK_2 r_2)\right]; \quad (2.3a)$$

$$H2(\omega) = S(\omega)\left[\frac{1}{r_1}\cos\theta\sin\theta\exp(-iK_1 r_1) \pm \frac{1}{r_2}\cos\theta\sin\theta\exp(-iK_2 r_2)\right]; \quad (2.3b)$$

where K_1 and K_2 are the complex propagation constants of the two shear-waves that have travelled distances r_1 and r_2 respectively. K_1 and K_2 are given by:

$$K_1 = \frac{\omega}{c_1} - i\alpha_1; \quad (2.4a)$$

$$K_2 = \frac{\omega}{c_2} - i\alpha_2; \quad (2.4b)$$

where c_1 and c_2 are the phase velocities and α_1 and α_2 are the absorption coefficients of the fast and slow shear-waves, respectively, and all are functions of frequency. Equation (2.3) demonstrates that a change in the sign of the *qS1* direction (from a positive angle to a negative angle with respect to the source polarization) will alter only the sign of the *H2*-component.

By writing K_2 in terms of $K_1 + \Delta K$ and r_2 as $r_1 + \Delta r$, it is possible to separate out the common earth effects operating on both shear-waves from the differential effects which apply to the slow

shear-wave only. In this way, the slow shear-wave term in equation (2.3) can be expressed as the fast shear-wave multiplied by some correction factor. This has been done in the equations below, where terms in $\Delta K \Delta r$ have been ignored:

$$H1(\omega) = \frac{1}{r_1} S(\omega)\exp(-iK_1 r_1)\ [A + C\,H \exp(-i(\Delta K r_1 + K_1 \Delta r))]; \qquad (2.5a)$$

$$H2(\omega) = \frac{1}{r_1} S(\omega)\exp(-iK_1 r_1)\ [B - B\,H \exp(-i(\Delta K r_1 + K_1 \Delta r))]; \qquad (2.5b)$$

where $A = \cos^2\theta$; $B = \cos\theta \sin\theta$; $C = \sin^2\theta$; $H = 1/(1 + \Delta r/r_1)$.

This shows the not unexpected result that any differences between the slow shear-wave and fast shear-wave (arrival time, amplitude and frequency content) can be attributed to differences between the complex propagation constants and differences in the ray paths of the two shear-waves. All the path difference effects can be ignored if $\Delta r/r_1 \ll 1$, which is true for weak anisotropy and raypaths where the effects of reflection and refraction can be ignored.

The way forward now is to express ΔK in terms of the differential velocity, Δc, and differential attenuation, ΔQ. This is done by first considering the differential absorption, $\Delta\alpha$, and then finding a link between this and the differential attenuation:

Letting $\Delta c = c_1 - c_2$ $\quad \Delta c \geq 0$; (2.6)

and $\Delta\alpha = \alpha_2 - \alpha_1$ $\quad \Delta\alpha \geq 0$ i.e. slow shear-wave suffers greater absorption; (2.7)

the real part of the slow shear-wave propagation constant, K_2 can be written:

$$\mathrm{Re}(K_2) = \frac{\omega}{c_2} = \frac{\omega}{c_1 - \Delta c} \approx \frac{\omega}{c_1} + \frac{\omega}{c_1} \cdot \frac{\Delta c}{c_1}; \qquad (2.8a)$$

where non linear powers of $\Delta c / c_1$ have been ignored in the Binomial expansion, and the imaginary part of K_2 is:

$$\mathrm{Im}(K_2) = \alpha_2 = \alpha_1 + \Delta\alpha. \qquad (2.8b)$$

Using $\Delta K = K_2 - K_1$ and subtracting equation (2.4a) from (2.8):

$$\Delta K = \frac{\omega \, \Delta c}{c_1^{\,2}} - i\Delta\alpha. \qquad (2.9)$$

Futterman (1962) formulated an expression linking the absorption coefficient to the energy loss per cycle, Q^{-1}, (referred to as the attenuation factor in this text) which is consistent with the analysis of Mason (1958):

$$Q^{-1}(\omega) = \frac{2\alpha(\omega)\, c}{\omega}; \qquad (2.10)$$

where the only intrinsic dependence on frequency occurs in α. Similar results have been obtained by Ganley and Kanasewich (1980). For many earth materials, the absorption coefficient, α, has been shown to vary linearly with frequency (Knopoff and MacDonald, 1958), implying that Q is independent of frequency. Thus, the absorption coefficient can be written:

$$\alpha(\omega) = \frac{\omega}{2\, c Q} \qquad (2.11)$$

Letting Q_1 and Q_2 be Q factors for the fast and slow shear-waves, respectively, and letting the difference between Q_1 and Q_2 be ΔQ, an explicit expression for the slow shear-wave absorption coefficient, $\alpha_2(\omega)$, can be written in terms of Q_1, ΔQ, c_1 and Δc:

$$\alpha_2(\omega) = \frac{\omega}{2c_2Q_2} = \frac{\omega}{2(c_1-\Delta c)(Q_1-\Delta Q)}. \qquad (2.12)$$

Ignoring terms in $\Delta c\Delta Q$ and powers of $\Delta c/c_1$ and $\Delta Q/Q_1$:

$$\alpha_2(\omega) \simeq \frac{\omega}{2c_1Q_1} + \frac{\omega}{2c_1Q_1}\frac{\Delta c}{c_1} + \frac{\omega}{2c_1Q_1}\frac{\Delta Q}{Q_1} = \alpha_1(\omega) + \Delta\alpha(\omega). \qquad (2.13)$$

Thus,

$$\Delta\alpha(\omega) = \alpha_1(\omega)\left[\frac{\Delta c}{c_1} + \frac{\Delta Q}{Q_1}\right]. \qquad (2.14)$$

This shows that the differential absorption coefficient depends on the sum of velocity and attenuation anisotropies as well as the background absorption, α_1. Hence, a differential absorption can arise even when there is no attenuation anisotropy. This is due to the shorter wavelength of *qS2* compared to *qS1*, resulting in a greater energy loss over the same distance. In this context, the *qS1* attenuation factor, Q_1, is known as the background attenuation, since its value affects both shear-waves.

Substituting (2.14) into (2.9) and using result in (2.5), the following expressions for the *H1*- and *H2*-component frequency spectra can be derived:

$$H1(\omega) = \frac{1}{r_1} S(\omega)\exp(-iK_1r_1)$$

$$[A + C\,H\exp(-ik_1r_1(\frac{\Delta c}{c_1} + \frac{\Delta r}{r_1}))\exp(-\alpha_1r_1(\frac{\Delta c}{c_1} + \frac{\Delta Q}{Q_1} + \frac{\Delta r}{r_1}))]; \qquad (2.15a)$$

$$H2(\omega) = \frac{1}{r_1} S(\omega)\exp(-iK_1 r_1)$$

$$[B - B\,H\exp(-ik_1 r_1(\frac{\Delta c}{c_1} + \frac{\Delta r}{r_1}))\exp(-\alpha_1 r_1(\frac{\Delta c}{c_1} + \frac{\Delta Q}{Q_1} + \frac{\Delta r}{r_1}))]; \qquad (2.15b)$$

where $k_1 = \mathrm{Re}(K_1)$.

These equations show the explicit dependence of the slow shear-wave on the two independent variables defining the anisotropy: $\Delta c/c_1$, the velocity anisotropy which is connected to the real elastic constants (and upon which Δr is dependent); and $\Delta Q/Q_1$, the attenuation anisotropy, which is connected to the imaginary elastic constants. Equation (2.15) can be rewritten:

$$H1(\omega) = \frac{1}{r_1} S(\omega)\exp(-iK_1 r_1)\ [A + C\,H\exp(-i\omega\delta t)\exp(-\omega\delta\gamma)]; \qquad (2.16a)$$

$$H2(\omega) = \frac{1}{r_1} S(\omega)\exp(-iK_1 r_1)\ [B - B\,H\exp(-i\omega\delta t)\exp(-\omega\delta\gamma)]; \qquad (2.16b)$$

$$\text{where } \delta t = \frac{r_1}{c_1}(\frac{\Delta c}{c_1} + \frac{\Delta r}{r_1}) \qquad (2.17)$$

$$\text{and } \delta\gamma = \frac{1}{2Q_1}(\delta t \div \frac{r_1}{c_1} \cdot \frac{\Delta Q}{Q_1}) = \frac{t_1}{2Q_1}(\frac{\delta t}{t_1} + \frac{\Delta Q}{Q_1}); \qquad (2.18a)$$

where δt and $\delta\gamma$ are observable quantities. δt is the time delay between the two split shear-waves and $\delta\gamma$ is defined as the *differential damping factor* between the two split shear-waves, and as such may provide a way of estimating attenuation anisotropy. Rearranging equation (2.18a) so that $\Delta Q/Q_1$ is the dependent variable:

$$\frac{\Delta Q}{Q_1} = \frac{Q_1 \delta\gamma - \delta t}{t_1} \; ; \qquad (2.18b)$$

from which it can be seen that the attenuation anisotropy is a function of four observable quantities: time delay, δt; *qS1* arrival time, t_1; *qS1* attenuation, Q_1; and the differential damping factor, $\delta\gamma$. As a result, any estimate of attenuation anisotropy may have a very large error associated with it because errors in the four observables will all make a contribution to the error in $\Delta Q/Q_1$.

Methods already exist for measuring t_1 and Q_1, and recent developments have been made in automatically estimating δt. The differential damping factor, $\delta\gamma$, however, has not been studied in any published literature, so techniques for estimating its value must be found if the attenuation anisotropy is to be calculated. One possibility is to work in the frequency domain, and consider spectral interference patterns formed by split shear-waves.

2.3 The spectral interference method

The theory behind this method is briefly outlined below, using the same notation as section 2.2 and following closely that of MacBeth and Crampin (1990b). Letting $P_1(\omega)$ and $P_2(\omega)$ be the power spectra of $H1(\omega)$ and $H2(\omega)$ respectively, MacBeth and Crampin show that interference patterns $I_1(\omega)$ and $I_2(\omega)$ can be extracted from the power spectra by dividing $P_1(\omega)$ and $P_2(\omega)$ by the sum of $P_1(\omega)$ and $P_2(\omega)$, giving:

$$I_1(\omega) = \frac{P_1(\omega)}{P_1(\omega) + P_2(\omega)} \; ; \qquad (2.19a)$$

and

$$I_2(\omega) = \frac{P_2(\omega)}{P_1(\omega) + P_2(\omega)} \; . \qquad (2.19b)$$

Further interference patterns can be set up by considering the difference between the phase spectra of the two components. Following MacBeth and Crampin, the phase of the two components can be written:

$$\phi_1(\omega) = \text{Arg}[H1(\omega)] = \phi_s(\omega) + \phi^1{}_i(\omega); \tag{2.20a}$$

$$\phi_2(\omega) = \text{Arg}[H2(\omega)] = \phi_s(\omega) + \phi^2{}_i(\omega); \tag{2.20b}$$

where $\phi_1(\omega)$ and $\phi_2(\omega)$ are the phase spectra of $H1(\omega)$ and $H2(\omega)$ respectively, $\phi_s(\omega)$ is the phase spectrum of the source modified by transmission effects other than splitting, and $\phi^1{}_i(\omega)$ and $\phi^2{}_i(\omega)$ are the perturbations of $\phi_s(\omega)$ due to interference between the two split shear-waves. $\phi_s(\omega)$ in (2.20) can be removed by subtracting (2.20b) from (2.20a):

$$\delta\phi(\omega) = \phi_1(\omega) - \phi_2(\omega) = \phi^1{}_i(\omega) - \phi^2{}_i(\omega), \tag{2.21}$$

or in terms of the real and imaginary components of $H1(\omega)$ $[= X^R + iX^I]$ and $H2(\omega)$ $[= Y^R + iY^I]$:

$$\delta\phi(\omega) = \tan^{-1} \frac{X^I Y^R - X^R Y^I}{X^I Y^I - X^R Y^R} \tag{2.22}$$

The real value of these interference patterns is that they are entirely independent of the source function and highlight only the differential propagation effects between the fast and slow shear-waves. This means that observations can be compared directly to theoretical formulations, using the expressions for $H1(\omega)$ and $H2(\omega)$ in (2.16) without having to know the source function. A good match between observations and theory will require the correct choice of

fast shear-wave polarization, time delay and differential damping factor. This forms the basis of an inversion procedure that automatically measures shear-wave splitting, discussed in section 2.5. However, it should be noted that the interference patterns described by equations (2.19) and (2.22) are insensitive to the sign of the *qS1* polarization relative to the source polarization, giving rise to an ambiguity in any *qS1* direction estimated from these interference patterns.

2.4 Effects of differential damping on interference patterns

MacBeth and Crampin (1990b) described the effects of time delay and polarization angle of the leading split shear-wave on the interference patterns in some detail while background attenuation and attenuation anisotropy were only lightly touched on. The following section gives some examples of how attenuation can significantly change the shape of the phase interference patterns, leading to the possiblity of monitoring changes in differential damping in repeated shear-wave experiments.

Interference patterns with no attenuation

Figure 2.2 shows the theoretical interference patterns for vertical propagation (such that $\Delta r = 0$) created using equations (2.19) and (2.22) where $H1(\omega)$ and $H2(\omega)$ were calculated from equation (2.16) with the parameters for models 1 and 2, given in Table 2.1. The patterns are plotted between frequencies 5Hz and 45Hz, representing a typical bandwidth in VSP surveys. The power interference patterns for the *H1*- and *H2*-components are given, while only the *H1*-component phase interference pattern is shown.

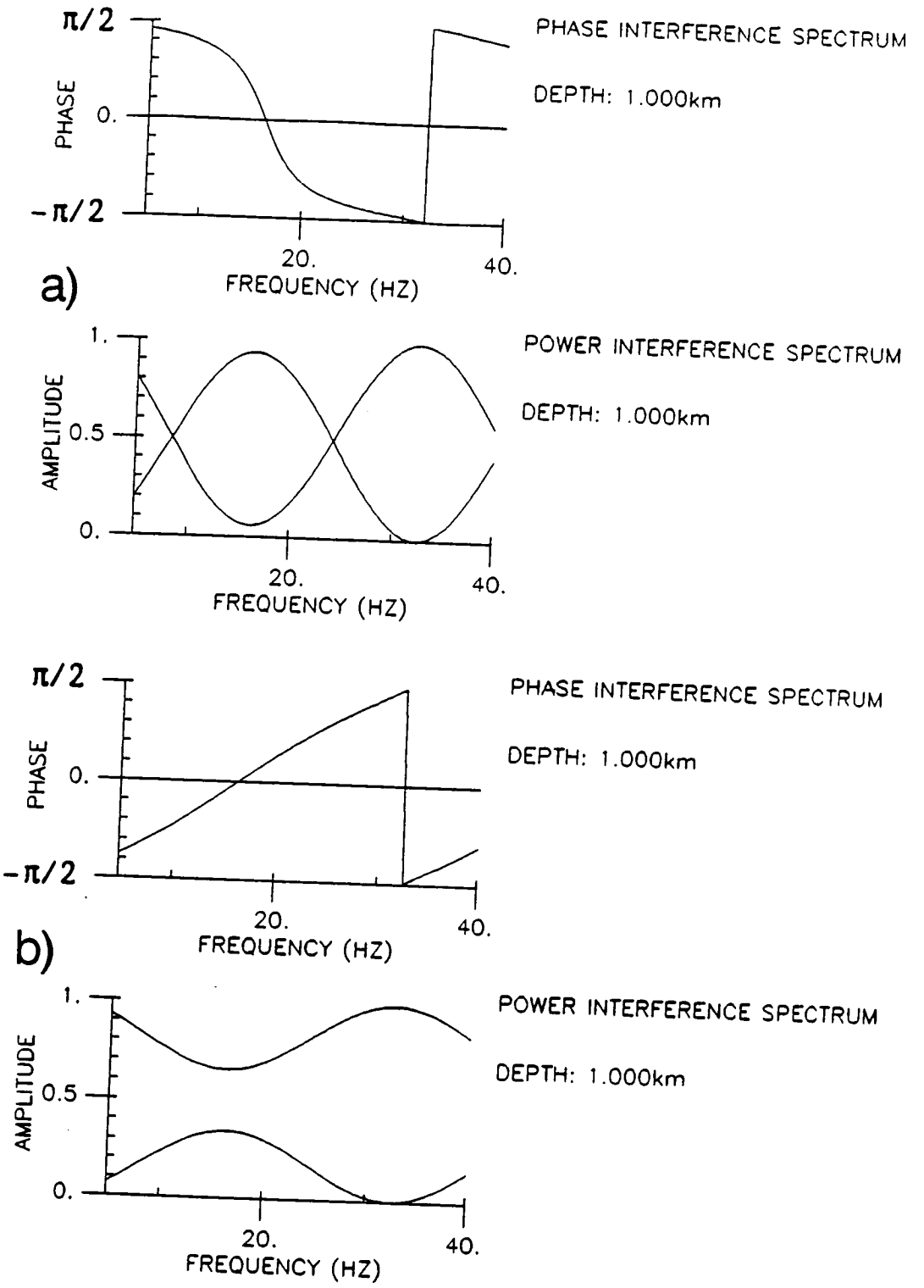

Figure 2.2 Spectral interference patterns created using equations (2.16), (2.19) and (2.22). **a)** Parameters from model 1 in Table 2.1. **b)** Parameters from model 2 in Table 2.1. No attenuation is present.

Model	θ (°)	c_1 (km/s)	Q_1	$\Delta c/c_1$ (%)	$\Delta Q/Q_1$ (%)	r_1 (km)
1	-52	1.3	∞	4	0	1
2	18	1.3	∞	4	0	1
3	-52	1.3	50	4	0	1
4	18	1.3	50	4	0	1
5	-52	1.3	∞	4	0	0.25
6	-52	1.3	50	4	0	0.25

Table 2.1

With neither fast or slow shear-wave attenuated, the interference patterns are fairly straight forward to interpret. Using MacBeth's results that the distance (in Hz) between every turning point along the frequency axis of the power interference spectrum corresponds to $1/2\delta t$, a time delay of 32ms can be measured. Similarly, the distance (in Hz) between every continuous zero phase crossing of the phase interference spectrum (only one at 17Hz in these Figures) should also correspond to $1/2\delta t$, but in this model, the distance between continuous crossings of the phase axis is $1/\delta t$. The reason for this is explained below.

Background attenuation

When an background Q factor of 50 is introduced to models 1 and 2, keeping all the other parameters the same (models 3 and 4 in Table 2.1), the interference patterns shown in Figure 2.3 are produced. Although $\Delta Q/Q_1$ remains zero in this model, differential damping will still arise from the velocity anisotropy as indicated in equation (2.18a). As MacBeth predicted, the introduction of attenuation has produced no difference between the power interference patterns in Figures 2.2 and 2.3. However, there are substantial differences between the phase interference patterns.

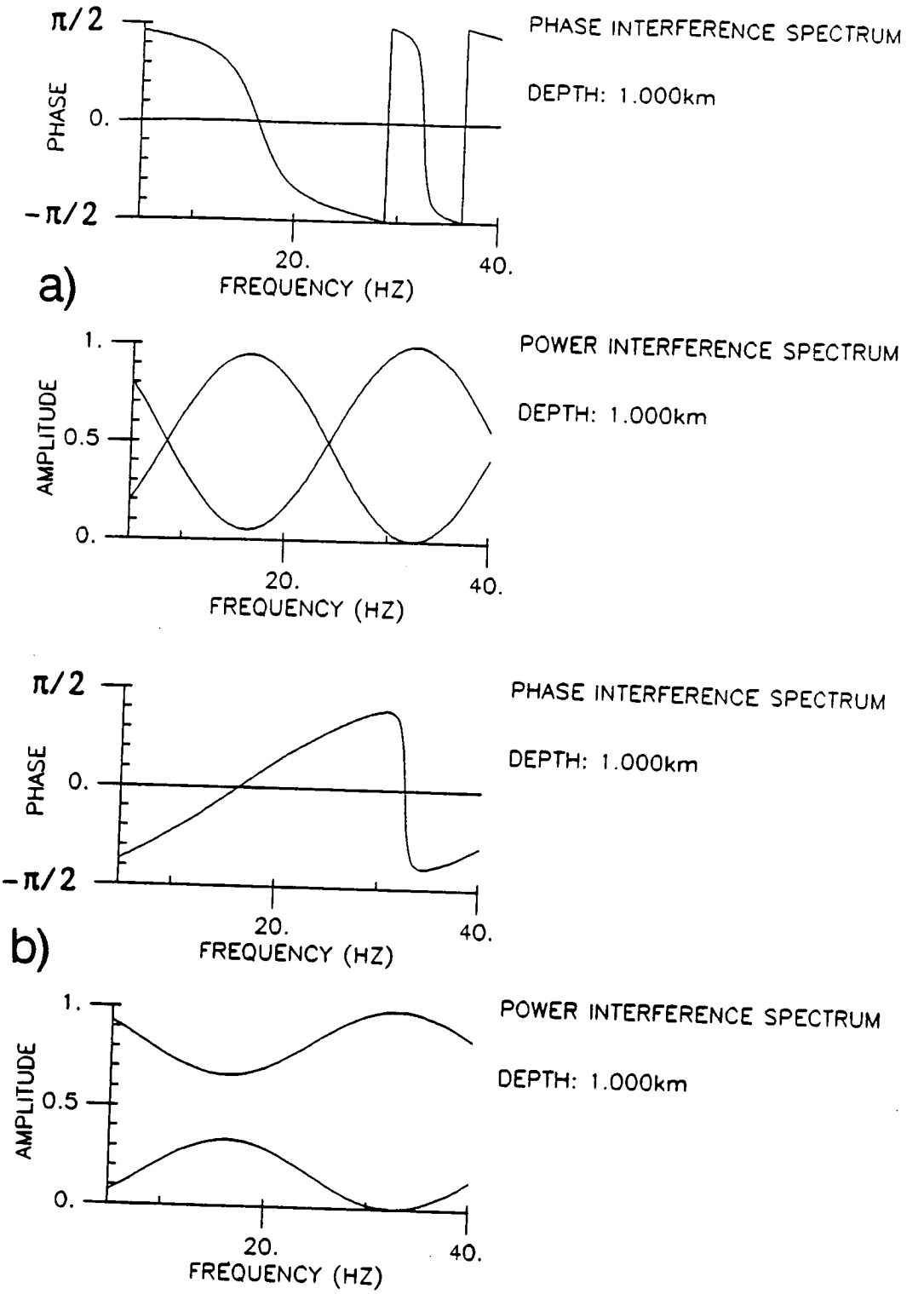

Figure 2.3 Spectral interference patterns from parameters specified in **a)** model 3 and **b)** model 4 in Table 2.1, with added background attenuation producing changes to the phase interference spectrum compared to Figure 2.2.

In the phase interference spectrum of Figure 2.3a, two discontinuities, or sudden changes from $-\pi/2$ to $\pi/2$, now exist where there was only one before and these surround a new continuous zero crossing which occurs at the position of the old discontinuity (32.5Hz). Thus, the distance along the frequency axis between continuous zero crossings is $1/2\delta t$ as predicted. The continuous crossing at 17Hz in Figure 2.2a remains the same in Figure 2.3a. The reasons for these effects can be seen when the real and imaginary parts of $H1(\omega)$ and $H2(\omega)$ in equation (2.16) are substituted into the expression for the phase interference pattern (equation 2.22). After some algebra, the final result is:

$$\delta\phi(\omega) = \tan^{-1} \frac{-G\,H\sin(\omega\delta t)}{C\,H\,G\,(D\,H\,G - D - F\,H\,G) - A\,(1 - D\,H\,G)}, \qquad (2.23)$$

where A, C, H have been defined earlier and $D = \cos(\omega\delta t)$; $F = -\sin(\omega\delta t)$; $G = \exp(-\omega\delta\gamma)$.

The continuous crossings of zero phase occur when the numerator in the above expression is zero ($\omega\delta t = n\pi$) and the denominator is non zero. This is independent of $\delta\gamma$, so these zero crossings will remain in the same place on the frequency axis regardless of how much differential damping is present. Discontinuous jumps across zero phase happen when the denominator becomes zero. Zero roots of the denominator are dependent on the differential damping between $qS1$ and $qS2$, and θ, the polarization of $qS1$ relative to the source polarization. In the case of no differential damping ($Q_1 = \infty$), zeros in the denominator occur at the same values of frequency as every second zero in the numerator.

In Figure 2.2a the discontinuous crossing of the phase axis "hides" a continuous crossing, which is revealed by the presence of differential damping in Figure 2.3a. In general, the discontinuities will move further apart as the differential damping increases.

The phase interference spectrum in Figure 2.3b has been altered in a different way to that in Figure 2.3a. Instead of introducing another discontinuity into the interference pattern, differential damping has had a smoothing effect. A qualitative explanation for this is that for *qSI* polarizations less than 45° from the source polarization ($\theta<45°$), the introduction of differential damping results in there being no zero roots of the denominator in equation (2.23). For a simpler understanding of the problem, the expression describing the denominator of equation (2.23) should be compared to the equation $y=\sin^2 x+c$, where y represents the value of the denominator and x is analogous to the frequency. For no differential damping, $c=0$ and y has one zero root at every $x=n\pi$ $\{n\varepsilon I\}$, where a discontinuity occurs in the phase interference spectrum. For $\theta<45°$, c is defined to be positive such that there are no zero roots for y, and the denominator is never zero resulting in no discontinuities in the phase interference spectrum. For $\theta>45°$, c is defined to be negative, so there are two zero roots for y at $x=n\pi\pm\sin^{-1}\sqrt{c}$, giving two discontinuities in the phase interference spectrum at every $x=n\pi$.

Results here indicate that the effects of differential damping are most prominent on the phase interference spectrum when the angle between the source polarization and the fast shear-wave is greater than 45°. However, this asusumes that the most sensitive part of the phase interference pattern to differential damping is present within

the bandwidth of the signal. Models 5 and 6 in Table 2.1 have a reduced path length, producing a time delay of 8ms, with $Q_1=\infty$ and $Q_1=50$ respectively. The interference patterns for these models are shown in Figure 2.4, and demonstrate that the presence of attenuation has had no effect on the phase interference patterns, because the discontinuous zero phase crossing in model 1 is now outside the frequency bandwidth.

Attenuation anisotropy

The effect of including attenuation anisotropy is indistinguishable from increasing the background attenuation (decreasing Q_1). This can be seen from equation (2.18a) where the same differential damping factor can be obtained from different values of ΔQ by altering Q_1, leading to identical phase interference patterns. Hence the conclusion at the end of section 2.2 still stands that attenuation anisotropy cannot be directly measured, but must be calculated as a function of the observables Q_1, $\delta\gamma$, t_1 and δt, which all contain errors.

Even in repeated experiments, such as monitoring EOR, changes in the phase interference pattern cannot be attributed to changes in $\Delta Q/Q_1$ alone, without knowing how Q_1 has changed (assuming that changes in t_1 and δt can be identified). This is especially true if the interference patterns are not well defined due to a small time delay relative to the bandwidth. In this situation, the presence of background attenuation and attenuation anisotropy will have no effects on the interference paterns, as Figure 2.4 demonstrates. The problem of measuring changes in attenuation anisotropy from repeated experiments is dealt with again in section 2.6

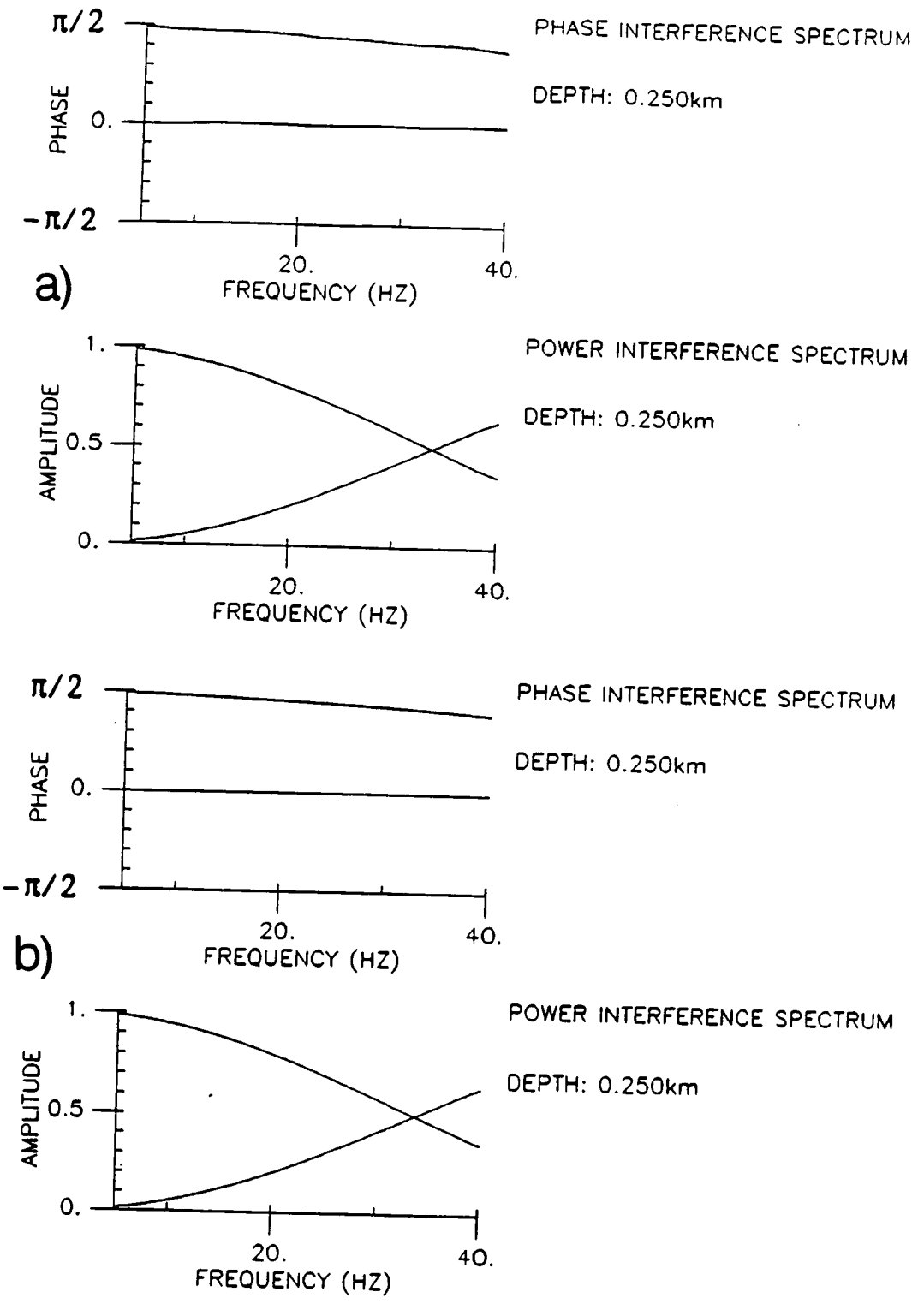

Figure 2.4 Spectral interference patterns from **a)** model 5 and **b)** model 6 parameters in Table 2.1. The time delay has been reduced to a quarter of its value in Figures 2.2 and 2.3. The presence of attenuation no longer has any effect on the phase interference spectrum in **b)**

2.5 Attenuation anisotropy from spectral ratios

One of the most commonly used methods for estimating isotropic attenuation is spectral ratios, described by Ganley and Kanasewich (1980). Application of this method to split shear-waves is investigated to determine whether shear-wave attenuation anisotropy can be estimated more easily compared to using spectral interference patterns.

If the polarization of the fast shear-wave is known, the two horizontal components, $H1(\omega)$ and $H2(\omega)$, can be rotated such that one component contains only the fast shear-wave - $S1(\omega)$, and the other component contains the slow shear-wave - $S2(\omega)$:

$$S1(\omega) = S(\omega) \frac{1}{r_1} \cos\theta \exp(-i\omega t_1) \exp(-\alpha r_1); \qquad (2.24a)$$

$$S2(\omega) = S(\omega) \frac{1}{r_2} \sin\theta \exp(-i\omega t_2) \exp(-\alpha r_2). \qquad (2.24b)$$

If it is assumed that the difference between r_1 and r_2 is negligible (writing r_1 in place of r_2) and $S1(\omega)$ is multiplied by $\sin\theta$ and $S2(\omega)$ is multiplied by $\cos\theta$, then the logarithm of the spectral ratio between $|S1(\omega)|$ and $|S2(\omega)|$ gives:

$$R_{21} = \ln \frac{|S2(\omega)|}{|S1(\omega)|} = (\alpha_2 - \alpha_1) r_1 = \Delta\alpha r_1. \qquad (2.25)$$

Without pre-multiplying $S1(\omega)$ and $S2(\omega)$ by $\sin\theta$ and $\cos\theta$ respectively, the expression for R_{21} would include a frequency independent constant. Assuming that absorption is a linear function

of frequency, then a plot of R_{12} versus frequency should give a straight line if the absorption coefficient is a linear function of frequency (Knopoff and MacDonald, 1958), passing through the origin, with gradient m_{21}, where

$$m_{21} = \frac{1}{Q_1}\left[\frac{\delta t}{t_1} + \frac{\Delta Q}{Q_1}\right]\pi t_1. \tag{2.26}$$

Equation (2.14) relating $\Delta\alpha$ to ΔQ and Q_1 was used in the above expression, with $\delta t/t_1$ being written in preference to $\Delta c/c_1$. The factor of π comes from $\omega=2\pi f$. The apparent difference in attenuation between $S1(\omega)$ and $S2(\omega)$, Q_d, can be written from (2.26) as:

$$Q_d = Q_1 \frac{1}{\delta t/t_1 + \Delta Q/Q_1}. \tag{2.27}$$

This clearly shows that Q_d is not an explicit expression for the attenuation anisotropy. Rearranging equation (2.27) so that $\Delta Q/Q_1$ is the dependent variable:

$$\frac{\Delta Q}{Q_1} = \frac{Q_1}{Q_d} - \frac{\delta t}{t_1}, \tag{2.28}$$

giving a similar expression for shear-wave attenuation anisotropy to that obtained from spectral interference in section 2.2. Comparison of equations (2.28) and (2.18b) shows that the method of spectral ratios has no distinct advantage over spectral interference other than that the measurement of Q_d may be easier. It can also be seen that

$$\frac{1}{Q_d} = \frac{\delta\gamma}{t_1}, \tag{2.29}$$


EX BIBL. U.C.N.W. BANGOR

giving a physical understanding for the differential damping factor, $\delta\gamma$, in terms of the difference in attenuation (not the attenuation anisotropy) affecting the two split shear-waves.

This section shows that even when the spectral ratio technique is used to determine attenuation anisotropy, the same problem found with spectral interference occurs, that the absolute attenuation, Q_1, and the absolute arrival time, t_1, of the faster split shear-wave must be known. At first, this appears to go against what one might have expected, since the difference in arrival times of the two split shear-waves can be estimated without knowing any other parameter.

However, knowledge of the time delay alone gives no information about the anisotropy other than that it exists. The absolute arrival time of the faster split shear-wave must also be known before the velocity anisotropy can be estimated from $\delta t / t_1$. Hence, it is not so unreasonable to expect that where the attenuation anisotropy depends on two directly observable differential quantities, δt and Q_d (or $\delta\gamma$), two absolute quantities (t_1 and Q_1) must also be known before an estimate of the attenuation anisotropy can be made.

2.6 Monitoring changes in attenuation anisotropy from repeated shear-wave experiments

The previous two sections have discussed measurement of attenuation anisotropy from single recordings of split shear-waves. Where shear-wave experiments are repeated over a period of time, for example during EOR processes, temporal changes in attenuation anisotropy may occur as the pore fluid content is altered and/or the

shapes or sizes of the pores change. This could provide a way of monitoring the movement of fluids injected into a reservoir, or the front of a thermal flood, thus helping with the exploitation of an oilfield.

Ultimately, the aim is to measure

$$\frac{\Delta Q^a}{Q_1^a} - \frac{\Delta Q^b}{Q_1^b}$$

where $\Delta Q^a / Q_1^a$ is the attenuation anisotropy measured from the initial shear-wave experiment, and $\Delta Q^b / Q_1^b$ is the attenuation anisotropy measured from some subsequent, identical, experiment, performed at a later time during EOR. Given the previously described problems associated with single measurements of $\Delta Q / Q_1$, is it any easier to measure differences in attenuation anisotropy from identical repeated experiments?

Model

Consider two repeated shear-wave experiments, "a" and "b". Expressions for the fast and slow shear-waves from each experiment can be written:

$$S1(\omega)^a = S(\omega) \frac{1}{r} \cos\theta \exp(-i\omega t_1^a) \exp(-\alpha^a r); \qquad (2.30a)$$

$$S2(\omega)^a = S(\omega) \frac{1}{r} \sin\theta \exp(-i\omega t_1^a) \exp(-i\omega\delta t^a) \exp(-\alpha^a r) \exp(-\Delta\alpha^a r); \qquad (2.30b)$$

and

$$S1(\omega)^b = S(\omega) \frac{1}{r} \cos\theta \exp(-i\omega t_1^b) \exp(-\alpha^b r); \qquad (2.30c)$$

$$S2(\omega)^b = S(\omega)\ \frac{1}{r}\ \sin\theta\ \exp(-i\omega t_1{}^b)\ \exp(-i\omega\delta t^b)\ \exp(-\alpha^b r)\ \exp(-\Delta\alpha^b r). \tag{2.30d}$$

It is assumed that all the shear-wave raypaths are approximately equal (written as r), and the polarizations of the split shear-waves do not change between experiments (true if the symmetry and orientation of the anisotropic structure remain constant).

Following the same type of analysis presented in the previous section, spectral ratios can be used to estimate apparent changes in attenuation between the two experiments. The problem remains whether these apparent changes can be related to actual changes in attenuation anisotropy. A total of six different ratios can be calculated from the four expressions (2.30a-d): $S1^a/S1^b$; $S2^a/S2^b$; $S2^a/S1^a$; $S2^b/S1^b$; $S2^a/S1^b$; $S2^b/S1^a$. Taking the two fast shear-waves first:

$$R_{11} = \ln \frac{|S1(\omega)^a|}{|S1(\omega)^b|} = C_{11} + \left[\frac{t_1{}^b}{Q_1{}^b} - \frac{t_1{}^a}{Q_1{}^a} \right] \pi f. \tag{2.31}$$

A plot of this expression versus frequency should yield a straight line if the absorption coefficient is a linear function of frequency (Knopoff and MacDonald, 1958) with gradient m_{11}:

$$m_{11} = \frac{t_1{}^b}{Q_1{}^b} - \frac{t_1{}^a}{Q_1{}^a}\ . \tag{2.32}$$

where the factor of π has been removed. Similar expressions can be obtained using the ratios between the fast and slow shear-waves from both experiments:

$$m_{21}{}^{a} = \frac{t_1{}^{a}}{Q_1{}^{a}} \left[\frac{\delta t^{a}}{t_1{}^{a}} + \frac{\Delta Q^{a}}{Q_1{}^{a}} \right]; \tag{2.33}$$

$$m_{21}{}^{b} = \frac{t_1{}^{b}}{Q_1{}^{b}} \left[\frac{\delta t^{b}}{t_1{}^{b}} + \frac{\Delta Q^{b}}{Q_1{}^{b}} \right]. \tag{2.34}$$

The remaining three possible gradients from the ratios, $S2^{a}/S2^{b}$, $S2^{a}/S1^{b}$ and $S2^{b}/S1^{a}$ are linear combinations of (2.32), (2.33) and (2.34), and as such do not offer any extra information.

From the above three expressions for m_{11}, $m_{21}{}^{a}$ and $m_{21}{}^{b}$, it is not possible to directly obtain changes in attenuation anisotropy. In other words, measuring changes in attenuation anisotropy is no easier than making estimates of attenuation anisotropy from single observations of shear-wave splitting. Once the initial parameters $Q_1{}^{a}$, $t_1{}^{a}$ and δt^{a} have been established, any number of changes in attenuation (and velocity) anisotropy can be made using differential measurements.

However, the problem of how to display usefully these changes in seismic character still remains. The work of Wang and Nur (1988) has shown that both *P*- and shear-wave velocities decrease as temperature increases in sandstones saturated with heavy oil. This work led to a series of repeated *P*-wave cross-borehole tomographic studies during a thermal EOR process (Justice et al., 1989). In these experiments, *P*-wave velocity tomograms were used to depict the velocity structure between two boreholes. As EOR progressed, the velocity tomograms indicated an area of decreasing velocity spreading out from the injector well.

The relative ease of tomogram interpretation makes it an ideal method for representing changes in any seismic parameter, as long as a reliable method is available for inverting measurements of the required seismic parameter into the form a tomogram. The inversion procedure is probably the single biggest obstacle to overcome, especially if anisotropy is introduced to the problem.

With regard to monitoring EOR, and with the success of Justice et al. (1989), perhaps the most logical way forward would be to concentrate on developing isotropic tomographic techniques which can be used to image changes in velocity and attenuation (both *P*-wave and shear-wave) from a series of repeated experiments. Combining reflection and cross-borehole is also another area requiring development, which if successful, will provide added horizontal resolution to tomograms derived from cross-borehole data alone. While the idea of monitoring changes in shear-wave attenuation anisotropy is good, the method for usefully displaying the changes still needs to be developed.

2.7 Automatic measurement of shear-wave splitting from spectral interference patterns

Two methods are presented here for automatically measuring shear-wave splitting making use of interference patterns. The first is a matching routine, where theoretical interference patterns are compared to those observed. The best match between theory and observations yields the time delay and *qS1* polarization (and possibly an estimate of differential damping, depending on the factors mentioned in the previous section). Since the interference patterns

are insensitive to the sign of the *qSl* polarization, a check is made in the time domain, using the direct time series method described in the next section, to resolve this. Table 2.2 outlines the program used to apply this procedure.

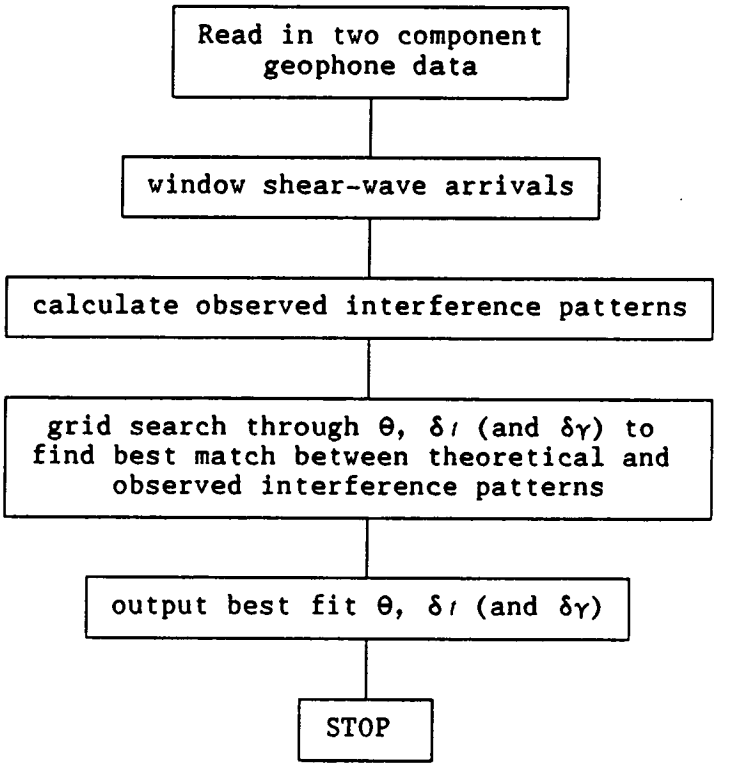

Table 2.2

Matches between predicted and observed power and phase interference spectra are estimated by the program in order to utilize as much of the information available as possible. A match is obtained by summing the absolute difference between the theoretical patterns and those observed for each discrete frequency lying within the bandwidth of the signal. This gives a single number representing the goodness of the fit. The program carries out a grid search of θ, δt

(and $\delta\gamma$) to find the values that yield the best fit between theory and observation. Differential damping may be left out of the matching algorithm if it is suspected that delays are small relative to the bandwidth of the signal.

The second method calculates power interference patterns at different geophone rotations, from the *H1* geophone being -90° to +89° from the source polarization. The rotation angle corresponding to minimum interference is found, where the *H1* geophone is parallel to either the fast or slow split shear-wave. This ambiguity is resolved by matching theoretical power interference patterns to those observed using the two possible *qS1* directions and varying the time delay until the best match between theory and observation is obtained. As in the previous method, the direct time series is used to find the correct polarity of the *qS1* polarization. Table 2.3 summarizes the computer routine. Since this method does not use the phase interference patterns, the presence of attenuation will not have any effect on the results.

In both methods, the upper and lower frequency limits for matching the interference patterns are defined as where the source power spectrum (the sum of the *H1*- and *H2*-component power spectra) falls to 10% of its peak value. Outside these limits the interference patterns are likely to be less reliable.

2.8 Automatic measurement of shear-wave splitting using the direct time series method

The third automatic method works entirely in the time domain. The theory is fairly straight forward and can be started by rewriting equation (2.3) in the time domain:

$$h1(t) = \frac{1}{r_1}\cos^2\theta\,[s(t)*e_1(t)] + \frac{1}{r_2}\sin^2\theta\,[s(t-\delta t)*e_2(t)]; \quad (2.35a)$$

$$h2(t) = \frac{1}{r_1}\cos\theta\sin\theta\,[s(t)*e_1(t)] - \frac{1}{r_2}\cos\theta\sin\theta\,[s(t-\delta t)*e_2(t)]; \quad (2.35b)$$

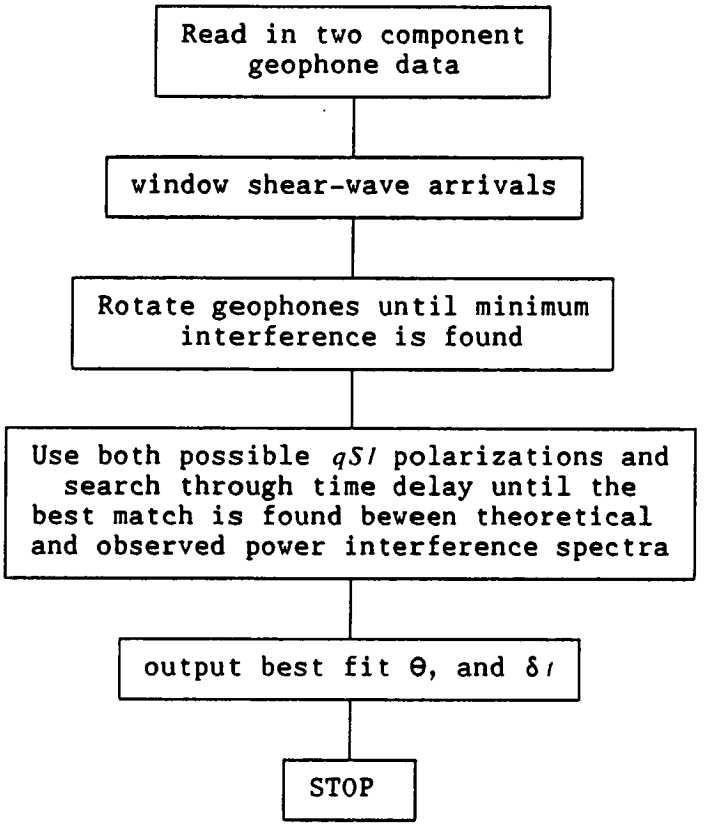

Table 2.3

where * = "convolved with" and $e_1(t)$ and $e_2(t)$ are the earth filters affecting the fast and slow shear-waves respectively. These equations can be simplified by assuming that the differential effects of $e_1(t)$ and $e_2(t)$ introduce only an amplitude factor between the split shear-waves:

$$h1(t) = [\ s(t)\cos^2\theta + A_2\, s(t-\delta t)\sin^2\theta\ ] * e_1(t); \quad (2.36a)$$

$$h2(t) = [\ s(t)\cos\theta\sin\theta - A_2\, s(t-\delta t)\cos\theta\sin\theta\ ] * e_1(t). \quad (2.36b)$$

A_2 is the difference in amplitude between the shear-waves associated with differential geometrical spreading and differential damping (A_2 = 1 where there is no differential geometrical spreading or differential damping). Compared to $\delta\gamma$ in section 2.2, A_2 is a very crude measure of the differential damping as it is independent of frequency. It merely represents a reduction in amplitude of the slow shear-wave relative to the fast shear-wave due to differential damping. For small time delays, this parameter is probably very close to unity, and is ignored in the following analysis.

If $h1(t)$ is parallel to the $qS1$ direction, equation (2.36) can be written:

$$h1(t) = s(t)\cos\theta * e_1(t); \tag{2.37a}$$

$$h2(t) = s(t-\delta t)\sin\theta * e_1(t). \tag{2.37b}$$

The amplitudes of $h1(t)$ and $h2(t)$ can be made equal by multiplying $h1(t)$ by $\sin\theta$ and $h2(t)$ by $\cos\theta$:

$$z1(t) = h1(t)\sin\theta = s(t)\sin\theta\cos\theta * e_1(t); \tag{2.38a}$$

$$z2(t) = h2(t)\cos\theta = s(t-\delta t)\sin\theta\cos\theta * e_1(t). \tag{2.38b}$$

If the time delay, δt, can be correctly identified and applied to $z1(t)$, then the difference between $z1(t)$ and $z2(t)$ will be zero for all t in the window containing the shear-wave arrival of interest.

The direct time series procedure for automatically measuring shear-wave splitting starts by applying an initial rotation to the geophones so that the *H1* geophone lies at -90° from the source polarization direction. The geophones are then rotated at 1° intervals in a clockwise direction until the *H1* geophone is +89° from the source direction. At each rotation angle, it is assumed that the *H1* geophone is parallel to the *qS1* direction such that θ is the angle between the *H1* geophone and source direction. The *H1*-component is multiplied by $\sin\theta$ and the *H2*-component by $\cos\theta$, following equation (2.23), giving two new components $H1_*$ and $H2_*$. Gradually increasing delays are added to the *H1*-component and at each delay time, the difference is calculated between $H1_*$ and $H2_*$. The rotation angle and delay corresponding to the minimum difference are output as the *qS1* direction and delay between *qS1* and *qS2*. Table 2.4 summarizes the program.

2.9 Testing the automatic techniques

To test the techniques, a synthetic VSP was constructed using the ANISEIS package. This involved placing 40 geophones at depths from 1.5km to 2.475km in an anisotropic model containing vertically aligned Hudson cracks at a strike of 52° from the X-direction. Figure 2.5 shows the model parameters which were chosen so that relatively small delays were present between split shear-waves, in a range between about 3ms and 22ms. Small delays were chosen because they provide a more testing environment for the automatic techniques. A zero offset, horizontal force source was used oriented in the +'ve X-direction. Background attenuation was included with the values indicated in Figure 2.5. The *H1*- and *H2*-component geophones were

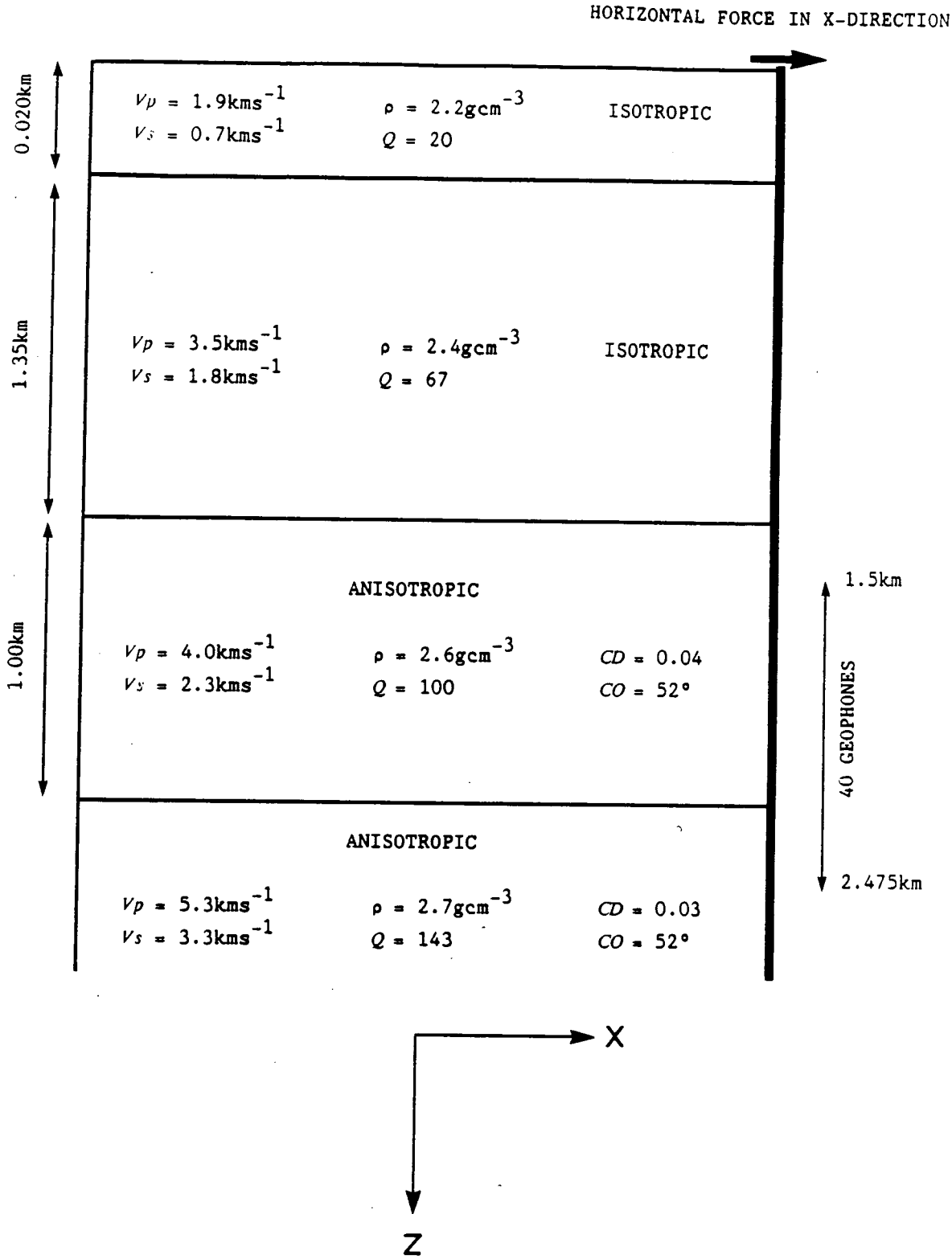

Figure 2.5 Specification of the zero offset VSP used to test the automatic techniques for measuring shear-wave splitting. Crack orientations (*CO*) are specified in degrees clockwise from the X-direction. The geophones were spaced at 25m intervals.

oriented in the X- and Y-directions respectively and are referred to as the X- and Y-component geophones. Theoretical time delays were calculated for this model, by using the ANISEIS package to determine the fast and slow shear-wave velocities in the anisotropic materials.

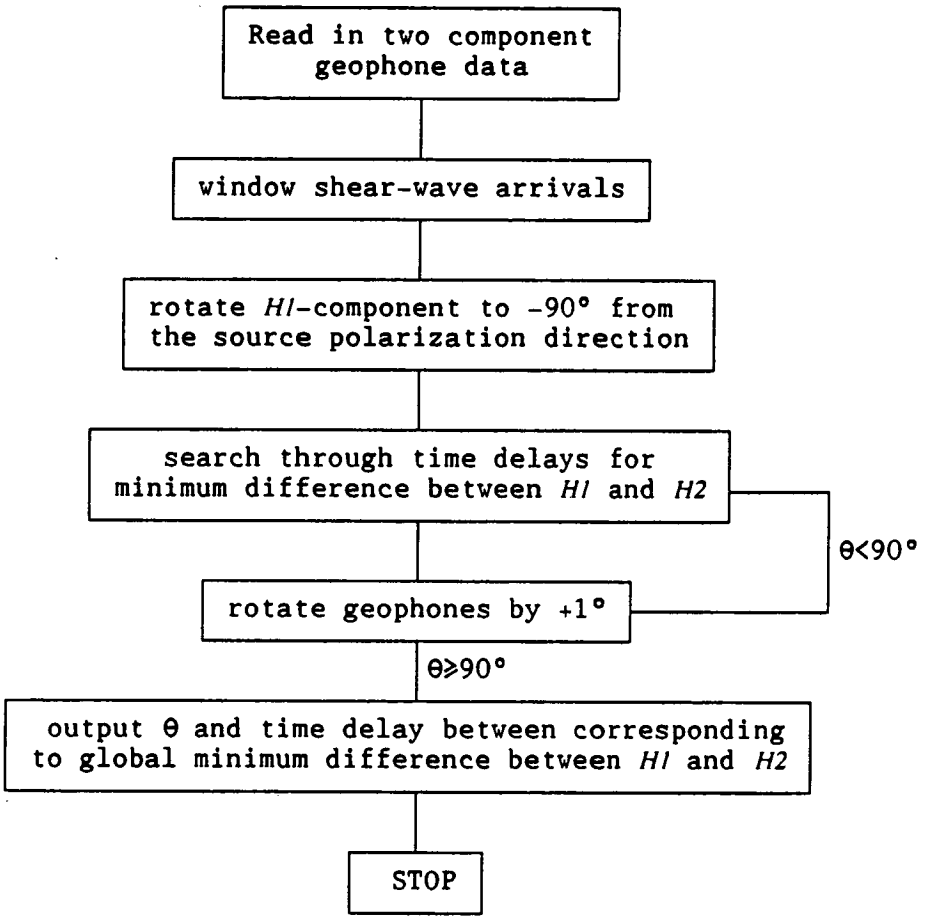

Table 2.4

Anisotropic model

Figure 2.6 shows synthetic seismograms from this model for both the X- and Y-components and horizontal plane PDs for every second geophone. The pulse shape used is symmetric about its arrival time and represents the end product of a deconvolution or cross-correlation process, discussed in Chapter 3. As Crampin (1978) shows, very little information can be obtained about the shear-wave

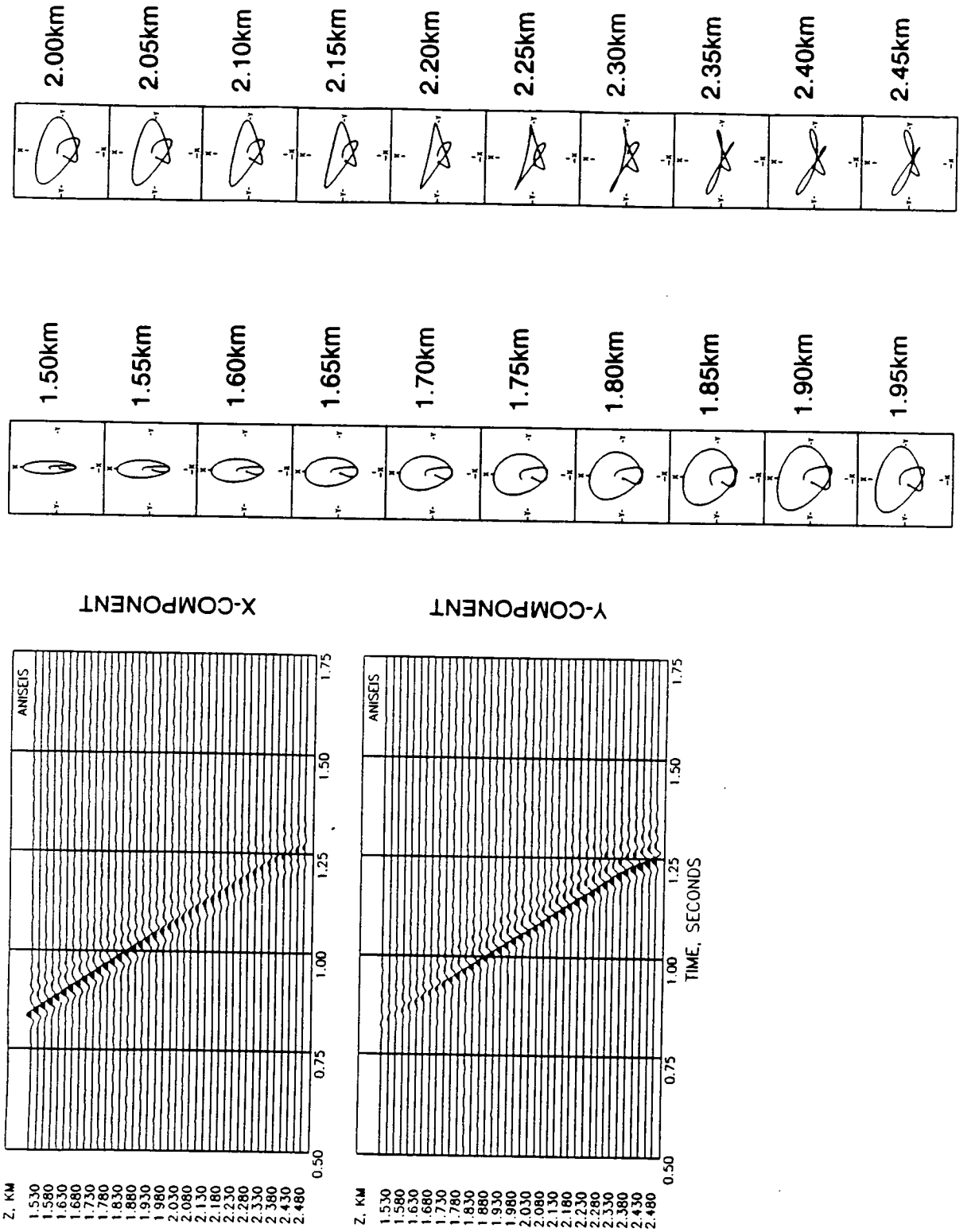

Figure 2.6 Horizontal component seismograms and PDs from the synthetic VSP in Figure 2.5. A zero phase source pulse was used, representing a deconvolved wavelet. The PDs show increasing time delays between the split shear-waves as depth increases, although this would not be easy to visually measure.

splitting from the seismograms. However, even the PDs appear difficult to interpret for fast shear-wave polarization and time delay due to the non-impulsive nature of the source, especially where the time delay is small.

The three automatic techniques were applied to these synthetic seismograms, with the same window parameters that were used for plotting the polarization diagrams. The results are shown in Figure 2.7. The matching of power and phase interference patterns, marked as "SPECTRAL INTERFERENCE" in Figure 2.7, shows that instabilities occur at the smallest time delays, below about 5ms. No attempt was made to estimate differential damping as the delays were too small and the frequency bandwidth too narrow to allow the phase interference patterns to be interpreted for this. The second spectral interference method, looking for minimum interference in the power interference patterns, "SPECTRAL INTERFERENCE 2" in Figure 2.7, produces consistent time delay results at all delays, with only small deviations from the theoretical *qSI* polarization. Results from the direct time series method are the most consistent with theoretical values of both time delay and polarization. Overall, the techniques are successful with respect to this ideal model.

Random noise was added to the synthetic data in Figure 2.6, with a signal/noise ratio of about 3/1, giving the seismograms and PDs shown in Figure 2.8. The noise has the same frequency characteristics as the signal, so cannot be removed by frequency filtering. The origin of this random noise is discussed in Chapter 3, and has implications for the North Sea VSP data presented in Chapter 4. It can be seen from the noisy PDs in Figure 2.8 that manual interpretation of these is not possible, as there is no sign of any consistent leading

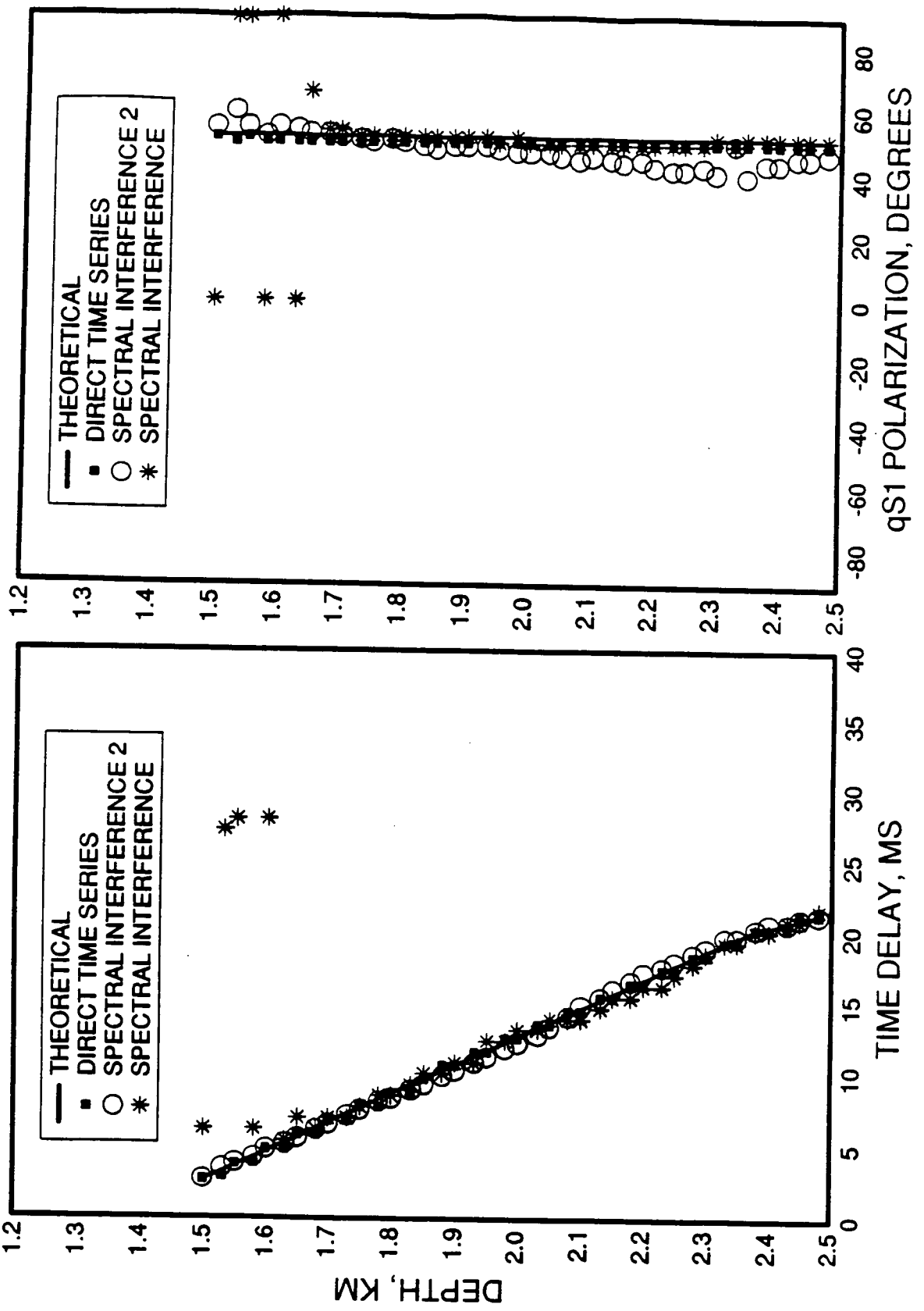

Figure 2.7 Results from the application of the three automatic techniques for picking *qS1* polarization and time delay to the shear-wave PDs in Figure 2.6. The "spectral interference 2" technique is the second frequency domain method described in section 2.5.

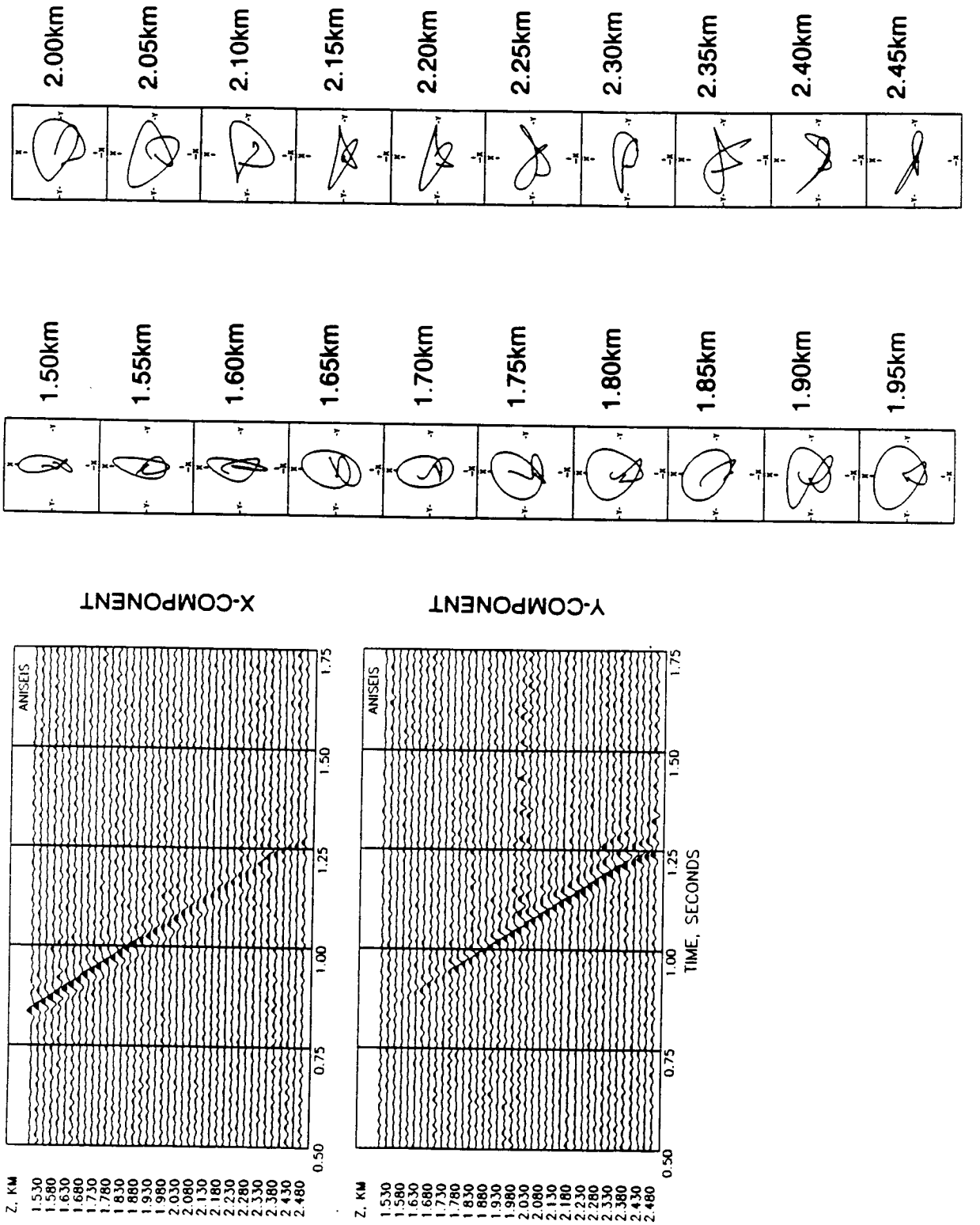

Figure 2.8 Synthetic seismograms and PDs from the model VSP in Figure 2.5 with random noise added at a signal/noise ratio of about 3/1. Frequency characteristics of the noise are the same as the source. The PDs are relatively distorted compared to those in Figure 2.6, rendering them impossible to reliably interpret manually.

shear-wave polarization and the general shape of the shear-wave motions is more complex compared to the PDs in Figure 2.6. Application of the three techniques to these data yields the results in Figure 2.9, showing significant scatter around the theoretical values, especially for small delays, less than about 8ms.

The signal/noise ratio of the random noise was reduced to 2/1 producing the seismograms and PDs in Figure 2.10. The PDs are now severely distorted compared to the noise free PDs in Figure 2.6. Surprisingly, Figure 2.11 shows that the automatic techniques still manage to pick trends corresponding to the theoretical values of time delay and *qS1* polarization. Some of the scatter arises because the spectral interference methods also pick out the negative *qS1* direction at -52°, and the direct time series method occasionally picks the *qS2* polarization at -38°. This is seen to a lesser extent in Figure 2.9.

Isotropic model

The automatic techniques were developed with the assumption that they would be applied to shear-wave data containing anisotropy. While almost all published observations of shear-waves to date have exhibited some form of shear-wave splitting, the techniques must be tested on isotropic data to determine their behaviour. Ideally they should give the zero time delay and a *qS1* polarization parallel to the source polarization. The same model described previously in Figure 2.5, but without any anisotropy, was used again, producing the seismograms in Figure 2.12. No noise was added, and since the source was oriented in the X-direction, no signal is present on the Y-component. The results from both spectral interference methods, plotted in Figure 2.13, correctly show zero time delay for all

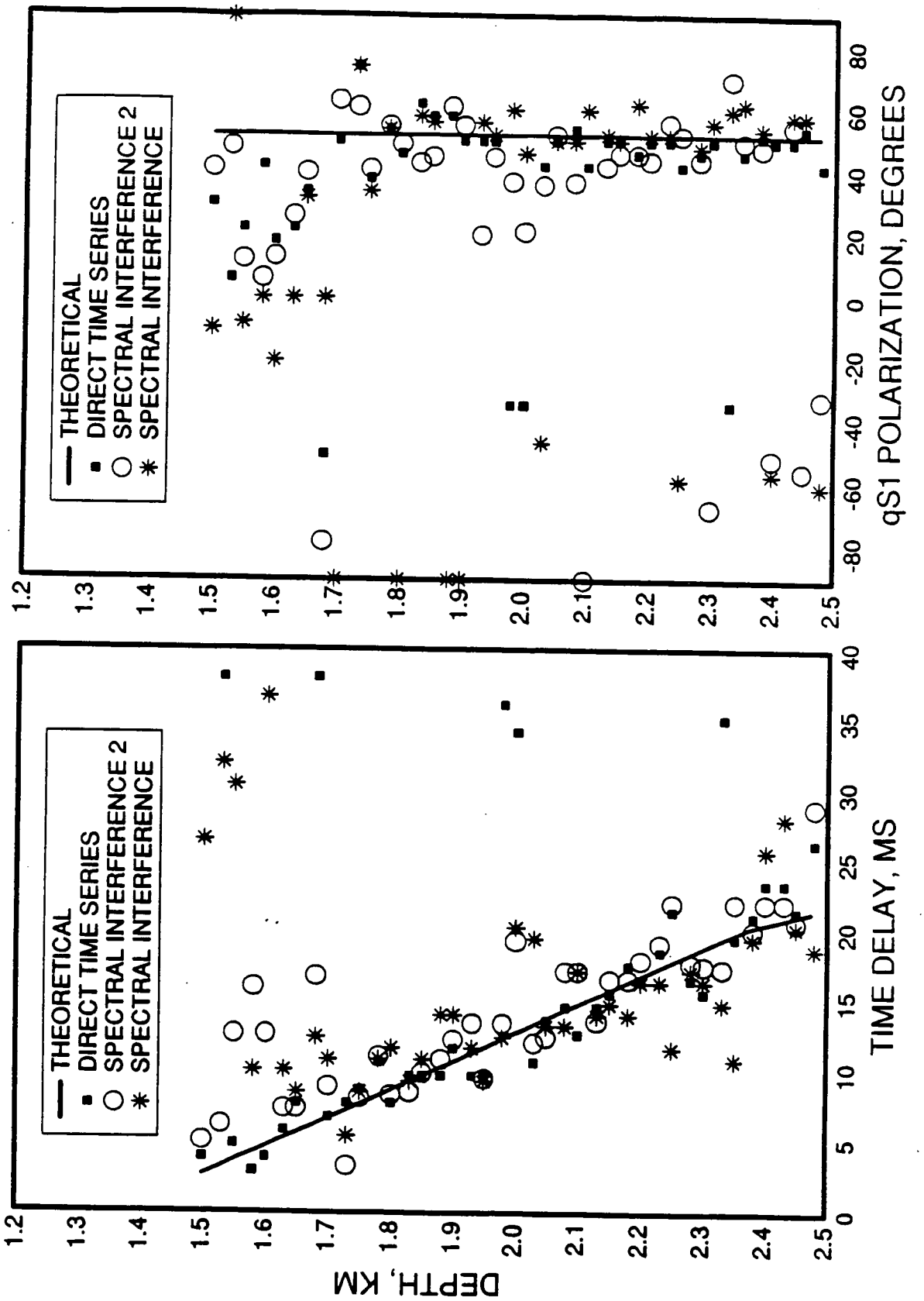

Figure 2.9 Application of the automatic techniques to the noisy PDs in Figure 2.8. Except at small time delays, all three methods make fairly good estimates of *qS1* polarization and time delay.

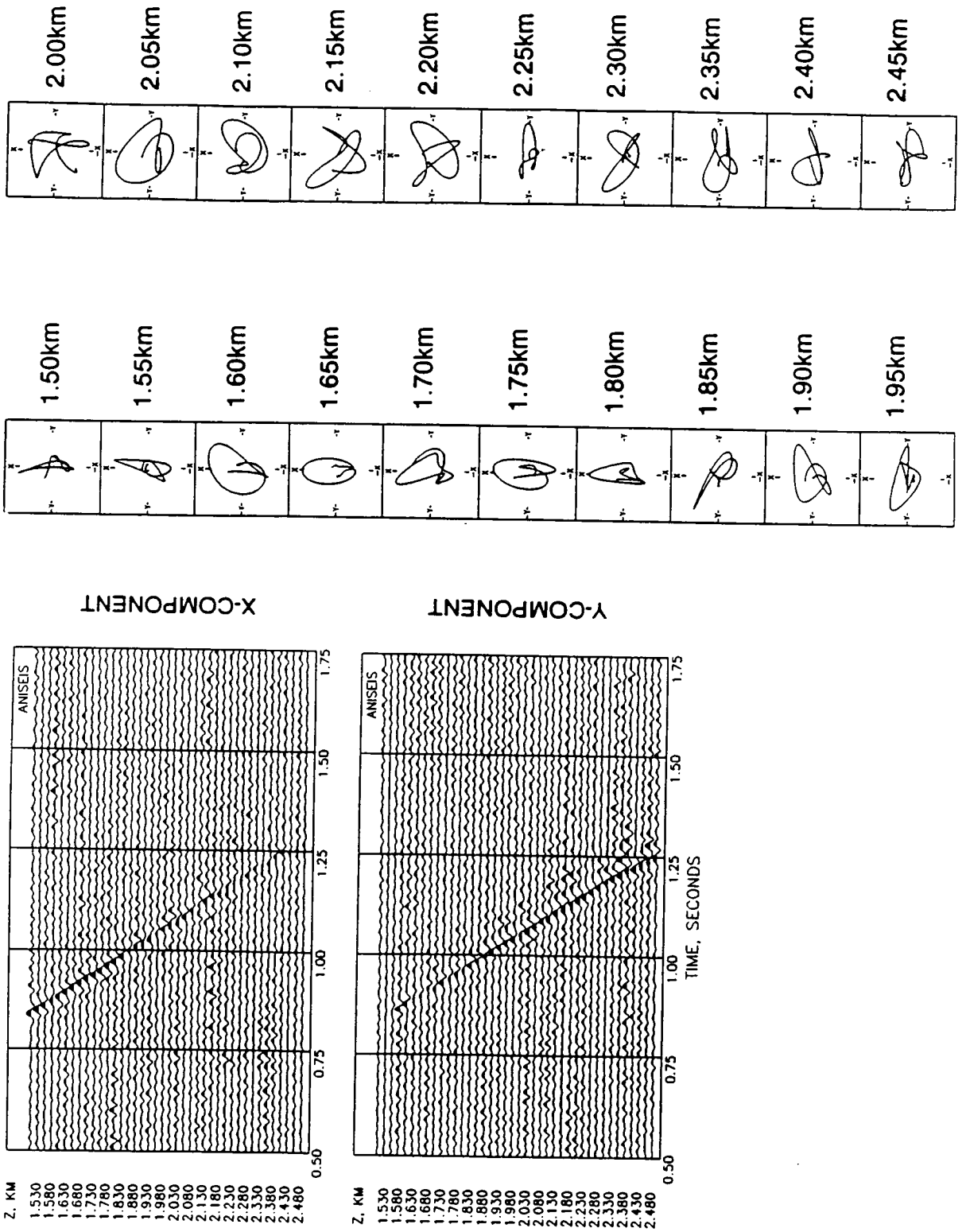

Figure 2.10 Synthetic seismograms and PDs from the model VSP in Figure 2.5 with random noise added at a signal/noise ratio of about 2/1. The shear-wave PDs are now severely distorted with no sign of any consistent changes between geophone levels.

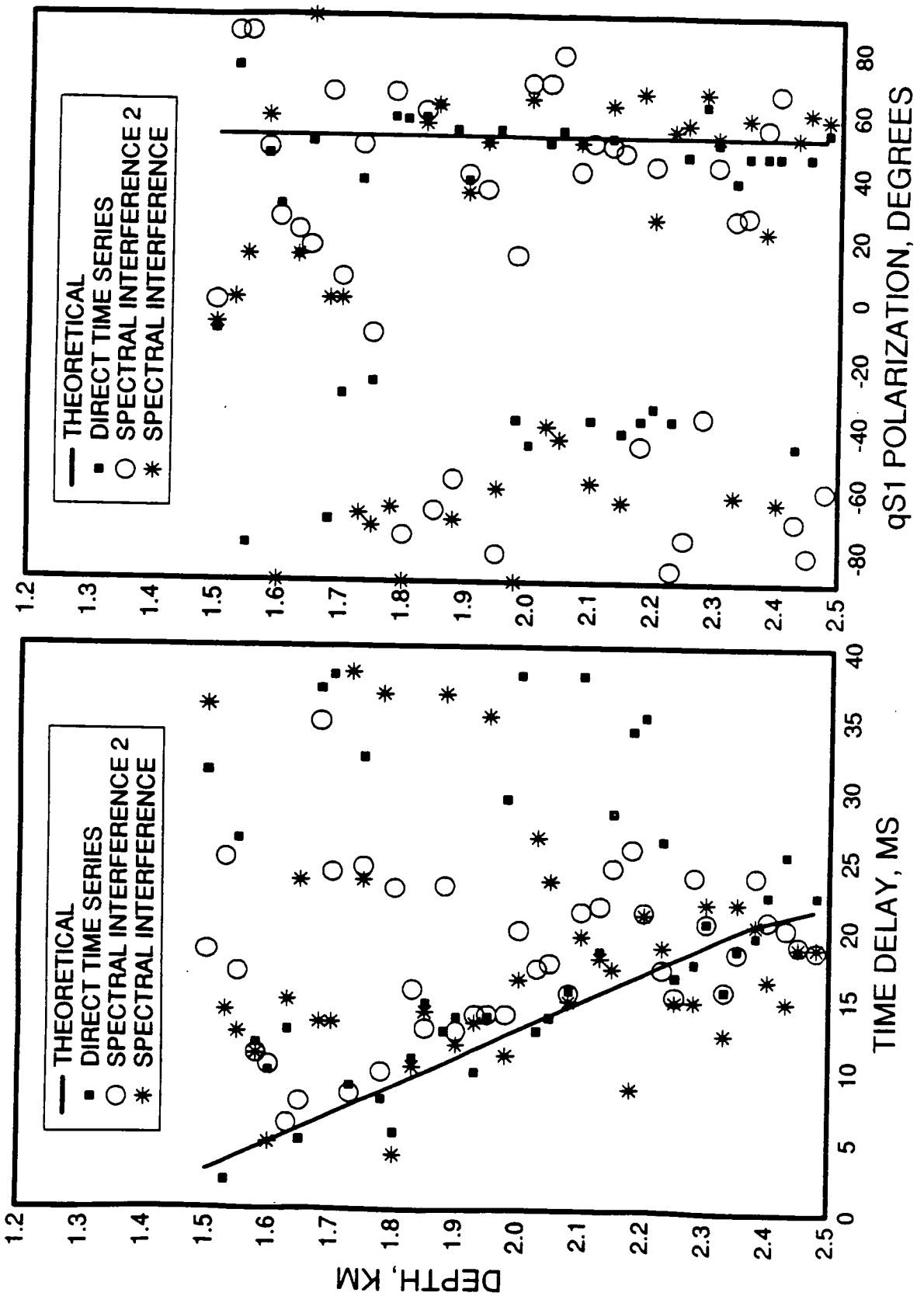

Figure 2.11 Application of the three automatic techniques to the noisy PDs shown in Figure 2.10. Even with severe distortion of the shear-waves, the automatic techniques have managed to pick out a general trend following the theoretical values of *qS1* polarization and time delay.

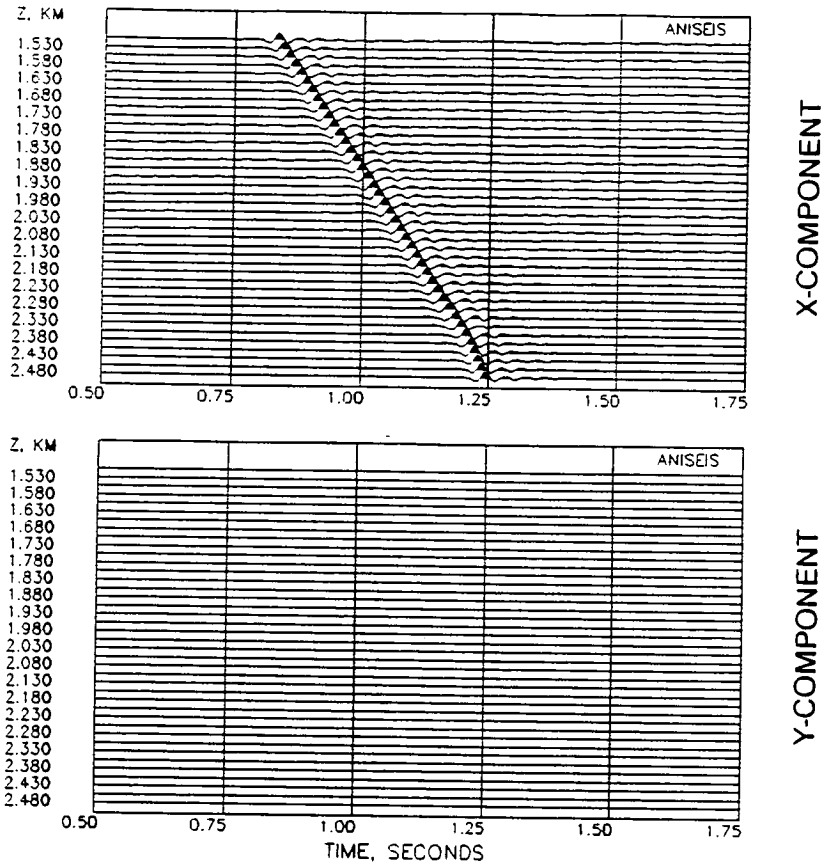

Figure 2.12 Synthetic seismograms from the isotropic model parameters specified in Figure 2.5, with the same source pulse shape used in previous seismogram sections. No noise has been added such that the Y-component is exactly zero at all times.

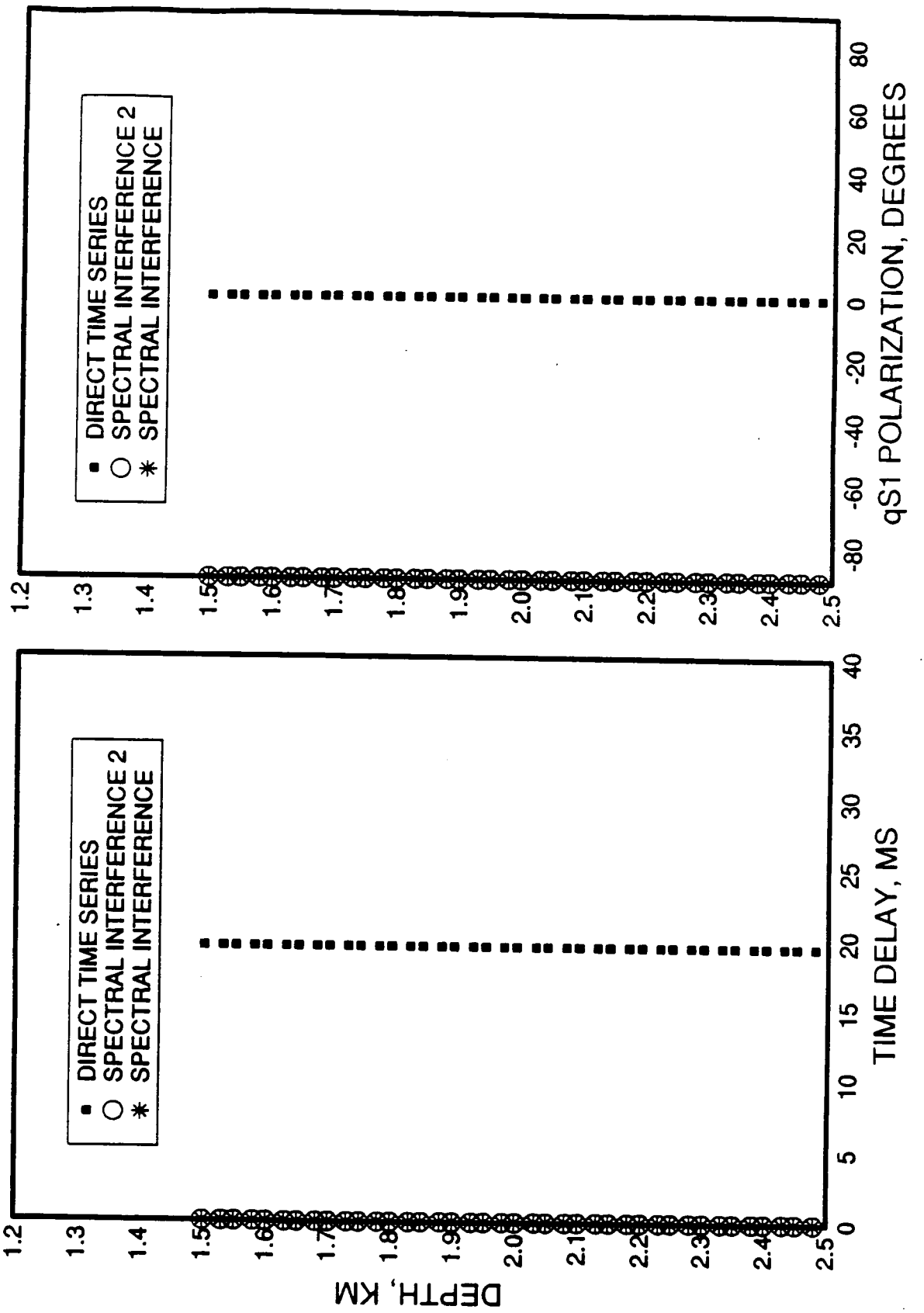

Figure 2.13 Results from applying the automatic techniques to the isotropic data in Figure 2.12. The non zero time delays picked by the direct time series method are a product of the Y-component being exactly zero, which would not be the case for real data.

geophones, but a *qSI* polarization orthogonal to the source polarization. The direct time series method gives a time delay equal to a quarter of the window length, which results from the artificial case where the Y-component is exactly zero, giving perfect isotropy. The *qSI* direction, however, correctly corresponds to the source direction.

Adding random noise with a signal/noise ratio of about 2/1 to the isotropic model produces the seismograms and PDs in Figure 2.14. The PDs are no longer linear and taken individually, they could be interpreted as containing evidence of anisotropy. From this model, Figure 2.15 shows that the first spectral interference method and the direct time series method produce *qSI* polarizations scattered around the source polarization, while the second spectral interference method gives a more random scatter of *qSI* polarizations. Time delay measurements from all methods are randomly scattered between zero and half the window length applied to the shear-wave arrivals (40ms), this being the maximum time delay allowed by the automatic techniques.

Non vertical propagation

For non vertically propagating shear-waves, the horizontal projection of the two split shear-waves polarizations may be quite severely distorted from orthogonality, even for small amounts of anisotropy. In this case, the techniques will break down to produce meaningless results. This problem may be overcome by rotating the conventional HR, HT and vertical axes into the dynamic axes, VT, HT and radial, where all downgoing shear-wave motion is contained on the VT and HT components. Except in cases of strong anisotropy, the two

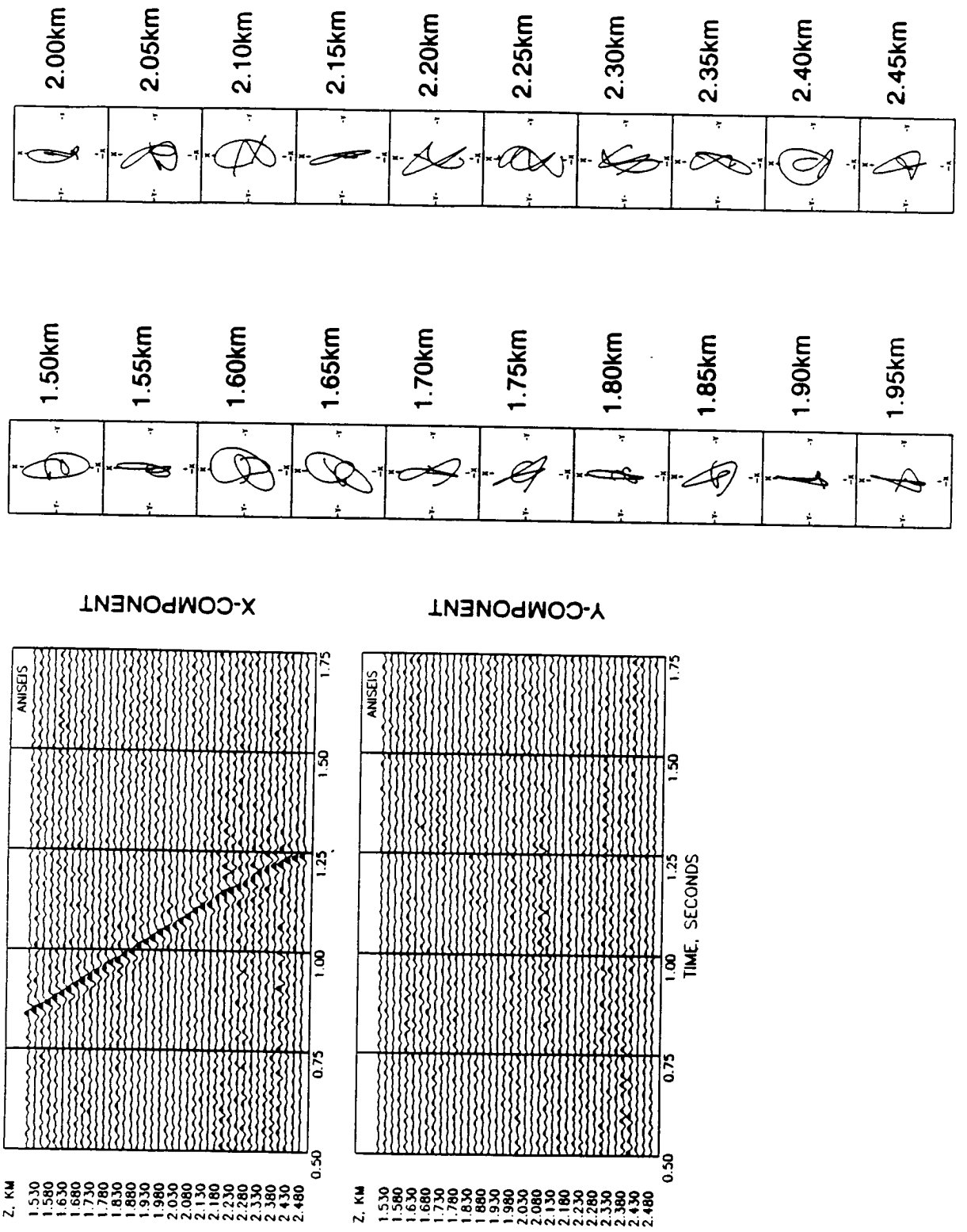

Figure 2.14 Isotropic synthetic seismograms and PDs with random noise added at a signal/noise ratio of about 2/1. The PDs show no consistency in shape between levels, but taken individually, they may be interpreted as showing signs of anisotropy.

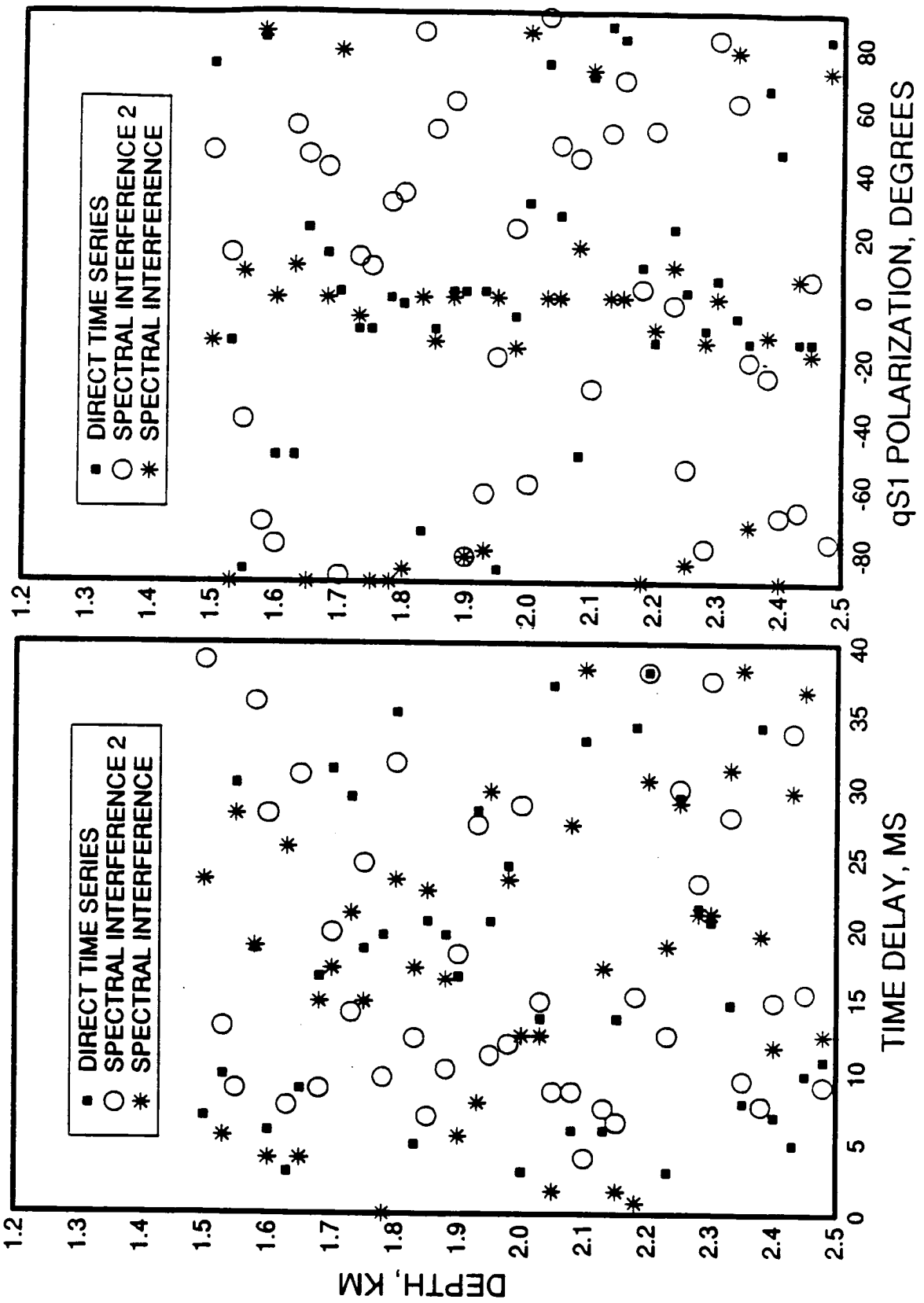

Figure 2.15 Results from applying the automatic techniques to the noisy isotropic data in Figure 2.14. Time delay measurements show a general random scatter of all possible time delays. *qS1* picks from the direct time series and first spectral interference methods show a loose clustering about the source polarization, while the second spectral interference method shows a more general scatter.

shear-wave polarizations will be approximately orthogonal in these axes so that the technique can be applied successfuly, remembering that for ease of interpretation, the measured *qS1* polarizations should be projected on to the horizontal plane.

2.10 Conclusions

In sections 2.4 and 2.5, it was demonstrated that measurements of differential shear-wave attenuation from single observations of shear-wave splitting are more difficult to obtain compared to estimates of differential shear-wave velocity anisotropy, due to the number of extra observations required.

If spectral interference patterns are used to estimate $\Delta Q/Q$, the frequency bandwidth of the shear-waves, and the time delay between split shear-waves must be large enough to define completely the shape of the phase interference pattern, otherwise differential damping has no effect on the shape of the interference patterns, meaning that no estimate of shear-wave attenuation anisotropy can be made. If spectral ratios are used to estimate $\Delta Q/Q$, a large frequency bandwidth is required in order that the gradient of the spectral ratio versus frequency can be measured as accurately as possible.

Changes in shear-wave attenuation anisotropy can be measured from repeated observations of shear-wave splitting if the initial, absolute paramaters, involving the arrival time of the fast shear-wave, the time delay between split shear-waves and the Q factor associated with the fast shear-wave, are first obtained. Once this has been done, only differences in subsequent recordings of split shear-waves need be measured.

The theory behind attenuation of shear-waves in an anisotropic media has yet to be satisfactorily concluded, so that little is known about how shear-wave attenuation anisotropy will be affected by changes in the fluid occupying pores or fractures causing the velocity anisotropy. As such, large changes in shear-wave attenuation anisotropy may be observed during an EOR process, thus providing a good method for monitoring the progress of EOR. However, problems still remain over how to display such changes in a readily interpretable form. The desired result is a map showing how the injected fluid or thermal flood front is progressing through the reservoir. With this problem in mind, perhaps the best progress in monitoring EOR will come from isotropic velocity tomography, and possibly isotropic attenuation tomography. If satisfactory results can be obtained by assuming isotropy, there seems little reason, commercially, to go through the trouble of developing a tomographic inversion scheme that works in the presence of anisotropy. Academically, though, it could be a very interesting problem.

Three automatic techniques for measuring shear-wave splitting were developed in sections 2.7 and 2.8 and tested on synthetic data. A noise free model containing anisotropy produced consistent measurements of time delay and *qSI* polarization from all methods, although the first spectral interference method was less reliable for small delays, less than about 5ms. This lower limit of time delay, however, depends on the useable frequency bandwidth of the shear-wave signal. In the presence of noise, estimates of time delay and *qSI* polarization were consistent with theoretical values, even down to signal/noise ratios of 2/1, although significant scatter was present.

It is, perhaps, surprising that the automatic techniques are able to pick out relatively consistent anisotropy parameters, even when the shear-wave PDs are severely distorted compared to the ideal noise free situation.

Application of the automatic techniques to a noisy, isotropic model produced a general scatter for values of time delay, while the *qSI* polarization estimates were loosely clustered around the source polarization for the first spectral interference method and the direct time series method. Thus, for these two methods, it may be concluded that when estimates of *qSI* polarization correspond to the source polarization, isotropy is present. The second spectral interference method gave more scattered *qSI* polarizations and time delays, making positive identification of isotropy more difficult from this method.

Chapter 3 - Processing shear-wave data

3.1 Introduction

Seismic data processing is an unusual collection of highly abstruse and objective mathematical techniques in signal processing, combined with the subjective approach of the human interpreter. The whole idea of single component seismic processing is to massage seismic data recorded in the field into a coherent cross-section of significant geological horizons in the earth's subsurface. Due to the subjective nature of the interpretation of these cross-sections, it is often not possible to tell if new processing techniques are really valuable, or just appear on glossy brochures making unsubstantiated claims!

In this thesis, the situation is significantly different from the one described above. Rather than interpreting seismic data in terms of geological structures, it is the changes to the wave as it propagates along a path from source to receiver that are of interest, in particular seismic velocity anisotropy. Furthermore, in Chapter 2, techniques were developed to measure objectively anisotropic effects, thus providing one method to determine whether processing actually does improve the quality of three-component shear-wave data or otherwise.

Two forms of processing (relevant to VSP data) are considered in this chapter. The first, deterministic source signature deconvolution, deals with the problems of compressing an originally long source signature into a more useful wavelet. In experiments where mode-converted shear-waves are studied for anisotropy (Chapter

4), it is helpful to have the shear-wave separated from the direct arriving *P*-waves. The second processing procedure to be looked at is F-K filtering. This is used to determine the effects of spatial smoothing on three-component shear-wave data.

Both processing techniques are applied to a synthetic VSP data set, the parameters of which are given in Figure 3.1 and are the same as those in Chapter 2, Figure 2.5. The three automatic measuring techniques described in Chapter 2 are applied to the output after processing to find out whether the shear-waves have been enhanced or distorted. Seismograms and shear-wave PDs are also displayed to illustrate the effects of processing.

3.2 Deterministic source signature deconvolution

Deconvolution is one of the most written about subjects in exploration seismology and takes many forms (e.g. see Hatton et al., 1986). Multiple supression, attenuation compensation, wavelet shaping and source signature compression are the most common reasons for applying deconvolution. Of these, the most straight forward is deterministic source signature deconvolution, where the shape of the source signature is known (from recordings close to the source) and can be removed from field recordings without having to make any assumptions about Earth models or estimations from the field records.

Deterministic source signature deconvolution can be applied in the time domain, by constructing a Wiener filter which will transform the input source function into a desired wavelet shape as nearly as

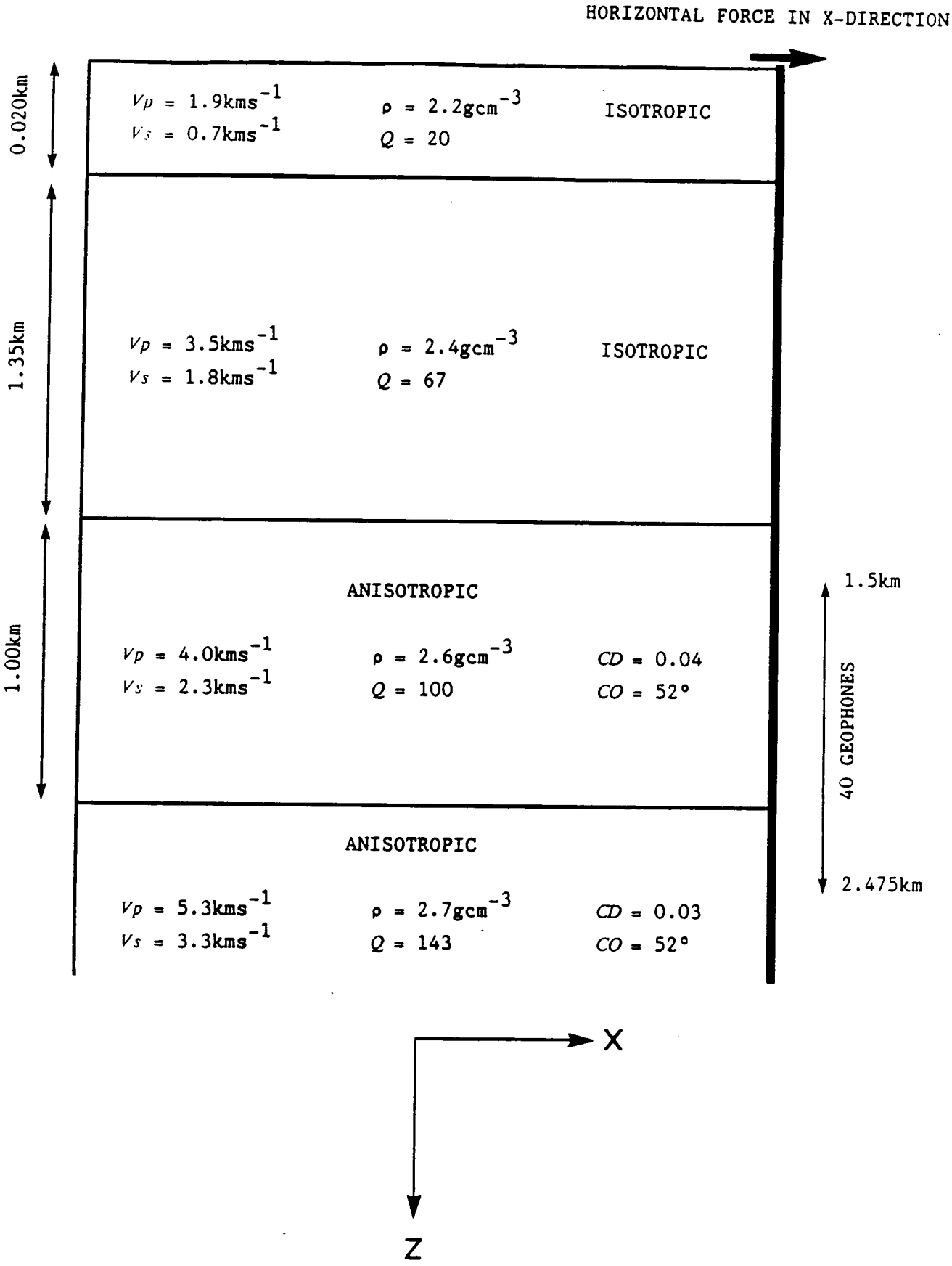

Figure 3.1. Parameters of the synthetic VSP used to demonstrate the effects of source signature deconvolution and F-K filtering. Spacing between geophones is 25m. The positive Y-direction points out of the page.

possible. This is then convolved with each of the three components to give the deconvolved (or "spiked") output traces. A band pass filter should be applied to the deconvolved output to limit its bandwidth to that of the source.

Alternatively, a frequency domain method for source signature deconvolution was developed where the Disctrete Fourier Transform (DFT) of each of the original three-components is divided by the DFT of the source signature (this is a division between complex numbers at the discrete frequencies of the DFT). The amplitude of the deconvolved spectra are effectively flattened by this method, thus removing the shape of the source pulse. This is much more straight forward than trying to construct a Wiener filter and it has the advantage of working in the frequency domain so that band pass filtering can be applied at the same time as deconvolution. The ideal shape of the output wavelet is zero phase, or symmetrical about its arrival time. This makes arrival time picking easier compared to trying to find the time of first break energy, because a peak or a trough is a much more prominent feature on a seismogram. Velocity dispersion, or interface effects may, however, modify the ideal wavelet shape so that it is no longer symmetrical. Ghosting and near field effects on recordings of the source signature may also modify the deconvolved pulse shape.

Both forms of source signature deconvolution can degrade the signal/noise ratio of the output traces compared to the original data: at frequencies where the amplitude spectrum of the source signature is small, a larger correction is applied to the amplitude spectrum of the recorded traces compared to where the amplitude spectrum of the source has large values. Consequently, noise

contained in the trace amplitude spectra at frequencies where the source amplitude spectrum is small will be amplified by a much larger factor than where the amplitude spectrum of the source is large, resulting in a decreased signal/noise ratio in the deconvolved traces. This is described in more detail below.

Synthetic VSP

The model VSP used to demonstrate source signature deconvolution is given in Figure 3.1. A source signature representing a single, 160in^3 airgun placed at 30 feet depth and recorded by a hydrophone 15 feet below the gun was used. The shape of this pulse is given in Figure 3.2a, and is characterised by a long duration monotonic ringing nature. The amplitude spectrum of this is shown in Figure 3.2b and has deep notches starting at 20Hz and repeating approximately every 13Hz. Although it is not physically realistic to use this sort of pulse shape in combination with the horizontal force source used in the synthetic VSP, this set-up is the simplest way to demonstrate the effects of source signature deconvolution on split shear-waves. The pulse shape is also the same as that used in the Vulcan VSPs in Chapter 4, so results here have direct implications for the analysis of those marine VSPs.

Figure 3.3a shows the output X- and Y-component seismograms from the model VSP. Applying source signature deconvolution process in the frequency domain between 2Hz and 55Hz gives the seismograms and PDs in Figure 3.4 (and also Figure 2.6). In Chapter 2, the automatic techniques for measuring shear-wave splitting were applied to the shear-wave arrivals in Figure 3.4, giving the correct results for *qS1* polarization and time delay. Hence, the simple conclusion is that deterministic source signature deconvolution can be applied to

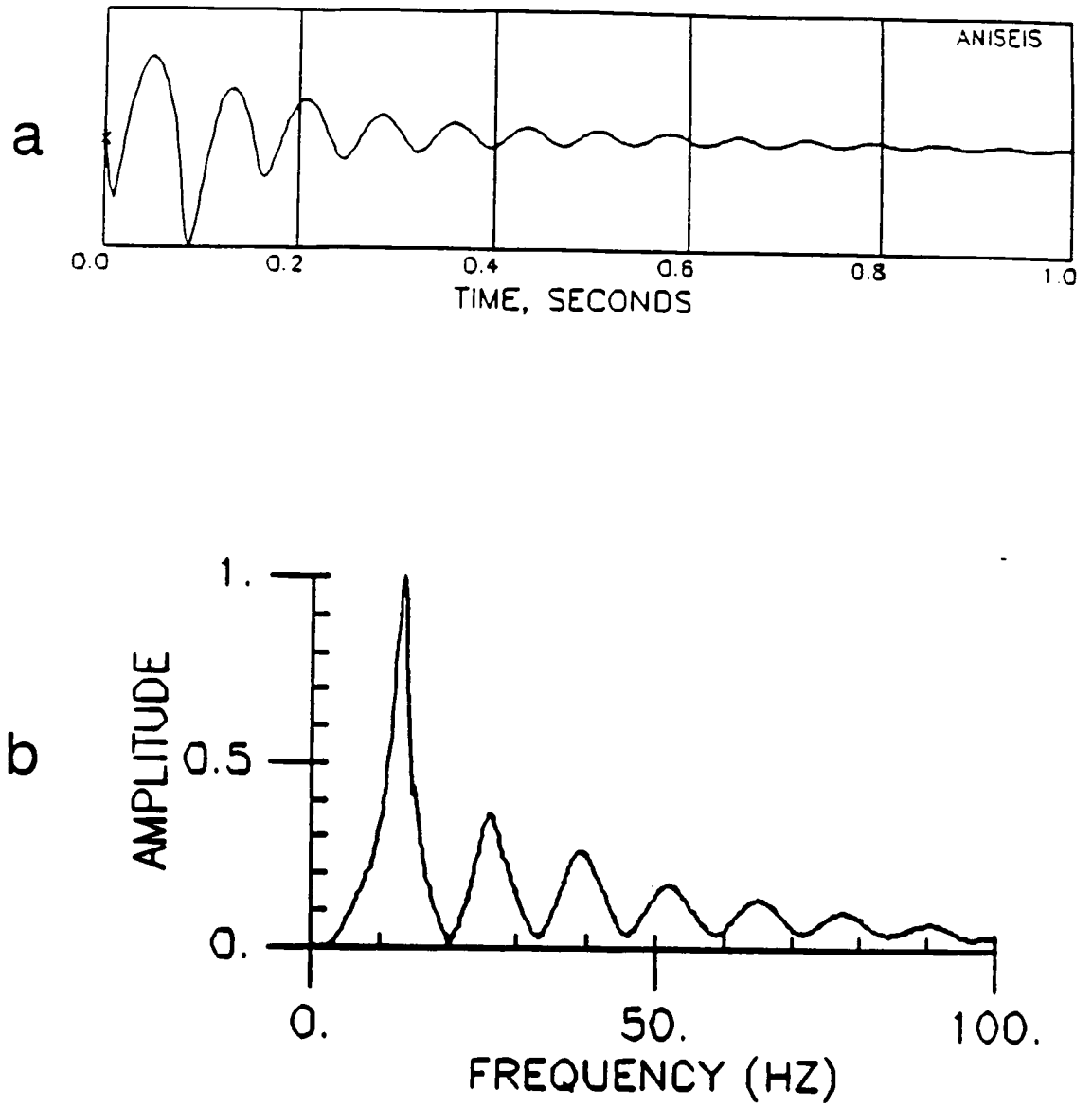

Figure 3.2. a) Source signature used to generate synthetic seismograms. This represents a single 160in^3 airgun placed at 30 feet below sea level and recorded by a hydrophone 15 feet below the gun. b) Amplitude spectrum of the source signature in a). Note the deep notches starting at 20Hz and repeating every 13Hz.

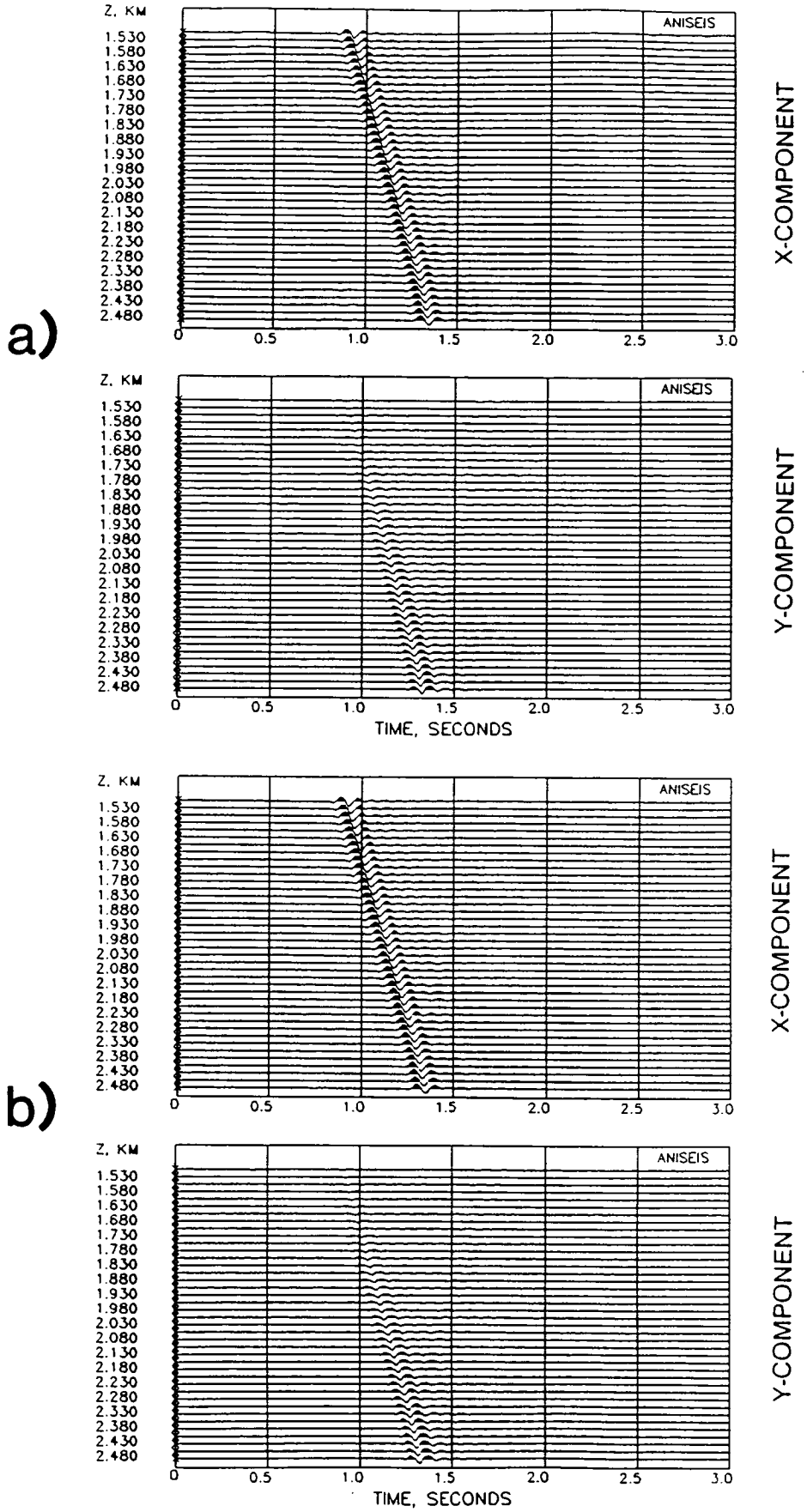

Figure 3.3. a) X- and Y-component seismograms from the synthetic VSP using the source signature in Figure 3.2a. b) As a) but with random noise added at a signal/noise ratio of 20/1. Due to the size of plots it is almost impossible to detect the noise.

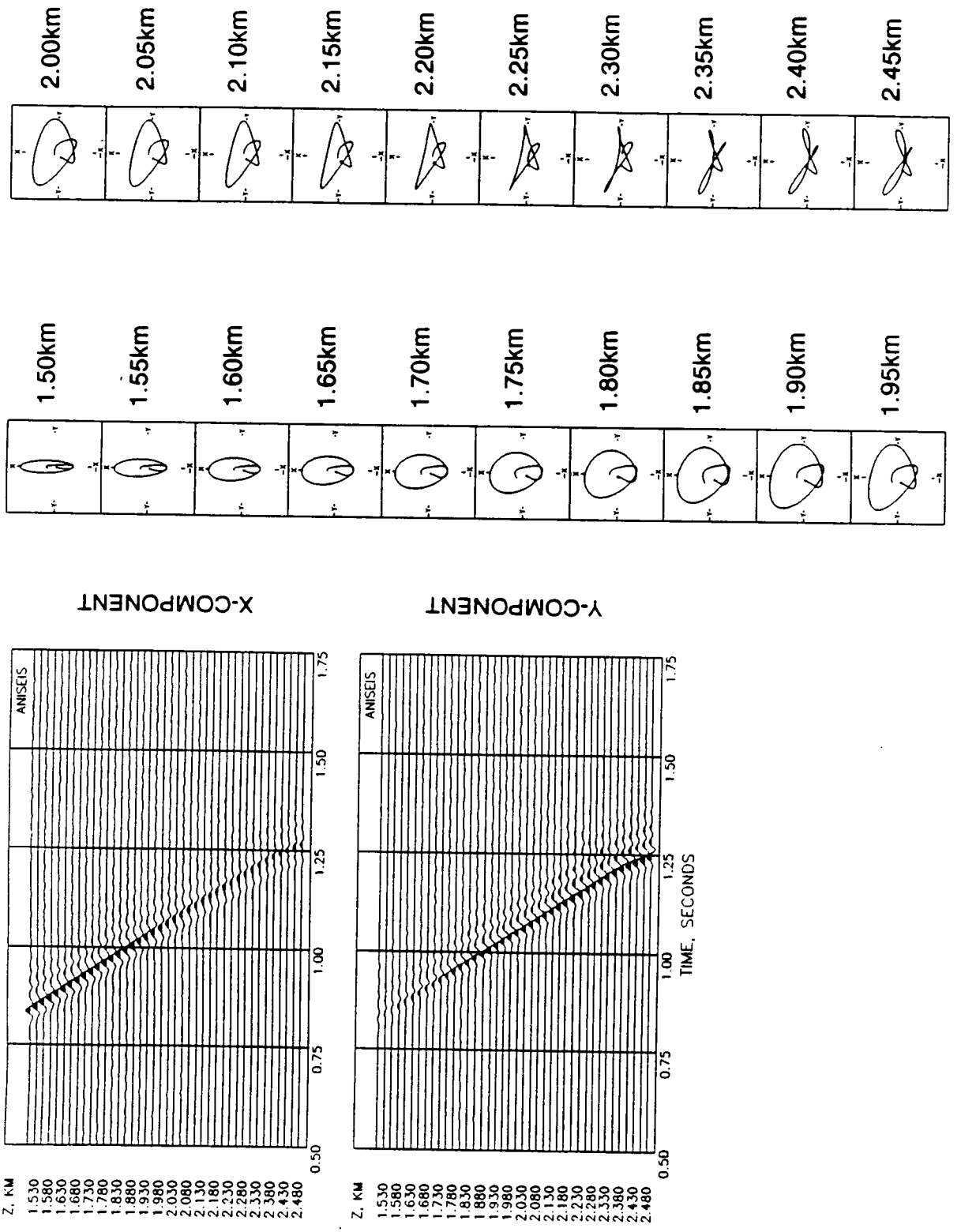

Figure 3.4. Seimograms ans PDs after source signature deconvolution of the seismograms in Figure 3.3a. This is a repeat of Figure 2.6 from which application of the three automatic techniques for measuring shear-wave splitting demonstrates that deterministic source signature deconvolution has not distorted shear-wave splitting information (Figure 2.7).

three-component data without distorting polarization information. The presence of attenuation in the model or in any real situation has no effect on this conclusion. The noise free PDs in Figure 3.4 can also be reproduced by inputting the deconvolved airgun signature directly into the model, thus bypassing the deconvolution stage.

However, with this particular source signature, there are problems when noise is present in the undeconvolved records. Figure 3.3b shows the same records as Figure 3.3a but with random noise added at a signal/noise ratio of 20/1. Due to the scale at which the seismograms are plotted, it is almost impossible to detect the addition of this noise. The effect of source signature deconvolution is to drastically reduce the signal/noise ratio to about 2/1, as indicated in Figure 3.5, a repeat of Figure 2.10. This dramatic change in the signal/noise ratio after deconvolution occurs because of the notches in the amplitude spectrum of the source which can be seen by considering the usual model for a signal recorded on a geophone:

$$x(t) = g(t) * e(t) * s(t) + n(t); \qquad (3.1)$$

where * means convolved with; $x(t)$ is the recorded seismic trace; $g(t)$ is the geophone response function; $e(t)$ is the effect of earth filtering; $s(t)$ is the source function and $n(t)$ is random noise.

In the frequency domain, equation (3.1) becomes:

$$X(\omega) = G(\omega)\ E(\omega)\ S(\omega) + N(\omega). \qquad (3.2)$$

Dividing by the FT of the source function, the deconvolved frequency spectrum, $DX(\omega)$, is obtained:

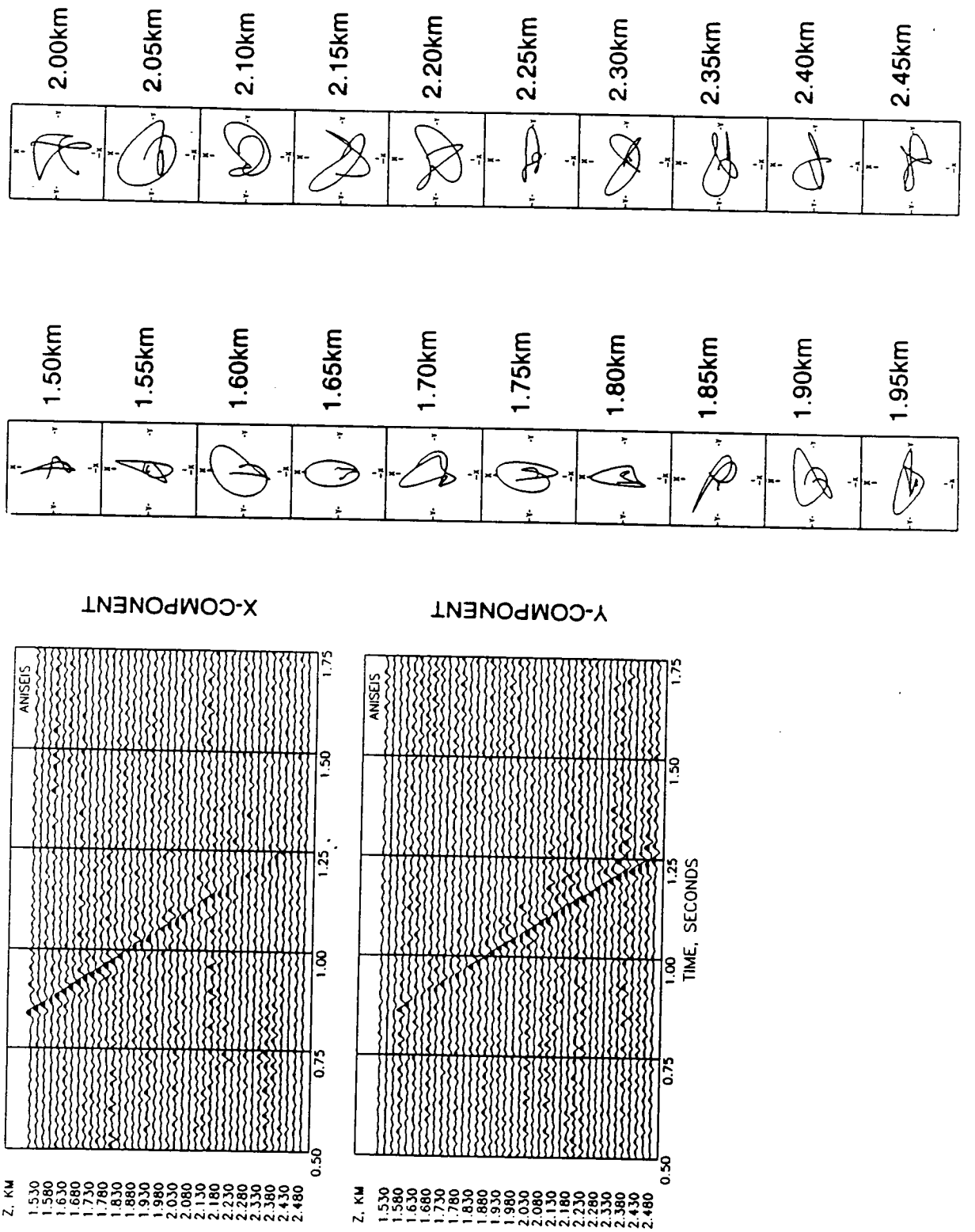

Figure 3.5. Seismograms and PDs after source signature deconvolution of the noisy seismograms in Figure 3.3b. Note the large difference between this Figure and Figure 3.4, which is exceptional considering the almost indetectible difference between Figures 3.3a and 3.3b. This Figure is a repeat of Figure 2.10 from which application of the three automatic techniques for measuring shear-wave splitting gave large scatter to estimates of *qS1* polarization and time delay (Figure 2.11).

$$DX(\omega) = \frac{X(\omega)}{S(\omega)} = G(\omega)\ E(\omega) + \frac{N(\omega)}{S(\omega)} . \qquad (3.3)$$

Assuming that the random noise does not have corresponding notches to the source (otherwise it would not be random), then at the notch frequencies, where $|S(\omega)|$ is small, the absolute value of the last term in equation (3.3), involving the noise, will be large compared to the first term, producing spikes in the amplitude spectrum of the deconvolved trace. This is the cause of the decrease in the signal/noise ratio in Figure 3.5.

The effects of this noise on estimates of shear-wave splitting have been discussed in Chapter 2, and generally produce a large scatter of *qSl* polarizations and time delay estimates about their theoretical values.

Reduction of this noise can be achieved by carrying out an interpolation of the deconvolved amplitude spectrum at frequencies where notches occur, using values of the deconvolved amplitude spectrum either side of the notch to estimate what the amplitude spectrum should be at notch frequencies. Since the phase spectrum is not necessarily continuous, no interpolation of this was attempted. In this way, spikes are removed from the deconvolved spectrum. A computer program was written to automatically apply this deconvolution process to seismic records.

Seismic traces resulting from this "notch" deconvolution are displayed in Figure 3.6, from which it can be seen that the signal to noise ratio has been substantially increased compared to Figure 3.3b. The PDs in Figure 3.6 are from the same geophone locations as

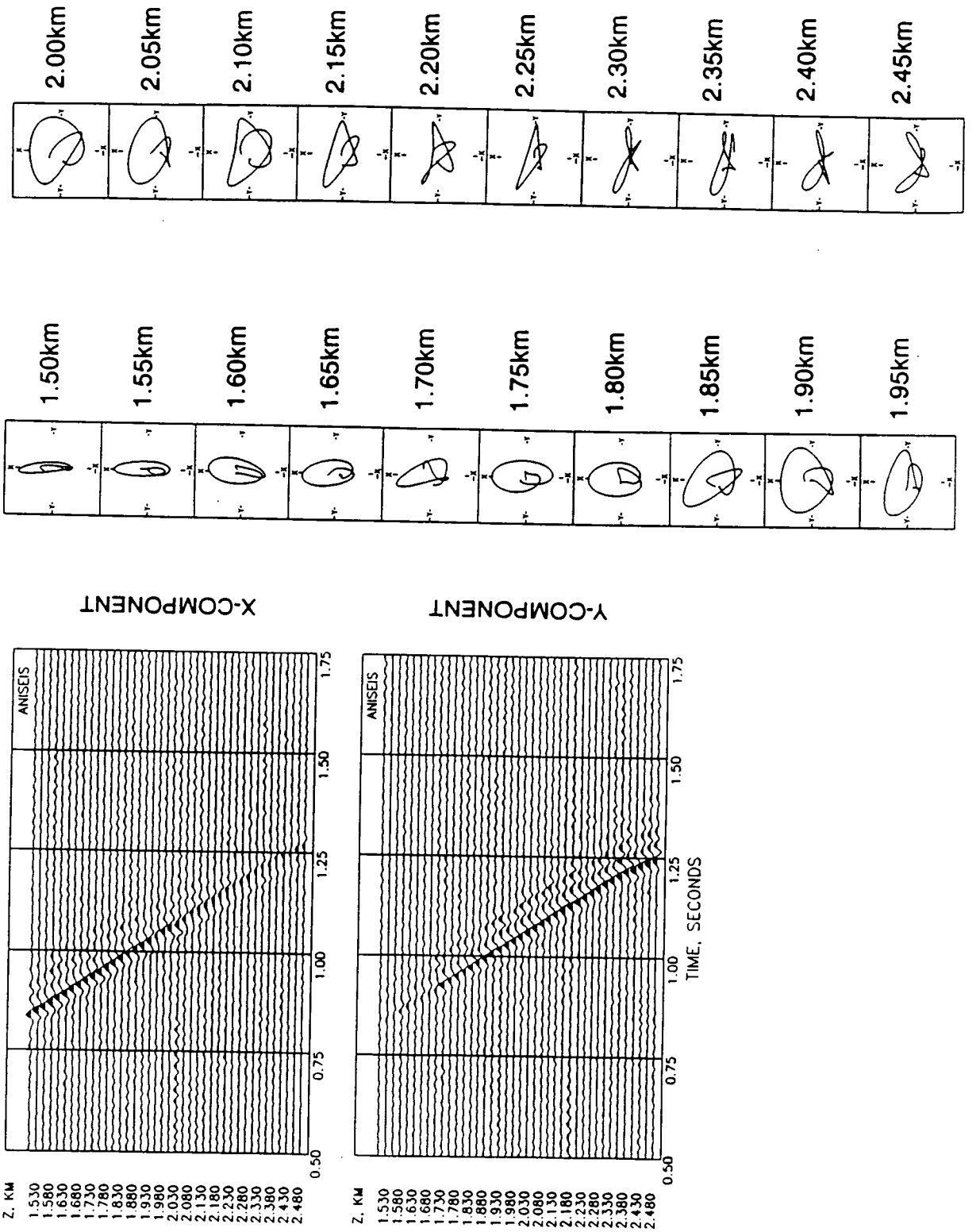

Figure 3.6. Seismograms and PDs after notch deconvolution of the seismograms in Figure 3.3. Note the much better signal/noise ratio compared to normal source signature deconvolution in Figure 3.5. Comparison of the PDs given here to those in Figure 3.4 suggests that this form of deconvolution has not destroyed polarization information.

Figure 3.4 and indicate that this modified form of deconvolution has not distorted the shear-wave polarizations and delays, but has enhanced them compared to those in Figure 3.5. Figure 3.7 shows the results of the three automatic techniques applied to the notch deconvolved shear-waves. Compared to Figure 2.11, Figure 3.7 shows much less scatter of measured *qS1* polarizations and time delays about their theoretical values. The results here also prove that while reducing noise, notch deconvolution does not distort polarizations.

Real field data are more complex than in this simple example, with multiple arrivals complicating the amplitude spectra of the traces. This has implications for the interpolation procedure discussed earlier, where the amplitude spectrum of a deconvolved trace is estimated at notch locations in the original source amplitude spectrum. With real data, there is a chance that too much interpolation will produce significant distortion of the deconvolved time series, giving incorrect shear-wave PDs. Thus, the amount of interpolation must be kept to a minimum to avoid this effect as much as possible.

3.3 F-K filtering

F-K filtering has been used for many years as a standard form of processing to separate wave types with different moveout velocities. In VSPs, F-K filtering has been used to separate downgoing energy from upgoing energy in order to obtain the equivalent of a reflection section using only the upgoing waves. For seismic reflection surveys, F-K filtering is used to remove ground roll which has a lower moveout velocity than reflected energy. March and Bailey (1983) give a good review of different aspects of filtering in the F-K domain.

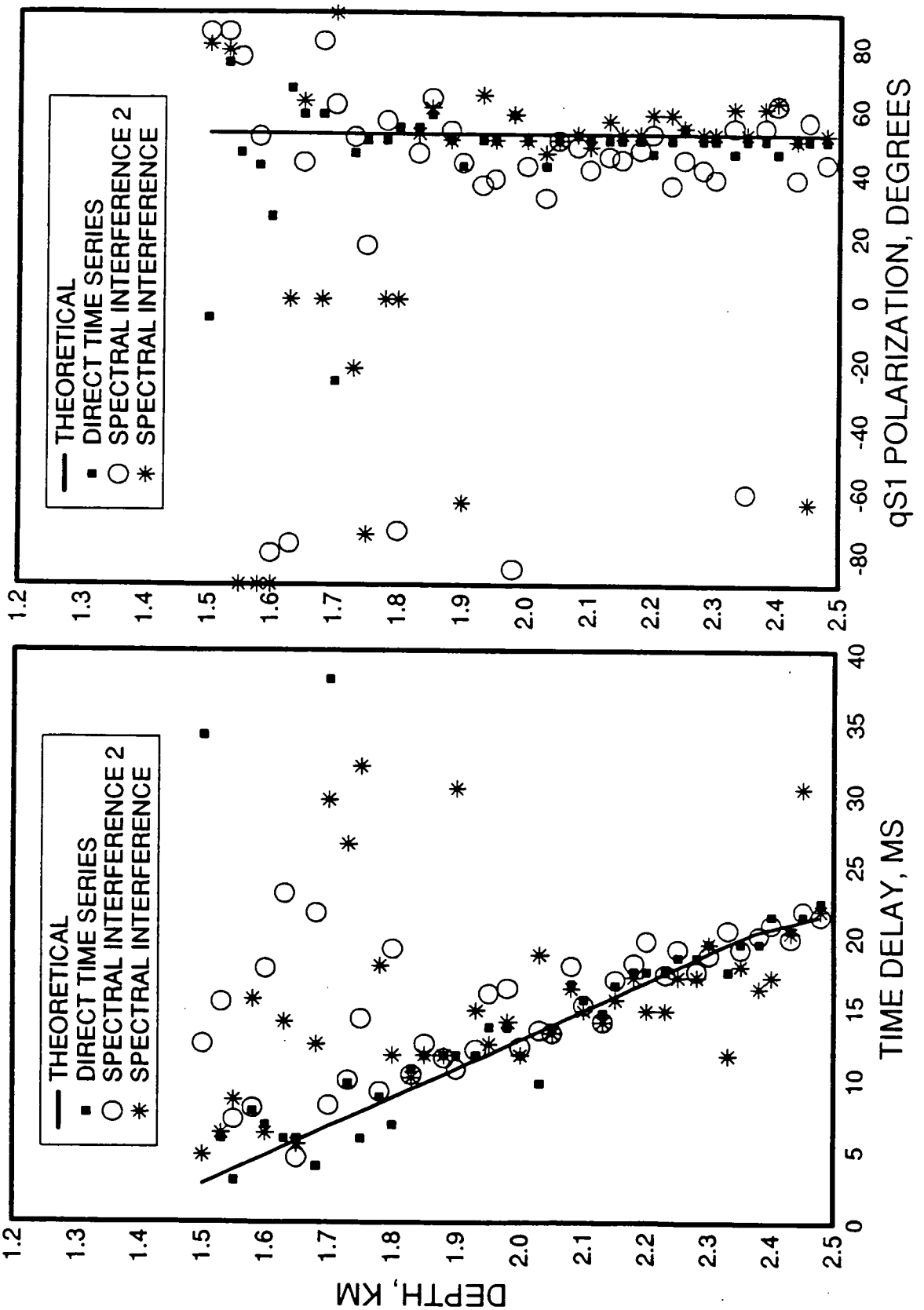

Figure 3.7. Estimates of *qS1* polarization and time delay from the data in Figure 3.6 using the three automatic techniques for measuring shear-wave splitting. This gives a clearer indication that notch deconvolution has not damaged shear-wave polarizations.

In this thesis, only downgoing waves are studied for the presence of anisotropy. As such, F-K filtering is used primarily to remove coherent upgoing energy and unwanted incoherent energy, such as scattering. This can be done by applying a fan shaped F-K filter enclosing the desired energy in the F-K plane and rejecting everything else. However, narrow fan shapes (excluding more and more of the F-K plane) will have severe spatial smoothing effects on the filtered seismic traces, which must be examined in relation to distorting shear-wave polarization information. The number of traces used in the F-K filter also has an effect on the amount of spatial smoothing. In the following examples, the F-K filters used are applied to all the traces in the seismic section. The application of a rolling F-K filter, using a smaller number of traces, would result in less smoothing and is appropriate in seismic sections containing events with radically different dip. However, the software package used for F-K filtering did not have the option of applying a rolling F-K filter and this form of F-K filtering was not investigated.

Anisotropic model

Taking the "notch" deconvolved seismic traces in Figure 3.6, the same fan shaped, acceptor F-K filter was applied to all three components, with the aim of removing any remaining incoherent noise present after the deconvolution stage. The edges of the filter were at 5ms/trace and 13ms/trace, representing a relatively tight filter giving rise to a large amount of spatial smoothing. A taper of width 9ms/trace was applied to both edges of the fan filter in order to subdue the amount of side lobe energy.

The filtered seismic traces are given in Figure 3.8, clearly showing that the signal to noise ratio has been increased compared to the traces in Figure 3.4. The shapes of the shear-wave PDs in Figure 3.8 also indicate that F-K filtering has not distorted polarizations as they are not significantly different from those in Figure 3.4. Figure 3.9 shows the results of applying the automatic techniques. An improved fit to the theoretical values of time delay and polarization is obtained compared to those in Figure 3.7 where only notch deconvolution has been applied. However, *qSl* estimates from the second spectral interference technique (looking for minimum interference) show that deviations from the true *qSl* polarization are consistent from level to level. This is a result of the spatial smoothing effects of F-K filtering, meaning that time delay and *qSl* estimates are no longer independent from level to level. The example here suggests it is only the second spectral interference technique that is affected by spatial smoothing, the other two methods picking good *qSl* polarizations.

In a real VSP, the orientation of the horizontal component geophones will not be constant as the tool may reorient itself between recording levels. This effect can be simulated in synthetic data by using real tool orientations, measured from boat 1 offset in the Vulcan VSP (Chapter 4). The orientation of the H1-component geophone relative to the X-direction is given in Figure 3.10, showing significant changes in orientation between levels. The X- and Y-components of the notch deconvolved traces in Figure 3.6 were rotated using these rotation angles, to give two new sections, with no consistent geophone orientation. These sections were then F-K filtered as before, using exactly the same shape of filter for both sections.

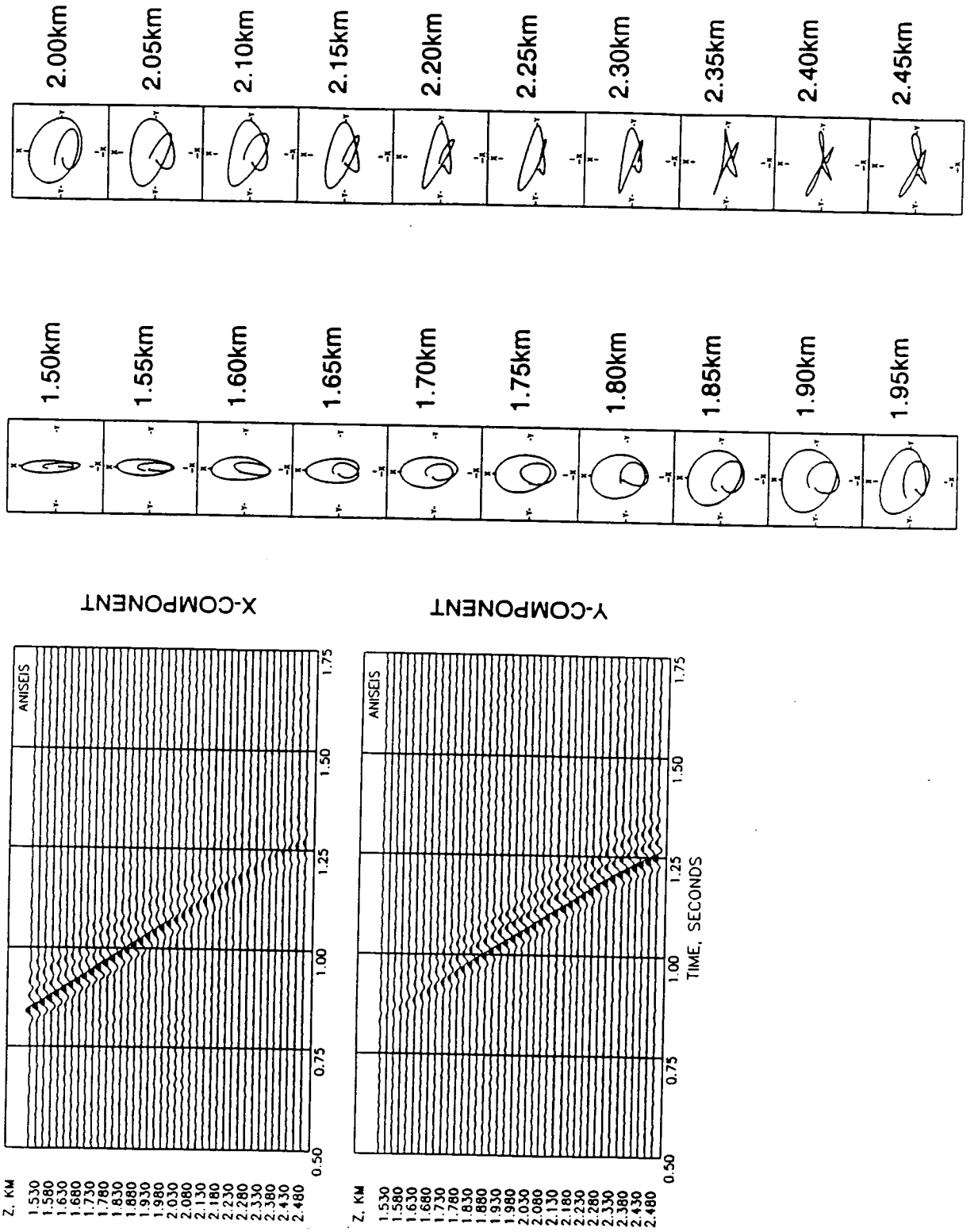

Figure 3.8. Seimograms and PDs after F-K filtering of the data in Figure 3.6. The signal/noise ratio has been further improved by this technique and the PDs suggest that polarization information has remained intact when compared to the noise free PDs in Figure 3.4.

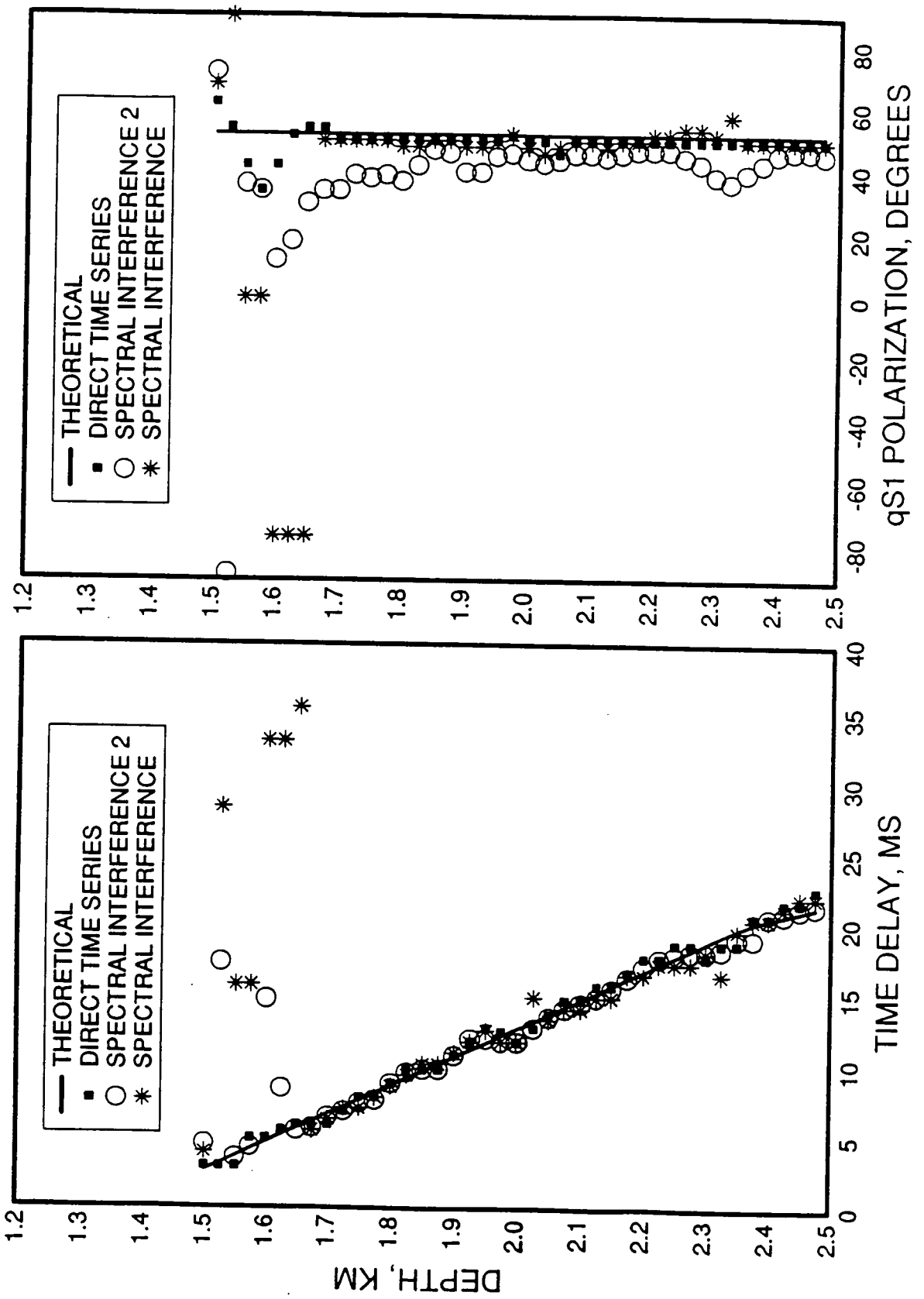

Figure 3.9. Automatic estimates of *qS1* polarization and time delay from the data in Figure 3.8. All three techniques show much smaller scatter of the time delay measurments around their theoretical values, while the second spectral interference technique gives small, but consistent differences for the *qS1* polarizations direction.

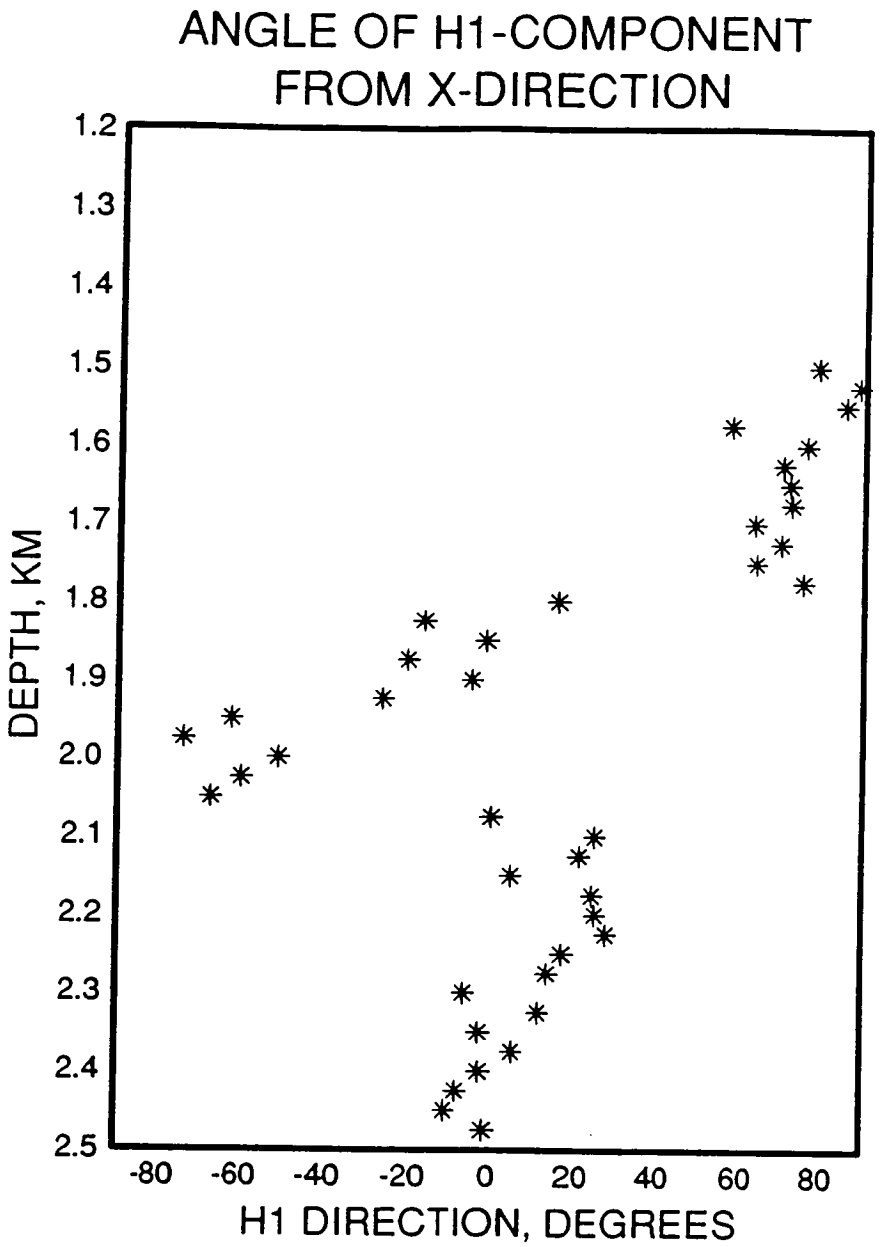

Figure 3.10. Rotation angles applied to the horizontal component seismograms in Figure 3.6. After rotation, the geophones are no longer consistently oriented, representing the natural rotation of a VSP tool as it is dragged up a well.

After F-K filtering, the geophone records were rotated back to their original X- and Y-directions. In real data, this corresponds to rotation into a consistent coordinate system using either gyro or *P*-wave polarization data. Shear-wave PDs after this processing are given in Figure 3.11, and show some differences in shape and orientation from those in Figure 3.6, especially the top seven displayed PDs. Application of the automatic techniques gives a much better idea how the rotations have affected the polarizations of shear-waves and results of this are shown in Figure 3.12. These show considerable deviations of the *qS1* polarization from its theoretical direction and increased scatter in time delay estimates compared to Figure 3.9. Clearly, it is not desirable to F-K filter three-component data until they have been rotated into a consistent coordinate system.

Isotropic model

In Chapter 2, the three automatic methods for measuring shear-wave splitting were applied to a noisy, isotropic, synthetic VSP to examine the effectiveness of the techniques to determine positively when isotropy was present. With the signal/noise ratio at about 2/1 (formed by normal source signature deconvolution of the airgun source with a signal/noise ratio of 20/1 in the undeconvolved traces), a large amount of scatter was present on all the measurements of time delay, while the first spectral interference method and the direct time series method both picked *qS1* polarizations loosely clustered about the source polarization. The second spectral interference

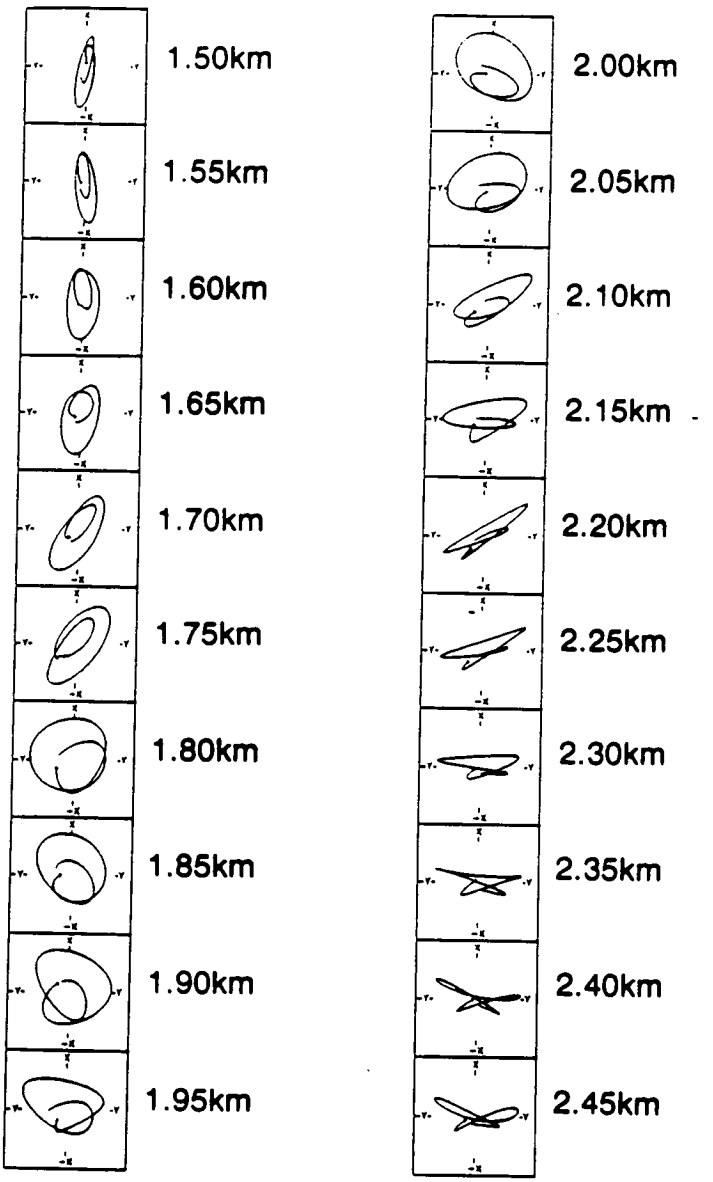

Figure 3.11. Shear-wave PDs of the X- and Y-component seismograms in Figure 3.6 after application of the rotations in Figure 3.10, then F-K filtering and finally reorientation back to the X- and Y-directions. Comparison with the PDs in Figure 3.4 indicates that some polarization distortion has arisen due to the processing of inconsistently oriented geophones.

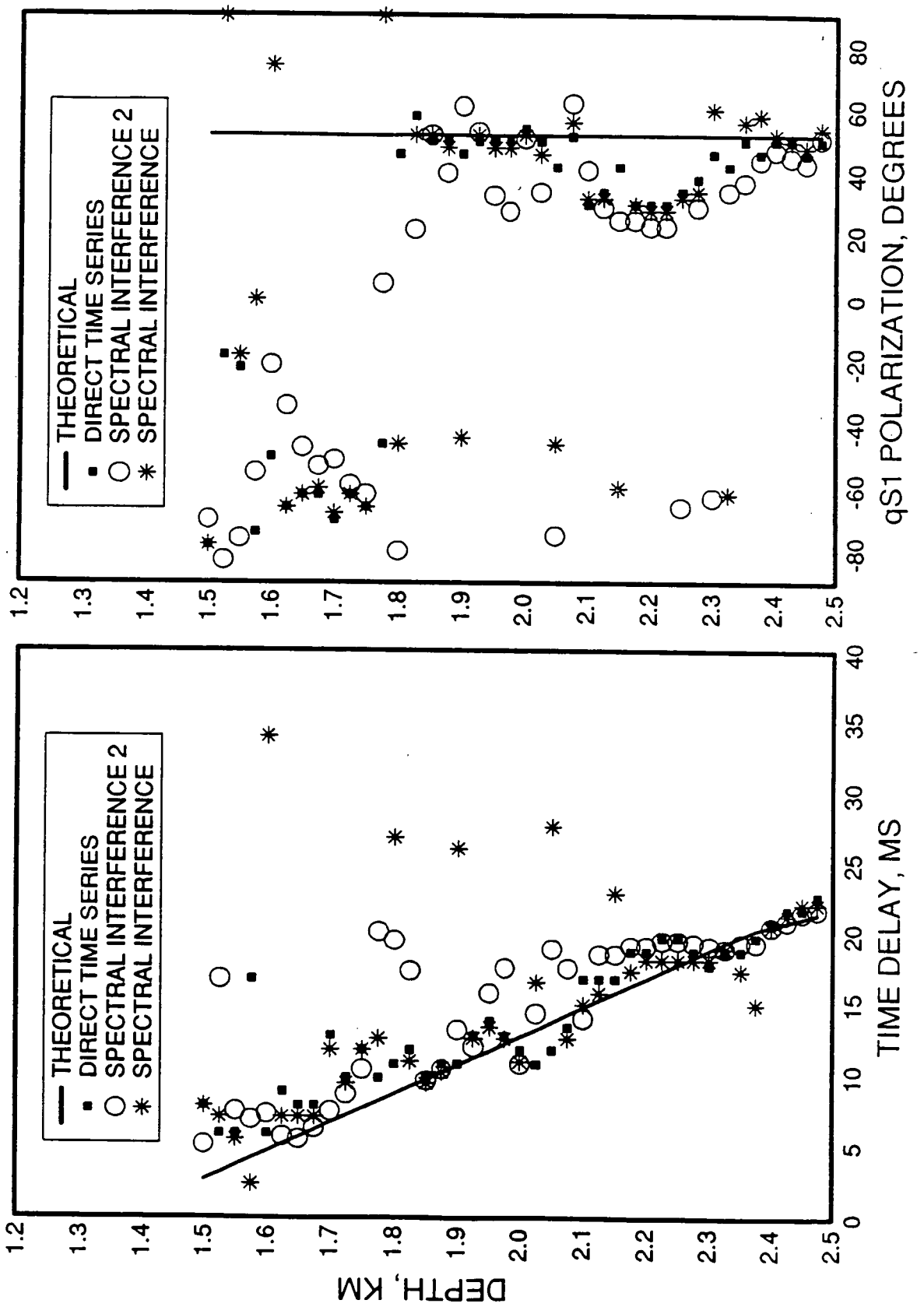

Figure 3.12. Automatic estimates of *qS1* polarization and time delay from the inconsistently oriented, F-K filtered data. Compared to results in Figure 3.9, time delays are much more scattered and large deviations of the *qS1* polarization from its theoretical value exist. This demonstrates that three-component data must be consistently oriented before application of F-K filtering.

technique produced more random *qSI* polarizations. Using this same, noisy isotropic model as a starting point, the effects of F-K filtering were studied to see if they introduced any consistent polarizations or time delays into what should be isotropic data.

The same fan-shaped F-K filter, as used with the anisotropic data, was applied to the X- and Y-components in Figure 2.14, Chapter 2. The seimograms and PDs after this processing are shown in Figure 3.13 and certainly demonstrate that F-K filtering has increased the signal/noise ratio to about 8/1. However, the remaining noise on the Y-component is now coherent, with very similar characteristics as the desired signal. Has this introduced consistent polarizations and delays in to the data? Although it is difficult to interpret PDs, those shown in Figure 3.13 do not appear to be particularly consistent from level to level, although only every second geophone is displayed here.

Results from the three automatic techniques are given in Figure 3.14. The first spectral interference technique and the direct time series method both show a bias towards picking small time delays, and *qSI* polarizations are much more tightly clustered around the source polarization compared to Figure 2.15. These observations suggest that F-K filtering has not introduced any appreciable anisotropic bias to the isotropic model.

The picture presented by the second spectral interference method is a little different. Here, consistent measurements, especially of time delay (between 1.7km and 1.9km), can be seen over a number of

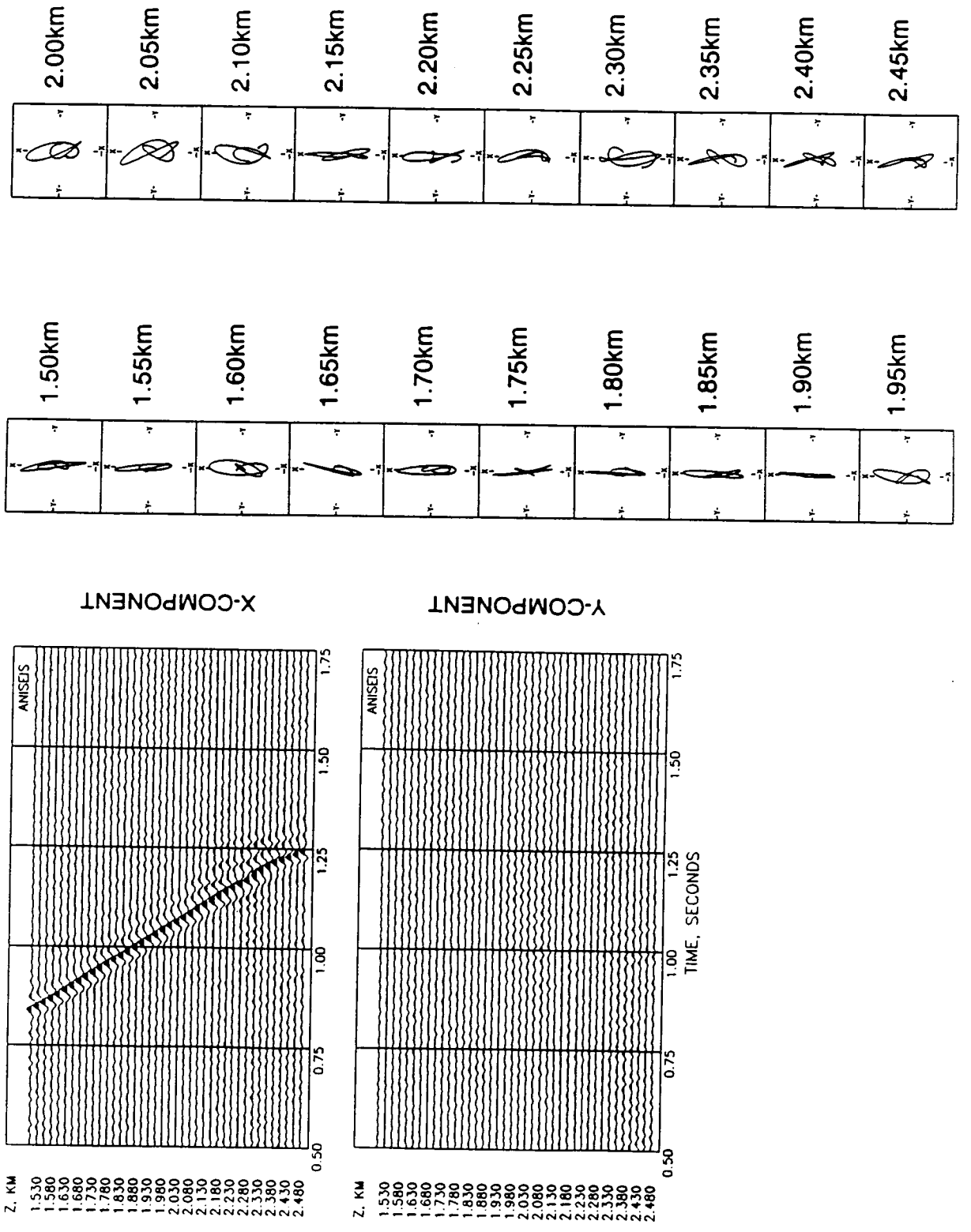

Figure 3.13. F-K filtered version of the noisy, isotropic seismograms and PDs given in Figure 2.14. Although the amplitude of the noise on the Y-component has been reduced, it is more coherent compared to Figure 2.14.

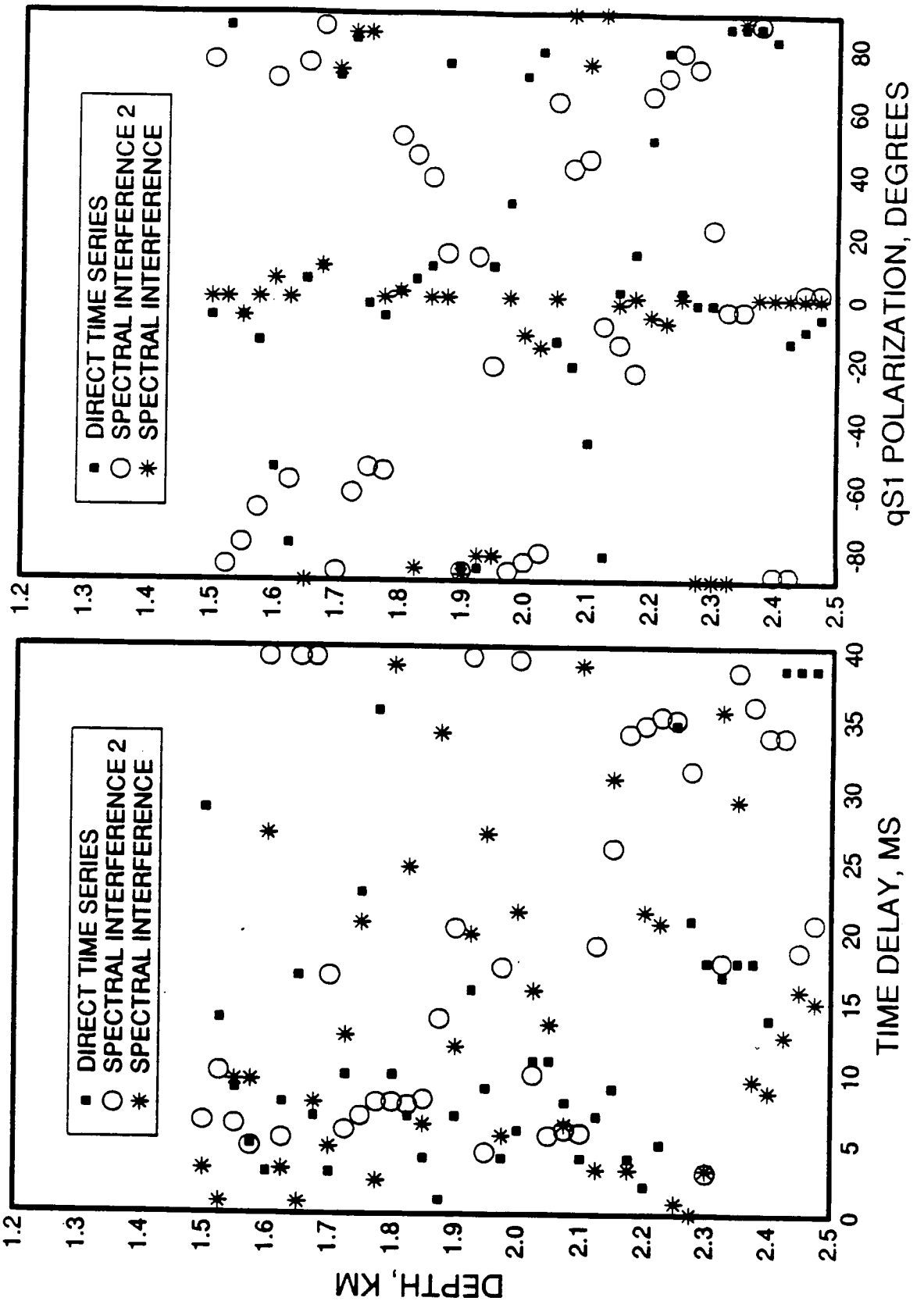

Figure 3.14. Automatic estimates of *qS1* polarization and time delay from the F-K filtered, isotropic data in Figure 3.13. The second spectral interference method shows consistent time delay picks over a number of depth intervals indicating that F-K filtering may introduce anisotrpic effects into originally noisy isotropic data.

geophone locations. In this case, consistent results from this method alone cannot be used as definite indication of anisotropy if the data have been F-K filtered. Only if all three techniques give similar answers can the results be treated with any reliability.

3.4 Processing reflection data

Obviously only land reflection data may be used for three-component shear-wave analysis because shear-waves do not propagate through a liquid! The huge expense of laying sea bottom geophones also prohibits any future attempts to carry out three-component marine reflection surveys. This section is a short discussion on some of the more commonly used processing steps involved in producing a reflection section and how they may affect recordings of shear-wave splitting.

Decay compensation

Many processing techniques rely heavily on the extraction of statistical information from stationary time series. Roughly similar amplitude levels throughout the data are therefore required. It is also important for quality control purposes to be able to bring all the data within a displayable dynamic range, requiring that the amplitudes of later arrivals are increased to the same level as the initial arrival of interest, which is the process of decay compensation. Regardless of how decay compensation is sought, it will involve a time dependent amplification factor being applied to the two horizontal components. The possibilty exists that polarization information contained in split shear-waves may be distorted by this processing step, the extent to which depends on how much the amplification factor varies from the begining of a fast shear-wave arrival to the end of the corresponding slow shear-wave.

The same decay function must be applied to both horizontal components otherwise polarization information will almost definitely be destroyed. Furthermore, if two orthogonal source polarizations are used, forming a four component data set, the same decay function should be applied to all four components. This is particularly important if Alford rotation (Alford, 1986) is to be applied in order to determine the natural axes of the azimuthally anisotropic medium.

Stacking

Stacking two-component shear-wave data has been studied in detail by Li (1990) Results from his work show that a form of polarization analysis must be carried out at the same time as the more standard velocity analysis. Each of the two-component traces in the common depth point (CDP) gather must be analysed to determine the polarizations of the fast and slow shear-waves and then rotated so that the fast and slow shear-waves are on separate components. In other words, the fast and slow shear-waves must be decoupled before stacking to prevent distortion of polarization information.

If the anisotropy is assumed to be caused entirely by parallel, vertical cracks (hexagonal symmetry with a horizontal symmetry axis), only one polarization angle need be determined for the whole CDP gather.

Li (personal communication) is developing a processing package where a polarization analysis correction (PAC) is applied to CDP gathers. Although this significantly increases computing time, it is the only method to reliably stack multicomponent reflection data.

Predictive deconvolution

Hatton et al. (1986) summarise predictive deconvolution when they say that it does "something nice to data, but we don't know what"! Where Wiener filtering us used, this form of deconvolution relies on the following statistical properties of the data:

1. The reflection series is random and white;
2. Noise is random and stationary;
3. The wavelet is minimum phase.

The effectiveness of the deconvolution will be loosely related to the suitability of these assumptions.

Its main purpose is to remove multiple energy, such as reflections from the weathered layer, from a seismic section, while also possibly applying some wavelet compression. In Wiener fitering, the deconvolution operator is designed from the autocorrelation function of a seismic trace. If anisotropy is present and both split shear-waves are recorded on the single component to be deconvolved, the autocorrelation function of the trace will contain energy at a lag corresponding to the delay between the fast and slow shear-waves. This energy may be mistakenly attributed to multiples and thus removed by predictive deconvolution with dire consequences for shear-wave splitting!

However, it is unlikely that the delay between split shear-waves will be large enough to be mistaken for multiple energy, although if any form of wavelet compression is applied then shear-wave splitting will be severely distorted.

These problems can be avoided by rotation of the two horizontal recording components so they are parallel and perpendicular to the fast shear-wave. It should then be safe to apply the same deconvolution operator to both components without distortion of polarization information.

3.5 Conclusions

Deterministic deconvolution to remove the shape of the source signature from seismic data, where the source signature is known from measurement, can be applied to three-component shear-wave data without distortion of polarization information. The same operator must be used for all three-components to ensure that this is the case. The orientations of the components do not matter for this type of processing.

Where the source signature has notches in its amplitude spectrum, source signature deconvolution can become unstable in the presence of noise, giving very poor signal/noise ratios for an originally good signal/noise ratio. A method was described for estimating what the amplitude spectrum of the deconvolved trace should be at frequencies where notches occur. This was successfully applied to synthetic, anisotropic data without distorting shear-wave splitting information.

Application of F-K filtering to noisy, synthetic, anisotropic data demonstrated that incoherent noise can be considerably suppressed, without destroying polarization information. However, where the orientations of the geophones are not constant, F-K filtering is

likely to severely distort shear-wave splitting information. Thus, three-component data must be rotated to a common orientation of axes (such as horizontal radial, horizontal transverse and vertical) before this type of filtering is applied.

From the examples shown in this Chapter, F-K filtering of isotropic data is unlikely to introduce patterns which will be mistakenly interpreted as anisotropy. However, the second (minimum interference) spectral interference technique for automatically measuring shear-wave splitting, described in Chapter 2, may be biased by F-K filtering to give *qSI* polarizations and time delays that could be interpreted as being produced by anisotropy. Hence, results from all three automatic techniques described in Chapter 2 must be considered before arriving at any conclusions concerning whether anisotropy is (or is not) present in data.

The section on processing reflection data merely acts to highlight some possible areas where standard processing techniques may severely distort polarization information. The most obvious way to overcome most of the problems is to rotate the two horizontal components to be parallel and perpendicular to the fast shear-wave direction. In this way, each component is processed in the same way as *P*-wave data, with the condition that exactly the same procedures are applied to both components.

Chapter 4 - The Vulcan gas field marine VSPs

4.1 Introduction

Four three-component, offset VSPs and one three-component, zero offset VSP were shot in the Vulcan gas field in July 1986. One of the prime aims for shooting these VSPs was to increase the resolution for determining faults within the Rotliegend sandstone reservoir compared to surface seismic reflection data (Noble et al., 1987). This chapter investigates the data for the presence of velocity anisotropy, with the aim of relating any anisotropy to stress directions within the reservoir. Processing procedures applied to the data are given in detail for one of the offset VSPs.

Generation of shear-waves in a marine environment

Most land based shear-wave studies use shear-wave sources such as VIBROSEIS, three or five hole shot geometries, ARIS, or OMNIPULSE. These source types generate shear-waves directly, which travel from source to receiver. This direct form of shear-wave generation is not possible in a marine environment, where the source is postioned in a water layer. Furthermore, it is not feasible to carry out marine shear-wave reflection profiles, because the receivers are also in a water layer. Consequently, the most economic marine shear-wave survey will be in the form of an offset VSP, where *P*- to shear-wave conversion takes place at significant velocity boundaries along ray paths from source to receiver. Ideally, to study velocity anisotropy in the region of a hydrocarbon reservoir, shear-waves mode-converted at the top of the cap-rock overlying the reservoir should be studied as these shear-waves have a simple path, travelling only through the cap-rack and reservoir rock. Shear-waves generated at shallower depths will have more complex propagation paths, possibly suffering

multiple shear-wave splitting if the minimum stress direction is not constant with depth (such that the stress aligned inclusions may have different orientations at different depths following changes in the direction of minimum stress near the Earth's surface (Crampin, 1990)).

A number of problems are associated with studying shear-waves generated by mode-conversion at the top of the cap-rock (necessitating wide incidence angles) and recorded within the reservoir region. These are listed below:

1. Only one polarization of shear-wave can be generated and this depends on the dip of the boundary where the mode-conversion occurs. If the polarization of the converted shear-wave lies in a symmetry plane of the anisotropic structure, no shear-wave splitting will be observed.

2. Relatively short path lengths through the reservoir mean that delays between split shear-waves may be very small, depending on how much velocity anisotropy is present. Small time delays are difficult to measure and generally have large percentage errors associated with them.

3. The non-vertical ray paths necessary for mode conversion lead to interpretation difficulties of shear-wave splitting in terms of the minimum stress direction. This is particularly true if the total velocity anisotropy is caused by a combination of EDA and PTL anisotropy, as mentioned earlier.

4. Shear-wave arrivals may be contaminated by *P*-wave energy which will seriously distort information contained in the shear-wave splitting. It may be possible to eliminate this problem if techniques to separate *P*- and shear-wave modes (Dankbaar, 1985; Dankbaar, 1987; Dillon, 1988; Esmersoy, 1990) can be successfully employed without distorting shear-wave polarizations.

4.2 The Vulcan gas field

Aeolian sandstones of the Early Permian Upper Rotliegend form extensive gas reservoirs in an E-W trending zone about 100km wide in the Southern Permian Basin, stretching from offshore Yorkshire across the southern North Sea into the northern part of The Netherlands and the North German lowlands (Thomsen, Damtoft and Andersen, 1986). The Vulcan gas field is part of this Rotliegendes sandstone, and lies within the axial region of the inverted Sole Pit Basin in the southern North Sea, about 60km offshore. The Rotliegendes sandstone in this area is composed predominantly of stacked aeolian sand dune facies with some adhesion-rippled interdune sediments and aeolian sheet sandstones. The reservoir rocks are sealed by the overlying Zechstein Carbonate and Evaporite transgression sequence of total thickness about 500m.

In the Victor gas field, about 30km northeast of Vulcan, Conway (1986) has subdivided the Rotliegendes sandstone into four zones based on lithology and the dominant facies. At the base, Zone 4 is a thin extensive unit of relatively uniform thickness deposited on a low-relief surface over the Carboniferous source rocks. It consists of fluvial sandstones derived from the higher topography of the London Brabant Massif to the southwest. Zone 3 represents the first subaerial phase of Rotliegendes deposition consisting predominantly of dunes with occasional sheet sands. A rise in the water table marks the end of Zone 3 and represents the start of Zone 2. It is characterised by at least 50% adhesion-ripple sediments interbedded with sheet sands and the occasional dune. Its highly argillaceous nature results in poor vertical permeabilities and is a potential permeability barrier on Victor. Zone 1 consists of mainly dune sands

and represents a return to more arid conditions with an increased sediment supply. The subsequent Zechstein transgression has caused reduction in reservoir porosity and permeability in the upper part of Zone 1 due to depostion of cement from the percolation of cement-bearing waters into the Rotliegendes. This post-diagenetic event caused disruption of the original bedding, distorting the dune sand laminae with water/air escape structures, slump structures and minor sedimentary faulting. In the Victor gas field, it is estimated that more than 50% of the Gas Volume is contained within Zone 1, which on average displays excellent reservoir properties.

Permeability tests in the Rotliegendes sandstone sequence in the Vulcan gas field indicate that Zone 3 has the best reservoir properties while Zone 1 displays a very poor permeability. The results for Zone 1 are in contrast to Conway's findings. This may be attributed to a larger depth of penetration of cement-bearing fluid from the Zechstein caprock in the Vulcan than for the Victor field, although this is unlikely as Glennie and Buller (1982) do not observe a penetration of more than 50m for the cement bearing fluid from the Zechstein into the Rotliegendes. Alternatively, the upper part of the sandstone sequence in the Vulcan field may be dominated by more sabkha type sedimentation resulting in poorer reservoir properties. Zone 3 lies approximately 115m below the top of the sandstone sequence, with a total thickness of around 75m. The gas/water contact is about 40m below the top of zone 3.

4.3 Possible causes of anisotropy

Bedding planes

Bedding planes are a possible cause of velocity anisotropy, but in a purely aeolian derived sandstone, the velocity contrast across bedding planes is probably small. Larger velocity contrasts may be expected in a mixed sabhka and aeolian type sedimentation environment such as Zones 2 and 4, where the presence of cement bearing fluid will act to strengthen the sandstone matrix compared to sandstone formed by subaerial deposition. The interleaving of the two sandstone types may give rise to velocity anisotropy. The symmetry of the anisotropic system is difficult to predict. If everything were plane layered, a cylindrical symmetry system with a vertical axis of symmetry would exist. However, the non-planar contours of dune sediments may significantly alter this view. In this case, the symmetry of the velocity anisotropy may be controlled to some extent by the shape of the dunes, which in turn is controlled by the wind strength and direction and the rate of sedimentation. Dune shapes may also play an important role in permeability anisotropy because dune top sands generally display better reservoir properties than dune base and interdune sands. This is due to larger sand grains being present in the upper parts of dunes giving good permeability (and porosity) properties. For transversely shaped dunes, it would be expected that permeability channels would be created along the dune crests, with reduced permeability orthogonal to the dune crests.

Fractures and microfractures

Natural fractures and microfractures have been observed in whole core, thin-section and SEM photographs throughout the Rotliegend

reservoir interval in the Argyll field (Bifani et al., 1986). No orientations are given, but since fracturing in rock is controlled by prevalent stress directions and magnitudes, they should fall into two categories; shear fractures and extension (tension) fractures.

Shear fractures

Shear fractures have a sense of displacement parallel to the fracture plane. They generally form at some acute angle to the maximum principal stress direction (σ_1) and at an obtuse angle to the minumum compressive stress direction (σ_3). Two possible fracture orientations are possible as indicated in Figure 4.1. The acute angle between shear fractures, known as the conjugate angle, is dependent primarily on the mechaninical properties of the rock, the absolute magnitude of σ_3 and the magnitude of σ_2 relative to σ_1 and σ_3 (as σ_2 approaches σ_1, the angle between σ_1 and the fracture plane decreases). These fractures are the result of compression and can occur at any depth where the rock is brittle.

Since all of the displacement is parallel to the fracture plane, there is little possiblilty of these fractures contributing positively to the porosity or permeability of a reservoir rock. Likewise, they probably will not produce much in the way of seismic anisotropy.

Extension and tension fractures

Extension fractures have a sense of displacement perpendicular and away from the fracture plane. They form parallel to σ_1 and σ_2 (Figure 4.1). Tension fractures are very similar to extension fractures and form when σ_3 is negative, or tensile. Unlike shear fractures, extension and tension fractures are open and as such

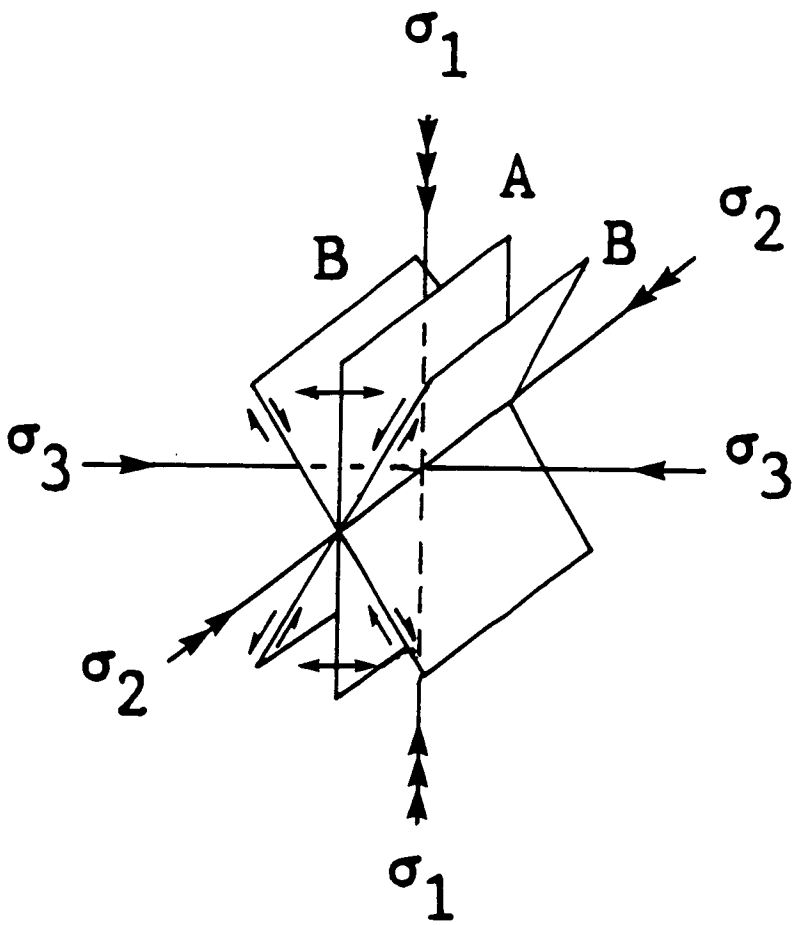

Figure 4.1. Fracture planes developed by extension (A) and shear (B) as a result of the applied stresses σ1, σ2 and σ3.

cannot exist below a certain depth. This initially led workers to believe that they were associated only with near surface conditions. However, if pore pressure is sufficiently large to exceed the minimum confining stress, σ_3, the rock will effectively be in tension. Since the tensile strength of rock is lower than its compressive strength by factors of hundreds, fracturing is much more likely under extension (whether regional or localised) than under compression. Consequently, the pore pressure may not have to be much larger than σ_3 to overcome the rock's low tensile strength, and initiate tension fractures. This is the principle on which hydrofracturing is based. High pore pressures are not uncommon in hydrocarbon reservoirs, indicating that where reservoirs have been fractured, this may be the most likely cause. Other possibilities exist and are reviewed by North (1985) and Nelson (1985).

Tension fractures offer good porosity and permeability prospects as they effectively form open channels. This also means that they can make a significant contribution to seismic anisotropy. Filling of these fractures with some crystallisation product, however, will have a negative effect on permeability as discussed by Nelson (1985).

Microcracks - Extensive Dilatancy Anisotropy

Shear, extension and tension fractures should not be confused with Extensive-Dilatancy Anisotropy (EDA) (Crampin, Evans and Atkinson, 1984; Crampin, 1985). The essential difference is that EDA is caused by deformation of the most compliant part of the rockmass as a result of the application of stress. This deformation may take the form of aligned pore spaces or microcracks and will change as the applied stress changes (i.e. this form of anisotropy is mobile). The fractures mentioned above are fixed in orientation throughout the

life of the rock and may start to close if the stress direction changes. If they become filled with crystalline material (with different seismic properties from the surrounding rock) such that they have an inherent strength, they will continue to contribute to the overall seismic anisotropy of the rock (although to a lesser extent because of the reduced velocity contrast between fracture filling and surrounding rock) even when they are not aligned with the current maximum horizontal stress direction. This can give rise to complex anisotropy, where fracturing occurs in combination with but an angle to EDA microcracks.

4.4 VSP geometry

The suite of VSPs consisted of four offsets placed around the well in the form of a cross (Figure 4.2). Geophones were located at 15.24m (50 feet) intervals down the well between T.D. (2453m) and 1600m. Above 1600m, the geophone spacing was increased to 30.48m (100 feet).

Note that this is not necessarily the best arrangement for observing shear-wave splitting because if the minimum compressive stress direction is parallel to the boat-rig azimuths, no splitting of the mode-converted shear-waves will occur in the horizontal plane. A better arrangement would be to have boat-rig azimuths placed at around 45° apart, thus ensuring that some of the offsets will produce shear-wave splitting.

A single, 160in^3, airgun was used as the seismic source for the VSPs, placed at a depth of 30 feet in a water depth of about 100 feet. The signature from this was recorded on a hydrophone 15 feet below the gun, an example of which is given in Figure 4.3. As can be seen, it is of particularly long duration due to reverberations of

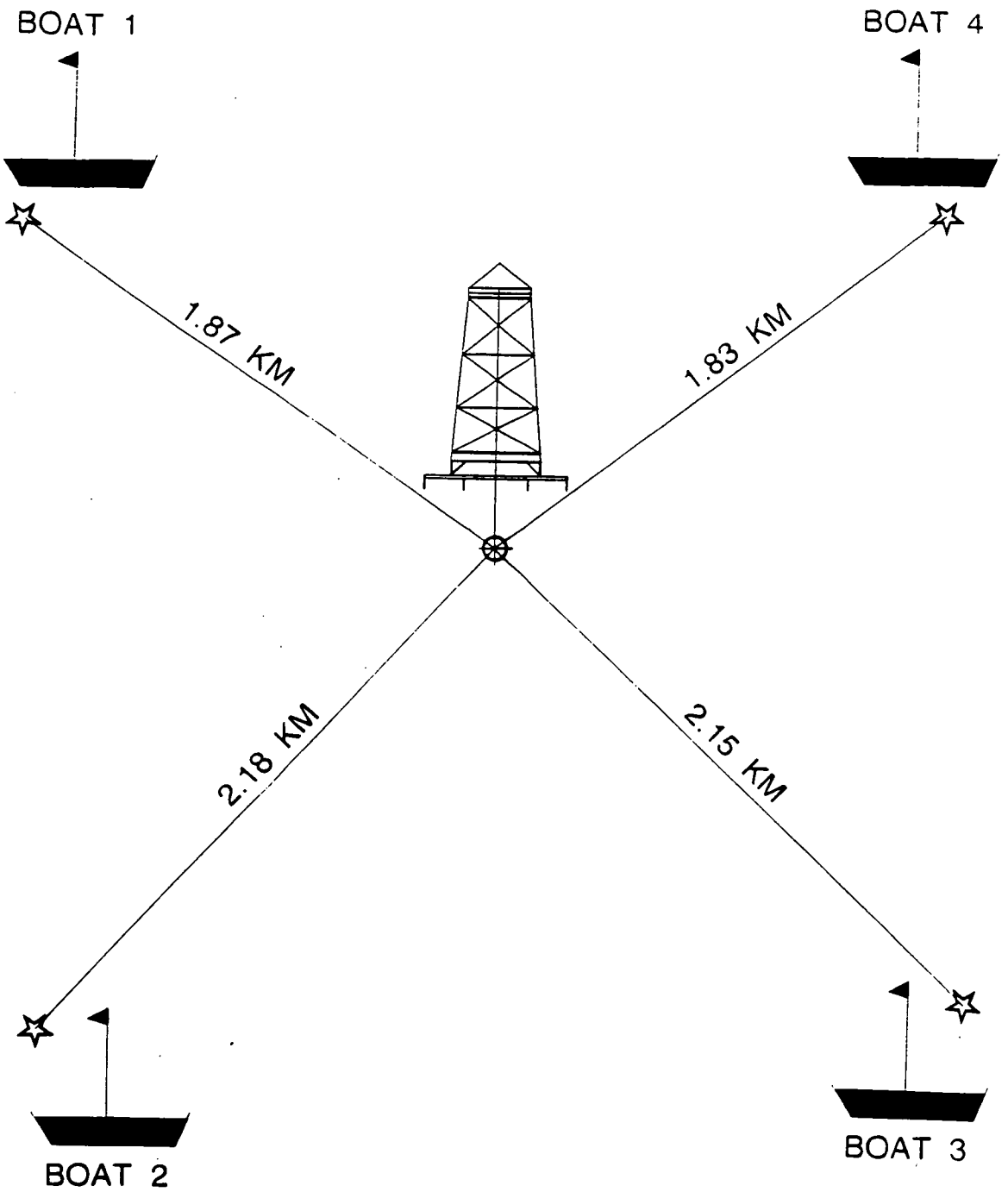

Figure 4.2. Plan of VSP layout showing the locations of the four offsets source locations. A further, rig source was located 53m from the well head.

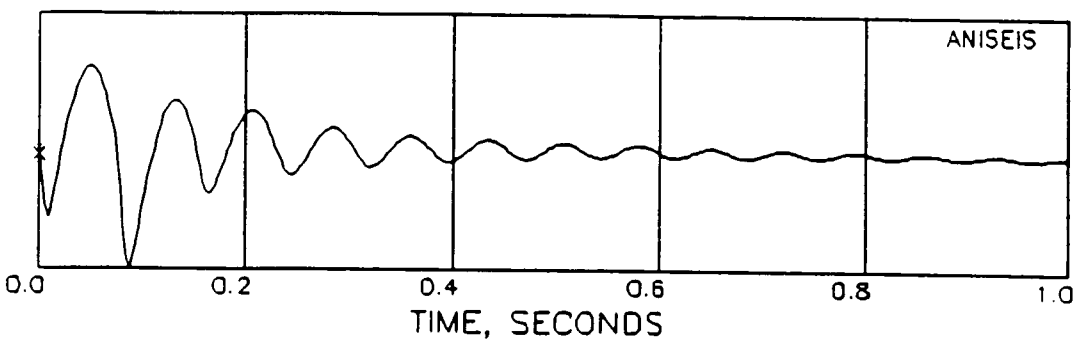

Figure 4.3. Source signature of a single 160in³ airgun at 30 feet depth. The signature displayed is the integrated output from a hydrophone placed 15 feet below the airgun.

the bubble pulse, caused mainly by the relatively large gun depth. The problems associated with such a source signature were discussed in Chapter 3, with the development of "notch" deconvolution to try and remove its shape from records.

Knowledge of the polarity of the recording axes is of fundamental importance to three-component seismology. Without this information, any directional measurements made from the data may be in error up to ±90°. The recording axes used in this VSP survey are shown in Figure 4.4 and is known as "right handed, vertical axis up", which uniquely determines the relative orientations of the three axes.

4.5 Processing field data

All the processing steps will be discussed and displayed for Offset 1, while only the final sections will be shown for the other three offsets.

Source signature deconvolution

Figure 4.5 shows the stacked, but undeconvolved three components from Offset 1. The three sections show relatively good signal to noise ratios, with the two horizontal components slightly worse than the vertical component. This is probably due to poorer coupling of the horizontal components. Despite this, it is assumed that the response of all three components is equal. All traces have been individually normalised so no comparison of relative energies can be made between different components. No AGC filter has been applied to any data displayed unless otherwise stated. Due to the length of the source signature, shown in Figure 4.3, it is difficult, although not

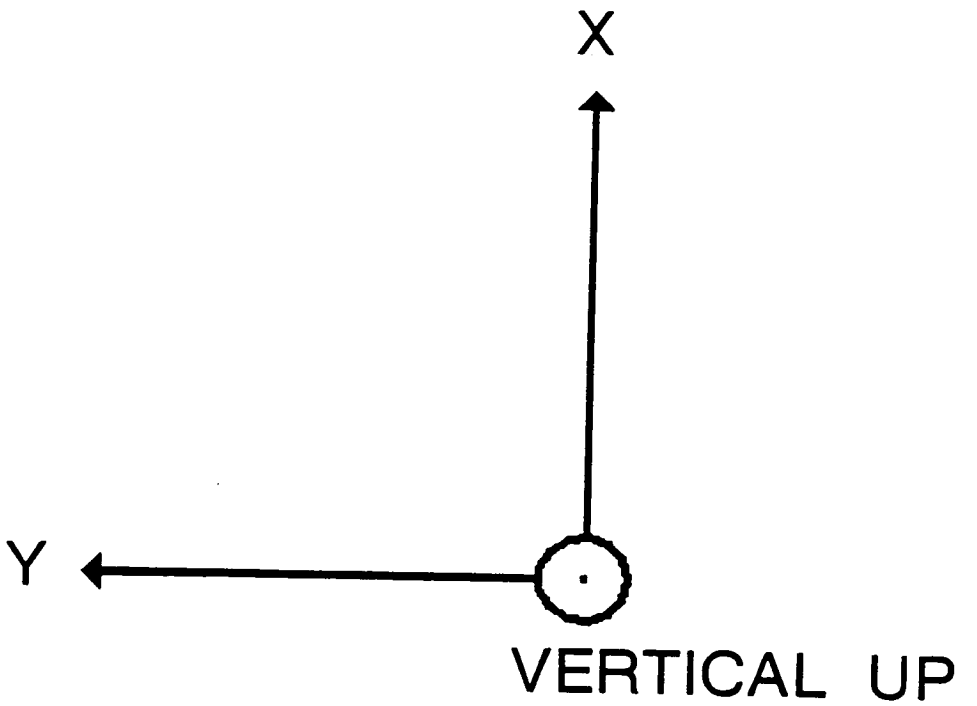

Figure 4.4. Recording coordinate system used by the three-component down hole tool. The system shown here is known as "right handed, vertical up".

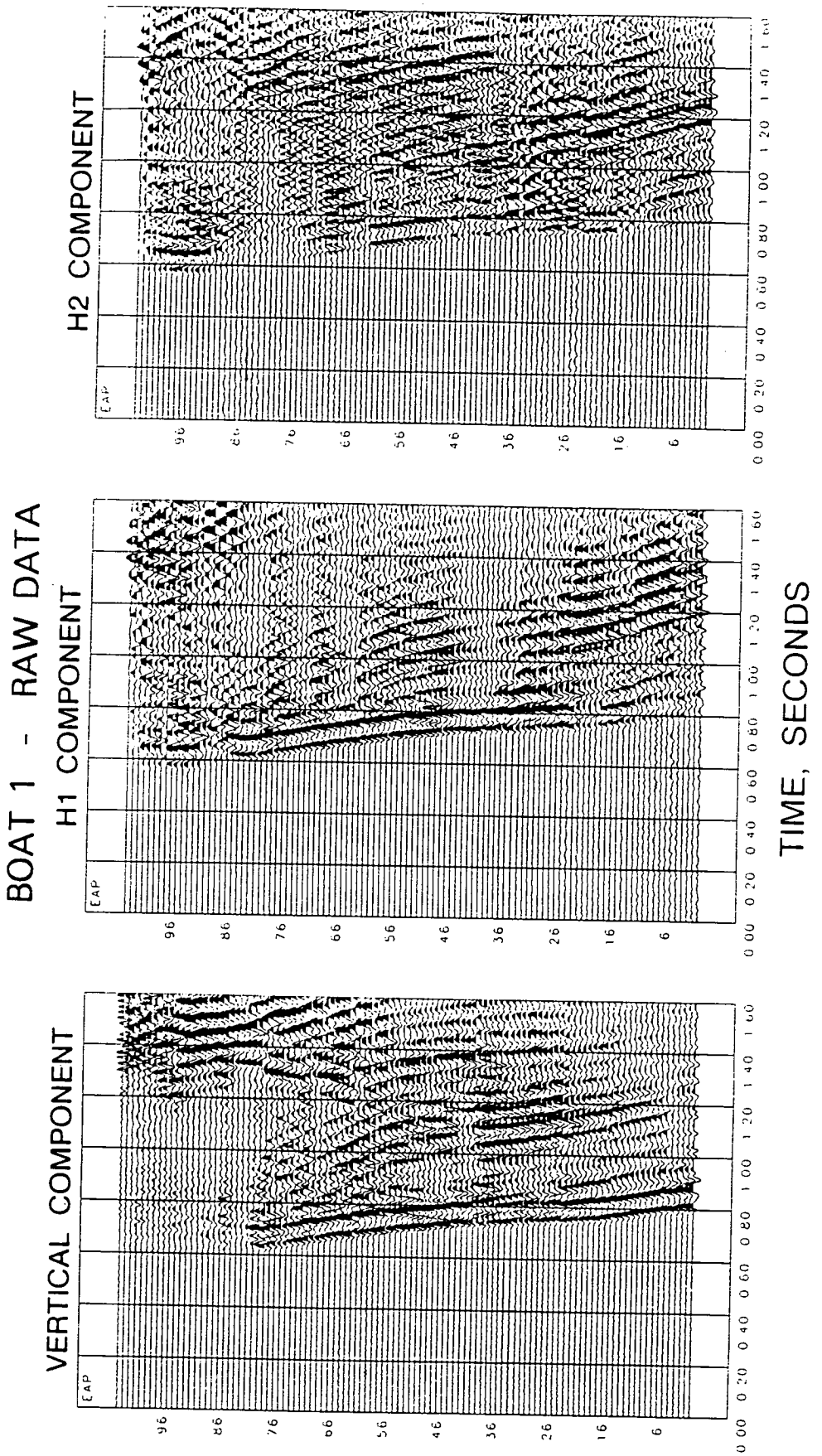

Figure 4.5. Raw data recorded from boat 1 source offset. The extended length of the source pulse makes it impossible to pick out any secondary arrivals.

impossible, to make out any arrivals other than the primary *P*-wave. Arrival time estimates for later phases would not be accurate and contamination by the initial *P*-waves would render any polarization information useless.

Both normal and "notch" source signature deconvolution were applied to the data from Offset 1. Deconvolution took place between the frequency limits of 2Hz and 55Hz. Stacking took place after deconvolution to take into account any changes in the source signature between shots. If the source signatures remained constant between shots, then it would not matter in what order stacking and deconvolution took place. Figure 4.6 compares the two deconvolutions of the H1-sections, from which it can be seen that notch deconvolution has improved the signal to noise ratio on the bottom third of the section, with the exception of a few individual traces. The improvement between notch and normal deconvolution is not a dramatic as with the synthetic example because the real data have more complex amplitude spectra, making interpolation much more difficult. This may be the cause of the noisy traces on the notch deconvolved section.

All three components from boat 1 are displayed in Figure 4.7 after notch deconvolution. Arrivals can be seen after the initial *P*-wave onset, such as the reflection at about 1.7km corresponding to the top of the cap-rock. Shear-wave arrivals can also be made out with their lower moveout velocities compared to the *P*-waves. However, further interpretation of the horizontal components cannot be made without rotating them to common axes. This can be done by considering the directions from which the *P*-waves arrive.

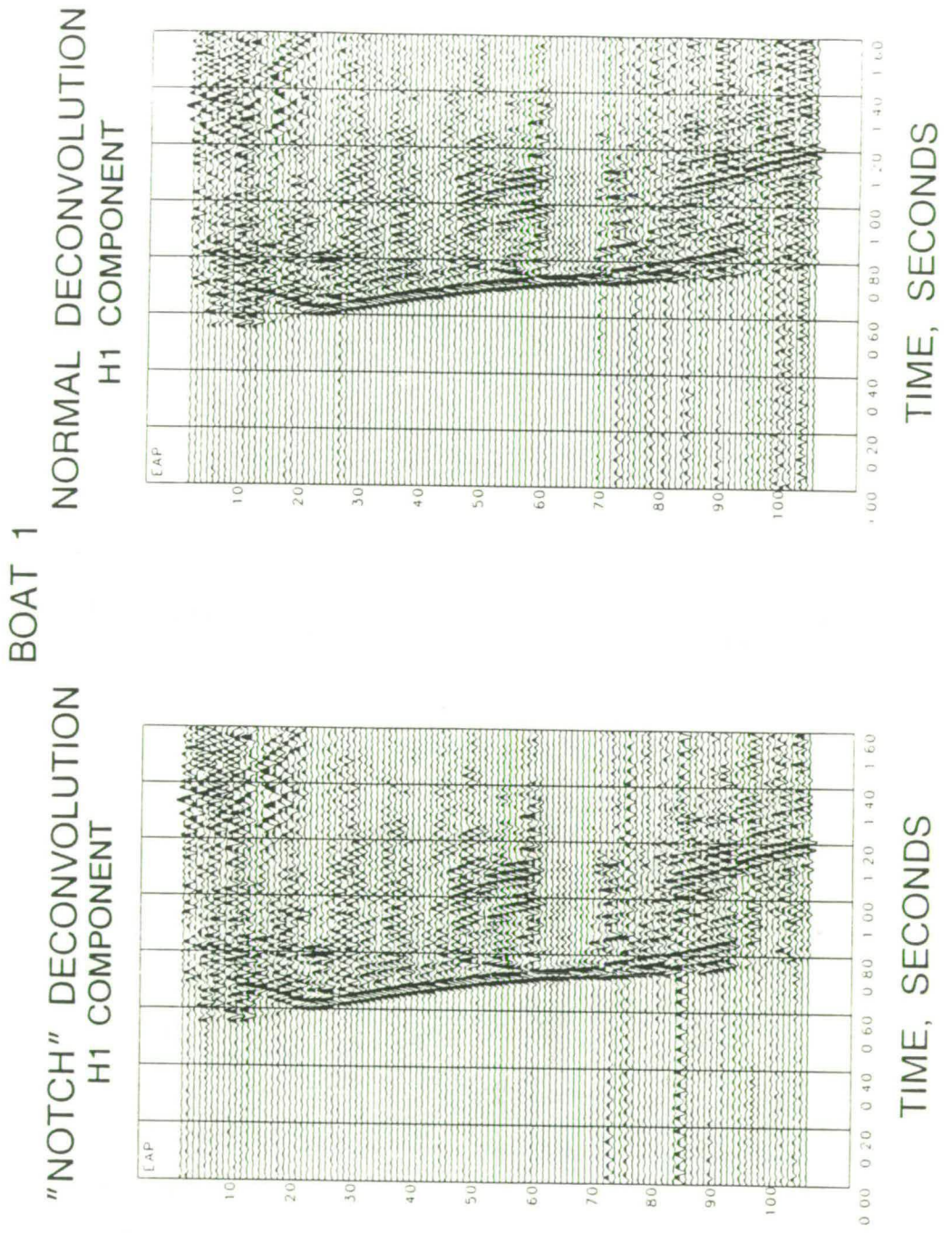

Figure 4.6. Comparison of normal source signature deconvolution and "notch" deconvolution applied to the X-component of boat 1. "Notch deconvolution produces better signal to noise ratio on the lower third portion of the section.

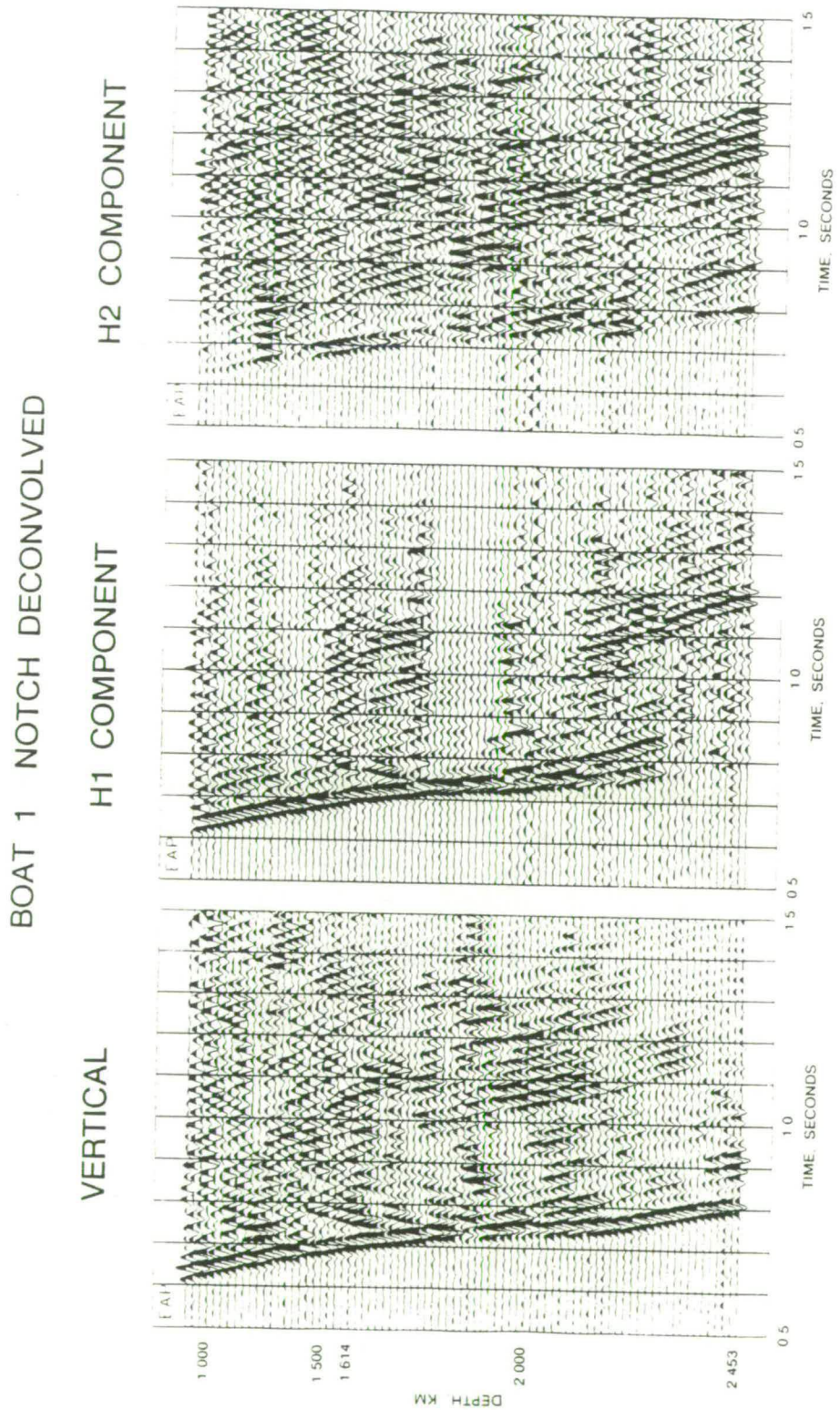

Figure 4.7. "Notch" deconvolution applied to all three components from boat 1. Evidence of secondary arrivals can now be seen.

Receiver rotation

Horizontal *P*-wave polarizations were estimated from the undeconvolved data where the signal to noise ratio was better than on the deconvolved records, with a covariance matrix method, following Kanasewich (1981). Since both offsets 1 and 2 were shot simultaneously (as were offsets 3 and 4), the *P*-wave polarization estimates should yield the same H1-component direction relative to North for each geophone level. Figure 4.8 shows the azimuth from North of the H1-component for each geophone level as measured from offsets 1 and 2, and shows relatively good correspondence between the offsets. Ideally, the two curves should be identical. *P*-wave polarizations could only be reliably measured for the bottom 79 geophones (0.96km to 2.45km), possibly due to larger hole diameter or more wash-out resulting in poorer sonde coupling with the side of the hole. Rotation of the horizontal components also included a change in polarity for the H2-component such that the rotated axes are left handed, vertical up, and thus compatible with a geographic coordinate system. The H1-component was rotated into the horizontal radial (HR) direction, pointing from the source to the receiver in the horizontal plane, leaving the H2-component in the horizontal transverse (HT) direction, pointing 90° clockwise from horizontal radial. The rotated sections are displayed in Figure 4.9 where three-component scaling has been applied. This form of scaling shows that very little *P*-wave energy is present on the HT-component, indicating that the rotation to HR and HT is successful. The same sort of scaling has been applied to all following seismic sections, so relative energies can be compared between components.

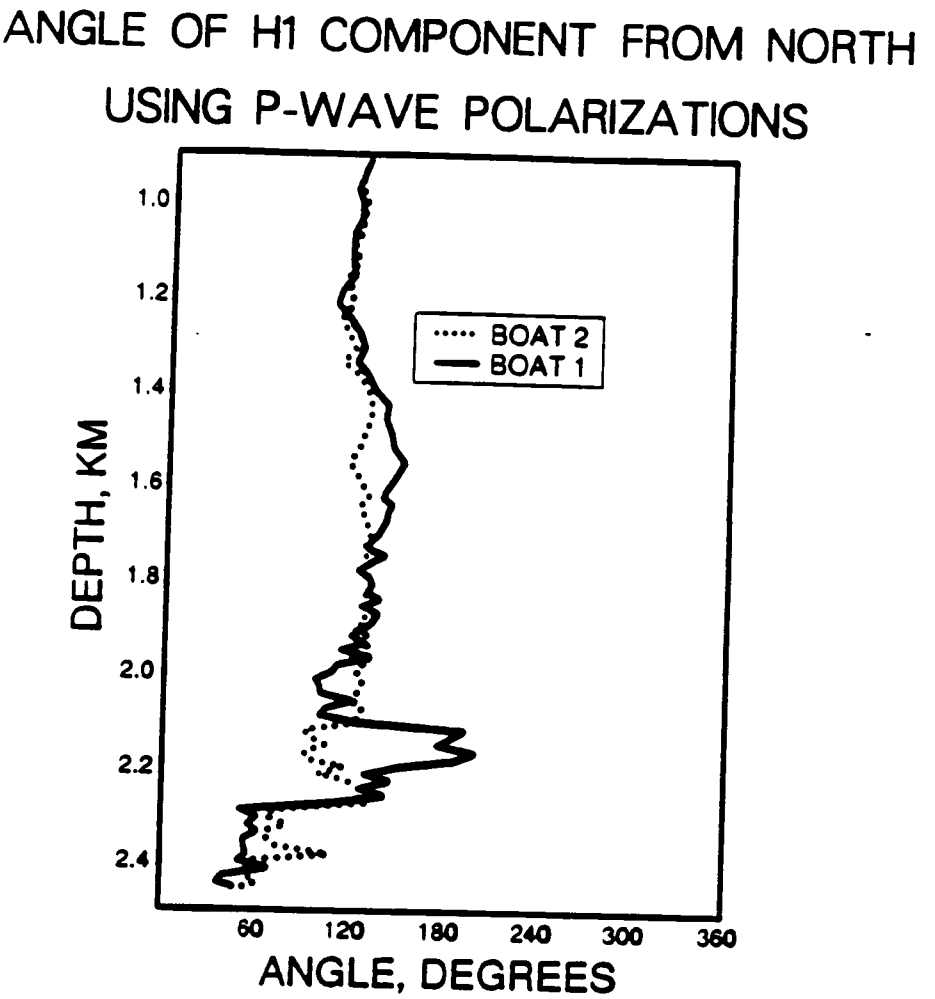

Figure 4.8. Measured orientations of the H1-component of the down hole tool from boat 1 and boat 2 offsets. Since these two offsets were shot at the same time, the two curves should be identical.

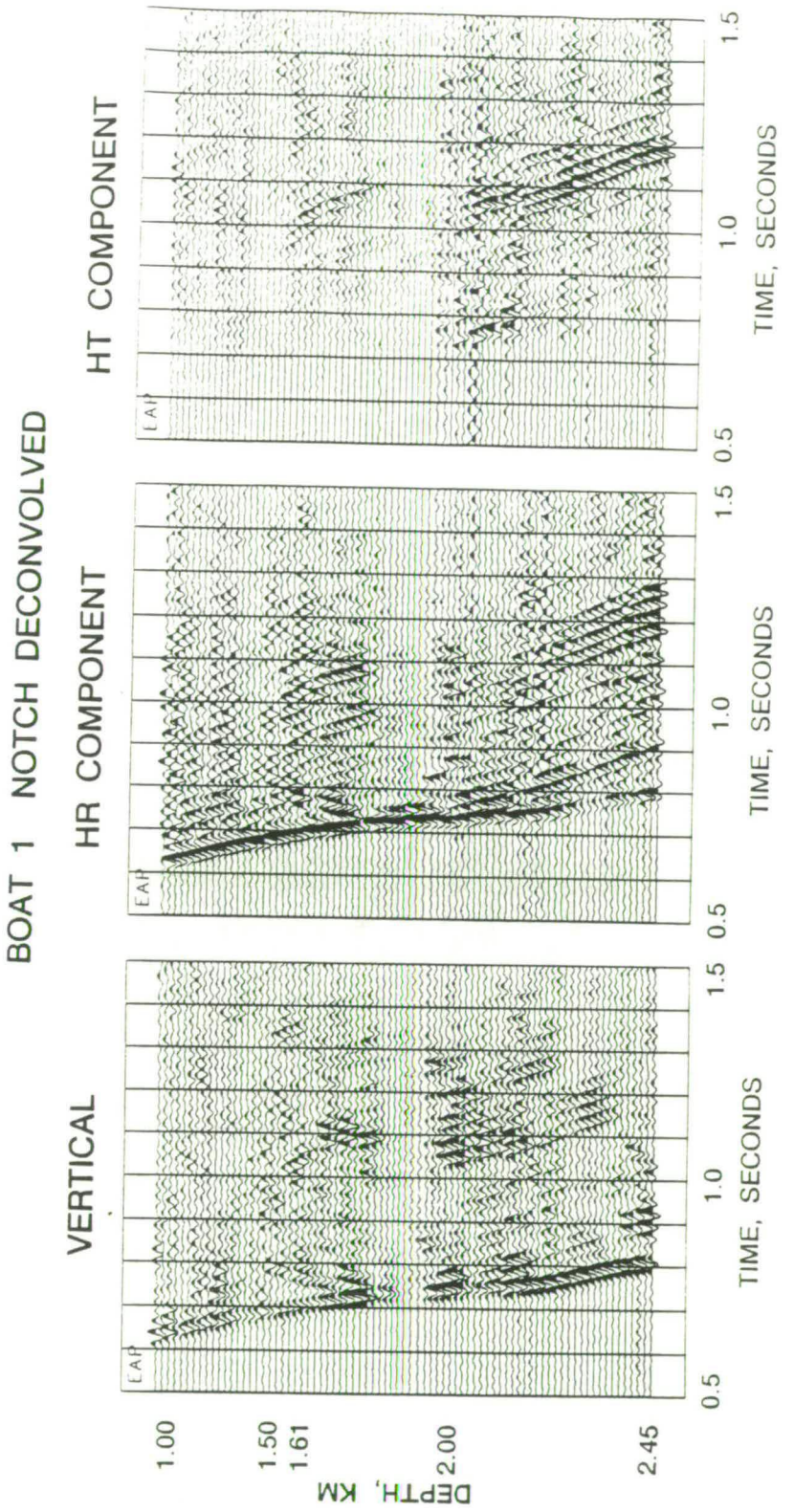

Figure 4.9. Boat 1 data rotated to vertical, horizontal radial (HR) and horizontal transverse (HT) directions from incoming *P*-waves. Three-component scaling has been applied so amplitudes can be compared between different components.

F-K filtering

The next stage of processing was to apply an F-K filter to all three components with the aim of removing coherent upgoing energy and reducing any incoherent energy as much as possible. A fan shaped pass filter was applied to all the traces from each component in the F-K domain with edges at 0ms/trace and 10ms/trace and a taper of 9ms/trace applied at each edge. This is a relatively tight filter and will act to smooth spatially the traces quite severely, but from the synthetic examples in Chapter 3, this smoothing should not distort any shear-wave splitting present. The resulting traces for offset 1 are shown in Figure 4.10 and demonstrate a marked improvement in the signal to noise ratio. Shear-waves generated at the top of the cap-rock can be seen more clearly now on the horizontal radial component, with significant separation from the direct *P*-waves below about 2.0km. However, noise is still present and represents that part of the incoherent noise lying within the F-K filter applied. This (now coherent) noise should have a much smaller amplitude than the signal in which we are interested.

P- and shear-wave separation

The final stage of processing was to try and separate the *P*-waves from the shear-waves in order to avoid *P*-wave contamination of any estimates of the polarizations of the faster split shear-waves (assuming anisotropy is sufficiently present to measure). A number of sophisticated methods have been developed to do this, such as Dankbaar (1985, 1987), Dillon (1988), Esmersoy (1990). However, at the time of processing, none of these methods was available due to commercial constraints. The simplest form of wave-mode separation is to rotate the vertical and radial components such that one component is lined up with the incoming *P*-waves (the Radial, R, component) and

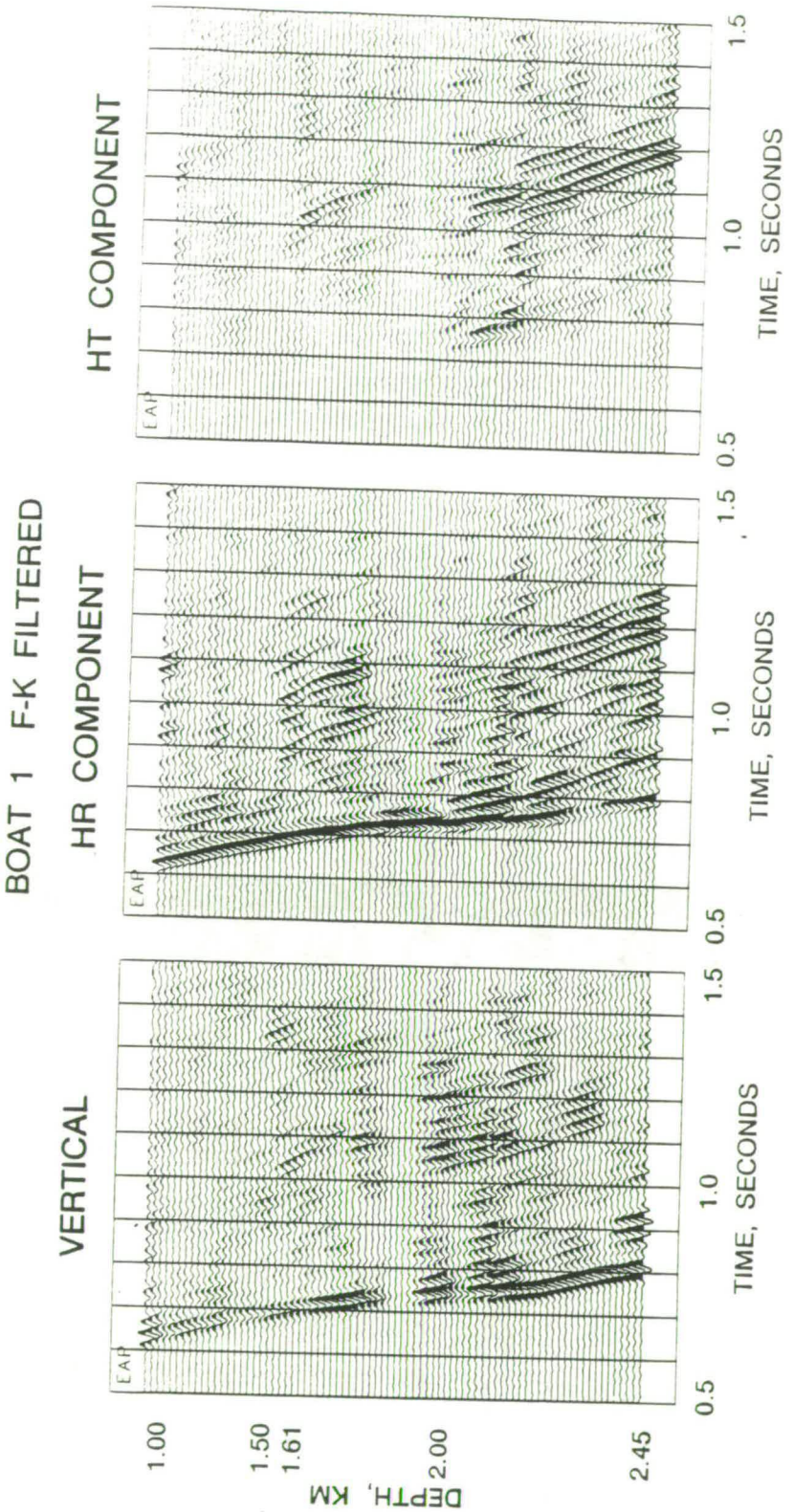

Figure 4.10. Three-component data from boat 1 after F-K filtering. The F-K filter has substantially improved the quality of the down going arrivals by removing incoherent noise and any upgoing energy.

the other is orthogonal to this (the vertical transverse, VT, component). These components form the dynamic axes. The assumption here is that the *P*-waves and shear-waves are orthogonal to each other, which may not be the case with direct *P*-waves and mode converted shear-waves and is almost never the case in anisotropic media. Despite this, the angle of incidence of the direct *P*-waves was measured using the polarization technique of Kanasewich (1981) and this angle was used to rotate the vertical and horizontal radial components to the R and VT directions at each geophone level.

Figure 4.11 shows the R, VT and HT components for all the offsets. The rotation procedure has worked remarkably well with all the *P*-wave components showing little or no evidence of shear-wave energy. Similarly, the VT components show quite distinct shear-waves generated at the top of the cap-rock at about 1.9km depth. Other, later arriving shear-waves can also be seen on some offsets and are probably the result of mode conversions above 1.0km depth. Overall, the four offsets show almost no sign of *P*-wave energy on the HT-component indicating that rotations to HR and HT directions are good. There are exceptions on offsets 1 and 4 where large amplitude *P*-wave energy is present on the HT-component at about 2.1km.

4.6 *P*-wave analysis

Direct *P*-wave arrival times from all offsets and the rig source were timed to within +/-0.2ms and used in a layer stripping algorithm to determine interval velocities between geophone levels. The small error represents the uncertainty in estimating the location of the central trough of the arriving wavelet and not the uncertainty in the travel time from source to receiver, which is more likely to be in the region of 0.5ms to 1.0ms due to gun timing errors, noise and

Figure 4.11 Three-component data from all offsets after notch deconvolution, F-K filtering and rotation to Radial, VT and HT directions. Clear mode-converted shear-waves can be seen on the VT-component on all offsets below about 2.0km. **a)** boat 1 **b)** boat 2 **c)** boat 3 **d)** boat 4.

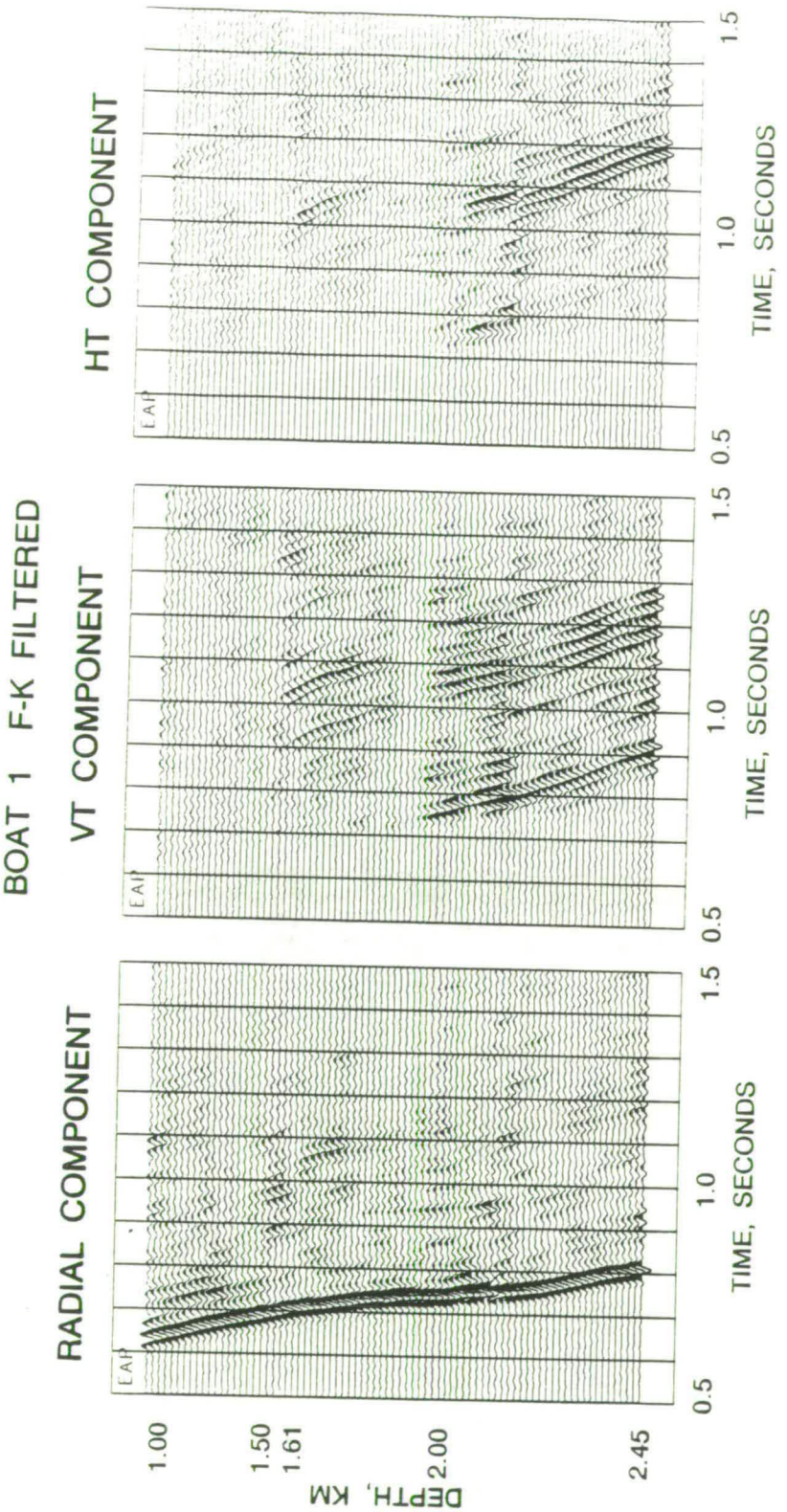
BOAT 1 F-K FILTERED
RADIAL COMPONENT
VT COMPONENT
HT COMPONENT
TIME, SECONDS
0.5
1.0
1.5
DEPTH, KM
1.00
1.50
1.61
2.00
2.45

Figure 4.11a

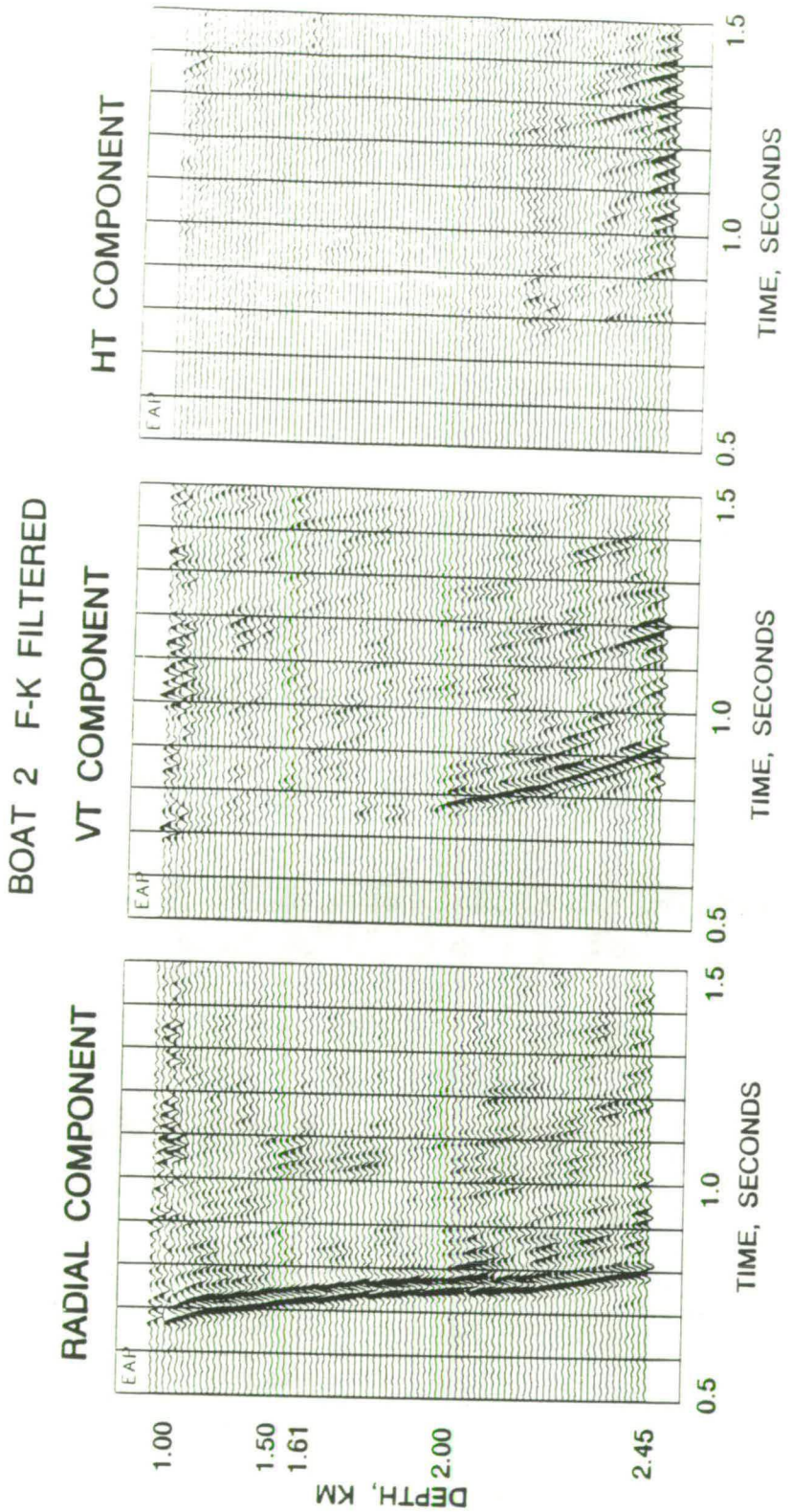
BOAT 2 F-K FILTERED
RADIAL COMPONENT
VT COMPONENT
HT COMPONENT
EAH
0.5
1.0
1.5
TIME, SECONDS
DEPTH, KM
1.00
1.50
1.61
2.00
2.45

Figure 4.11b

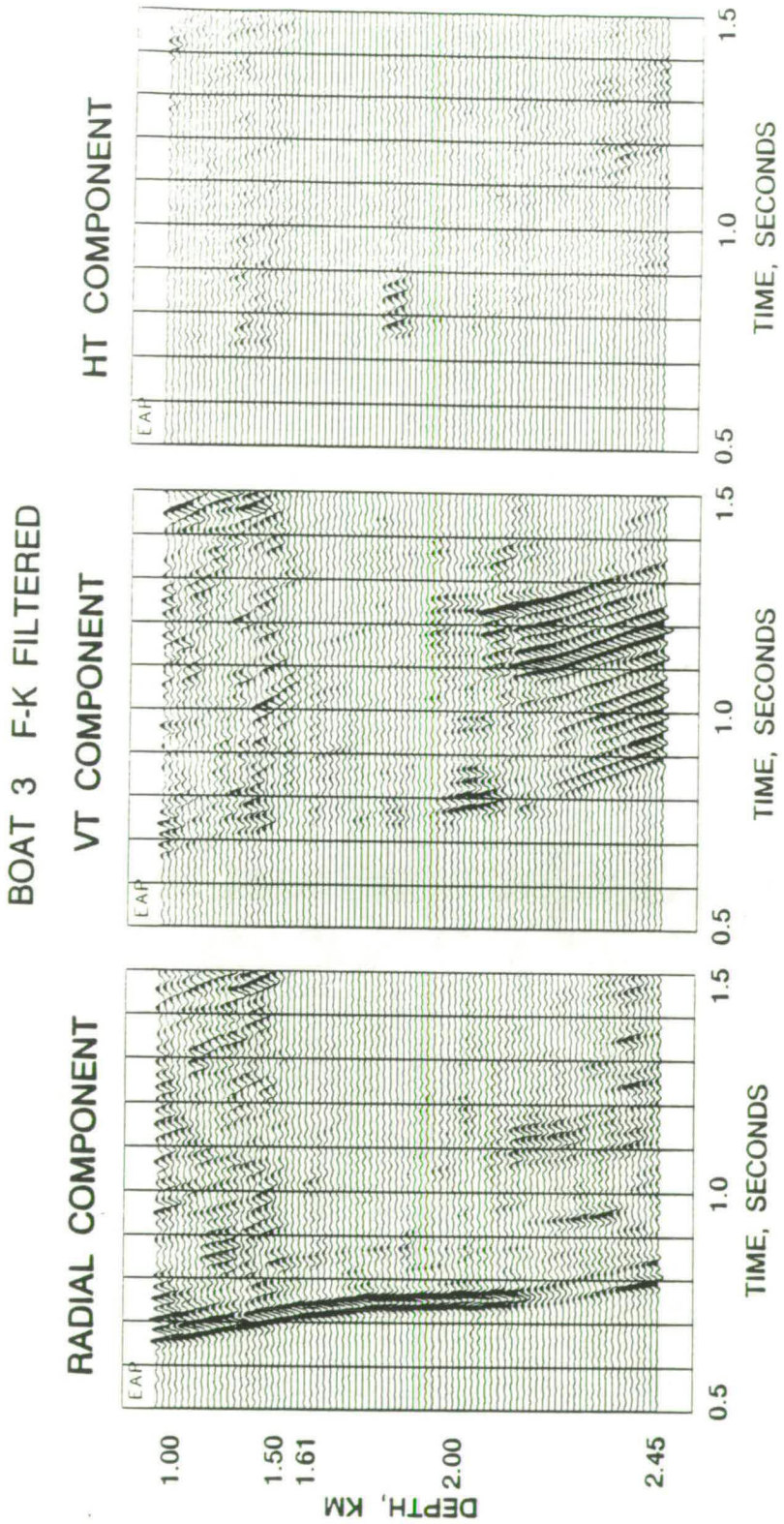
BOAT 3 F-K FILTERED
RADIAL COMPONENT
VT COMPONENT
HT COMPONENT
EAP
TIME, SECONDS
0.5
1.0
1.5
DEPTH, KM
1.00
1.50
1.61
2.00
2.45

Figure 4.11c

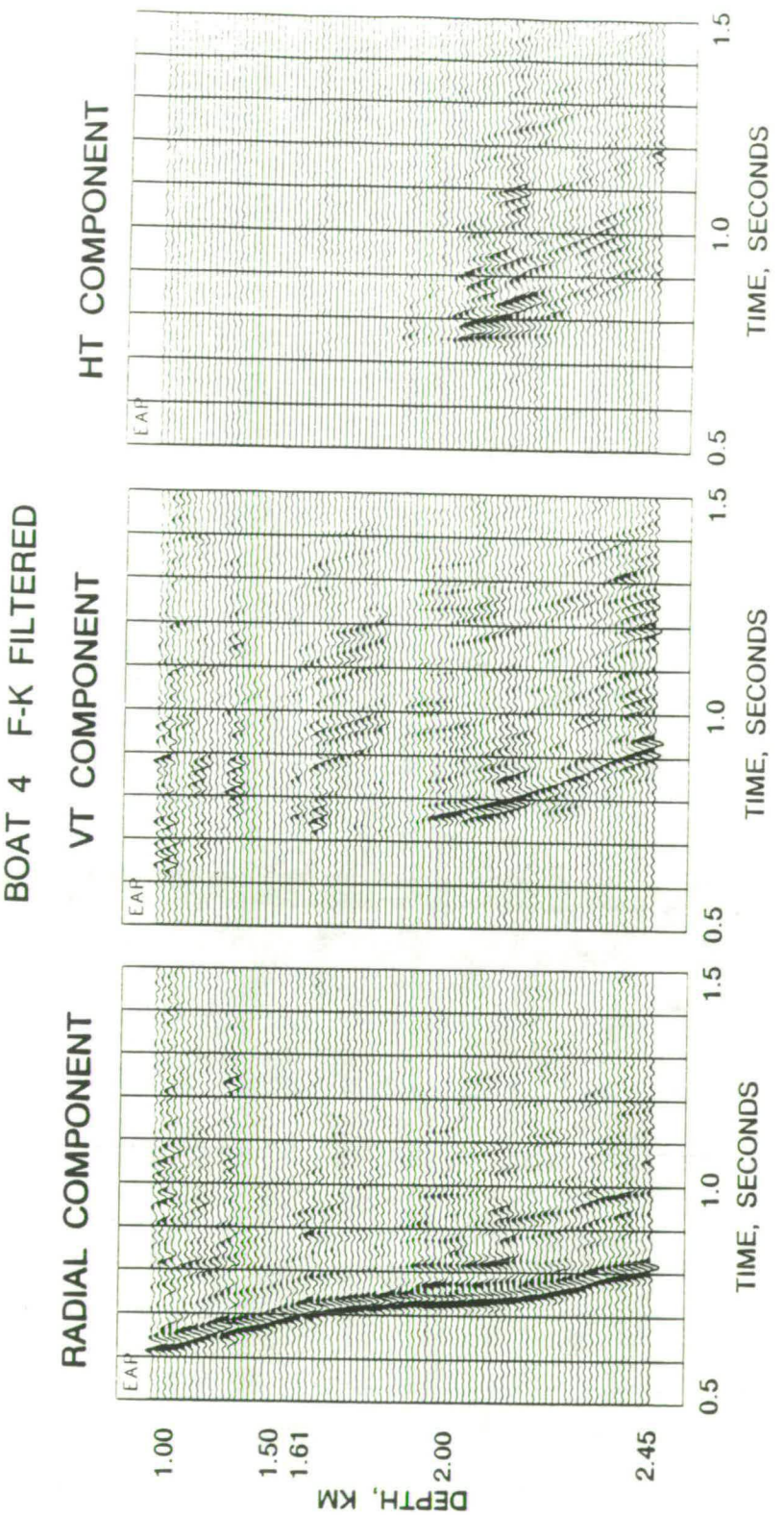
BOAT 4 F-K FILTERED
RADIAL COMPONENT
VT COMPONENT
HT COMPONENT
EAH
0.5
1.0
1.5
TIME, SECONDS
DEPTH, KM
1.00
1.50
1.61
2.00
2.45

Figure 4.11d

dispersion altering the wavelet shape. The same velocity structure was used above 1.0km for all offsets, where no arrival time information was available. These velocities were measured from the sonic log for the well. Errors due to this velocity structure are not expected to bias calculated interval velocities below the top few geophone levels. Velocities from this procedure, for all source locations, are shown in Figure 4.12 for depths below 2.0km, which includes details of the reservoir sands. Errors bounds on the interval velocities due to the +/-0.2ms timing error were calculated by repeating the layer stripping algorithm 200 times and randomly adding or subtracting 0.2ms to each arrival time. Even using this small error the uncertainty in each interval velocity estimate is not insignificant.

The general trend for all source locations is a gradual decrease in velocity from the Zechstein carbonate sequence into Zone 1 of the reservoir sands. This gradual decrease, rather than a sudden jump in velocity can be attributed to the top of Zone 1 being better cemented than its base through the percolation of cement bearing waters down from the overlying Zechstein. The trend for Zone 2 is a slight increase in velocity, due to the wetter depositional environment producing better cemented sandstone compared to the base of Zone 1 containing aeolian deposits. Zone 3 shows a decrease in velocity, due to the presence of porous aeolian sandstones saturated with gas. The presence of gas in a highly porous rock can have a marked effect on the compressional wave velocity. Zone 4 exhibits an increase in velocity, again due to the wetter environment producing better cemented rock.

Figure 4.12. Interval velocities calculated by the layer stripping method. Errors due to the +/-0.2ms timing inaccuracy were found by repeating the layer stripping algorithm 200 times and randomly adding values between +0.2ms and -0.2ms to the measured arrival times. These represent the worst possible errors due to timing. **a)** boat 1 **b)** boat 2 **c)** boat 3 **d)** boat 4 **e)** rig source.

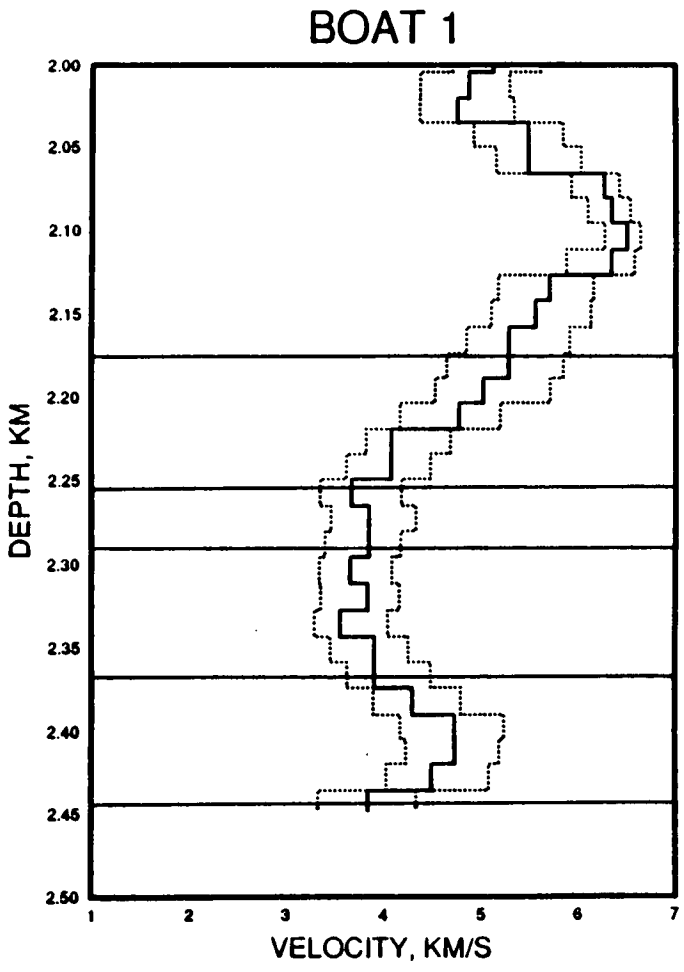

Figure 4.12a

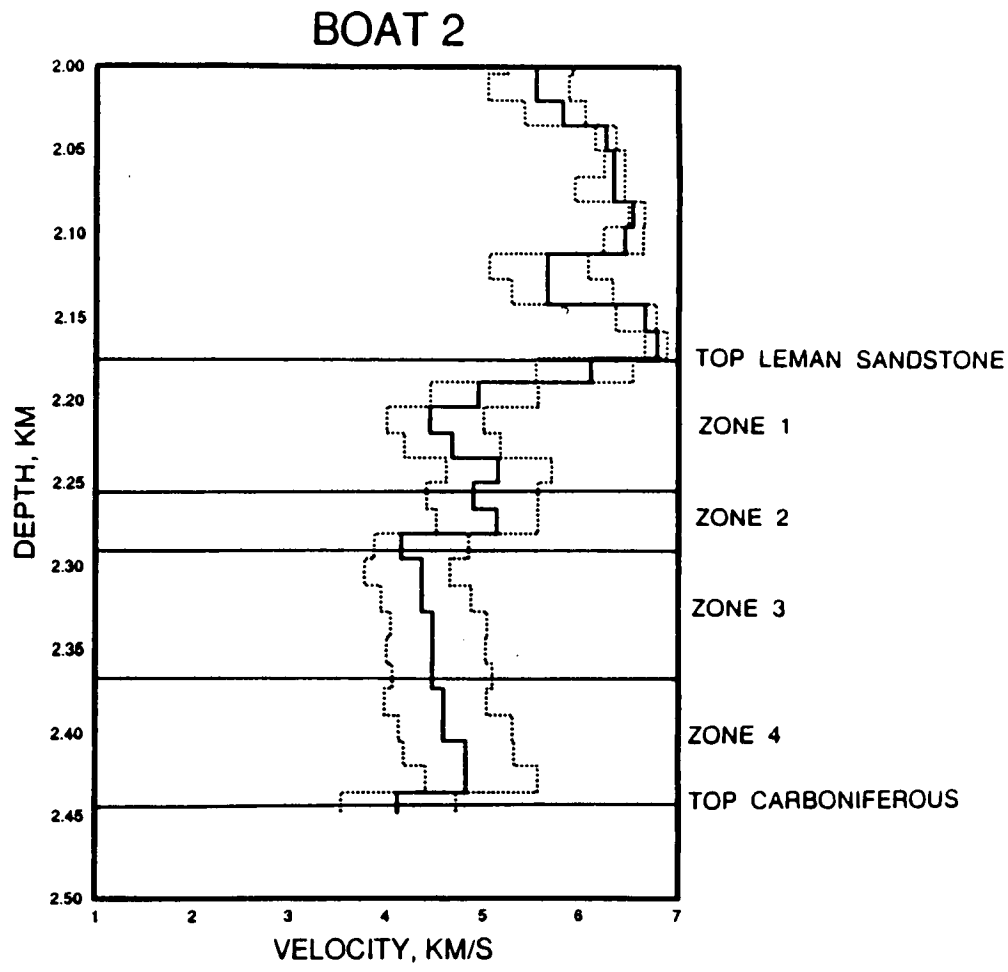

Figure 4.12b

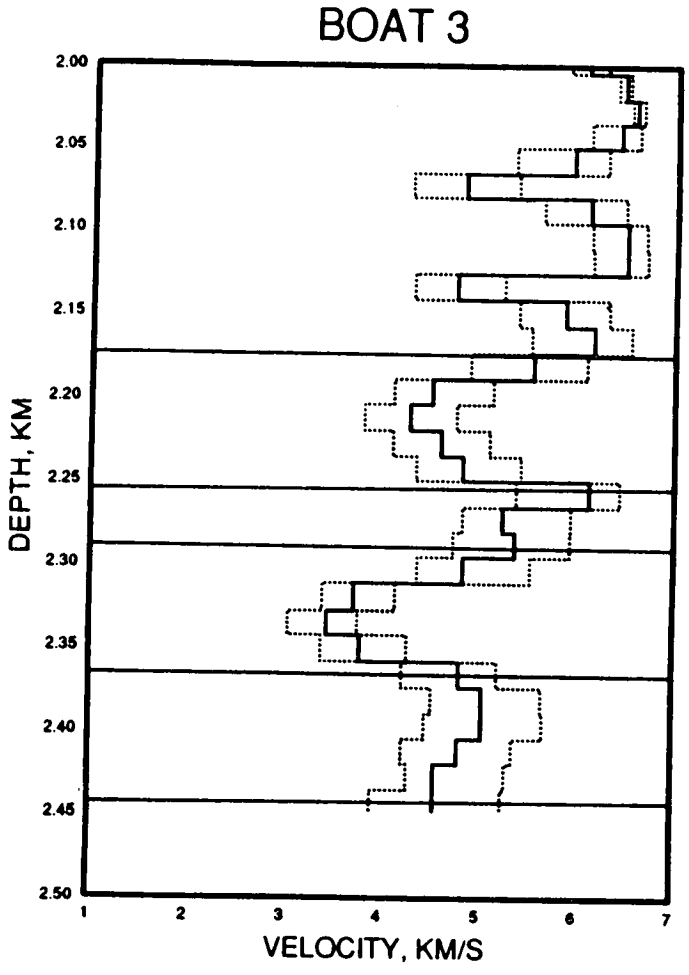

Figure 4.12c

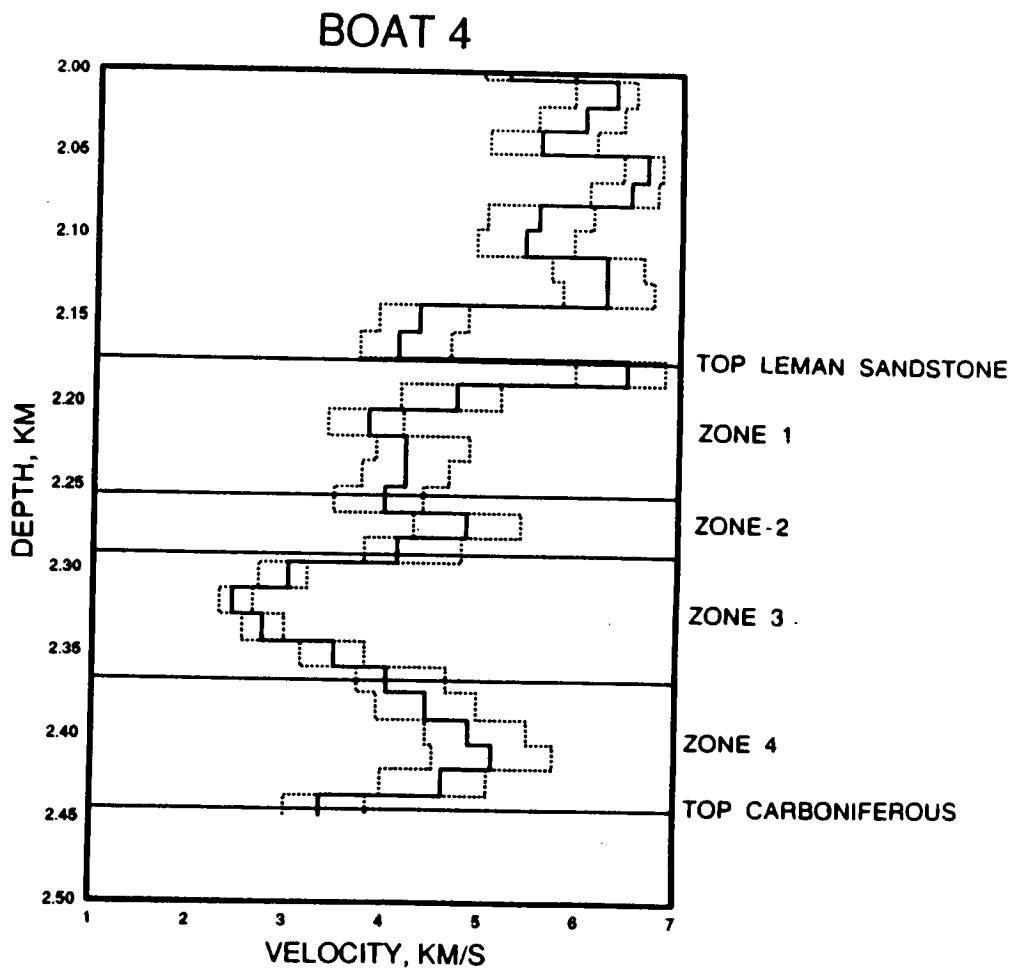

Figure 4.12d

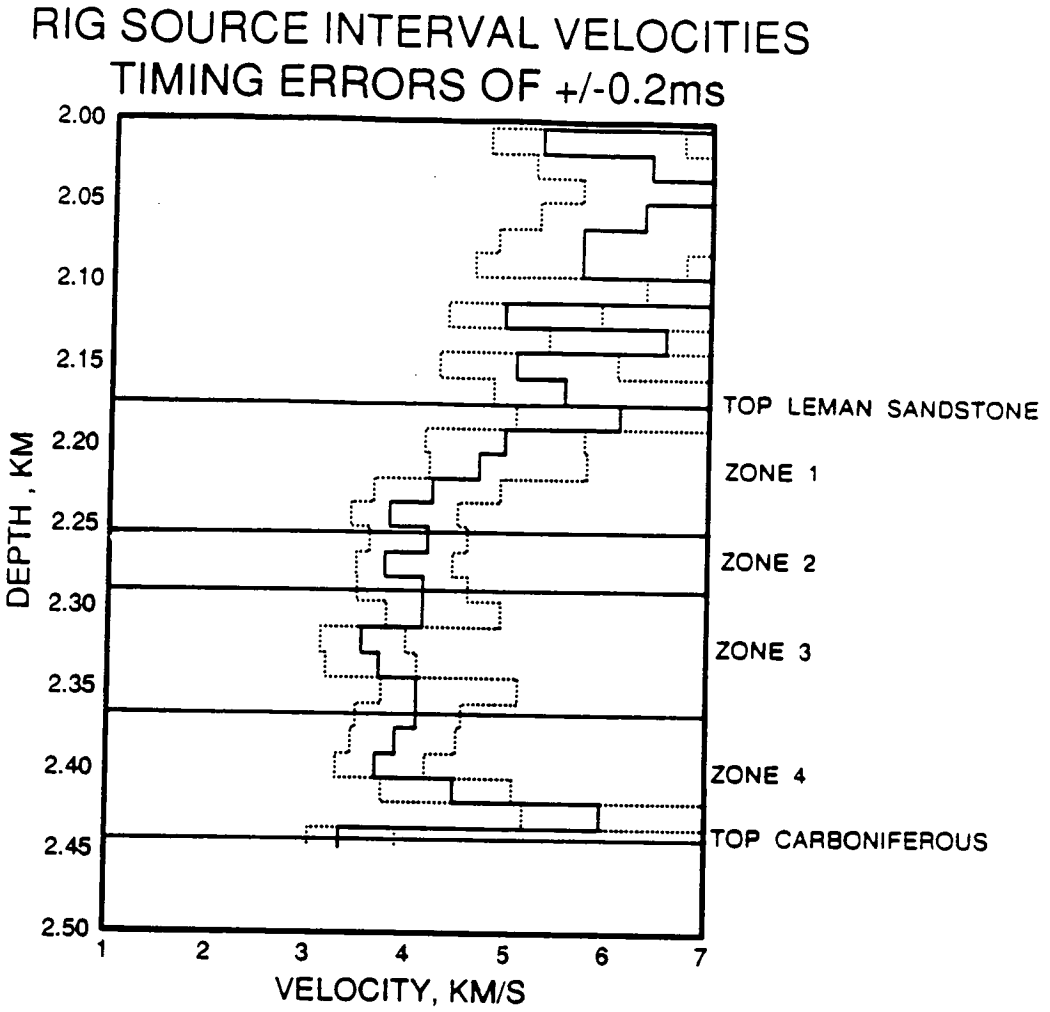
RIG SOURCE INTERVAL VELOCITIES
TIMING ERRORS OF +/-0.2ms
DEPTH, KM
2.00
2.05
2.10
2.15
2.20
2.25
2.30
2.35
2.40
2.45
2.50
1
2
3
4
5
6
7
VELOCITY, KM/S
TOP LEMAN SANDSTONE
ZONE 1
ZONE 2
ZONE 3
ZONE 4
TOP CARBONIFEROUS

Figure 4.12e

The layer stripping algorithm assumes isotropy and plane, horizontal layers which, if true, would result in identical interval velocities being calculated for all source locations, with some scatter associated with the errors in reading arrival times. Horizontal layering appears to be confirmed by reflection surveys in the vicinity of the VSP and if it is assumed that errors in reading arrival times will not produce consistently different results between the four offsets then the effects of azimuthal anisotropy may be studied in Figure 4.13 where the interval velocities from all four offsets have been plotted together. If azimuthal anisotropy were present, the expected results in Figure 4.13 would be similar interval velocities produced from diametrically opposite sources, and different velocities from orthogonally directed sources. The observations do not support such a result and indicate a general scatter at each interval, associated with errors in reading arrival times and deviations from the assumption of plane, horizontal, homogeneous layering. However, this does not prove that azimuthal anisotropy is not present, merely that its effects are hidden by the errors associated with measuring *P*-wave interval velocities from layer stripping.

The assumption of plane, homogeneous layers can be circumvented in the calculation of interval velocities by using *P*-wave incidence angles in conjunction with the measured arrival times. The method assumes a plane wavefront approaching two adjacent geophones with incidence angle ϕ. Given the spacing between the geophones, Δz, the differential path length can be calculated from:

$$\Delta L = \Delta z \cos\phi \qquad (4.1)$$

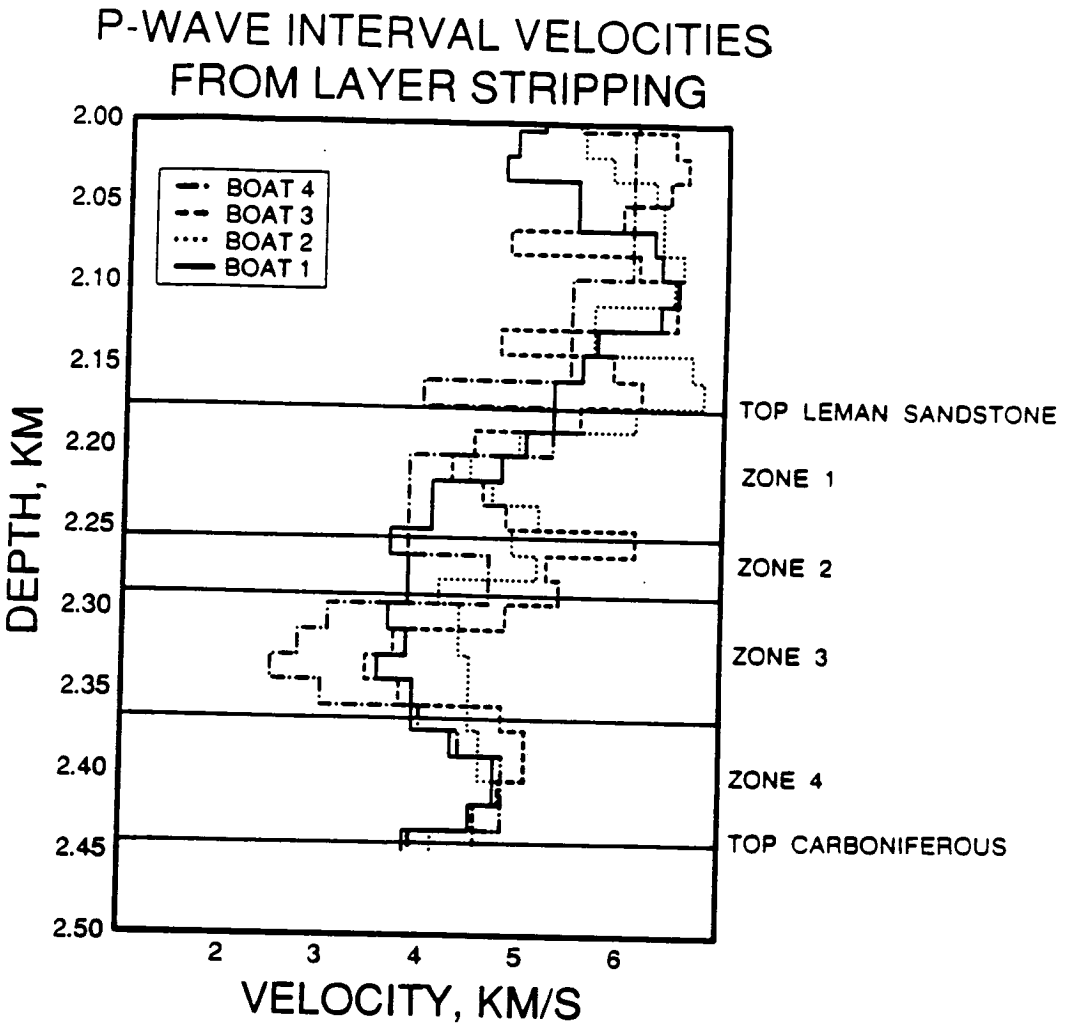

Figure 4.13. Interval velocities from the four boat offsets plotted together in an attempt to find azimuthal anisotropy. Large scatter of the velocities show that it is not possible to determine anisotropy from these data.

and the interval velocity, v_i, can be calculated using the difference in arrival times between the two geophone, Δt:

$$v_i = \Delta L / \Delta t. \tag{4.2}$$

This method also assumes that the measured *P*-wave incidence angles correspond to the direction of travel of the energy. Crampin et al. (1982) show that even in the presence of strong anisotropy, the direction of *P*-wave particle motion closely follows the direction of the ray direction. Interval velocities were calculated using the *P*-wave incidence angles shown in Figure 4.14, where all four offsets show a minimum value in incidence angle in Zone 3, indicating that this is a low velocity zone. Figure 4.15 gives the interval velocities from this procedure and shows the same general trend as the interval velocities from layer stripping, albeit with a larger scatter. The main problem with this method is that as the interval velocity increases, its error also increases, as the percentage error in the difference between the two adjacent arrival times increases. Hence the larger scatter in interval velocities in the cap-rock and Zone 2 making it impossible to interpret the results for azimuthal anisotropy.

Comparison between the averaged interval velocities from the four offsets calculated by layer stripping and by incidence angles in Figure 4.16 shows higher velocities from the incidence angle method throughout most of the reservoir section. However, the same general trend can be seen from both methods.

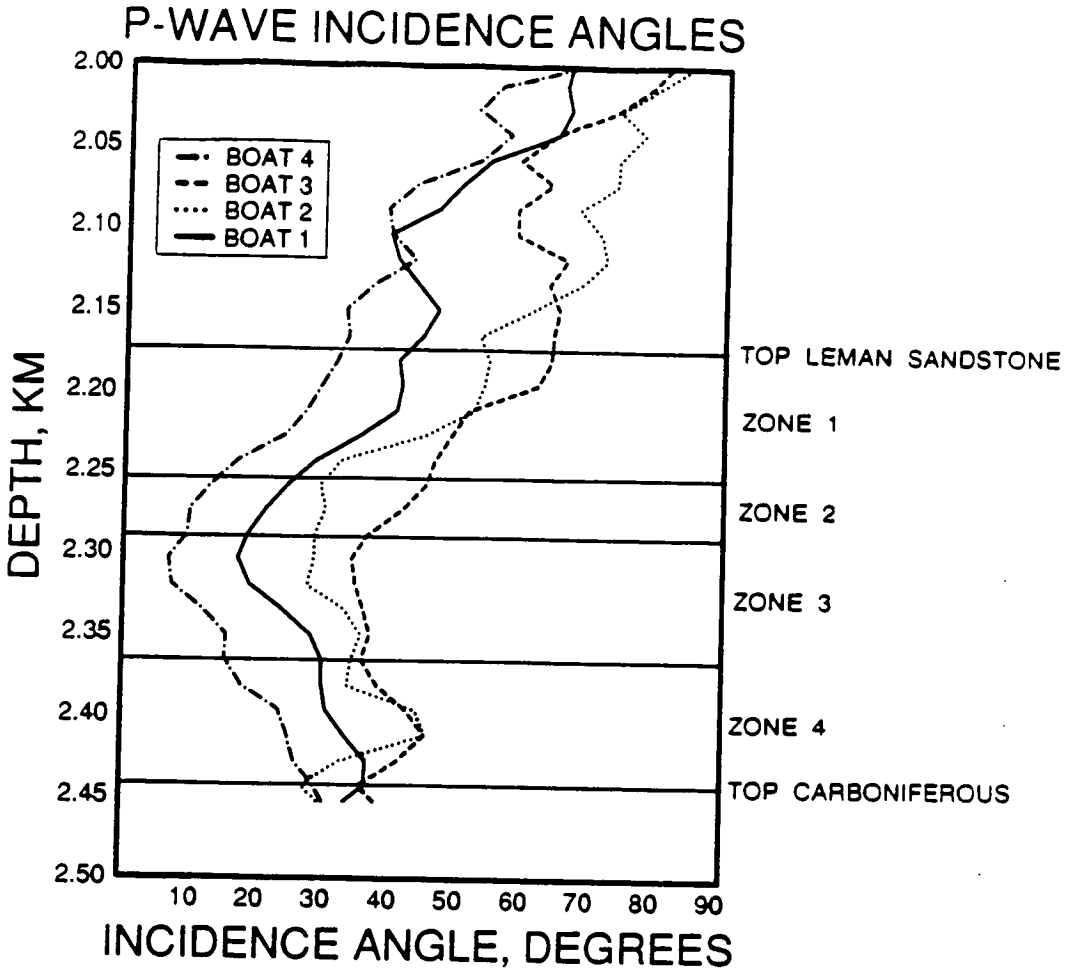

Figure 4.14. P-wave incidence angles measured from the four boat offsets. The same angles were used to rotate the vertical and radial components to "P" and "SV" directions.

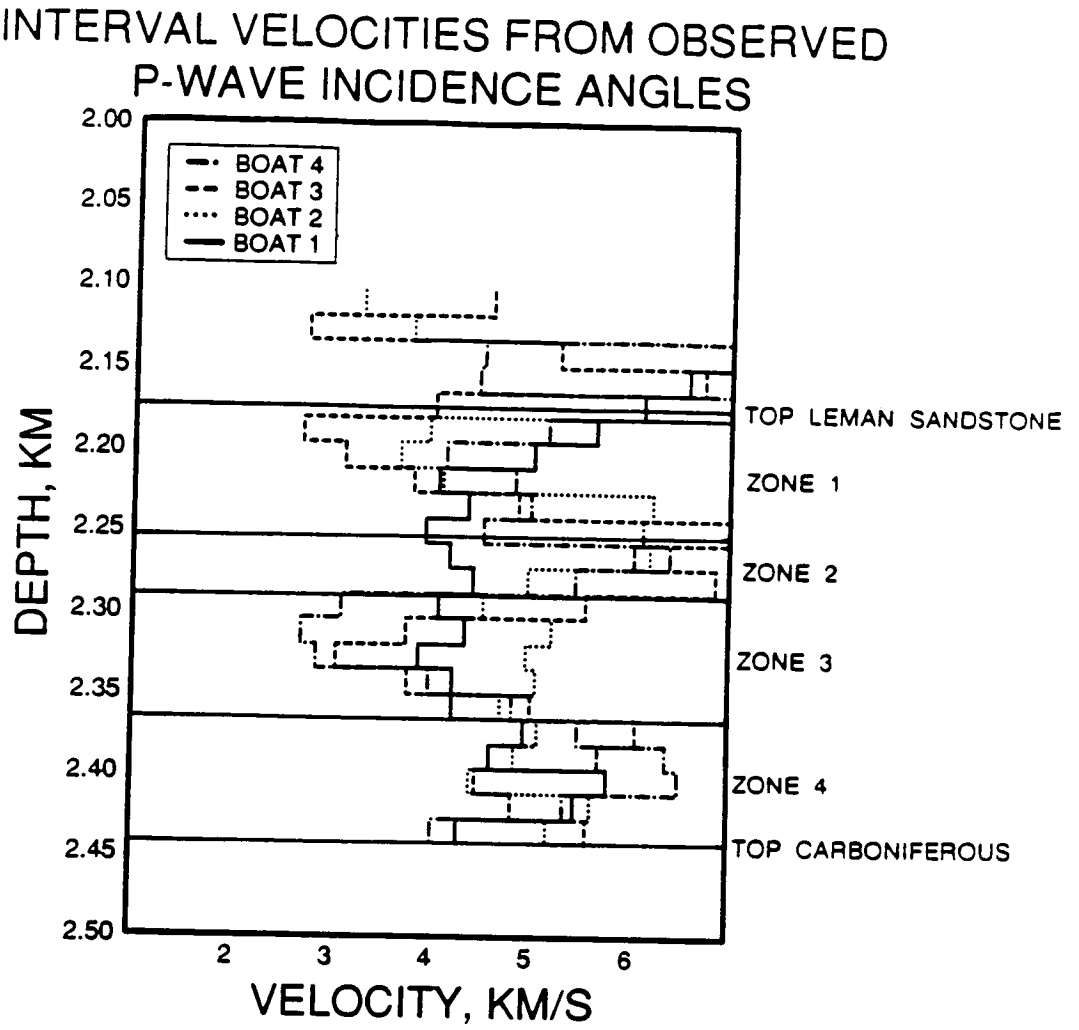

Figure 4.15. Interval velocities from the four boat offsets estimated using the incidence angles in combination with the arrival times. As with the layer stripping results, too much random scatter is present to determine if azimuthal anisotropy is present.

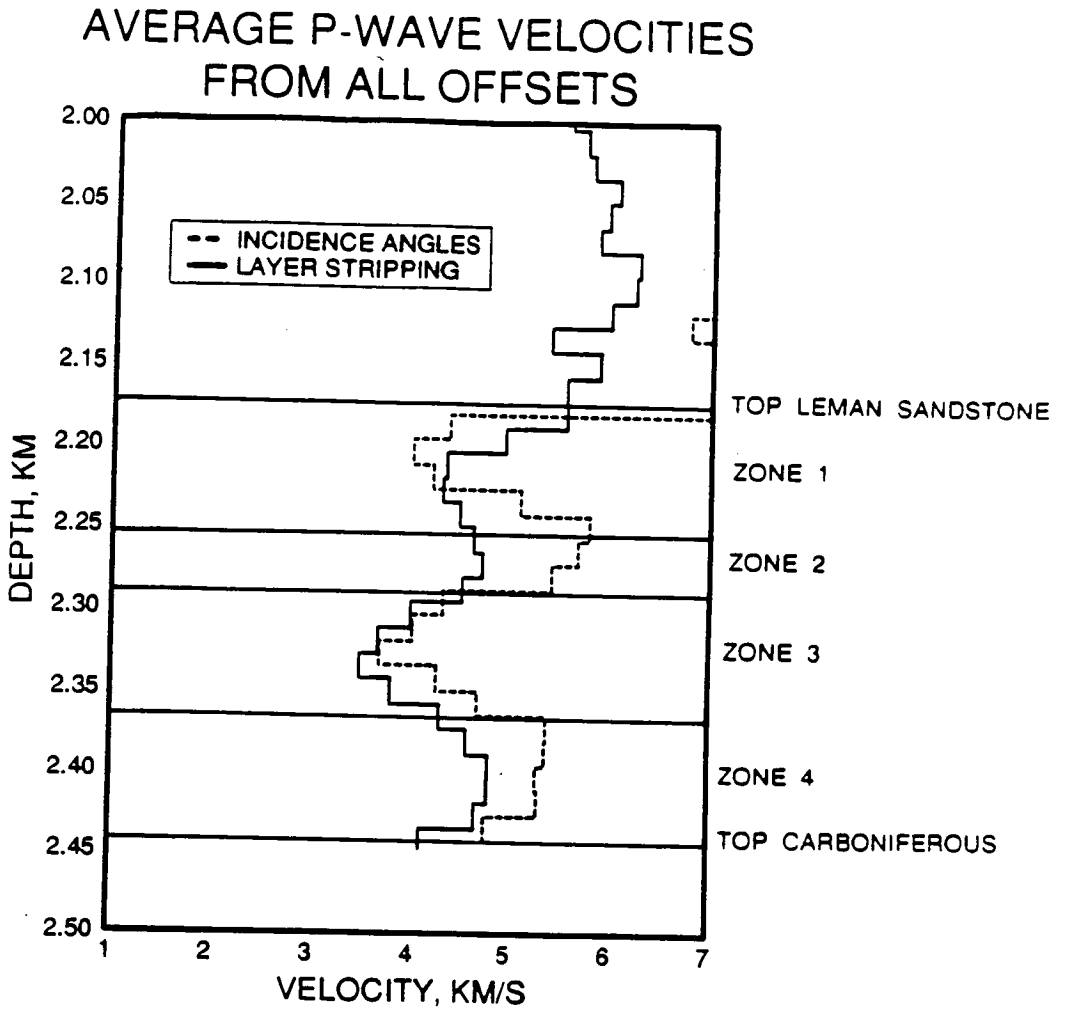

Figure 4.16. Comparison of the layer stripping technique with the incidence angle technique for calculating interval velocities. The two curves are the combination of the four boat offsets. thin layer anisotropy is indicated in zones 2 and 4, where the incidence angle velocities are larger than thos from layer stripping.

The consistent nature of the difference between layer stripping velocities and incidence angle velocities suggests that random measurement errors are not the cause as these would produce random differences between the two methods. One possible explanation is smaller than expected *P*-wave incidence angles, due possibly to the effective gain on the vertical component being greater than that on the horizontals. Anisotropy would not be expected to produce such large deviations of the *P*-wave particle motion from the ray direction (Crampin et al., 1982).

Thin layer anisotropy

Figure 4.17 shows an example of *P*-wave velocity variation in a homogeneous medium containing 20% thin layer anisotropy. It can be seen that significant differences from the vertical *P*-wave velocity do not occur for rays with incidence angles smaller than 30°. Even at a 45° angle of incidence, there is only about an 8% difference from the vertical *P*-wave velocity. *P*-wave incidence angles in Figure 4.14 show that the largest incidence angle in the reservoir region, from boat 3, is about 60° at the top of Zone 1, while the incidence angles from boat 4 do not exceed 30° anywhere in the reservoir rock. The generally low (<45°) incidence angles suggest that it may be very difficult to recognise thin layer anisotropy by comparing interval velocities from the near zero incidence rig source to those from the offset sources.

Figure 4.18 shows the averaged layer stripping interval velocities from all four boat offsets compared to the rig source layer stripping velocities. Zones 2 and 4 indicate lower rig source velocities compared to the boat offsets, although if errors are taken into

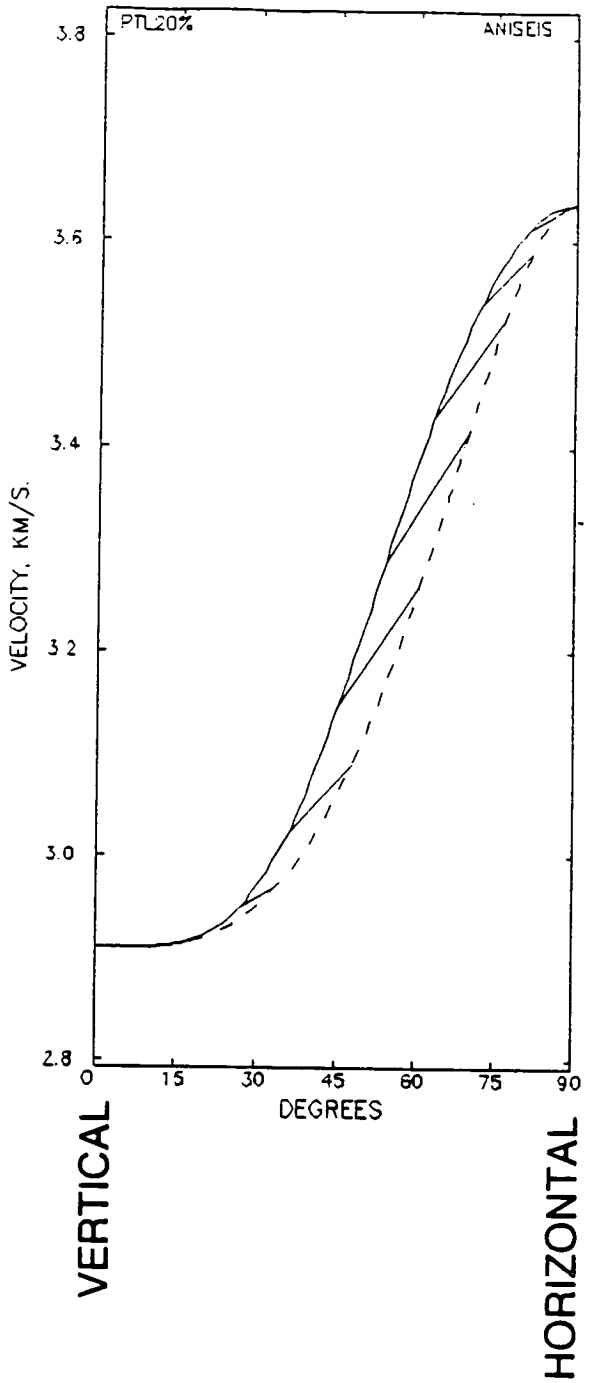

Figure 4.17. *P*-wave velocity variations in a medium containing 20% *P*-wave velocity anisotropy. The numbers along the X-axis give the angle of incidence. The solid line represents the phase velocity and the dotted line the group velocity. The lines joining the phase and group velocities shows the in-plane deviation of the group velocity direction from the phase velocity direction.

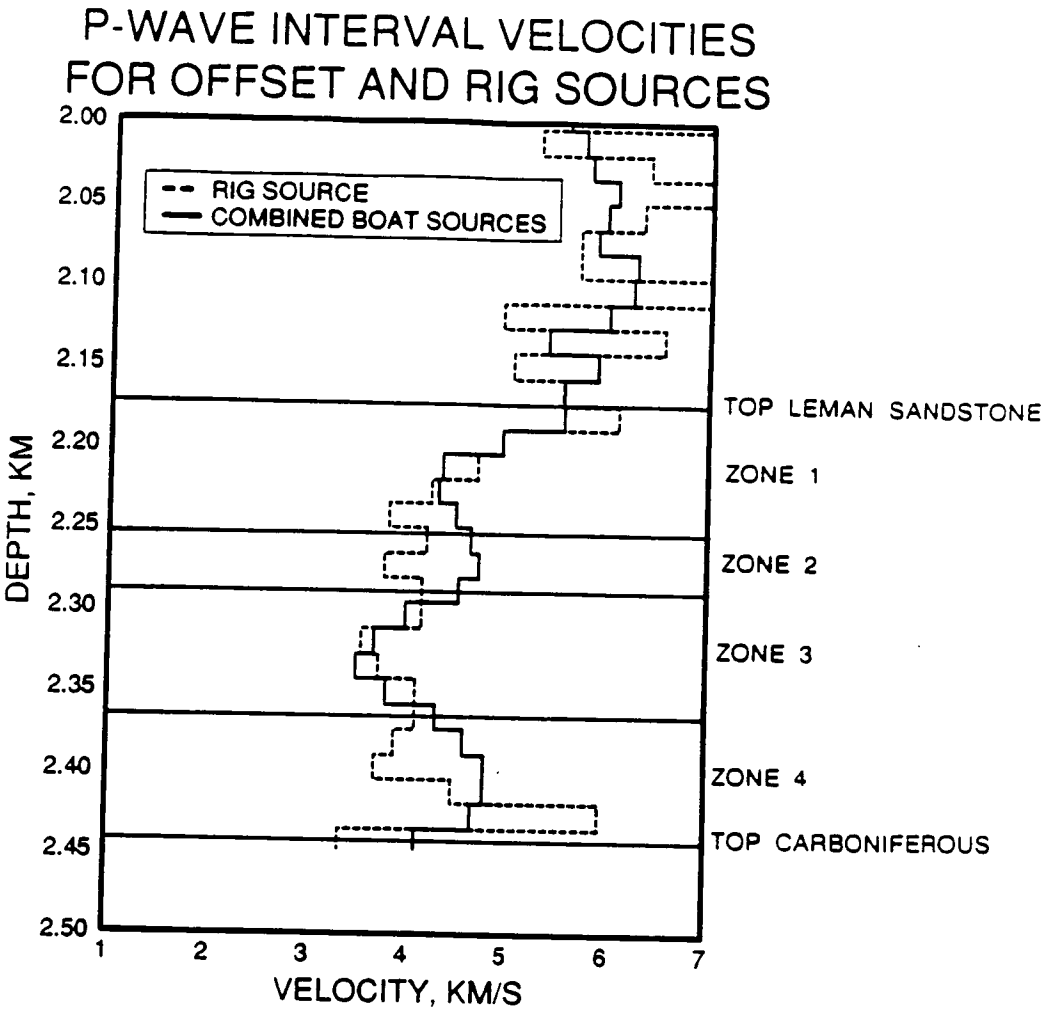

Figure 4.18. Comparison of the average *P*-wave interval velocities from the four boat offsets with the interval velocities from the rig source. Differences can be seen in zones 2 and 4 of the reservoir sands, where the rig source velocities are lower than those from the boat offsets suggesting the presence of thin layer anisotropy.

consideration, it is less likely that the difference is significant. However, assuming the results are correct and thin layer anisotropy is present in Zones 2 and 4, it can be related to the wetter conditions under which the reservoir sands were deposited in these zones. If more fluvial type depostion is interleaved with aeolian deposition as in these two zones, the resulting cyclic stack of sediments may exhibit thin layer anisotropy.

Vp/Vs ratios

Measuring the cap-rock shear-wave arrival times allows the calculation of *Vp/Vs* ratios within the reservoir sands. The method used assumes orthogonality of the *P* and shear-waves (apparently confirmed by the success of the rotation into R and VT components shown in Figure 4.11) and that the direction of energy transport is parallel to the *P*-wave particle motion and orthogonal to the shear-wave particle motion. The presence of relatively strong velocity anisotropy could invalidate these assumptions.

Vp/Vs ratios were calculated by dividing the difference in shear-wave arrival times by the difference in *P*-wave arrival times at adjacent geophones. The results of this are shown in Figure 4.19, and indicate low values, around 1.5, in Zone 3. These low values are possibly due to a decrease in the compressional modulus (controlling the *P*-wave velocity) of the rock in this zone, while the shear modulus (controlling the shear-wave velocity) remains unchanged. The presence of gas filled rather than liquid filled pores may be the cause of this decrease in *Vp/Vs*. The rest of the sandstone gives

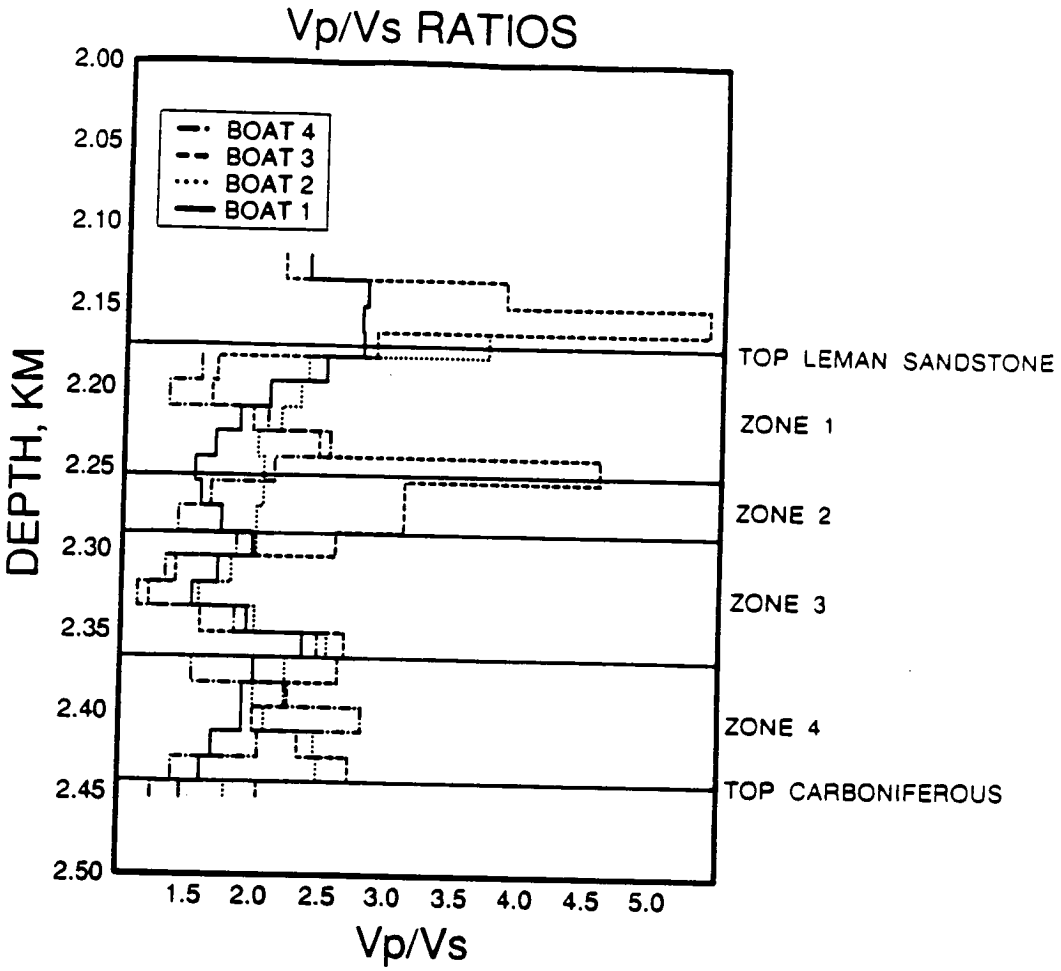

Figure 4.19. Vp/Vs ratios calculated from P-wave and shear-wave arrival times for all four boat offsets.

Vp/Vs ratios near 1.9, corresponding to values observed by Gardner and Harris (1968). Errors in *Vp/Vs* estimates are likely to be large such that little more than general trends may be interpreted from Figure 4.19.

Evidence of faulting from downgoing waves

The lower third of the R section from offset 3 in Figure 4.11c shows high amplitude arrivals after the initial *P*-wave onset, a phenomenon not observed on the other three offsets. In particular, a very high amplitude arrival of opposite polarity from the direct *P*-wave is visible between 2.2km and 2.35km at about 0.94s. Considering the large time delay between this arrival and the initial onset, suggesting a considerably different ray path, it is surprising that the later arrival has the same particle motion as the direct arrival, a result seen by the lack of energy corresponding to this arrival on the VT section. The direct *P*-wave in this depth region also contains signs of a second, slightly slower *P*-wave wave interfering with the direct arrival.

These observations may be explained by the presence of a fault, or faults, that have the effect of introducing more than one possible direct ray path from source to receiver. Sharp lateral discontinuities may also introduce diffracted arrivals with localised vertical extent such as that at about 0.94s. No proposed location for any faulting can be given from these arrivals without a significant effort going into modelling with a ray tracing program. Analysis of the upgoing wavefield from this same offset by Noble et al (1987) confirms the presence of faulting in the Rotliegendes sandstone, with salt in the Zechstein sequence acting as a plane of decollement.

Conclusions on P-wave analysis

P-wave analysis confirms the presence of four distinct zones within the reservoir sands, with Zone 3 displaying the best reservoir characeristics. Determination of *P*-wave anisotropy is a little less conclusive with no evidence of azimuthal variation of velocity. Vertical velocity variations may be observed in Zones 2 and 4 of the reservoir sands, where more fluvial type deposition occured, leading to better bedding definition in the sands. Offset 3 shows possible evidence of faulting with what looks like a double first arrival, and a later arriving diffraction of limited vertical extent with the same particle motion as the direct *P*-wave.

4.7 Shear-wave analysis

The VT sections from all four offsets indicate the presence of good quality shear-waves generated at the top of the cap-rock. The aim of this shear-wave analysis is to investigate whether these shear-waves exhibit any signs of shear-wave splitting, and if so, to try and relate it to stress directions, or fractures, in the reservoir.

Polarization diagrams

One of the classic methods for analysing shear-waves for anisotropy is to interpret PDs visually to find the polarization of the leading split shear-wave and the time delay separating the two split shear-waves. In the past, PDs have been most commonly, and most usefully, plotted in the horizontal plane, using the horizontal radial and horizontal transverse components for nearly vertically

propagating shear-waves, such that all measured polarizations lie in the same plane of observation. Clearly, it is desirable to replace visual techniques by automatic techniques for estimating the parameters of shear-wave splitting.

Problems can be encountered when applying automatic techniques for measuring shear-wave splitting to the horizontal components of shear-wave motion because the polarizations of two split shear-waves in this plane may not be orthogonal for non vertical propagation. This will severely distort estimates of *qS1* polarization and time delay for those automatic techniques that assume orthogonality of the split shear-waves. However, in all hexagonally anisotropic media, the polarizations of the two split shear-waves in any given direction of propagation are orthogonal to each other in the plane described by their particle motion. This is still approximately true in media containing slightly perturbed variations of hexagonal anisotropy such as combinations of thin layer anisotropy and weak (< 5%) crack anisotropy

With this problem in mind, the three automatic techniques developed and tested in Chapter 2 were applied to the cap-rock shear-wave arrivals in the dynamic axes (using the VT and HT components in Figure 4.11), projecting the estimated *qS1* direction on to the horizontal plane.

The bottom 20 geophones were used for shear-wave analysis, these lying throughout the four zones of the reservoir rock. As a quality check on the data, horizontal plane *P*-wave PDs were plotted in Figure 4.20. In an ideal situation, these should be linear in the radial direction, with all energy contained in the sagittal plane and

Figure 4.20. Horizontal plane polarization diagrams for the direct arriving P-wave. The bottom 20 geophones are displayed using a 40ms window. a) boat 1 b) boat 2 c) boat 3 d) boat 4.

Boat 1 P–waves

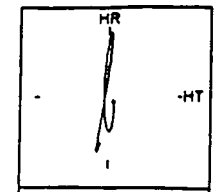

HORIZONTAL PLANE
GEOPHONE 1
DEPTH: 2.166km
WINDOW START: 0.731s
WINDOW LENGTH: 0.040s

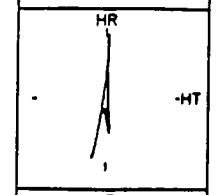

HORIZONTAL PLANE
GEOPHONE 2
DEPTH: 2.181km
WINDOW START: 0.733s
WINDOW LENGTH: 0.040s

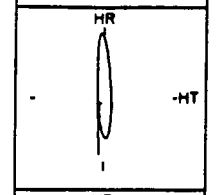

HORIZONTAL PLANE
GEOPHONE 3
DEPTH: 2.196km
WINDOW START: 0.733s
WINDOW LENGTH: 0.040s

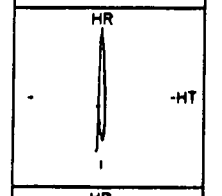

HORIZONTAL PLANE
GEOPHONE 4
DEPTH: 2.212km
WINDOW START: 0.737s
WINDOW LENGTH: 0.040s

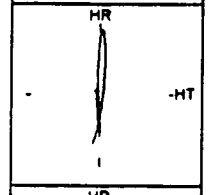

HORIZONTAL PLANE
GEOPHONE 5
DEPTH: 2.227km
WINDOW START: 0.738s
WINDOW LENGTH: 0.040s

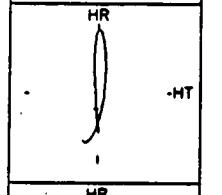

HORIZONTAL PLANE
GEOPHONE 6
DEPTH: 2.243km
WINDOW START: 0.745s
WINDOW LENGTH: 0.040s

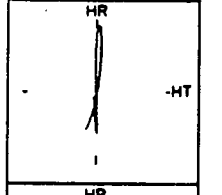

HORIZONTAL PLANE
GEOPHONE 7
DEPTH: 2.258km
WINDOW START: 0.745s
WINDOW LENGTH: 0.040s

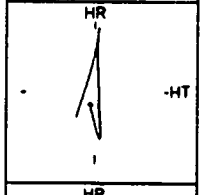

HORIZONTAL PLANE
GEOPHONE 8
DEPTH: 2.273km
WINDOW START: 0.749s
WINDOW LENGTH: 0.040s

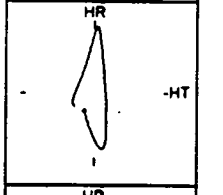

HORIZONTAL PLANE
GEOPHONE 9
DEPTH: 2.289km
WINDOW START: 0.754s
WINDOW LENGTH: 0.040s

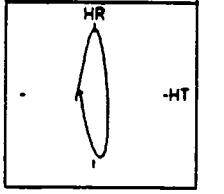

HORIZONTAL PLANE
GEOPHONE 10
DEPTH: 2.304km
WINDOW START: 0.756s
WINDOW LENGTH: 0.040s

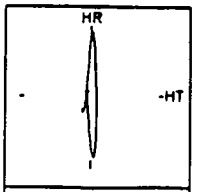

HORIZONTAL PLANE
GEOPHONE 11
DEPTH: 2.320km
WINDOW START: 0.760s
WINDOW LENGTH: 0.040s

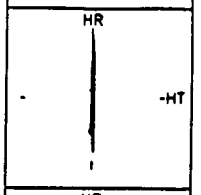

HORIZONTAL PLANE
GEOPHONE 12
DEPTH: 2.335km
WINDOW START: 0.763s
WINDOW LENGTH: 0.040s

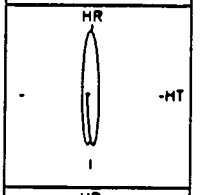

HORIZONTAL PLANE
GEOPHONE 13
DEPTH: 2.351km
WINDOW START: 0.767s
WINDOW LENGTH: 0.040s

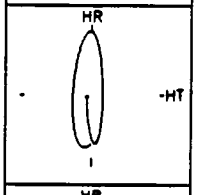

HORIZONTAL PLANE
GEOPHONE 14
DEPTH: 2.366km
WINDOW START: 0.770s
WINDOW LENGTH: 0.040s

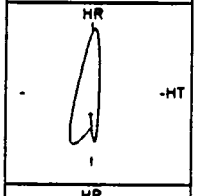

HORIZONTAL PLANE
GEOPHONE 15
DEPTH: 2.382km
WINDOW START: 0.775s
WINDOW LENGTH: 0.040s

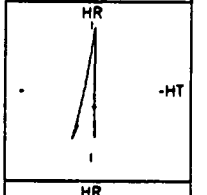

HORIZONTAL PLANE
GEOPHONE 16
DEPTH: 2.397km
WINDOW START: 0.776s
WINDOW LENGTH: 0.040s

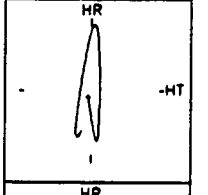

HORIZONTAL PLANE
GEOPHONE 17
DEPTH: 2.412km
WINDOW START: 0.777s
WINDOW LENGTH: 0.040s

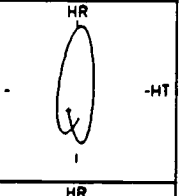

HORIZONTAL PLANE
GEOPHONE 18
DEPTH: 2.428km
WINDOW START: 0.782s
WINDOW LENGTH: 0.040s

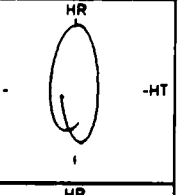

HORIZONTAL PLANE
GEOPHONE 19
DEPTH: 2.443km
WINDOW START: 0.784s
WINDOW LENGTH: 0.040s

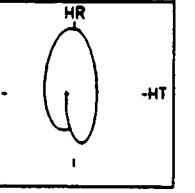

HORIZONTAL PLANE
GEOPHONE 20
DEPTH: 2.453km
WINDOW START: 0.785s
WINDOW LENGTH: 0.040s

Figure 4.20a

Boat 2 P–waves

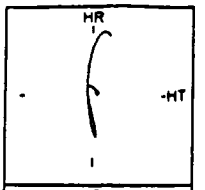

HORIZONTAL PLANE
GEOPHONE 1
DEPTH: 2.166km
WINDOW START: 0.730s
WINDOW LENGTH: 0.040s

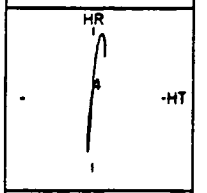

HORIZONTAL PLANE
GEOPHONE 2
DEPTH: 2.181km
WINDOW START: 0.733s
WINDOW LENGTH: 0.040s

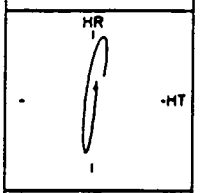

HORIZONTAL PLANE
GEOPHONE 3
DEPTH: 2.196km
WINDOW START: 0.737s
WINDOW LENGTH: 0.040s

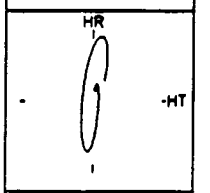

HORIZONTAL PLANE
GEOPHONE 4
DEPTH: 2.212km
WINDOW START: 0.741s
WINDOW LENGTH: 0.040s

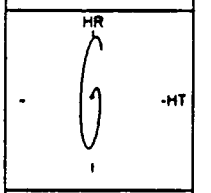

HORIZONTAL PLANE
GEOPHONE 5
DEPTH: 2.227km
WINDOW START: 0.741s
WINDOW LENGTH: 0.040s

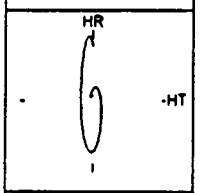

HORIZONTAL PLANE
GEOPHONE 6
DEPTH: 2.243km
WINDOW START: 0.743s
WINDOW LENGTH: 0.040s

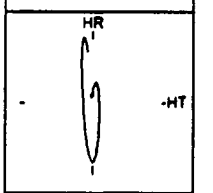

HORIZONTAL PLANE
GEOPHONE 7
DEPTH: 2.258km
WINDOW START: 0.745s
WINDOW LENGTH: 0.040s

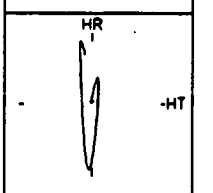

HORIZONTAL PLANE
GEOPHONE 8
DEPTH: 2.273km
WINDOW START: 0.747s
WINDOW LENGTH: 0.040s

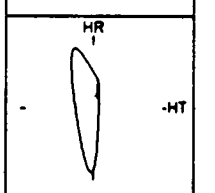

HORIZONTAL PLANE
GEOPHONE 9
DEPTH: 2.289km
WINDOW START: 0.752s
WINDOW LENGTH: 0.040s

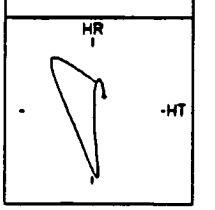

HORIZONTAL PLANE
GEOPHONE 10
DEPTH: 2.304km
WINDOW START: 0.754s
WINDOW LENGTH: 0.040s

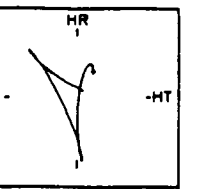

HORIZONTAL PLANE
GEOPHONE 11
DEPTH: 2.320km
WINDOW START: 0.758s
WINDOW LENGTH: 0.040s

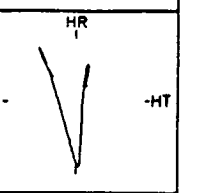

HORIZONTAL PLANE
GEOPHONE 12
DEPTH: 2.335km
WINDOW START: 0.758s
WINDOW LENGTH: 0.040s

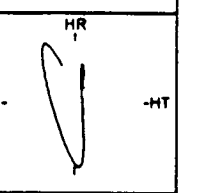

HORIZONTAL PLANE
GEOPHONE 13
DEPTH: 2.351km
WINDOW START: 0.760s
WINDOW LENGTH: 0.040s

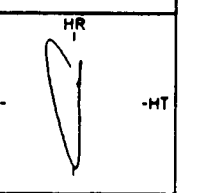

HORIZONTAL PLANE
GEOPHONE 14
DEPTH: 2.366km
WINDOW START: 0.763s
WINDOW LENGTH: 0.040s

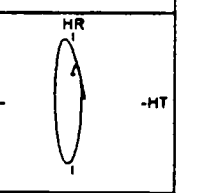

HORIZONTAL PLANE
GEOPHONE 15
DEPTH: 2.382km
WINDOW START: 0.768s
WINDOW LENGTH: 0.040s

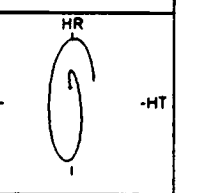

HORIZONTAL PLANE
GEOPHONE 16
DEPTH: 2.397km
WINDOW START: 0.769s
WINDOW LENGTH: 0.040s

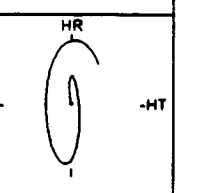

HORIZONTAL PLANE
GEOPHONE 17
DEPTH: 2.412km
WINDOW START: 0.770s
WINDOW LENGTH: 0.040s

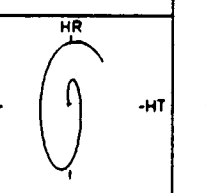

HORIZONTAL PLANE
GEOPHONE 18
DEPTH: 2.428km
WINDOW START: 0.773s
WINDOW LENGTH: 0.040s

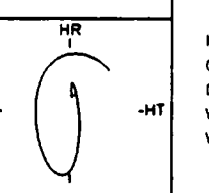

HORIZONTAL PLANE
GEOPHONE 19
DEPTH: 2.443km
WINDOW START: 0.777s
WINDOW LENGTH: 0.040s

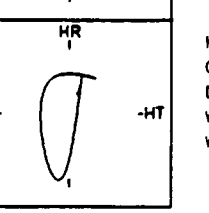

HORIZONTAL PLANE
GEOPHONE 20
DEPTH: 2.453km
WINDOW START: 0.779s
WINDOW LENGTH: 0.040s

Figure 4.20b

Boat 3 P–waves

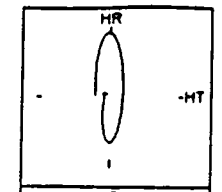

HORIZONTAL PLANE
GEOPHONE 1
DEPTH: 2.166km
WINDOW START: 0.731s
WINDOW LENGTH: 0.040s

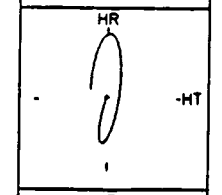

HORIZONTAL PLANE
GEOPHONE 2
DEPTH: 2.181km
WINDOW START: 0.732s
WINDOW LENGTH: 0.040s

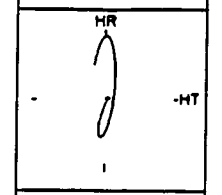

HORIZONTAL PLANE
GEOPHONE 3
DEPTH: 2.196km
WINDOW START: 0.732s
WINDOW LENGTH: 0.040s

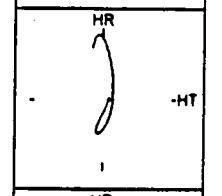

HORIZONTAL PLANE
GEOPHONE 4
DEPTH: 2.212km
WINDOW START: 0.733s
WINDOW LENGTH: 0.040s

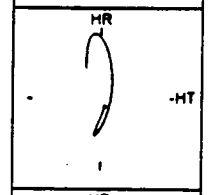

HORIZONTAL PLANE
GEOPHONE 5
DEPTH: 2.227km
WINDOW START: 0.739s
WINDOW LENGTH: 0.040s

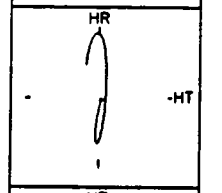

HORIZONTAL PLANE
GEOPHONE 6
DEPTH: 2.243km
WINDOW START: 0.742s
WINDOW LENGTH: 0.040s

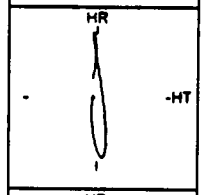

HORIZONTAL PLANE
GEOPHONE 7
DEPTH: 2.258km
WINDOW START: 0.747s
WINDOW LENGTH: 0.040s

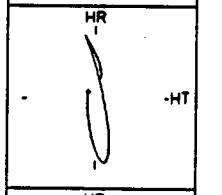

HORIZONTAL PLANE
GEOPHONE 8
DEPTH: 2.273km
WINDOW START: 0.750s
WINDOW LENGTH: 0.040s

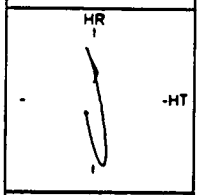

HORIZONTAL PLANE
GEOPHONE 9
DEPTH: 2.289km
WINDOW START: 0.755s
WINDOW LENGTH: 0.040s

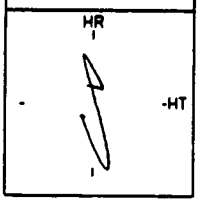

HORIZONTAL PLANE
GEOPHONE 10
DEPTH: 2.304km
WINDOW START: 0.758s
WINDOW LENGTH: 0.040s

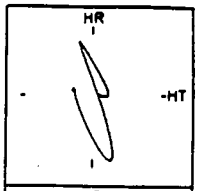

HORIZONTAL PLANE
GEOPHONE 11
DEPTH: 2.320km
WINDOW START: 0.760s
WINDOW LENGTH: 0.040s

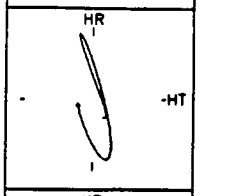

HORIZONTAL PLANE
GEOPHONE 12
DEPTH: 2.335km
WINDOW START: 0.765s
WINDOW LENGTH: 0.040s

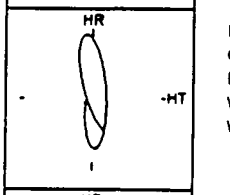

HORIZONTAL PLANE
GEOPHONE 13
DEPTH: 2.351km
WINDOW START: 0.768s
WINDOW LENGTH: 0.040s

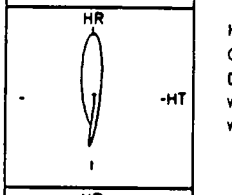

HORIZONTAL PLANE
GEOPHONE 14
DEPTH: 2.366km
WINDOW START: 0.768s
WINDOW LENGTH: 0.040s

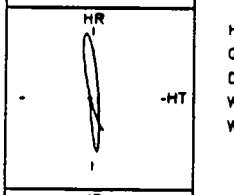

HORIZONTAL PLANE
GEOPHONE 15
DEPTH: 2.382km
WINDOW START: 0.772s
WINDOW LENGTH: 0.040s

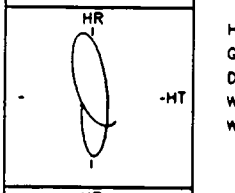

HORIZONTAL PLANE
GEOPHONE 16
DEPTH: 2.397km
WINDOW START: 0.776s
WINDOW LENGTH: 0.040s

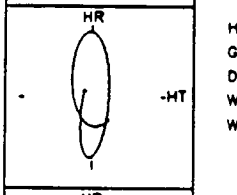

HORIZONTAL PLANE
GEOPHONE 17
DEPTH: 2.412km
WINDOW START: 0.778s
WINDOW LENGTH: 0.040s

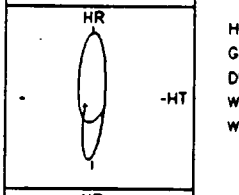

HORIZONTAL PLANE
GEOPHONE 18
DEPTH: 2.428km
WINDOW START: 0.782s
WINDOW LENGTH: 0.040s

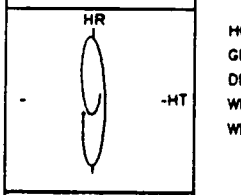

HORIZONTAL PLANE
GEOPHONE 19
DEPTH: 2.443km
WINDOW START: 0.784s
WINDOW LENGTH: 0.040s

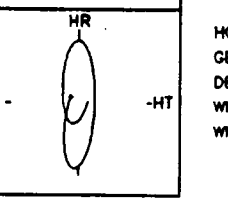

HORIZONTAL PLANE
GEOPHONE 20
DEPTH: 2.453km
WINDOW START: 0.784s
WINDOW LENGTH: 0.040s

Figure 4.20c

Boat 4 P—waves

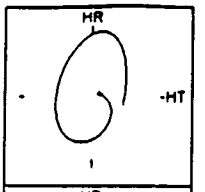

HORIZONTAL PLANE
GEOPHONE 1
DEPTH: 2.166km
WINDOW START: 0.727s
WINDOW LENGTH: 0.040s

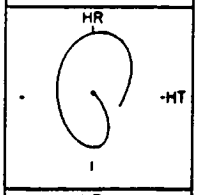

HORIZONTAL PLANE
GEOPHONE 2
DEPTH: 2.181km
WINDOW START: 0.730s
WINDOW LENGTH: 0.040s

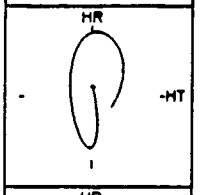

HORIZONTAL PLANE
GEOPHONE 3
DEPTH: 2.196km
WINDOW START: 0.734s
WINDOW LENGTH: 0.040s

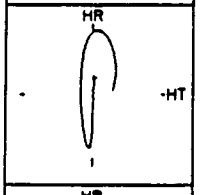

HORIZONTAL PLANE
GEOPHONE 4
DEPTH: 2.212km
WINDOW START: 0.736s
WINDOW LENGTH: 0.040s

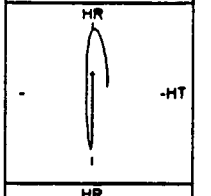

HORIZONTAL PLANE
GEOPHONE 5
DEPTH: 2.227km
WINDOW START: 0.740s
WINDOW LENGTH: 0.040s

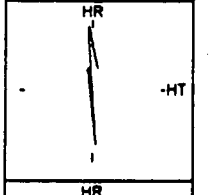

HORIZONTAL PLANE
GEOPHONE 6
DEPTH: 2.243km
WINDOW START: 0.742s
WINDOW LENGTH: 0.040s

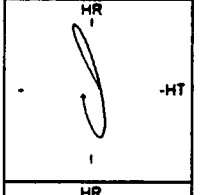

HORIZONTAL PLANE
GEOPHONE 7
DEPTH: 2.258km
WINDOW START: 0.750s
WINDOW LENGTH: 0.040s

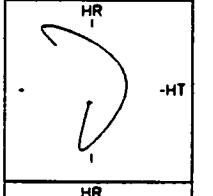

HORIZONTAL PLANE
GEOPHONE 8
DEPTH: 2.273km
WINDOW START: 0.750s
WINDOW LENGTH: 0.040s

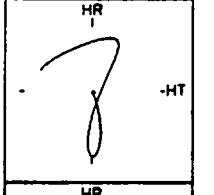

HORIZONTAL PLANE
GEOPHONE 9
DEPTH: 2.289km
WINDOW START: 0.752s
WINDOW LENGTH: 0.040s

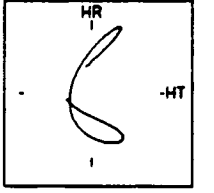

HORIZONTAL PLANE
GEOPHONE 10
DEPTH: 2.304km
WINDOW START: 0.754s
WINDOW LENGTH: 0.040s

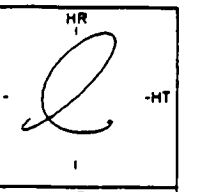

HORIZONTAL PLANE
GEOPHONE 11
DEPTH: 2.320km
WINDOW START: 0.770s
WINDOW LENGTH: 0.040s

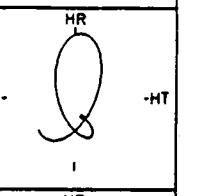

HORIZONTAL PLANE
GEOPHONE 12
DEPTH: 2.335km
WINDOW START: 0.773s
WINDOW LENGTH: 0.040s

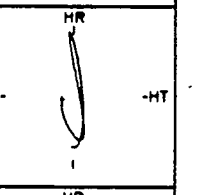

HORIZONTAL PLANE
GEOPHONE 13
DEPTH: 2.351km
WINDOW START: 0.774s
WINDOW LENGTH: 0.040s

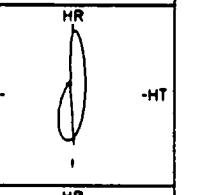

HORIZONTAL PLANE
GEOPHONE 14
DEPTH: 2.366km
WINDOW START: 0.775s
WINDOW LENGTH: 0.040s

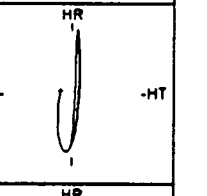

HORIZONTAL PLANE
GEOPHONE 15
DEPTH: 2.382km
WINDOW START: 0.779s
WINDOW LENGTH: 0.040s

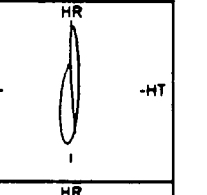

HORIZONTAL PLANE
GEOPHONE 16
DEPTH: 2.397km
WINDOW START: 0.779s
WINDOW LENGTH: 0.040s

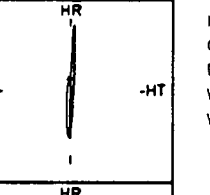

HORIZONTAL PLANE
GEOPHONE 17
DEPTH: 2.412km
WINDOW START: 0.783s
WINDOW LENGTH: 0.040s

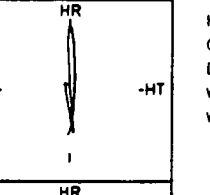

HORIZONTAL PLANE
GEOPHONE 18
DEPTH: 2.428km
WINDOW START: 0.786s
WINDOW LENGTH: 0.040s

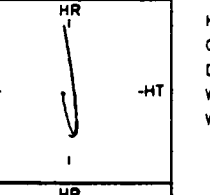

HORIZONTAL PLANE
GEOPHONE 19
DEPTH: 2.443km
WINDOW START: 0.791s
WINDOW LENGTH: 0.040s

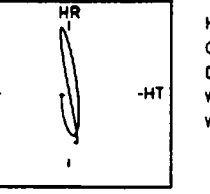

HORIZONTAL PLANE
GEOPHONE 20
DEPTH: 2.453km
WINDOW START: 0.795s
WINDOW LENGTH: 0.040s

Figure 4.20d

none on the HT component. None of the four offsets indicates that this is true: a large amount of energy is present on the HT component. In fact, some of the *P*-wave PDs look like shear-wave PDs exhibiting shear-wave splitting! This is a major cause for concern because it implies that shear-wave PDs may be similarly affected, possibly obscuring any shear-wave splitting. These non linear *P*-wave motions are probably the result of non planar interfaces, or lateral variations in lithology, producing scattered energy out of the sagittal plane. The same will probably happen to shear-waves, which may be especially sensitive to topography at interfaces where mode conversions take place.

Dynamic plane, shear-wave PDs are given in Figure 4.21, and it is to these that the three automatic techniques were applied, with an 80ms window allowing a maximum delay between split shear-waves of 40ms. Due to the longer time window used on the shear-waves PDs, they appear more complex than the *P*-wave PDs where a 40ms window was used. Choice of window start times and length are fairly critical as best results from the automatic techniques are obtained when only the two split shear-waves of interest are included. If the window is too long, other shear-wave arrivals may be present which will act to distort any estimates of polarization and time delay. A window which is too short will effectively cut off the end of the slow shear-wave, which again will distort estimates of polarization and time delay. The relative complexity of the shear-wave PDs compared to those of the *P*-wave makes visual interpretation particularly difficult, if not impossible, especially if an objective result is desired. Due to the lack of continuity in the shape of the shear-wave PDs between adjacent geophone levels, even the automatic techniques may not pick regularly varying shear-wave splitting parameters.

Figure 4.21. Dynamic plane PDs for the cap-rock mode converted shear-waves. The bottom 20 geophones are displayed using an 80ms window.

Boat 1 cap–rock shear–waves

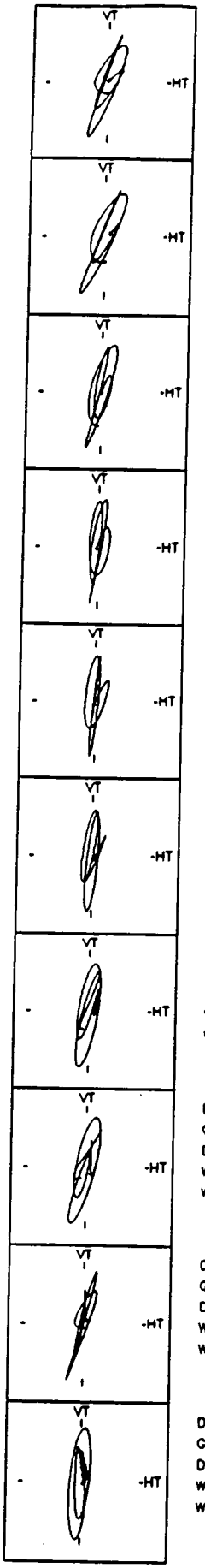

DYNAMIC PLANE
GEOPHONE 1
DEPTH: 2.166km
WINDOW START: 0.773s
WINDOW LENGTH: 0.080s

DYNAMIC PLANE
GEOPHONE 2
DEPTH: 2.181km
WINDOW START: 0.779s
WINDOW LENGTH: 0.080s

DYNAMIC PLANE
GEOPHONE 3
DEPTH: 2.196km
WINDOW START: 0.782s
WINDOW LENGTH: 0.080s

DYNAMIC PLANE
GEOPHONE 4
DEPTH: 2.212km
WINDOW START: 0.786s
WINDOW LENGTH: 0.080s

DYNAMIC PLANE
GEOPHONE 5
DEPTH: 2.227km
WINDOW START: 0.790s
WINDOW LENGTH: 0.080s

DYNAMIC PLANE
GEOPHONE 6
DEPTH: 2.243km
WINDOW START: 0.795s
WINDOW LENGTH: 0.080s

DYNAMIC PLANE
GEOPHONE 7
DEPTH: 2.258km
WINDOW START: 0.801s
WINDOW LENGTH: 0.080s

DYNAMIC PLANE
GEOPHONE 8
DEPTH: 2.273km
WINDOW START: 0.806s
WINDOW LENGTH: 0.080s

DYNAMIC PLANE
GEOPHONE 9
DEPTH: 2.289km
WINDOW START: 0.813s
WINDOW LENGTH: 0.080s

DYNAMIC PLANE
GEOPHONE 10
DEPTH: 2.304km
WINDOW START: 0.818s
WINDOW LENGTH: 0.080s

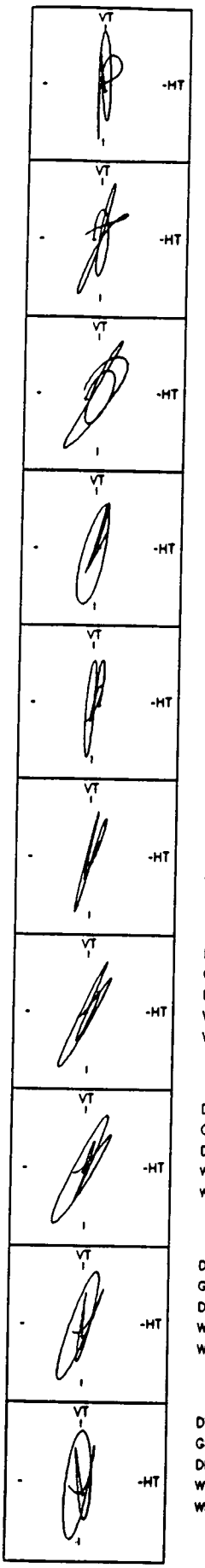

DYNAMIC PLANE
GEOPHONE 11
DEPTH: 2.320km
WINDOW START: 0.823s
WINDOW LENGTH: 0.080s

DYNAMIC PLANE
GEOPHONE 12
DEPTH: 2.335km
WINDOW START: 0.830s
WINDOW LENGTH: 0.080s

DYNAMIC PLANE
GEOPHONE 13
DEPTH: 2.351km
WINDOW START: 0.836s
WINDOW LENGTH: 0.080s

DYNAMIC PLANE
GEOPHONE 14
DEPTH: 2.366km
WINDOW START: 0.845s
WINDOW LENGTH: 0.080s

DYNAMIC PLANE
GEOPHONE 15
DEPTH: 2.382km
WINDOW START: 0.850s
WINDOW LENGTH: 0.080s

DYNAMIC PLANE
GEOPHONE 16
DEPTH: 2.397km
WINDOW START: 0.853s
WINDOW LENGTH: 0.080s

DYNAMIC PLANE
GEOPHONE 17
DEPTH: 2.412km
WINDOW START: 0.857s
WINDOW LENGTH: 0.080s

DYNAMIC PLANE
GEOPHONE 18
DEPTH: 2.428km
WINDOW START: 0.861s
WINDOW LENGTH: 0.080s

DYNAMIC PLANE
GEOPHONE 19
DEPTH: 2.443km
WINDOW START: 0.865s
WINDOW LENGTH: 0.080s

DYNAMIC PLANE
GEOPHONE 20
DEPTH: 2.453km
WINDOW START: 0.871s
WINDOW LENGTH: 0.080s

Figure 4.21a

Boat 2 cap–rock shear–waves

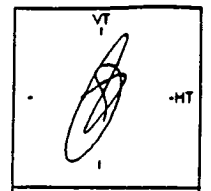

DYNAMIC PLANE
GEOPHONE 1
DEPTH: 2.166km
WINDOW START: 0.788s
WINDOW LENGTH: 0.080s

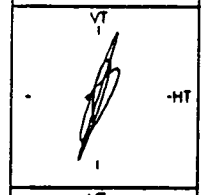

DYNAMIC PLANE
GEOPHONE 2
DEPTH: 2.181km
WINDOW START: 0.790s
WINDOW LENGTH: 0.080s

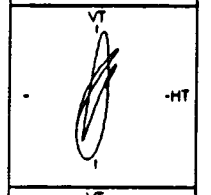

DYNAMIC PLANE
GEOPHONE 3
DEPTH: 2.196km
WINDOW START: 0.796s
WINDOW LENGTH: 0.080s

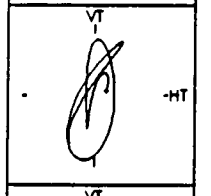

DYNAMIC PLANE
GEOPHONE 4
DEPTH: 2.212km
WINDOW START: 0.801s
WINDOW LENGTH: 0.080s

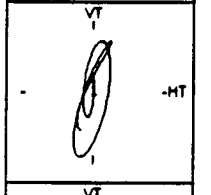

DYNAMIC PLANE
GEOPHONE 5
DEPTH: 2.227km
WINDOW START: 0.806s
WINDOW LENGTH: 0.080s

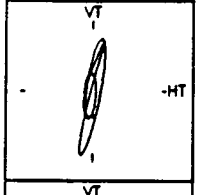

DYNAMIC PLANE
GEOPHONE 6
DEPTH: 2.243km
WINDOW START: 0.812s
WINDOW LENGTH: 0.080s

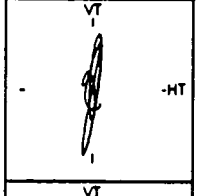

DYNAMIC PLANE
GEOPHONE 7
DEPTH: 2.258km
WINDOW START: 0.818s
WINDOW LENGTH: 0.080s

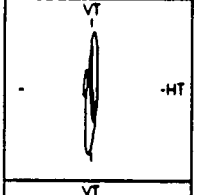

DYNAMIC PLANE
GEOPHONE 8
DEPTH: 2.273km
WINDOW START: 0.820s
WINDOW LENGTH: 0.080s

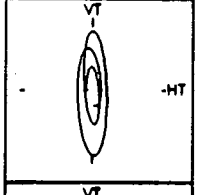

DYNAMIC PLANE
GEOPHONE 9
DEPTH: 2.289km
WINDOW START: 0.826s
WINDOW LENGTH: 0.080s

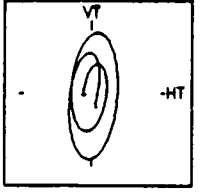

DYNAMIC PLANE
GEOPHONE 10
DEPTH: 2.304km
WINDOW START: 0.831s
WINDOW LENGTH: 0.080s

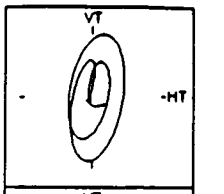

DYNAMIC PLANE
GEOPHONE 11
DEPTH: 2.320km
WINDOW START: 0.835s
WINDOW LENGTH: 0.080s

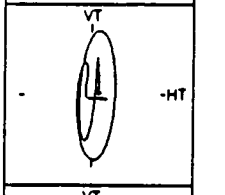

DYNAMIC PLANE
GEOPHONE 12
DEPTH: 2.335km
WINDOW START: 0.840s
WINDOW LENGTH: 0.080s

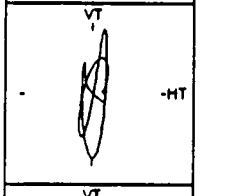

DYNAMIC PLANE
GEOPHONE 13
DEPTH: 2.351km
WINDOW START: 0.844s
WINDOW LENGTH: 0.080s

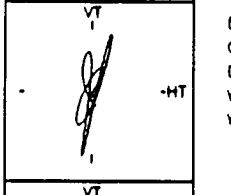

DYNAMIC PLANE
GEOPHONE 14
DEPTH: 2.366km
WINDOW START: 0.848s
WINDOW LENGTH: 0.080s

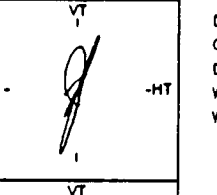

DYNAMIC PLANE
GEOPHONE 15
DEPTH: 2.382km
WINDOW START: 0.853s
WINDOW LENGTH: 0.080s

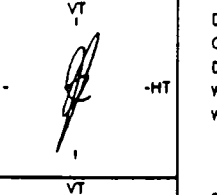

DYNAMIC PLANE
GEOPHONE 16
DEPTH: 2.397km
WINDOW START: 0.861s
WINDOW LENGTH: 0.080s

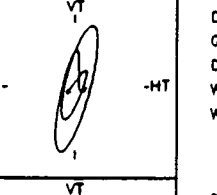

DYNAMIC PLANE
GEOPHONE 17
DEPTH: 2.412km
WINDOW START: 0.866s
WINDOW LENGTH: 0.080s

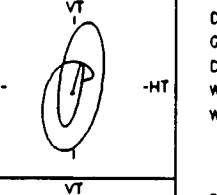

DYNAMIC PLANE
GEOPHONE 18
DEPTH: 2.428km
WINDOW START: 0.871s
WINDOW LENGTH: 0.080s

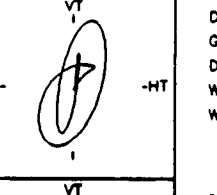

DYNAMIC PLANE
GEOPHONE 19
DEPTH: 2.443km
WINDOW START: 0.877s
WINDOW LENGTH: 0.080s

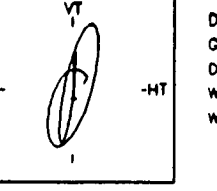

DYNAMIC PLANE
GEOPHONE 20
DEPTH: 2.453km
WINDOW START: 0.881s
WINDOW LENGTH: 0.080s

Figure 4.21b

Boat 3 cap–rock shear–waves

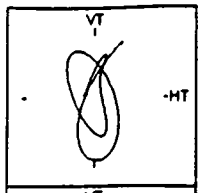

DYNAMIC PLANE
GEOPHONE 1
DEPTH: 2.166km
WINDOW START: 0.776s
WINDOW LENGTH: 0.080s

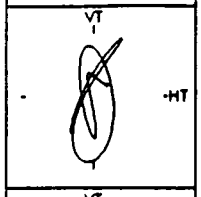

DYNAMIC PLANE
GEOPHONE 2
DEPTH: 2.181km
WINDOW START: 0.792s
WINDOW LENGTH: 0.080s

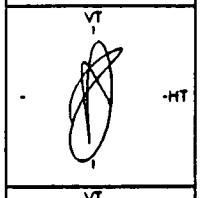

DYNAMIC PLANE
GEOPHONE 3
DEPTH: 2.196km
WINDOW START: 0.795s
WINDOW LENGTH: 0.080s

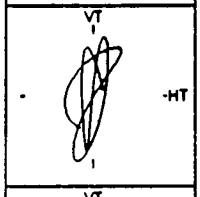

DYNAMIC PLANE
GEOPHONE 4
DEPTH: 2.212km
WINDOW START: 0.801s
WINDOW LENGTH: 0.080s

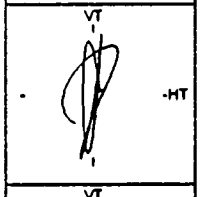

DYNAMIC PLANE
GEOPHONE 5
DEPTH: 2.227km
WINDOW START: 0.805s
WINDOW LENGTH: 0.080s

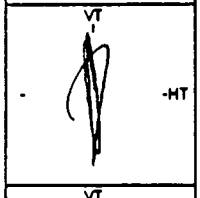

DYNAMIC PLANE
GEOPHONE 6
DEPTH: 2.243km
WINDOW START: 0.810s
WINDOW LENGTH: 0.080s

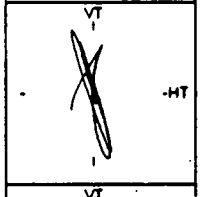

DYNAMIC PLANE
GEOPHONE 7
DEPTH: 2.258km
WINDOW START: 0.814s
WINDOW LENGTH: 0.080s

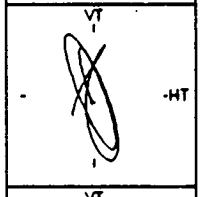

DYNAMIC PLANE
GEOPHONE 8
DEPTH: 2.273km
WINDOW START: 0.820s
WINDOW LENGTH: 0.080s

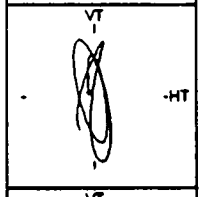

DYNAMIC PLANE
GEOPHONE 9
DEPTH: 2.289km
WINDOW START: 0.827s
WINDOW LENGTH: 0.080s

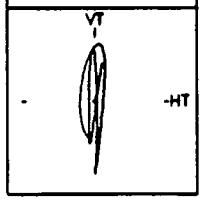

DYNAMIC PLANE
GEOPHONE 10
DEPTH: 2.304km
WINDOW START: 0.832s
WINDOW LENGTH: 0.080s

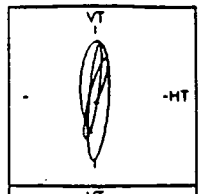

DYNAMIC PLANE
GEOPHONE 11
DEPTH: 2.320km
WINDOW START: 0.836s
WINDOW LENGTH: 0.080s

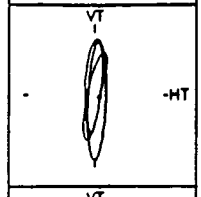

DYNAMIC PLANE
GEOPHONE 12
DEPTH: 2.335km
WINDOW START: 0.841s
WINDOW LENGTH: 0.080s

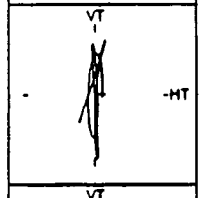

DYNAMIC PLANE
GEOPHONE 13
DEPTH: 2.351km
WINDOW START: 0.846s
WINDOW LENGTH: 0.080s

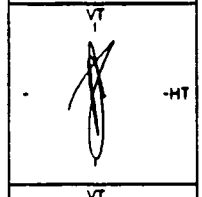

DYNAMIC PLANE
GEOPHONE 14
DEPTH: 2.366km
WINDOW START: 0.852s
WINDOW LENGTH: 0.080s

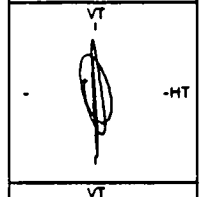

DYNAMIC PLANE
GEOPHONE 15
DEPTH: 2.382km
WINDOW START: 0.959s
WINDOW LENGTH: 0.080s

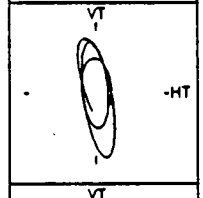

DYNAMIC PLANE
GEOPHONE 16
DEPTH: 2.397km
WINDOW START: 0.862s
WINDOW LENGTH: 0.080s

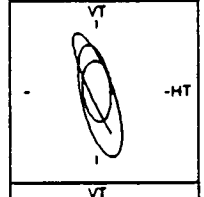

DYNAMIC PLANE
GEOPHONE 17
DEPTH: 2.412km
WINDOW START: 0.869s
WINDOW LENGTH: 0.080s

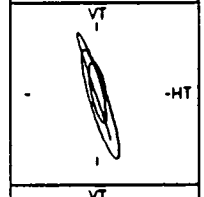

DYNAMIC PLANE
GEOPHONE 18
DEPTH: 2.428km
WINDOW START: 0.874s
WINDOW LENGTH: 0.080s

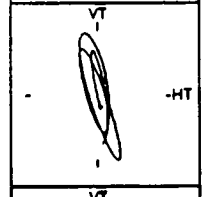

DYNAMIC PLANE
GEOPHONE 19
DEPTH: 2.443km
WINDOW START: 0.878s
WINDOW LENGTH: 0.080s

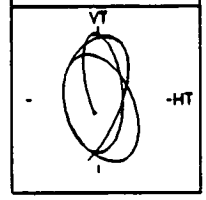

DYNAMIC PLANE
GEOPHONE 20
DEPTH: 2.453km
WINDOW START: 0.883s
WINDOW LENGTH: 0.080s

Figure 4.21c

Boat 4 cap–rock shear–waves

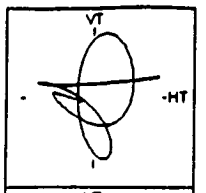

DYNAMIC PLANE
GEOPHONE 1
DEPTH: 2.166km
WINDOW START: 0.779s
WINDOW LENGTH: 0.080s

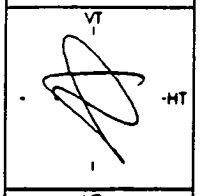

DYNAMIC PLANE
GEOPHONE 2
DEPTH: 2.181km
WINDOW START: 0.786s
WINDOW LENGTH: 0.080s

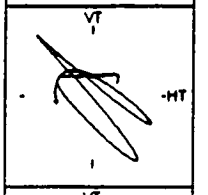

DYNAMIC PLANE
GEOPHONE 3
DEPTH: 2.196km
WINDOW START: 0.790s
WINDOW LENGTH: 0.080s

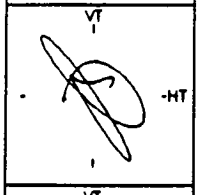

DYNAMIC PLANE
GEOPHONE 4
DEPTH: 2.212km
WINDOW START: 0.796s
WINDOW LENGTH: 0.080s

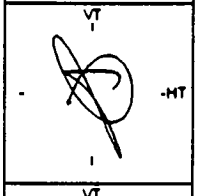

DYNAMIC PLANE
GEOPHONE 5
DEPTH: 2.227km
WINDOW START: 0.801s
WINDOW LENGTH: 0.080s

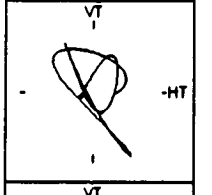

DYNAMIC PLANE
GEOPHONE 6
DEPTH: 2.243km
WINDOW START: 0.807s
WINDOW LENGTH: 0.080s

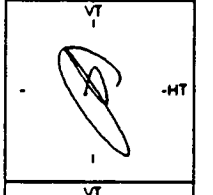

DYNAMIC PLANE
GEOPHONE 7
DEPTH: 2.258km
WINDOW START: 0.812s
WINDOW LENGTH: 0.080s

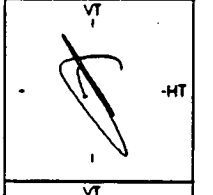

DYNAMIC PLANE
GEOPHONE 8
DEPTH: 2.273km
WINDOW START: 0.816s
WINDOW LENGTH: 0.080s

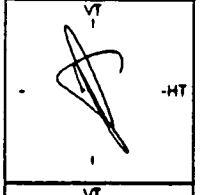

DYNAMIC PLANE
GEOPHONE 9
DEPTH: 2.289km
WINDOW START: 0.822s
WINDOW LENGTH: 0.080s

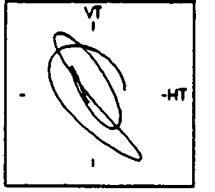

DYNAMIC PLANE
GEOPHONE 10
DEPTH: 2.304km
WINDOW START: 0.827s
WINDOW LENGTH: 0.080s

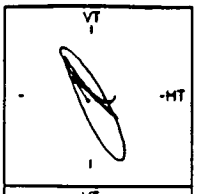

DYNAMIC PLANE
GEOPHONE 11
DEPTH: 2.320km
WINDOW START: 0.835s
WINDOW LENGTH: 0.080s

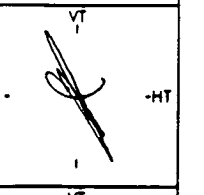

DYNAMIC PLANE
GEOPHONE 12
DEPTH: 2.335km
WINDOW START: 0.844s
WINDOW LENGTH: 0.080s

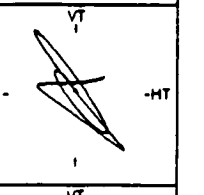

DYNAMIC PLANE
GEOPHONE 13
DEPTH: 2.351km
WINDOW START: 0.848s
WINDOW LENGTH: 0.080s

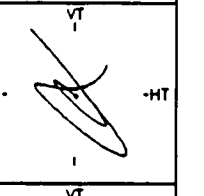

DYNAMIC PLANE
GEOPHONE 14
DEPTH: 2.366km
WINDOW START: 0.855s
WINDOW LENGTH: 0.080s

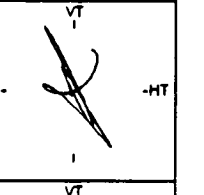

DYNAMIC PLANE
GEOPHONE 15
DEPTH: 2.382km
WINDOW START: 0.863s
WINDOW LENGTH: 0.080s

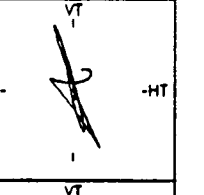

DYNAMIC PLANE
GEOPHONE 16
DEPTH: 2.397km
WINDOW START: 0.867s
WINDOW LENGTH: 0.080s

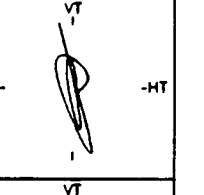

DYNAMIC PLANE
GEOPHONE 17
DEPTH: 2.412km
WINDOW START: 0.871s
WINDOW LENGTH: 0.080s

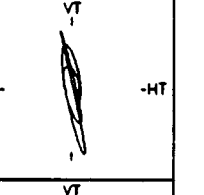

DYNAMIC PLANE
GEOPHONE 18
DEPTH: 2.428km
WINDOW START: 0.874s
WINDOW LENGTH: 0.080s

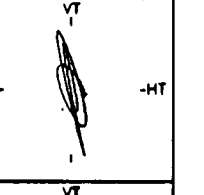

DYNAMIC PLANE
GEOPHONE 19
DEPTH: 2.443km
WINDOW START: 0.881s
WINDOW LENGTH: 0.080s

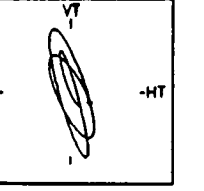

DYNAMIC PLANE
GEOPHONE 20
DEPTH: 2.453km
WINDOW START: 0.887s
WINDOW LENGTH: 0.080s

Figure 4.21d

Automatic measurements of shear-wave splitting

The *qS1* polarization and time delay estimates from the spectral interference and direct time series automatic techniques are given on Figure 4.22. Each offset is discussed individually below:

Offset 1 shows no real consistency in the time delay estimates, although the first spectral interference technique picks delays clustered around 11ms throughout the reservour section. The *qS1* polarization estimates give a much more consistent picture, with a relatively tight clustering about 10° from the horizontal radial direction. Relative to true North, this direction gives a *qS1* polarization of N45°W. Most of the outlying polarization estimates correspond to the slow shear-wave polarization, as seen in synthetic results from Chapter 2.

Offset 2 also shows a general scatter of time delays, with the *qS1* polarizations clustered around 0° and -90° from the HR direction. These results are similar to those from the F-K filtered isotropic model in Chapter 3, suggesting that there is no shear-wave splitting from this offset.

Offset 3 gives similar results to offset 2, with *qS1* polarizations scattered around 0°, -90° and +90° from HR.

Offset 4 shows the most consistent time delays and *qS1* polarizations of all the offsets, which is surprising considering the amount of noise on the *P*-waves. Constant delays of about 10-15ms can be seen throughout the reservoir sands, although there is a suggestion of a decreasing trend. *qS1* polarizations are clustered around two

Figure 4.22. Automatic measuring technique for measuring shear-wave splitting parameters applied to the shear-waves in Fig. 33. Time delay and fast shear-wave polarization estimates are shown. **a)** boat 1 **b)** boat 2 **c)** boat 3 **d)** boat 4.

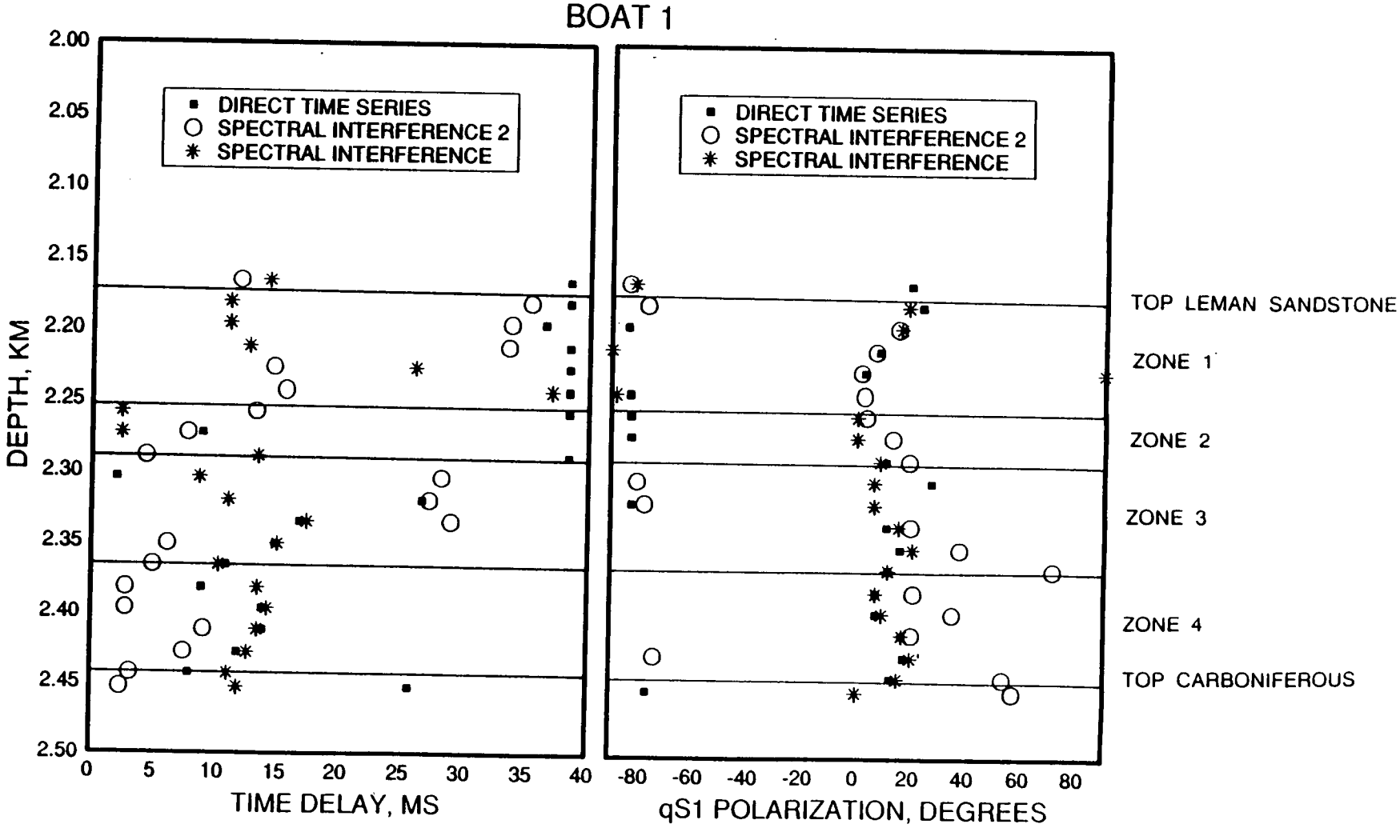
BOAT 1
DIRECT TIME SERIES
SPECTRAL INTERFERENCE 2
SPECTRAL INTERFERENCE
DIRECT TIME SERIES
SPECTRAL INTERFERENCE 2
SPECTRAL INTERFERENCE
DEPTH, KM
2.00
2.05
2.10
2.15
2.20
2.25
2.30
2.35
2.40
2.45
2.50
0
5
10
15
20
25
30
35
40
TIME DELAY, MS
-80
-60
-40
-20
0
20
40
60
80
qS1 POLARIZATION, DEGREES
TOP LEMAN SANDSTONE
ZONE 1
ZONE 2
ZONE 3
ZONE 4
TOP CARBONIFEROUS

Figure 4.22a

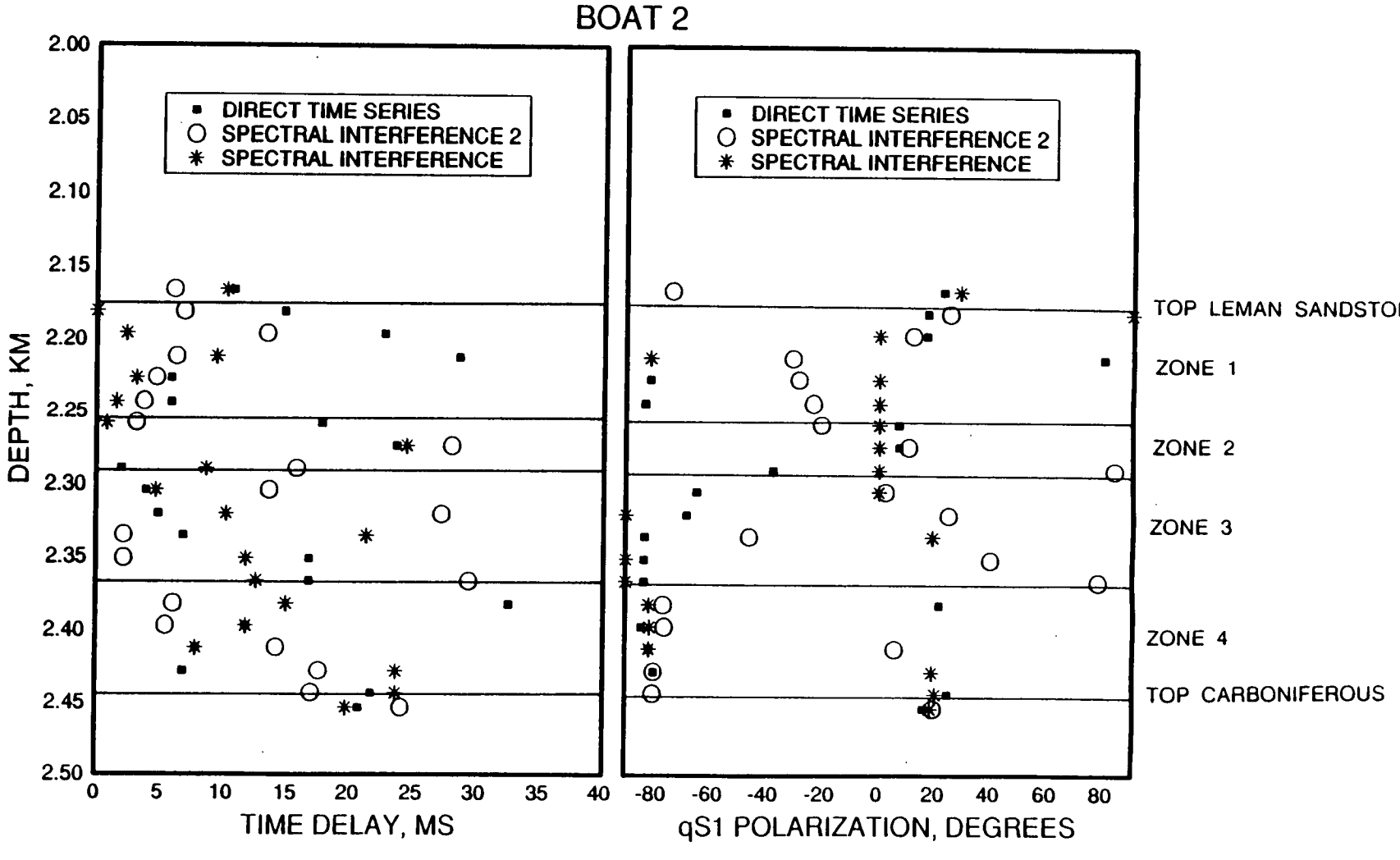
BOAT 2
DIRECT TIME SERIES
SPECTRAL INTERFERENCE 2
SPECTRAL INTERFERENCE
DIRECT TIME SERIES
SPECTRAL INTERFERENCE 2
SPECTRAL INTERFERENCE
DEPTH, KM
2.00
2.05
2.10
2.15
2.20
2.25
2.30
2.35
2.40
2.45
2.50
0
5
10
15
20
25
30
35
40
TIME DELAY, MS
-80
-60
-40
-20
0
20
40
60
80
qS1 POLARIZATION, DEGREES
TOP LEMAN SANDSTONE
ZONE 1
ZONE 2
ZONE 3
ZONE 4
TOP CARBONIFEROUS

Figure 4.22b

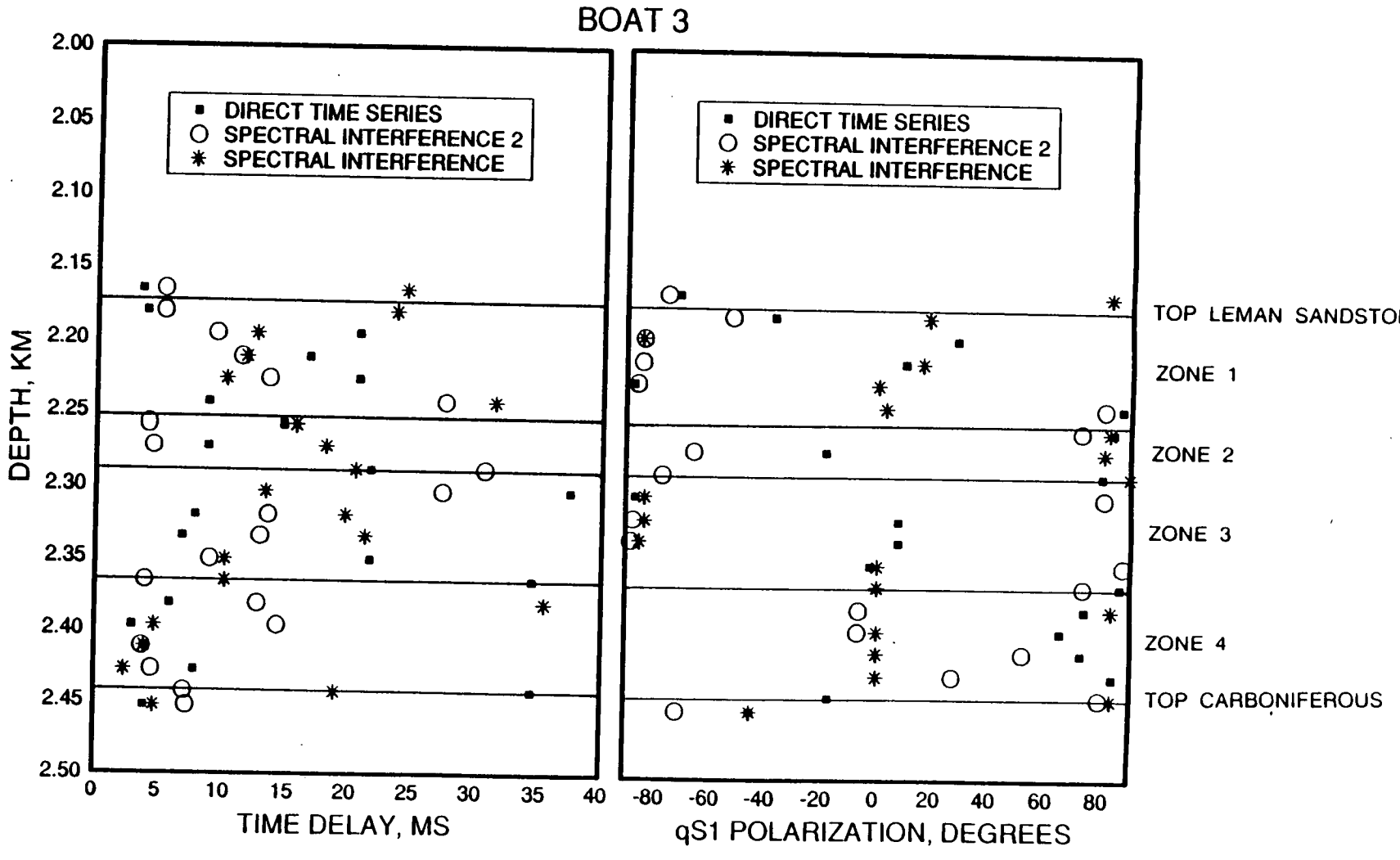
BOAT 3
DIRECT TIME SERIES
SPECTRAL INTERFERENCE 2
SPECTRAL INTERFERENCE
DEPTH, KM
2.00
2.05
2.10
2.15
2.20
2.25
2.30
2.35
2.40
2.45
2.50
0
5
10
15
20
25
30
35
40
TIME DELAY, MS
-80
-60
-40
-20
0
20
40
60
80
qS1 POLARIZATION, DEGREES
TOP LEMAN SANDSTONE
ZONE 1
ZONE 2
ZONE 3
ZONE 4
TOP CARBONIFEROUS

Figure 4.22c

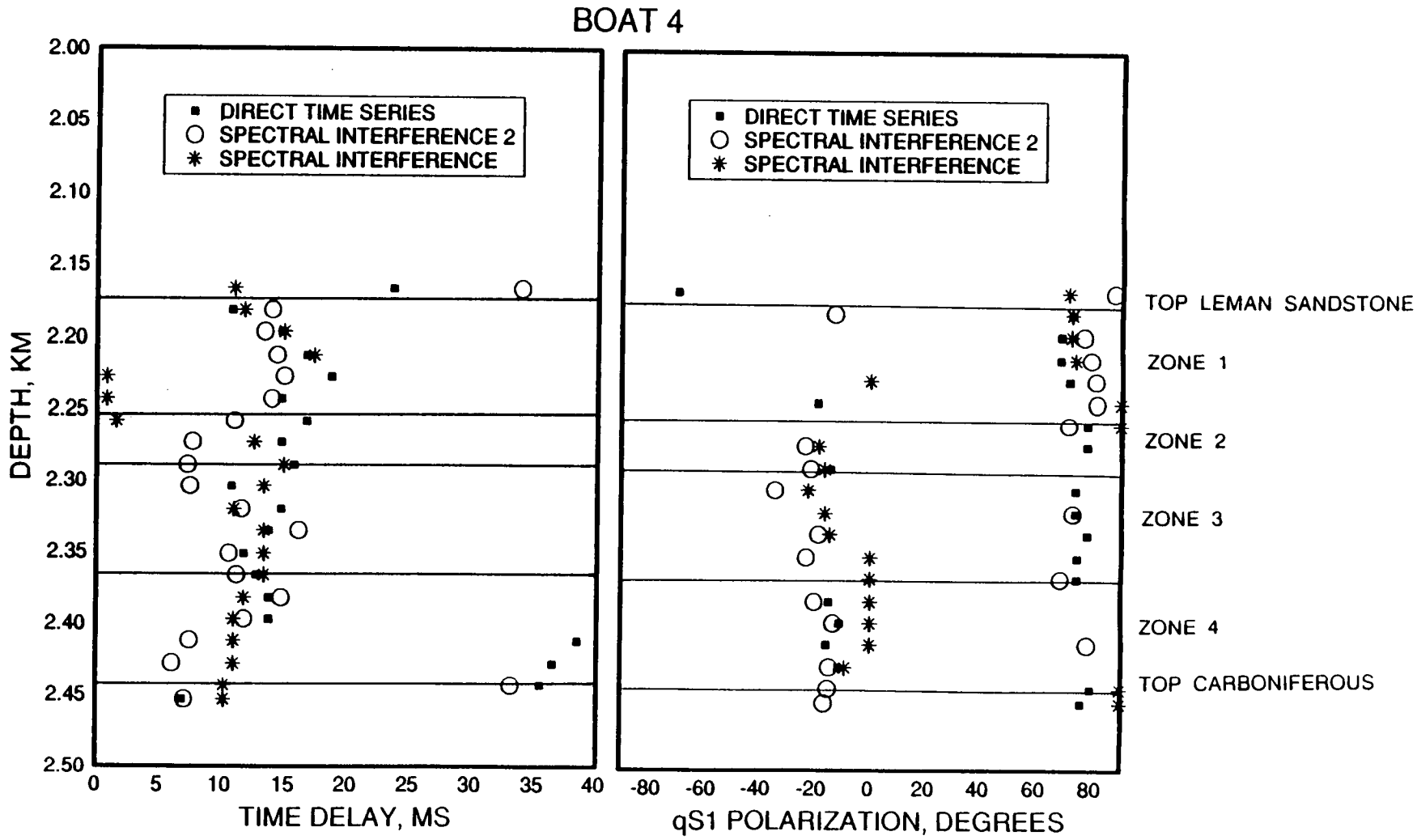
BOAT 4
DIRECT TIME SERIES
SPECTRAL INTERFERENCE 2
SPECTRAL INTERFERENCE
DEPTH, KM
2.00
2.05
2.10
2.15
2.20
2.25
2.30
2.35
2.40
2.45
2.50
0
5
10
15
20
25
30
35
40
TIME DELAY, MS
-80
-60
-40
-20
0
20
40
60
80
qS1 POLARIZATION, DEGREES
TOP LEMAN SANDSTONE
ZONE 1
ZONE 2
ZONE 3
ZONE 4
TOP CARBONIFEROUS

Figure 4.22d

directions, -10° and 80°, these being 90° apart. One of these directions will correspond to the slow shear-wave as seen in some of the synthetic data in Chapter 2 and 3. Assuming the direction from offset 1 is correct, the most likely *qS1* polarization from this offset should be about 80°. Relative to true North, this is N48°W.

Interpretation of shear-wave results

These shear-wave results obviously do not provide a clear cut solution to the type of anisotropy present, although a good reason for this exists. The polarization measurements from offsets 1 and 4 give a remarkably consistent *qS1* direction of between N45°W and N48°W (average N47°W), with an error of about +/-15° to allow for scatter in estimates of the *qS1* polariztions. This direction is almost exactly parallel to the offset 3 azimuth and very close to being perpendicular to the offset 2 azimuth, meaning that any shear-waves propagating from these source locations to the well travel in a symmetry plane, where no splitting occurs. Results from the automatic techniques appear to confirm the lack of splitting from these offsets.

The estimated *qS1* direction of N47°W +/-15° coincides with the maximum horizontal stress direction calculated from earthquake focal mechanisms (Marrow and Turbitt, 1988) and borehole breakout data (Klein and Barr, 1986). This adds some weight to the reliability of the shear-wave data and the automatic measuring techniques, but does not really provide any answers about the detailed nature of the anisotropy, especially within the reservoir.

The relatively constant time delay estimates from offset 4 suggest that all the shear-wave anisotropy is contained in the cap-rock, and the resevoir sands are effectively isotropic.

A possible alternative explanation for these results is that rough topography at interfaces between rocks of substantially different velocity, such as at the top and bottom of the cap-rock, produce shear-wave polarization anomalies similar to those created by anisotropy. This could explain the constant delay times throughout the reservoir as the polarization anomalies are introduced at one or more interfaces above the reservoir section. Regular trends in topographic features may explain the consistency in polarization estimates between offsets 1 and 4. This is discussed in more detail below.

4.8 Discussion

P-wave arrival time analysis suggests that lateral variations of lithology and/or non planar interfaces between rock units are present, giving a scatter to the interval velocities calculated from the four offset sources and the rig source. The non linear *P*-wave PDs also provide evidence for lateral velocity variations. Such features may obscure evidence for shear-wave anisotropy, or even imprint shear-waves with effects very similar to those of anisotropy. Hence, it is important to recognise the existence of such complications if only to discount them from the interpretation of shear-wave splitting.

Random scattering

An apparently important influencing factor over the amount of scatter present in the Vulcan *P*-wave and shear-wave PDs is the incidence angle of the seismic waves relative to internal boundaries. As the angle of incidence of a ray increases, the effect that any lateral variations have is increased. This phenomenon is clearly demonstrated in the Paris Basin VSP (Bush, 1990) where six source locations were used, with increasing offset from the wellhead. The five closest offsets produced consistent observations of shear-wave splitting at all geophone positions down the well, while the furthest offset produced much more scattered shear-wave polarizations from one geophone location to the next, similar to what is observed in the Vulcan VSPs.

The effects of random scattering on shear-wave polarizations has been studied in Chapter 2 and 3, and indicates that even after processing, automatically measured *qS1* polarizations tend to coincide with the source polarization direction, indicating isotropy. Hence, random scattering can be discounted as an explanation for the observed shear-wave splitting from offsets 1 and 4, and some sort of consistent structure causing shear-wave splitting (which could be anisotropic or otherwise) must be sought.

Non planar interfaces

Horizontal plane *P*-wave polarizations measured from boats 1 and 2 indicate that the transition from Zechstein cap-rock sediments to Rotliegend reservoir sands is not a plane interface. Between 2.1km and 2.2km, the measured *P*-wave polarizations from these two offsets should yield similar tool orientations relative to North (since these offsets used the same tool locations). Referral back to Figure 4.8

shows a difference of almost 90° between the two estimates between within this depth range. Also at these levels, a significant amount of energy can be seen on the HT component from offset 1, with similar arrival times to the *P*-waves and indicates that it is this offset that is in error rather than offset 2. The most likely cause for the inconsistent rotation directions is irregular topography, but it is surprising that the *P*-waves are affected so much.

A non planar boundary between the Zechstein transgression sequence and the Rotliegend sands is not unexpected. Under the arid conditions of the Permian, with a low sediment influx, sedimentation failed to keep up with subsidence of the Sole Pit. At the time of the mid Permian Zechstein transgression, the surface of the desert has been estimated to be 200-300m below global sea level (Smith, 1979; Ziegler, 1982). Under these basinal conditions, once started, the Zechstein transgression appears to have been achieved exceedingly fast, the dune tops (up to 50m high) being inundated in as little as eight months (Glennie, 1983). This rapidity in the rise of waters seems to have produced virtually no marine erosion of the linear dunes exposed around Durham so that their former relief is still largely preserved (Glennie, 1986). A similar Rotliegend dune relief is believed to be preserved under the North Sea (Glennie and Buller, 1983), but there, the dunes are probably of transverse or barchan (horse shoe shaped) type (Glennie, 1983). Thus, it seems very likely that the top of the Rotliegend sandstone forms a non planar interface with the base of the Zechstein transgression, with amplitude variations up to 50m in height over a lateral distance of some 200-300m. This is on a par with seismic wavelengths.

Liu and Crampin (1990) describe the effects of the internal shear-wave window and show how shear-wave splitting phenomenon can be produced by an isotropic model for rays travelling with relatively large incidence angles. Such effects do not occur for mode converted shear-waves, with *SV*-type motion, that are incident upon plane, horizontal interfaces, as the phenomenon depends on differences between the *SV* and *SH* reflection and transmission coefficients. However, if the interfaces are not horizontal, polarization anomalies may be introduced to mode converted *SV*-waves, with the same characteristics as shear-wave splitting. The topographic features at the base of the cap-rock may well act to produce such effects.

Is it possible that dune relief at the top of the Rotliegend sandstone could produce consistent *qS1* polarization directions from offsets 1 and 4? The low sedimentation rate at the end of the Permian suggests that the sand dunes were of barchan type which have a much smaller lateral extent than transverse or longitudinal seif type dunes. Barchan sand dunes also have a greater variety of bedding orientations than other dune types, meaning that it is very unlikely that consistent polarization directions would arise from offsets 1 and 4 (which are also consistent with the null results from offsets 2 and 3) where the shear-waves sample in excess of 300m of dune topography. However, dune topography will very likely add to the scatter observed in the measurements of *qS1* polarizations and time delays.

Shear-wave anisotropy

Ruling out the effects of random scattering and non planar interfaces as the cause for the observed shear-wave splitting, the most likely remaining explanation is shear-wave velocity anisotropy, induced by unequal horizontal stresses (past or present). Assuming this is true, the measured time delays from offset 4 further suggest that the anisotropy is restricted to the cap-rock, as there is no indication of time delays increasing within the reservoir sands.

If the velocity anisotropy observed in the cap-rock is caused by present day stresses, forming extensive-dilatancy anisotropy, which seems to be confirmed by independent stress direction measurements (Marrow and Turbitt, 1988; Klein and Barr, 1986), then the the same maximum horizontal stress direction may be cautiously inferred to exist within the reservoir sands. Caution must be exercised because the reservoir is hydraulically isolated (by the cap-rock) from the overlying hydraulic system. The fluid pressures in the reservoir are likely to be greater than outside, forming an overpressured system, which may locally alter stress conditions. However, this is more likely to affect the magnitudes of the stresses rather than the directions of the principal stress directions. Without positive measurements of anisotropy within the reservoir itself, it is not possible to give a statement regarding the precise nature of the reservoir stress conditions.

4.9 Conclusions

Analysis of *P*-wave arrival times from four offset VSPs in the Vulcan gas field show the existance of four zones within the reservoir sands, which can be related to different depositional environments. A low *Vp/Vs* ratio in zone 3 indicated the presence of gas saturated sands agreeing with well data.

No consistent azimuthal variations could be seen from *P*-wave interval velocities calculated from the four different offsets directions, as too much scatter was present. Similarly, no positive evidence for thin layer anisotropy could be obtained by comparing interval velocities from the four offset VSPs with the rig source VSP.

P-wave and cap-rock shear-wave PDs within the reservoir sands revealed significant amounts of scattered energy, probably resulting from lateral changes in lithology and/or non planar interfaces. The presence of this noise reduced the reliability of estimates of shear-wave splitting from shear-waves within the reservoir sands.

Despite this, a fast shear-wave polarization direction of N47°W was estimated by applying three automatic techniques to the mode converted shear-waves below the top of the cap-rock. Time delay results suggest that velocity anisotropy is confined to within the cap-rock, with little or no measurable anisotropy in the reservoir. Assuming stress directions do not dramatically change from the cap-rock to the reservoir and that the velocity anisotropy is caused by vertical, stress aligned cracks or fractures, the estimated *qS1* direction will be parallel to the maximum horizontal stress direction within the reservoir.

However, two of the offsets were either parallel or perendicular to the *qSl* direction, meaning that the shear-waves were not split as they travelled in symmetry planes. The other two offsets were about 10° from symmetry planes resulting in one of the split shear-waves having a very low amplitude and therefore easily distorted by noise. It is therefore an important conclusion of this chapter, that to study shear-wave splitting from converted *P*-waves, offsets at 45° to the estimated maximum horizontal compressive stress direction are desireable, so that shear-wave arrivals display more prominent splitting.

Overall, the problem of scattering arises because relatively large incidence angles are used, which tend to amplify the effects of lateral variations of lithology and non planar interfaces. It it not possible to reduce this problem by using smaller offsets because the quality of mode converted shear-waves would decrease. Thus, there is a trade off between scattering and shear-wave quality. This may be a general problem associated with all such marine VSPs where mode converted shear-wave are generated at wide offsets.

Chapter 5 - The Geysers steam reservoir VSP

5.1 Introduction

P- and shear-wave VSPs were carried out by the Lawrence Berkeley Laboratories in the Geysers Steam Field about 100km north of San Francisco in the northern California Coast Ranges (Figure 5.1), with the object of determining crack orientations and crack densities existing within the geothermal reservoir rock from shear-wave splitting (Majer et al., 1988).

The Geysers Steam Field is the largest commercial producer of electricity from geothermal energy in the world and occupies an area of about 300km^2, bounded on the southwest by the Mercuryville fault zone and on the northeast by the Collayomi fault zone (Figure 5.2). Northeast of the Collayomi fault zone, the geothermal reservoir becomes hot water dominated. The northwest and southeast boundaries of the steam reservoir are less well defined. The steam reservoir lies within the core of the Mayacmas Mountains, formed by major uplift between the Maacama and Collayomi fault zones due to north-northeast compression (McLaughlin, 1981). Rocks of the central and eastern Franciscan belts compose the uplifted core of the Mayacmas antiform and underlie the entire area of the Geysers Steam Field. The reservoir rocks around the site of the VSP consist of slightly metamorphosed graywacke that has been sheared and fractured. A 400m to 600m thick caprock of highly weathered greenstone, characterised by a reddish brown colour and crumbly nature at the surface, overlies the reservoir graywacke.

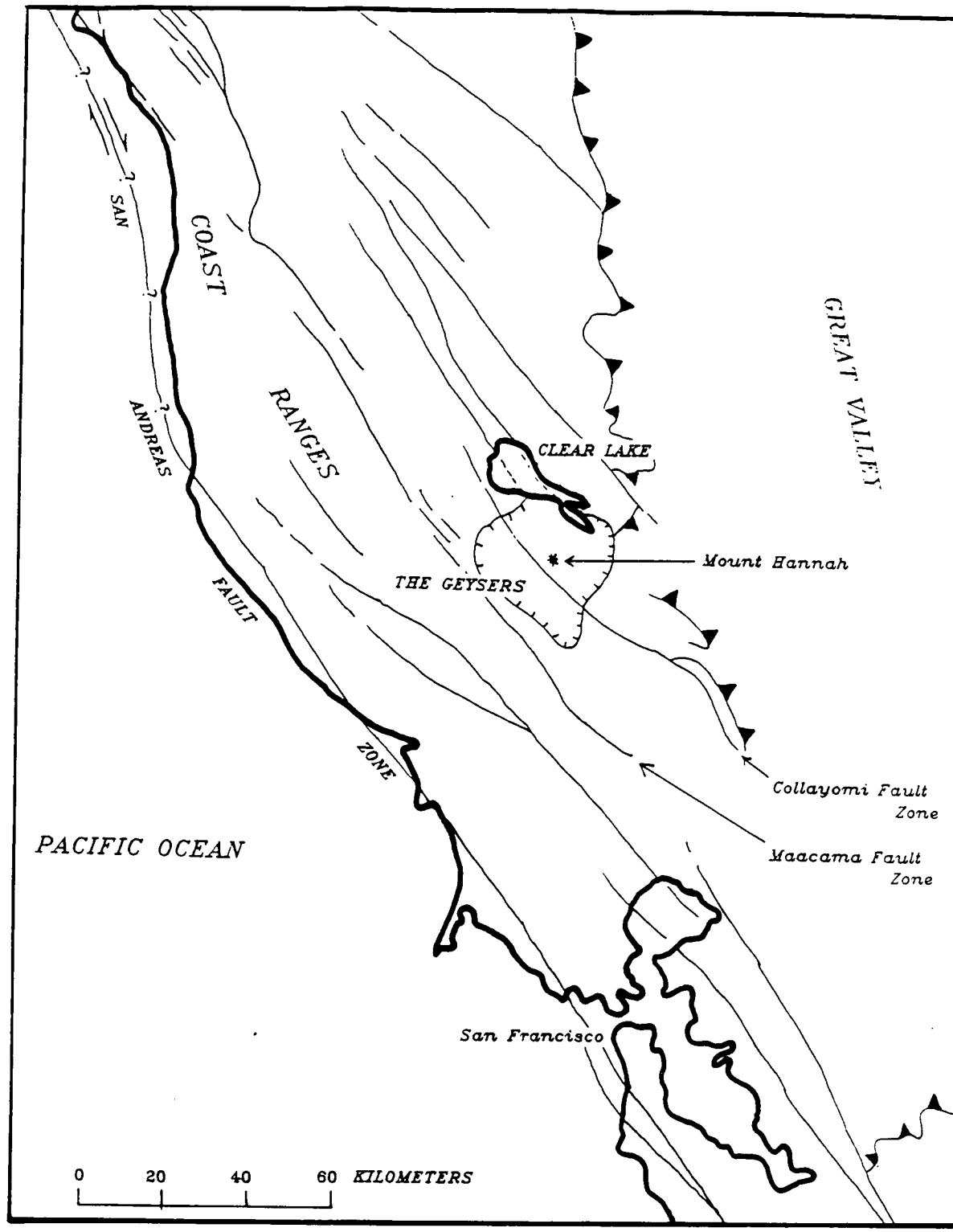

Figure 5.1. Location map showing outline of The Geysers geothermal reservoir. Major fault zones are also marked in, most of which belong to the San Andreas fault system. The steam dominated part of the reservoir lies to the southwest of the Collayomi fault zone.

FAULTING OVER THE GEYSERS STEAM RESERVOIR (McLaughlin, 1981)

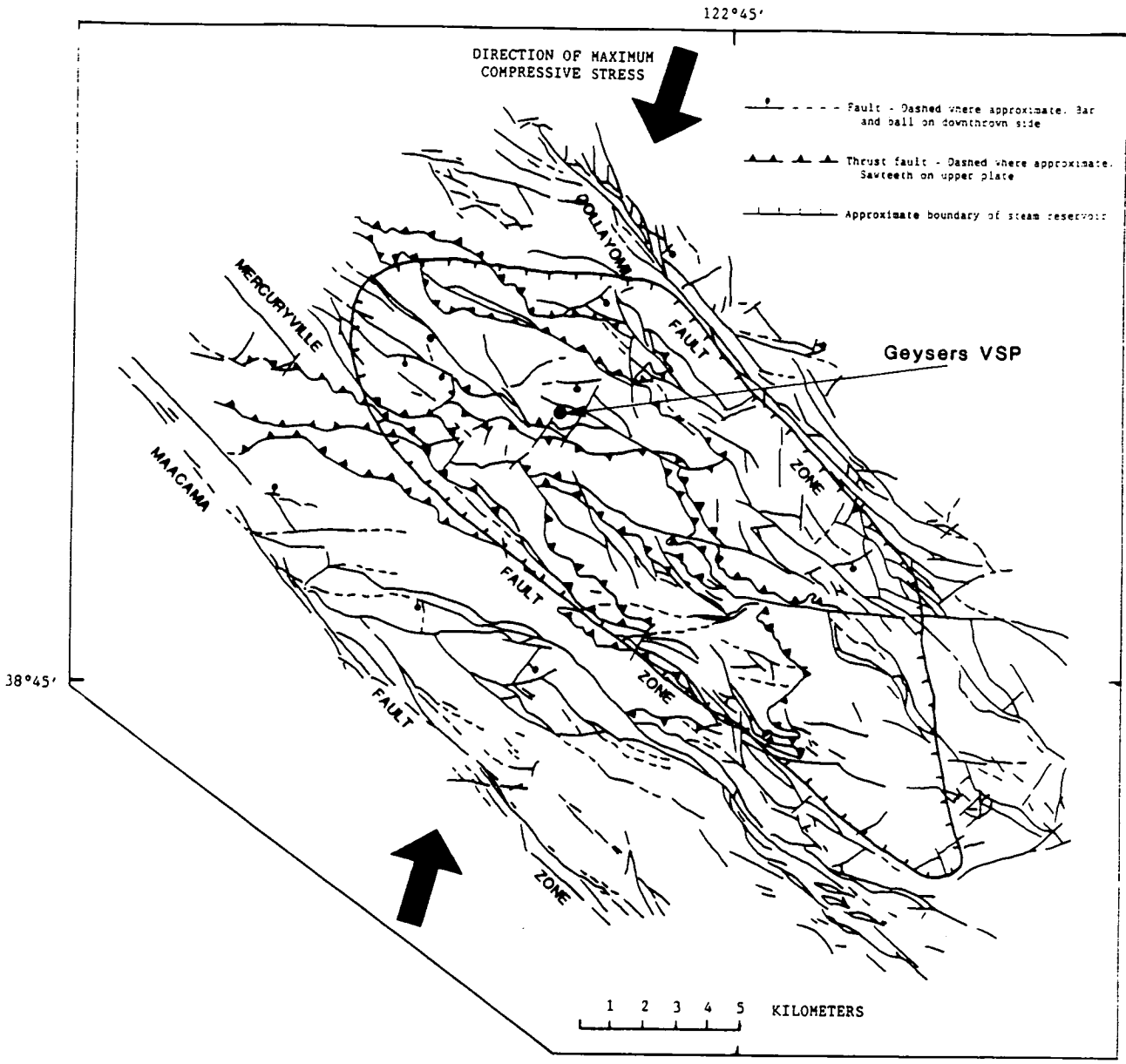

Figure 5.2. North-west to south-east faulting in the Geysers steam field, with directions of compressional stress derived from fault plane mechanisms (after McLaughlin, 1981). The stress directions are approximately perpendicular to the directions of minimum compressional stress found by Zoback and Zoback (1980). The site of the VSP area marked.

VSP geometry

Two VSP source locations were used, both on the same azimuth from the well head and running along the strike of a southwest dipping slope (Figure 5.3).

At the near offset source (166m from the well head), a *P*-wave VIBROSEIS source and a transversely oriented shear-wave (*SH*) VIBROSEIS source were used. It was not possible to orient the horizontal vibrator in an in-line (*SV*) direction because there was insufficient space to turn the VIBROSEIS truck. A single three-component geophone was used, placed at 21 locations between 792m and 1401m. Deeper geophone locations were not possible because the tool burned out in the extremely hot down hole conditions.

The far offset VSP, described in detail by Majer et al. (1988), had a source location 518m from the wellhead. *P*-, *SV*- and *SH*-oriented vibrators were used at this source position, recorded by a single three-component tool placed at 12 depths between 305m and 640m, making a nine-component experiment.

There were no coinciding geophone locations for the two offsets, which makes it more difficult to determine whether a single proposed horizontal, plane layered, anisotropic structure correctly models observations from both source positions. An example cross-section of how rays from each source location travel to the geophones is presented in Figure 5.4. The large differences in ray path incidence angles between source positions mean that the effects of anisotropy on shear-waves from each source will be substantially different, which can provide more control when estimating the type of anisotropic structure present.

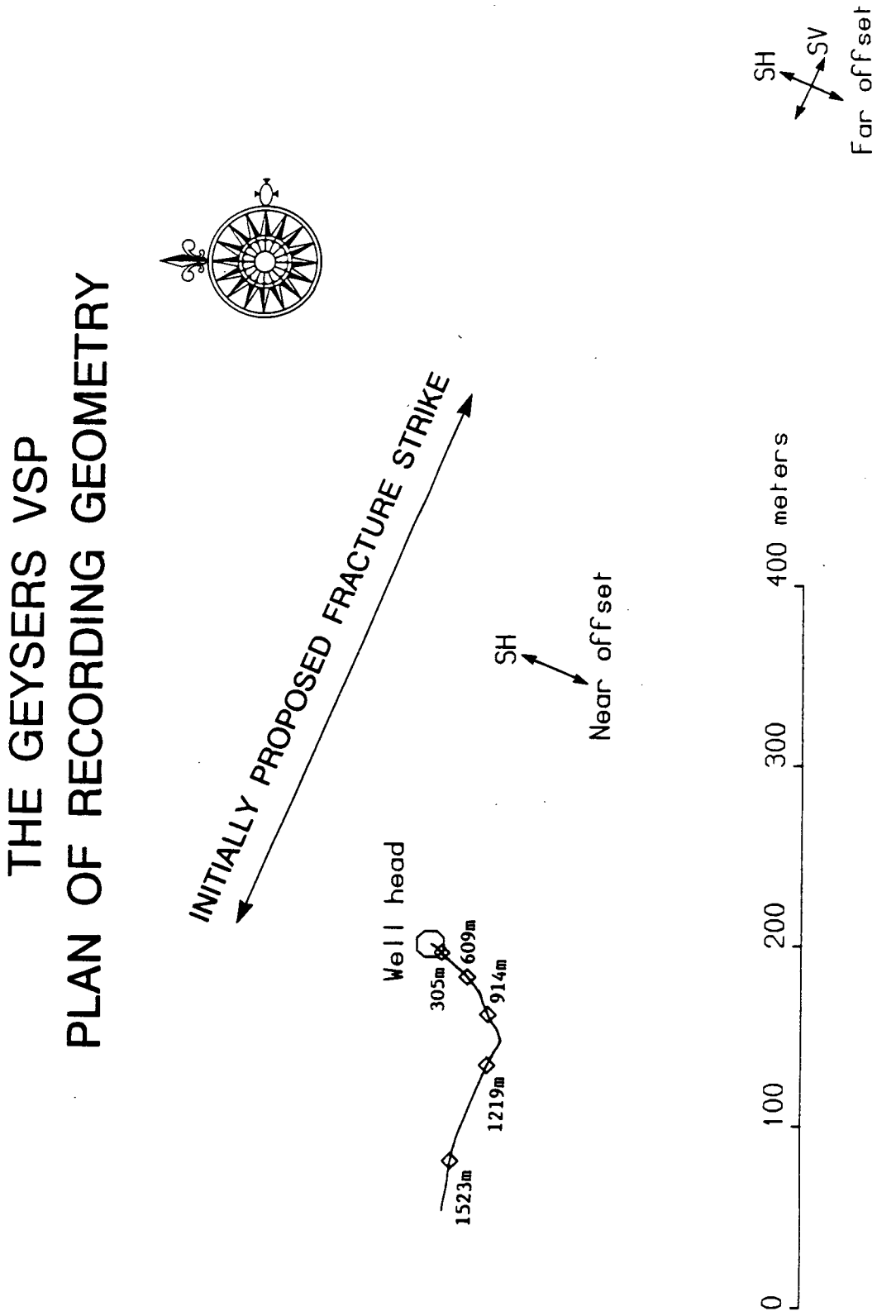

Figure 5.3. Plan of the Geysers' VSPs showing both source offset locations. The initially proposed fracture strike is indicated, after Majer et al. (1988). A plan view of the well deviation is also marked, showing that the upper 1000m of the well deviates only slightly.

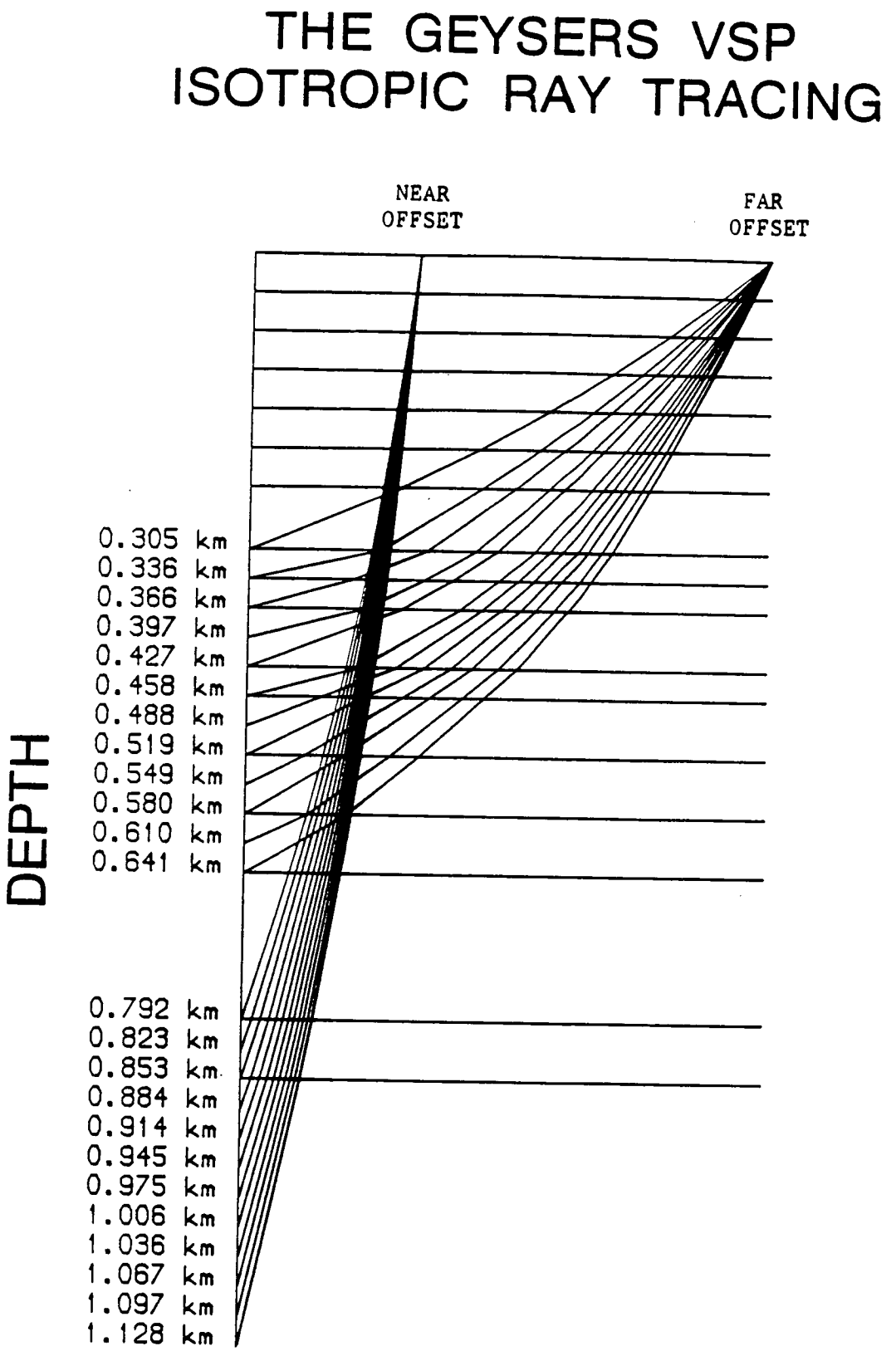

Figure 5.4. Example ray paths from the two source offsets to the geophone locations. The far offset produces rays with much larger incidenace angles compared to the near offset.

It is not known whether the geophone axes were right or left handed. This means that while the radial and vertical directions can be defined accurately (i.e. radial positive away from the source, vertical positive up), there will be an ambiguity in the polarity of the transverse component. Consequently, there will be a similar ambiguity in any interpreted directions of cracks/fractures relative to the radial direction.

5.2 Far offset observations and previous modelling

P-waves

There was no control or measurement of the alignments of the three orthogonal geophone axes. Following Majer et al. (1988) and Shearer (1988), the horizontal component geophones from the far offset source were rotated to horizontal radial and transverse directions by performing polarization analysis, described by Kanasewich (1981), to maximize the horizontal radial amplitudes of the initial *P*-wave arrival at each geophone level. The rotated *P*-wave seismograms are shown in Figure 5.5 where three-component scaling has been used such that relative amplitudes can be compared between different components.

Comparable results were obtained by Majer et al. and Shearer. Note that the rotation method is valid even in strongly anisotropic rock, because the polarization direction of the *P*-wave arrival closely follows the ray (group velocity) direction even though both may deviate substantially from the normal to the surface of constant phase in the presence of strong anisotropy (Crampin et al., 1982). Further rotations of the geophones to correct for the slight

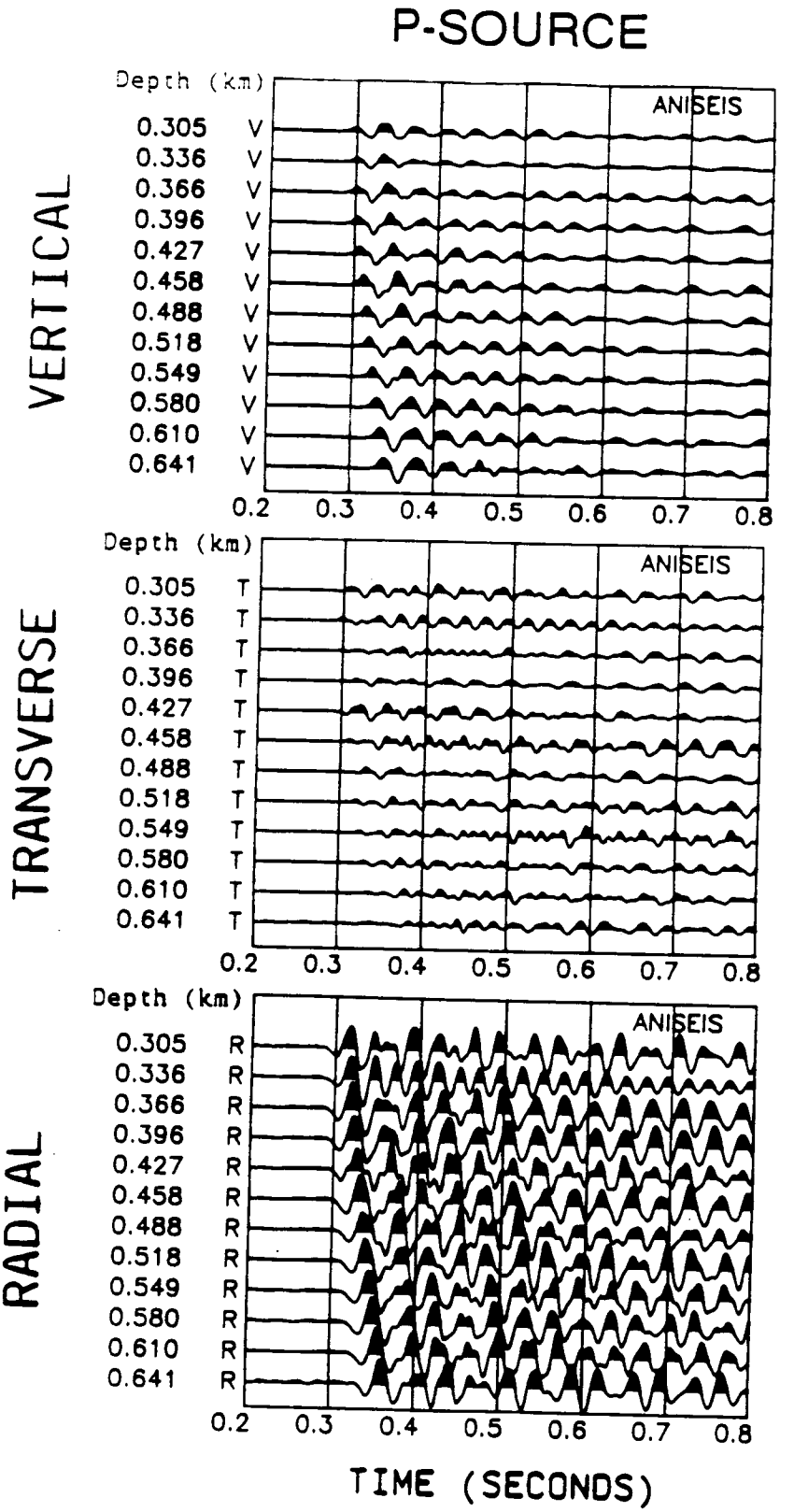

Figure 5.5. Observed seismograms from the far offset *P*-source. The horizontal components were rotated to radial and transverse using incoming *P*-wave polarizations.

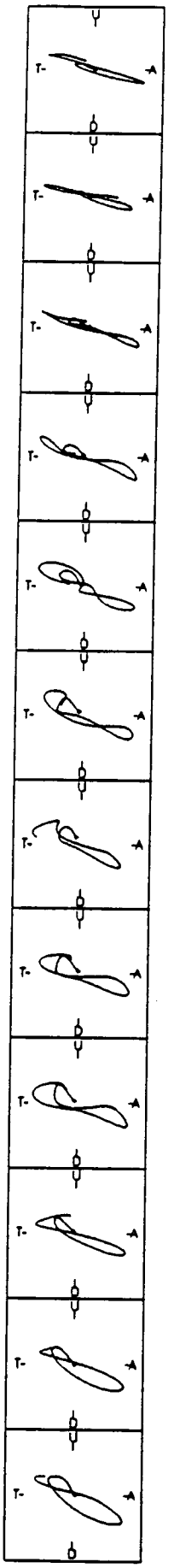

SAGITTAL PLANE
GEOPHONE 1
DEPTH: 0.305km
WINDOW START: 0.285s
WINDOW LENGTH: 0.055s

SAGITTAL PLANE
GEOPHONE 2
DEPTH: 0.336km
WINDOW START: 0.289s
WINDOW LENGTH: 0.055s

SAGITTAL PLANE
GEOPHONE 3
DEPTH: 0.366km
WINDOW START: 0.291s
WINDOW LENGTH: 0.055s

SAGITTAL PLANE
GEOPHONE 4
DEPTH: 0.396km
WINDOW START: 0.296s
WINDOW LENGTH: 0.055s

SAGITTAL PLANE
GEOPHONE 5
DEPTH: 0.427km
WINDOW START: 0.299s
WINDOW LENGTH: 0.055s

SAGITTAL PLANE
GEOPHONE 6
DEPTH: 0.458km
WINDOW START: 0.305s
WINDOW LENGTH: 0.055s

SAGITTAL PLANE
GEOPHONE 7
DEPTH: 0.488km
WINDOW START: 0.311s
WINDOW LENGTH: 0.055s

SAGITTAL PLANE
GEOPHONE 8
DEPTH: 0.518km
WINDOW START: 0.312s
WINDOW LENGTH: 0.055s

SAGITTAL PLANE
GEOPHONE 9
DEPTH: 0.549km
WINDOW START: 0.317s
WINDOW LENGTH: 0.055s

SAGITTAL PLANE
GEOPHONE 10
DEPTH: 0.580km
WINDOW START: 0.320s
WINDOW LENGTH: 0.055s

SAGITTAL PLANE
GEOPHONE 11
DEPTH: 0.610km
WINDOW START: 0.323s
WINDOW LENGTH: 0.055s

SAGITTAL PLANE
GEOPHONE 12
DEPTH: 0.641km
WINDOW START: 0.327s
WINDOW LENGTH: 0.055s

Figure 5.6. Sagittal plane polarization diagrams of the first 55ms of the *P*-wave motion, showing relatively linear motion and large incidence angles.

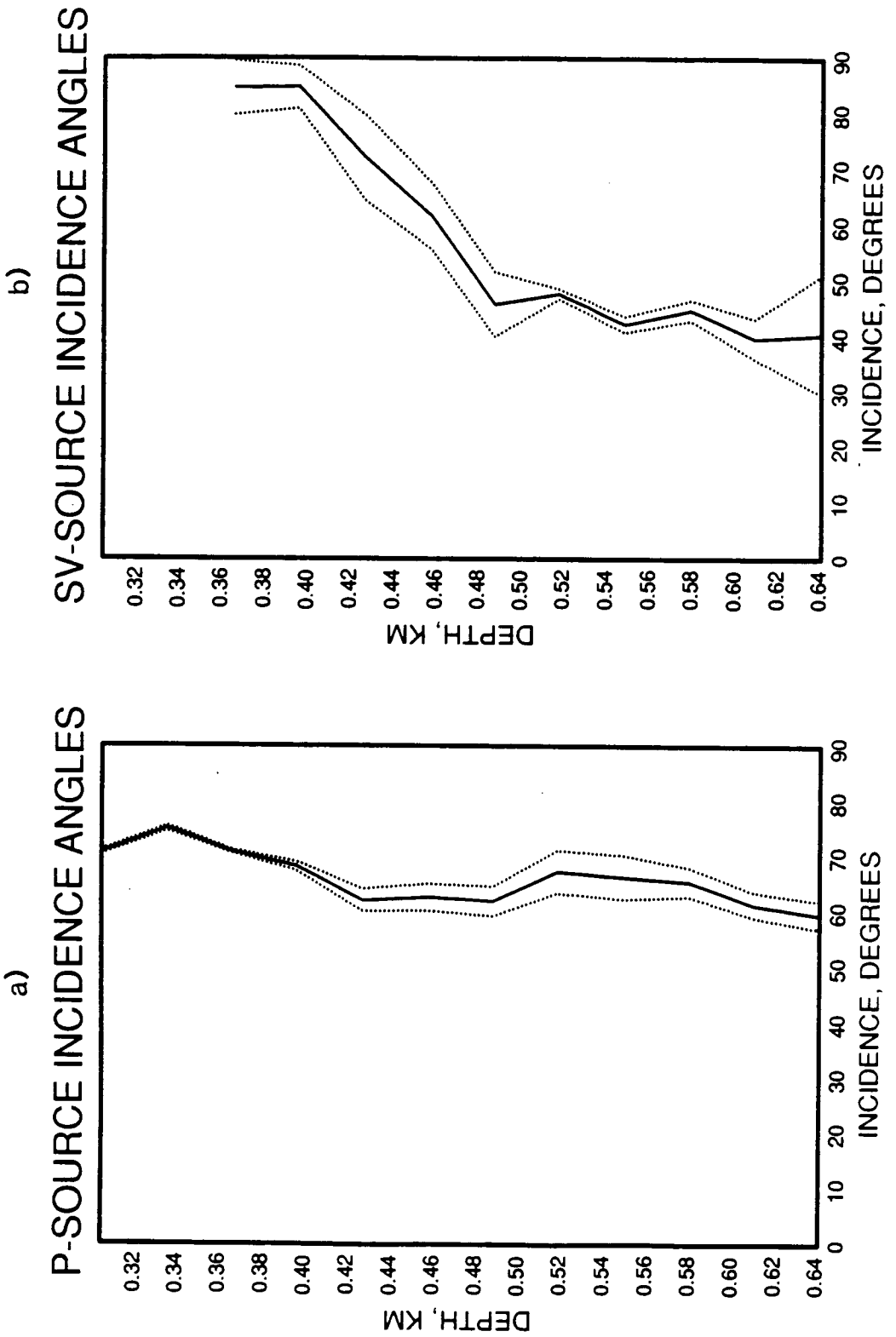

Figure 5.7. a) Measured *P*-wave incidence angles, with associated errors (marked by the dotted lines). Relatively constant incidences are present throughout the depth range of the VSP. **b)** Measured incidence angles from the *SV*-source shear-waves. This shows a significant change in incidence angle as depth increases.

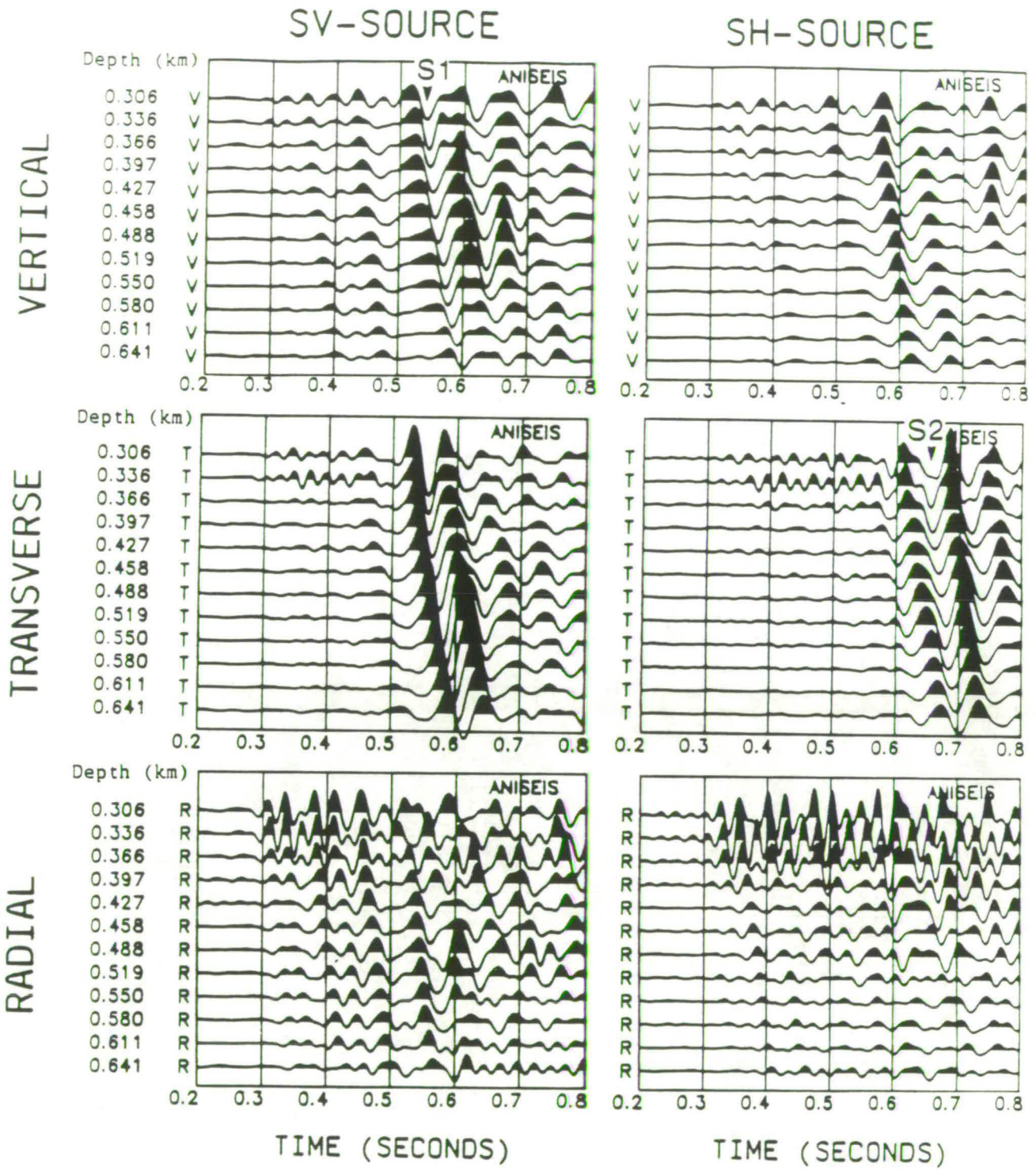

Figure 5.8. Observed seismograms from the far offset shear-wave sources. The horizontal components have been rotated to radial and transverse from *P*-wave polarizations measured from the *P*-source data. Note the relatively high frequency noise at the top few geophone levels on the horizontal components.

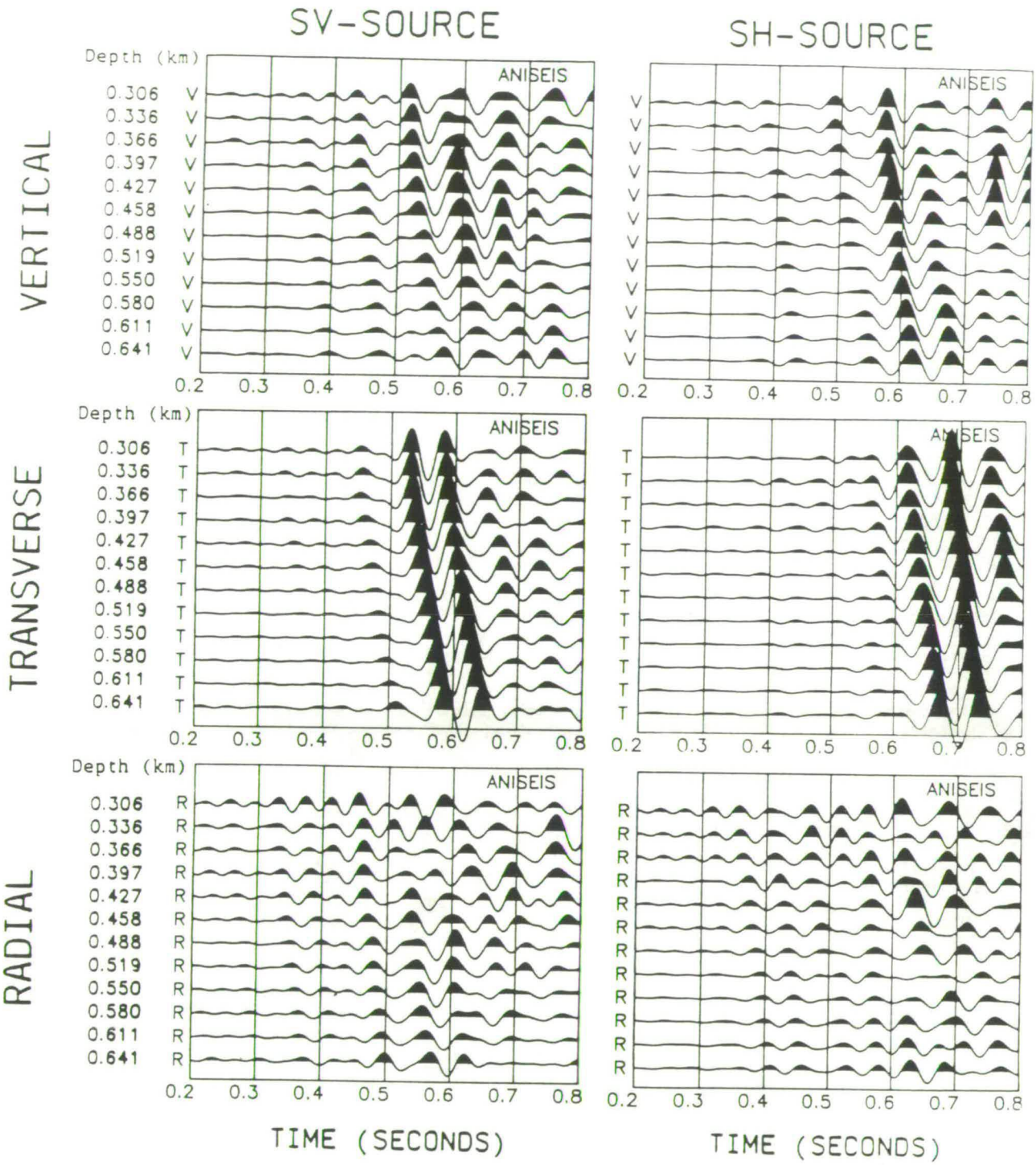

Figure 5.9. Far offset shear-wave seismograms after application of a 26Hz low pass filter to remove high frequency noise on the horizontal components. The filter has worked well, producing much cleaner shear-wave arrivals on the top geophones compared to Figure 5.8.

As with the *P*-waves, large incidence angles are indicated, this time by the lack of energy on the horizontal radial component. Application of the polarization technique to the shear-waves from the *SV*-source (Figure 5.7b) shows a decrease in incidence angles with increasing depth. The marked difference between *P*-wave and *SV*-wave incidence angles suggests the *Vp/Vs* ratio is not constant with depth.

The most obvious observation regarding anisotropy, described by Majer et al. (1988), is the large (0.1s) delay in arrival times between the *SV*- and *SH*-sources, the *SV*-source producing the earlier arriving shear-waves. It was proposed that this delay, over raypaths of less than 1000m, was caused by an exceptionally large velocity anisotropy, consistent with propagation through vertical cracks parallel to the radial direction (Majer et al., 1988) as indicated in Figure 5.3. Shearer (1988) presented a synthetic model containing such cracks producing a shear-wave velocity anisotropy of about 15% which matched the arrival times from both shear-wave sources relatively well.

However, if the anisotropic structure was caused, strictly, by parallel vertical cracks striking in the well head to source (radial) direction, there would be sagittal symmetry and no cross coupling: no *qSV*-arrival from the *SH*-source; and no *qSH*-arrival from the *SV*-source. In fact, the observed *qSH*-arrival from the *SV*-source is almost twice as large as the vertical component arrival, and both vertical component and *qSH*-arrivals from the *SH*-source display

similar amplitudes. Consequently, the structure around the well departs substantially from simple parallel vertical cracks. These relationships are most clearly displayed in polarization diagrams (PDs).

Horizontal plane (radial/transverse) and sagittal plane (vertical/radial) PDs from both shear-wave sources are shown in Figure 5.10a and 5.10b with a 100ms window following the shear-wave arrivals down the section. The beginning of the horizontal plane *SV*-source PDs in Figure 5.10a (marked by a small cross) indicates leading shear-wave polarizations between about 20° and 45° anticlockwise from radial. Due to the limited number of observations of *qSI* polarization, it is not possible to determine uniquely an anisotropic structure. In Figure 5.11, the horizontal projections of fast shear-waves in two different types of anisotropic media are shown. The boxed area show the incidences samples by the far offset VSP. In Figure 5.11a, the anisotropy is caused by parallel, vertical cracks striking 70° clockwise from radial, while in Figure 5.11b, the anisotropy is produced by parallel cracks, dipping 35° from vertical and striking in the radial direction. The boxed areas show the incidences sampled by the far offset VSP, and within these areas for both anisotropic structures, very similar *qSI* polarizations are present, corresponding approximately with those observed. The dipping cracks structure, as used by Shearer (1988) in his anisotropic model, is discussed later.

If the anisotropy is assumed to be caused only by vertical, parallel inclusions, the *SV*-source observations suggest a crack/fracture strike between North and N20°E. Earthquake focal mechanisms in the Geysers area (Majer and McEvilly, 1979; Bufe et

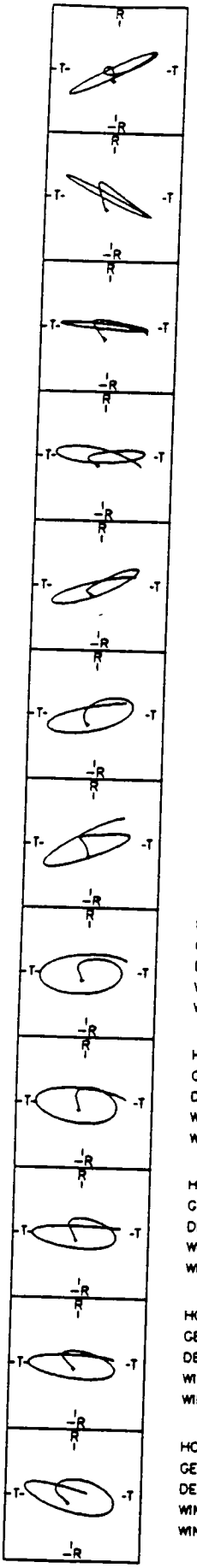

HORIZONTAL PLANE
GEOPHONE 1
DEPTH: 0.305km
WINDOW START: 0.483s
WINDOW LENGTH: 0.100s

HORIZONTAL PLANE
GEOPHONE 2
DEPTH: 0.336km
WINDOW START: 0.483s
WINDOW LENGTH: 0.100s

HORIZONTAL PLANE
GEOPHONE 3
DEPTH: 0.366km
WINDOW START: 0.490s
WINDOW LENGTH: 0.100s

HORIZONTAL PLANE
GEOPHONE 4
DEPTH: 0.396km
WINDOW START: 0.492s
WINDOW LENGTH: 0.100s

HORIZONTAL PLANE
GEOPHONE 5
DEPTH: 0.427km
WINDOW START: 0.497s
WINDOW LENGTH: 0.100s

HORIZONTAL PLANE
GEOPHONE 6
DEPTH: 0.458km
WINDOW START: 0.500s
WINDOW LENGTH: 0.100s

HORIZONTAL PLANE
GEOPHONE 7
DEPTH: 0.488km
WINDOW START: 0.507s
WINDOW LENGTH: 0.100s

HORIZONTAL PLANE
GEOPHONE 8
DEPTH: 0.518km
WINDOW START: 0.513s
WINDOW LENGTH: 0.100s

HORIZONTAL PLANE
GEOPHONE 9
DEPTH: 0.549km
WINDOW START: 0.520s
WINDOW LENGTH: 0.100s

HORIZONTAL PLANE
GEOPHONE 10
DEPTH: 0.580km
WINDOW START: 0.528s
WINDOW LENGTH: 0.100s

HORIZONTAL PLANE
GEOPHONE 11
DEPTH: 0.610km
WINDOW START: 0.535s
WINDOW LENGTH: 0.100s

HORIZONTAL PLANE
GEOPHONE 12
DEPTH: 0.641km
WINDOW START: 0.535s
WINDOW LENGTH: 0.100s

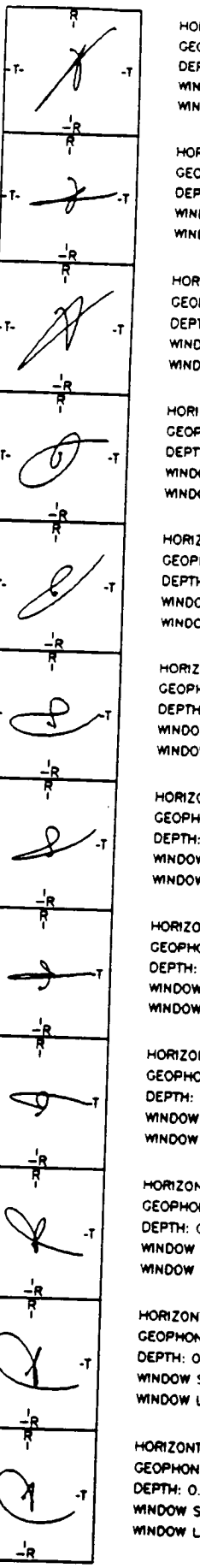

HORIZONTAL PLANE
GEOPHONE 1
DEPTH: 0.305km
WINDOW START: 0.516s
WINDOW LENGTH: 0.100s

HORIZONTAL PLANE
GEOPHONE 2
DEPTH: 0.336km
WINDOW START: 0.516s
WINDOW LENGTH: 0.100s

HORIZONTAL PLANE
GEOPHONE 3
DEPTH: 0.366km
WINDOW START: 0.516s
WINDOW LENGTH: 0.100s

HORIZONTAL PLANE
GEOPHONE 4
DEPTH: 0.396km
WINDOW START: 0.524s
WINDOW LENGTH: 0.100s

HORIZONTAL PLANE
GEOPHONE 5
DEPTH: 0.427km
WINDOW START: 0.529s
WINDOW LENGTH: 0.100s

HORIZONTAL PLANE
GEOPHONE 6
DEPTH: 0.458km
WINDOW START: 0.532s
WINDOW LENGTH: 0.100s

HORIZONTAL PLANE
GEOPHONE 7
DEPTH: 0.488km
WINDOW START: 0.541s
WINDOW LENGTH: 0.100s

HORIZONTAL PLANE
GEOPHONE 8
DEPTH: 0.518km
WINDOW START: 0.543s
WINDOW LENGTH: 0.100s

HORIZONTAL PLANE
GEOPHONE 9
DEPTH: 0.549km
WINDOW START: 0.550s
WINDOW LENGTH: 0.100s

HORIZONTAL PLANE
GEOPHONE 10
DEPTH: 0.580km
WINDOW START: 0.554s
WINDOW LENGTH: 0.100s

HORIZONTAL PLANE
GEOPHONE 11
DEPTH: 0.610km
WINDOW START: 0.558s
WINDOW LENGTH: 0.100s

HORIZONTAL PLANE
GEOPHONE 12
DEPTH: 0.641km
WINDOW START: 0.567s
WINDOW LENGTH: 0.100s

Figure 5.10a

Figure 5.10. Shear-wave PDs from the far offset *SV*- and *SH*-sources. A small cross marks the beginning of the motion. a) Horizontal plane PDs, window length 100ms; b) Sagittal plane PDs, window length 100ms; c) Normal plane PDs, window length 180ms.

SV-SOURCE

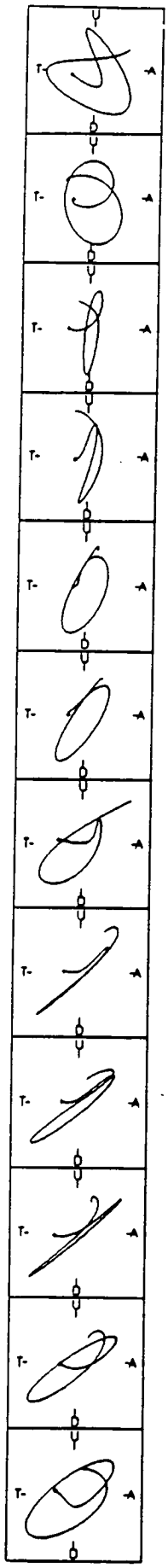

SAGITTAL PLANE
GEOPHONE 1
DEPTH: 0.305km
WINDOW START: 0.483s
WINDOW LENGTH: 0.100s

SAGITTAL PLANE
GEOPHONE 2
DEPTH: 0.336km
WINDOW START: 0.483s
WINDOW LENGTH: 0.100s

SAGITTAL PLANE
GEOPHONE 3
DEPTH: 0.366km
WINDOW START: 0.490s
WINDOW LENGTH: 0.100s

SAGITTAL PLANE
GEOPHONE 4
DEPTH: 0.396km
WINDOW START: 0.492s
WINDOW LENGTH: 0.100s

SAGITTAL PLANE
GEOPHONE 5
DEPTH: 0.427km
WINDOW START: 0.497s
WINDOW LENGTH: 0.100s

SAGITTAL PLANE
GEOPHONE 6
DEPTH: 0.458km
WINDOW START: 0.500s
WINDOW LENGTH: 0.100s

SAGITTAL PLANE
GEOPHONE 7
DEPTH: 0.488km
WINDOW START: 0.507s
WINDOW LENGTH: 0.100s

SAGITTAL PLANE
GEOPHONE 8
DEPTH: 0.518km
WINDOW START: 0.513s
WINDOW LENGTH: 0.100s

SAGITTAL PLANE
GEOPHONE 9
DEPTH: 0.549km
WINDOW START: 0.520s
WINDOW LENGTH: 0.100s

SAGITTAL PLANE
GEOPHONE 10
DEPTH: 0.580km
WINDOW START: 0.528s
WINDOW LENGTH: 0.100s

SAGITTAL PLANE
GEOPHONE 11
DEPTH: 0.610km
WINDOW START: 0.535s
WINDOW LENGTH: 0.100s

SAGITTAL PLANE
GEOPHONE 12
DEPTH: 0.641km
WINDOW START: 0.535s
WINDOW LENGTH: 0.100s

SH-SOURCE

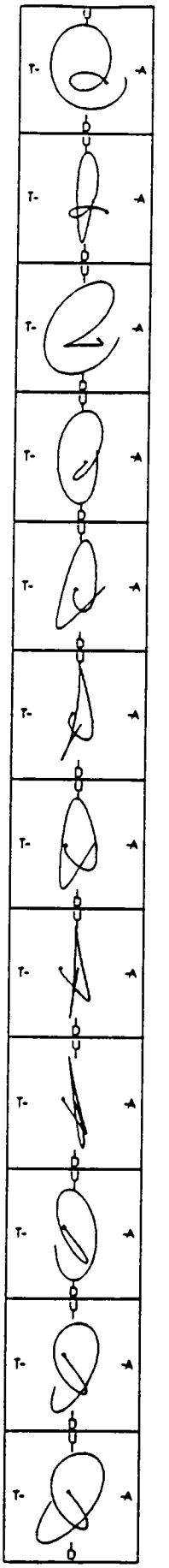

SAGITTAL PLANE
GEOPHONE 1
DEPTH: 0.305km
WINDOW START: 0.516s
WINDOW LENGTH: 0.100s

SAGITTAL PLANE
GEOPHONE 2
DEPTH: 0.336km
WINDOW START: 0.516s
WINDOW LENGTH: 0.100s

SAGITTAL PLANE
GEOPHONE 3
DEPTH: 0.366km
WINDOW START: 0.516s
WINDOW LENGTH: 0.100s

SAGITTAL PLANE
GEOPHONE 4
DEPTH: 0.396km
WINDOW START: 0.524s
WINDOW LENGTH: 0.100s

SAGITTAL PLANE
GEOPHONE 5
DEPTH: 0.427km
WINDOW START: 0.529s
WINDOW LENGTH: 0.100s

SAGITTAL PLANE
GEOPHONE 6
DEPTH: 0.458km
WINDOW START: 0.532s
WINDOW LENGTH: 0.100s

SAGITTAL PLANE
GEOPHONE 7
DEPTH: 0.488km
WINDOW START: 0.541s
WINDOW LENGTH: 0.100s

SAGITTAL PLANE
GEOPHONE 8
DEPTH: 0.518km
WINDOW START: 0.543s
WINDOW LENGTH: 0.100s

SAGITTAL PLANE
GEOPHONE 9
DEPTH: 0.549km
WINDOW START: 0.550s
WINDOW LENGTH: 0.100s

SAGITTAL PLANE
GEOPHONE 10
DEPTH: 0.580km
WINDOW START: 0.554s
WINDOW LENGTH: 0.100s

SAGITTAL PLANE
GEOPHONE 11
DEPTH: 0.610km
WINDOW START: 0.558s
WINDOW LENGTH: 0.100s

SAGITTAL PLANE
GEOPHONE 12
DEPTH: 0.641km
WINDOW START: 0.567s
WINDOW LENGTH: 0.100s

Figure 5.10b

SV-SOURCE

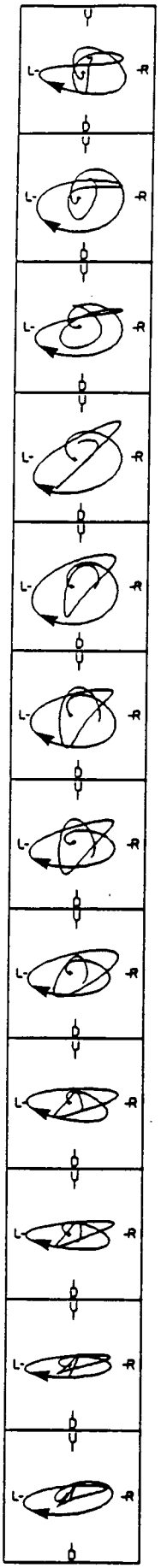

NORMAL PLANE
GEOPHONE 1
DEPTH: 0.305km
WINDOW START: 0.483s
WINDOW LENGTH: 0.180s

NORMAL PLANE
GEOPHONE 2
DEPTH: 0.336km
WINDOW START: 0.483s
WINDOW LENGTH: 0.180s

NORMAL PLANE
GEOPHONE 3
DEPTH: 0.366km
WINDOW START: 0.490s
WINDOW LENGTH: 0.180s

NORMAL PLANE
GEOPHONE 4
DEPTH: 0.396km
WINDOW START: 0.492s
WINDOW LENGTH: 0.180s

NORMAL PLANE
GEOPHONE 5
DEPTH: 0.427km
WINDOW START: 0.497s
WINDOW LENGTH: 0.180s

NORMAL PLANE
GEOPHONE 6
DEPTH: 0.458km
WINDOW START: 0.500s
WINDOW LENGTH: 0.180s

NORMAL PLANE
GEOPHONE 7
DEPTH: 0.488km
WINDOW START: 0.507s
WINDOW LENGTH: 0.180s

NORMAL PLANE
GEOPHONE 8
DEPTH: 0.518km
WINDOW START: 0.513s
WINDOW LENGTH: 0.180s

NORMAL PLANE
GEOPHONE 9
DEPTH: 0.549km
WINDOW START: 0.520s
WINDOW LENGTH: 0.180s

NORMAL PLANE
GEOPHONE 10
DEPTH: 0.580km
WINDOW START: 0.528s
WINDOW LENGTH: 0.180s

NORMAL PLANE
GEOPHONE 11
DEPTH: 0.610km
WINDOW START: 0.535s
WINDOW LENGTH: 0.180s

NORMAL PLANE
GEOPHONE 12
DEPTH: 0.641km
WINDOW START: 0.535s
WINDOW LENGTH: 0.180s

SH-SOURCE

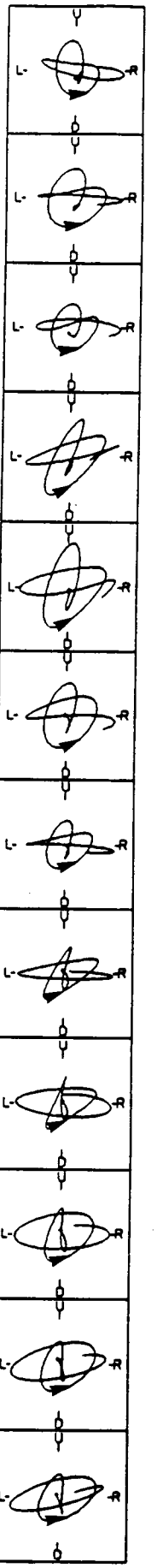

NORMAL PLANE
GEOPHONE 1
DEPTH: 0.305km
WINDOW START: 0.516s
WINDOW LENGTH: 0.180s

NORMAL PLANE
GEOPHONE 2
DEPTH: 0.336km
WINDOW START: 0.516s
WINDOW LENGTH: 0.180s

NORMAL PLANE
GEOPHONE 3
DEPTH: 0.366km
WINDOW START: 0.516s
WINDOW LENGTH: 0.180s

NORMAL PLANE
GEOPHONE 4
DEPTH: 0.396km
WINDOW START: 0.524s
WINDOW LENGTH: 0.180s

NORMAL PLANE
GEOPHONE 5
DEPTH: 0.427km
WINDOW START: 0.529s
WINDOW LENGTH: 0.180s

NORMAL PLANE
GEOPHONE 6
DEPTH: 0.458km
WINDOW START: 0.532s
WINDOW LENGTH: 0.180s

NORMAL PLANE
GEOPHONE 7
DEPTH: 0.488km
WINDOW START: 0.541s
WINDOW LENGTH: 0.180s

NORMAL PLANE
GEOPHONE 8
DEPTH: 0.518km
WINDOW START: 0.543s
WINDOW LENGTH: 0.180s

NORMAL PLANE
GEOPHONE 9
DEPTH: 0.549km
WINDOW START: 0.550s
WINDOW LENGTH: 0.180s

NORMAL PLANE
GEOPHONE 10
DEPTH: 0.580km
WINDOW START: 0.554s
WINDOW LENGTH: 0.180s

NORMAL PLANE
GEOPHONE 11
DEPTH: 0.610km
WINDOW START: 0.558s
WINDOW LENGTH: 0.180s

NORMAL PLANE
GEOPHONE 12
DEPTH: 0.641km
WINDOW START: 0.567s
WINDOW LENGTH: 0.180s

Figure 5.10c

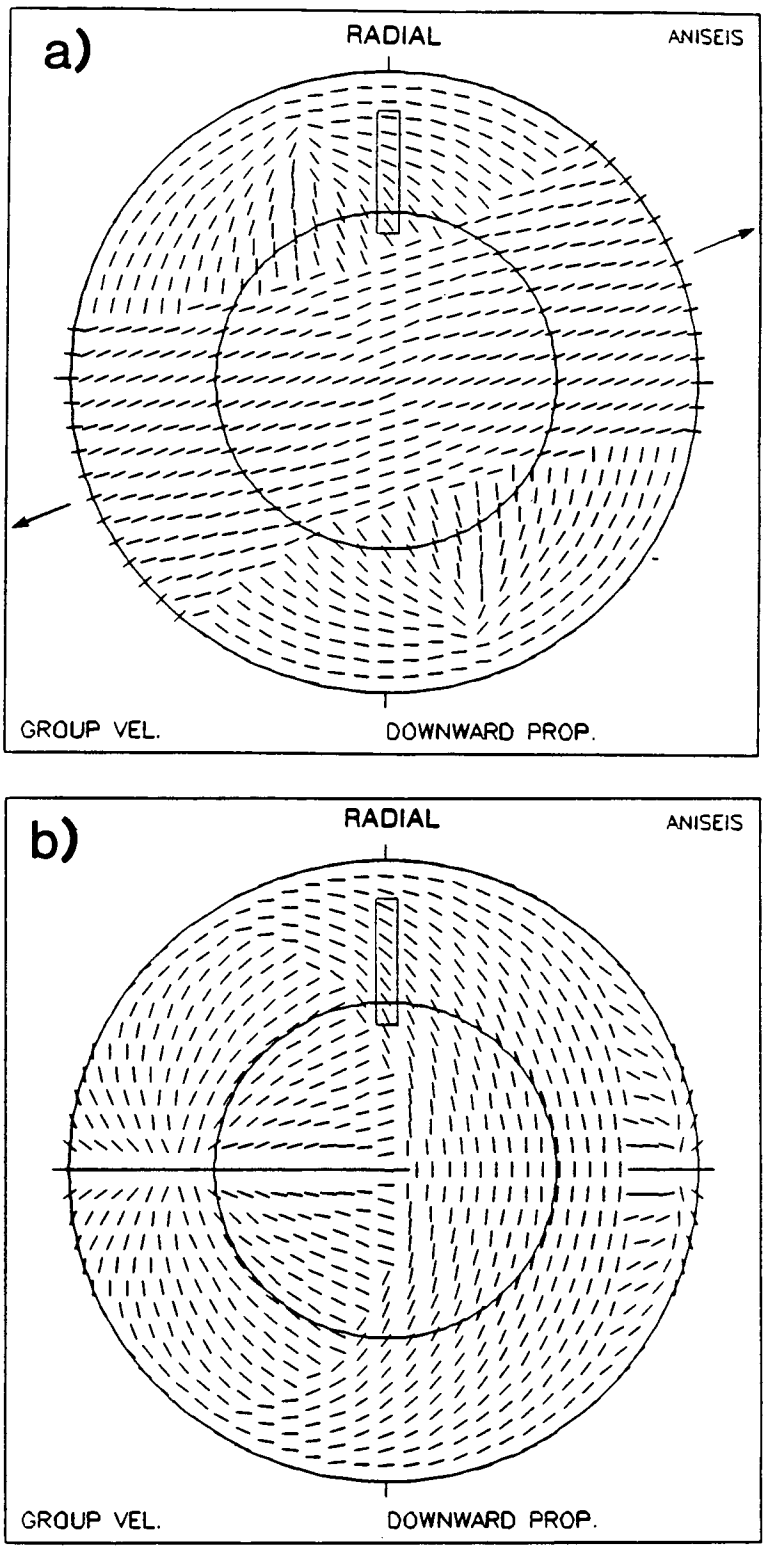

Figure 5.11. Equal area plots of fast shear-wave polarizations in homogeneous media containing anisotropy. The inner circle marks incidence angles of 45°. The boxed areas mark the incidences with which the *SV*-source shear-waves arrive at the twelve geophone locations from the far offset source location. **a)** Thin, parallel, vertical cracks striking 70° clockwise from the radial direction. **b)** Thin, parallel cracks, dipping 35° from vertical and striking in the radial direction.

al., 1981) and observations of borehole elongation (Zoback et al., 1987) give a maximum horizontal stress direction between north and N40°E, similar to this estimated crack/fracture strike which suggests that the velocity anisotropy is controlled by stress conditions. Such a crack orientation will not reproduce the large time delay between shear-wave source types.

However, since stress conditions can vary significantly near the free surface, stress controlled cracks/fractures need not necessarily be vertical. Shearer (1988) presented a second model containing cracks inclined at 35° from vertical with over 20% shear-wave anisotropy. This model reproduced the correct time delay between shear-wave source types and contained some cross-component energy, but not as much as was observed. Although polarization diagrams were not presented, Shearer admits that his model does not produce a good match with observations.

The horizontal plane *SH*-source PDs in Figure 5.10a indicate that the leading shear-wave motion is consistently in the radial direction. Furthermore, if the sagittal plane PDs from this source are studied in Figure 5.10b, the initial particle motion is polarized parallel to the direction of the ray making it *P*-wave motion rather than shear-wave (hence the reason that no incidence angle estimates are given for shear-wave from the *SH*-source). This observation rather complicates any interpretation of shear-wave polarizations from the *SH*-source. It is also very difficult to come up with an explanation why shear-waves from the *SV*-source are not similarly contaminated with *P*-wave energy.

In Figure 5.10c, the normal plane shear-wave PDs from both shear-wave source types are given using a window length of 180ms. Compared to the other two projections, these show by far the most consistent motion throughout all the geophone locations, even with the increased window length. The initial *P*-wave energy from the *SH*-source can be seen clearly as an initial vertical polarization on all twelve geophones. Although the *SV*-source PDs are not contaminated with *P*-waves, normal plane shear-wave PDs are impossible to interpret in terms of a horizontal fracture/crack strike direction unless sufficient observations can be made at a range of azimuths (Liu et al., 1989). Even if it were possible to interpret the normal plane PDs, the initialcurnear polarization present on the horizontal plane PDs is not present in the normal plane.

The remarkable consistency in the shape of the PDs from both source types suggests that if velocity anisotropy is the cause of the observed shear-wave motions, the rays from source to all receivers must see a similar anisotropic structure. If the anisotropy were spread evenly throughout the depth range of the VSP, it would be expected that the shear-wave PDs would show significant changes in shape with increasing depth. It might also be expected that the time delay between the two source types would become larger as well. Thus, if anisotropy is present, most of its effects on the shear-waves must have occurred above the top geophone, such that shear-waves to deeper geophones undergo only slight changes.

5.3 Near offset observations

Unlike the far offset geophones, the near offset geophones were within the steam reservoir region, the water/steam interface being at 1.2km. Note that because of increasing temperature with increasing depth, the steam lies below the water.

Three-component seismograms from the *P*-wave source are given in Figure 5.12. Rotation of the horizontal components was carried out using *P*-wave polarizations, as with the far offset horizontal components. A problem here, though, is that the deviation of the well was greater than the incidence angles of the *P*-waves at some depths. This makes rotation of the horizontal components to radial and transverse unreliable. The large amount of noise seen at some levels on the horizontal components also makes rotations unreliable. It is somewhat surprising that noise on the horizontal components has such large amplitudes, and may be attributed to poor coupling of the horizontal geophones to the borehole wall.

Horizontal plane PDs for the first 20ms of the *P*-wave motion are given in Figure 5.13. These indicate relatively linear motion for most levels, but linearly polarized noise can be mistaken for *P*-wave energy if the PDs are considered alone. For example, the bottom geophone shows fairly linear motion, but the horizontal seismograms prove this motion to be noise. At all similar levels, the rotations estimated from *P*-wave polarizations may be wildly inaccurate and the effects of well deviation make matters worse.

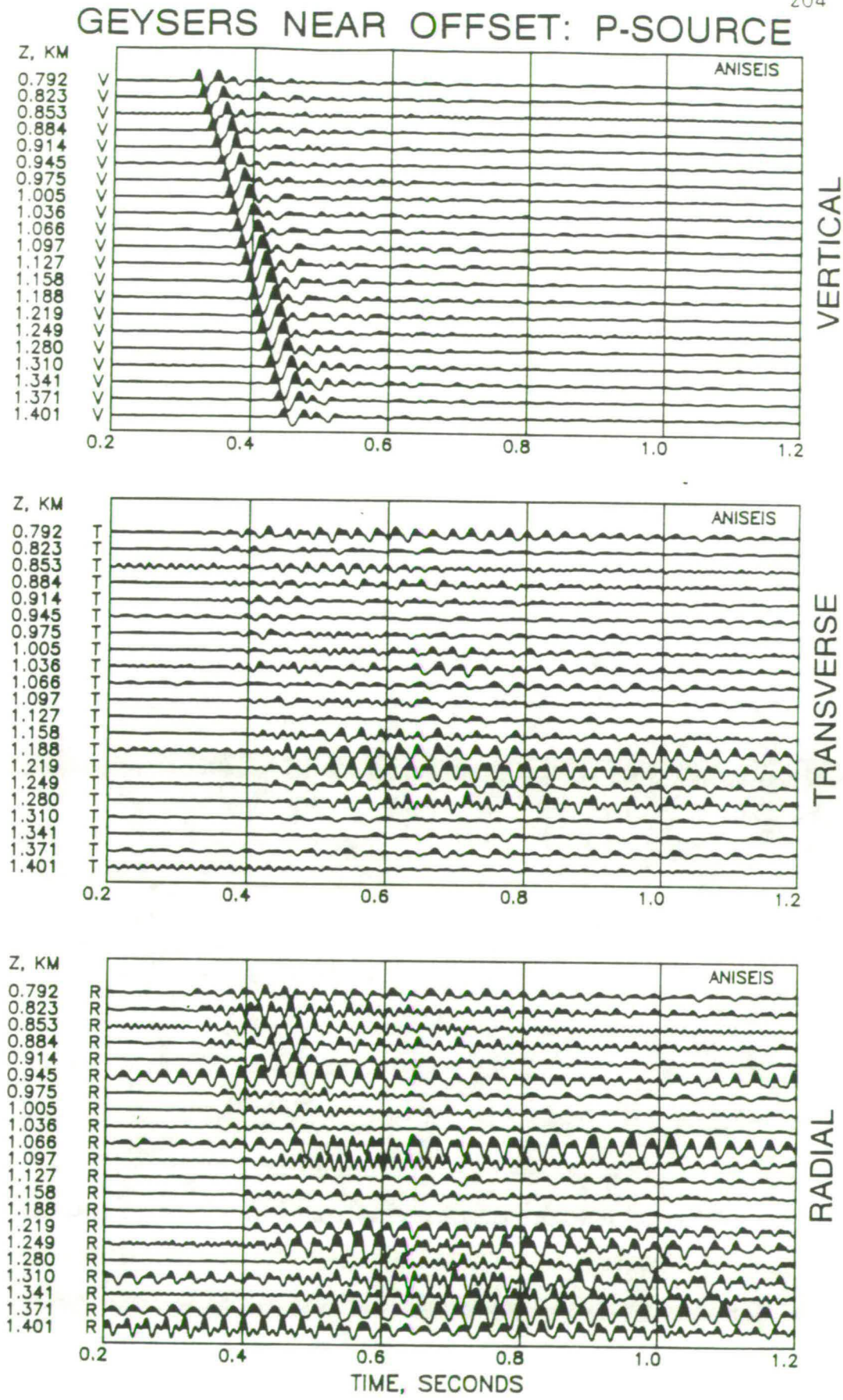

Figure 5.12. Observed seismograms from the near offset *P*-wave source. The horizontal components have been rotated to radial and transverse directions from incoming *P*-wave polarizations, but due to the large incidence angles and high amplitude noise on the horizontal components, many of the rotations are not reliable.

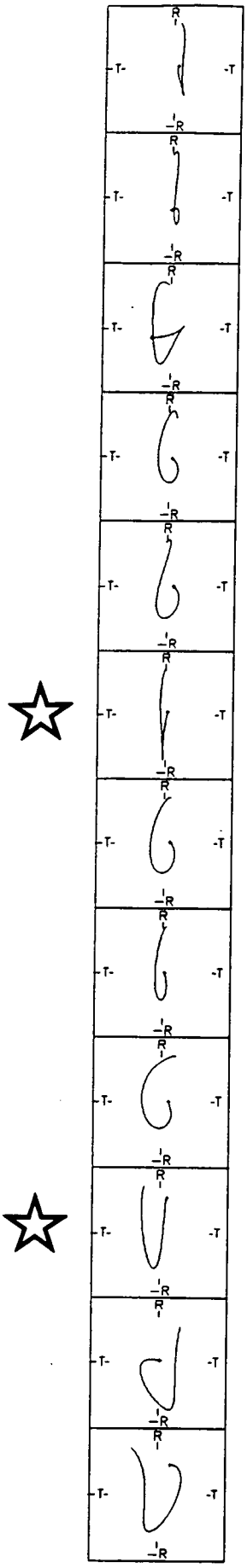

HORIZONTAL PLANE
GEOPHONE 1
DEPTH: 0.792km
WINDOW START: 0.309s
WINDOW LENGTH: 0.020s

HORIZONTAL PLANE
GEOPHONE 2
DEPTH: 0.823km
WINDOW START: 0.319s
WINDOW LENGTH: 0.020s

HORIZONTAL PLANE
GEOPHONE 3
DEPTH: 0.853km
WINDOW START: 0.324s
WINDOW LENGTH: 0.020s

HORIZONTAL PLANE
GEOPHONE 4
DEPTH: 0.884km
WINDOW START: 0.332s
WINDOW LENGTH: 0.020s

HORIZONTAL PLANE
GEOPHONE 5
DEPTH: 0.914km
WINDOW START: 0.338s
WINDOW LENGTH: 0.020s

HORIZONTAL PLANE
GEOPHONE 6
DEPTH: 0.945km
WINDOW START: 0.344s
WINDOW LENGTH: 0.020s

HORIZONTAL PLANE
GEOPHONE 7
DEPTH: 0.975km
WINDOW START: 0.351s
WINDOW LENGTH: 0.020s

HORIZONTAL PLANE
GEOPHONE 8
DEPTH: 1.005km
WINDOW START: 0.357s
WINDOW LENGTH: 0.020s

HORIZONTAL PLANE
GEOPHONE 9
DEPTH: 1.036km
WINDOW START: 0.363s
WINDOW LENGTH: 0.020s

HORIZONTAL PLANE
GEOPHONE 10
DEPTH: 1.066km
WINDOW START: 0.368s
WINDOW LENGTH: 0.020s

HORIZONTAL PLANE
GEOPHONE 11
DEPTH: 1.097km
WINDOW START: 0.377s
WINDOW LENGTH: 0.020s

HORIZONTAL PLANE
GEOPHONE 12
DEPTH: 1.127km
WINDOW START: 0.382s
WINDOW LENGTH: 0.020s

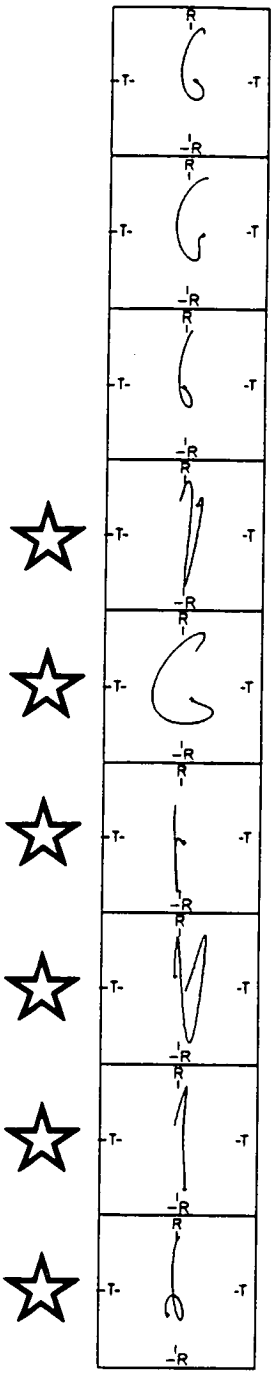

HORIZONTAL PLANE
GEOPHONE 13
DEPTH: 1.158km
WINDOW START: 0.388s
WINDOW LENGTH: 0.020s

HORIZONTAL PLANE
GEOPHONE 14
DEPTH: 1.188km
WINDOW START: 0.393s
WINDOW LENGTH: 0.020s

HORIZONTAL PLANE
GEOPHONE 15
DEPTH: 1.219km
WINDOW START: 0.400s
WINDOW LENGTH: 0.020s

HORIZONTAL PLANE
GEOPHONE 16
DEPTH: 1.249km
WINDOW START: 0.408s
WINDOW LENGTH: 0.020s

HORIZONTAL PLANE
GEOPHONE 17
DEPTH: 1.280km
WINDOW START: 0.412s
WINDOW LENGTH: 0.020s

HORIZONTAL PLANE
GEOPHONE 18
DEPTH: 1.310km
WINDOW START: 0.417s
WINDOW LENGTH: 0.020s

HORIZONTAL PLANE
GEOPHONE 19
DEPTH: 1.341km
WINDOW START: 0.425s
WINDOW LENGTH: 0.020s

HORIZONTAL PLANE
GEOPHONE 20
DEPTH: 1.371km
WINDOW START: 0.432s
WINDOW LENGTH: 0.020s

HORIZONTAL PLANE
GEOPHONE 21
DEPTH: 1.401km
WINDOW START: 0.438s
WINDOW LENGTH: 0.020s

Figure 5.13. Horizontal plane PDs from the near offset *P*-wave source, using a window length of 20ms. At most levels the motion is quite linear, but this does not necessarily mean that the horizontal components have been properly rotated. Reference must be made to the seismograms to estimate how much noise is present at a particular geophone level. Stars to the left of certain PDs indicate where rotations are not reliable.

This difficulty in the rotation process emphasises the need to have good knowledge of geophone orientations downwell if any form of polarization analysis is required. A gyro attached to the downhole tool would have overcome any shortcomings encountered with *P*-wave polarizations.

Figure 5.14 shows the *SH*-source seismograms, rotated to radial and transverse from the *P*-wave data. Other than correlation in the field and stacking multiple sweeps to the same geophone position, no processing has been applied to these data. The vertical component contains low amplitude *P*-wave arrivals, which may be a result of some vertical motion from the shear-wave vibrator. Considering that shear-wave sources generally cannot input as much energy into the ground as *P*-wave sources, it is surprising that the amplitude of the noise on the horizontal components in Figure 5.14 is much smaller compared to the *P*-wave records. However, the noise on the *P*-wave records is of much higher frequency than the signal on the shear-wave records such that any similar noise on the shear-wave records may have been removed by filtering in the field.

The particularly long duration of the shear-wave arrivals on the radial component makes it difficult to decide which peak or trough to choose as the arrival time, although a central trough is present, about which the signal is symmetrical. The peak frequency of the signal is about 10Hz, with a very narrow bandwidth. Since the sweep frequencies were from 10Hz to 55Hz, this peak frequency is unexpected, possibly caused by a very large amount of attenuation being present or poor coupling between the vibrator baseplate and ground. If attenuation is responsible for the low frequency nature of

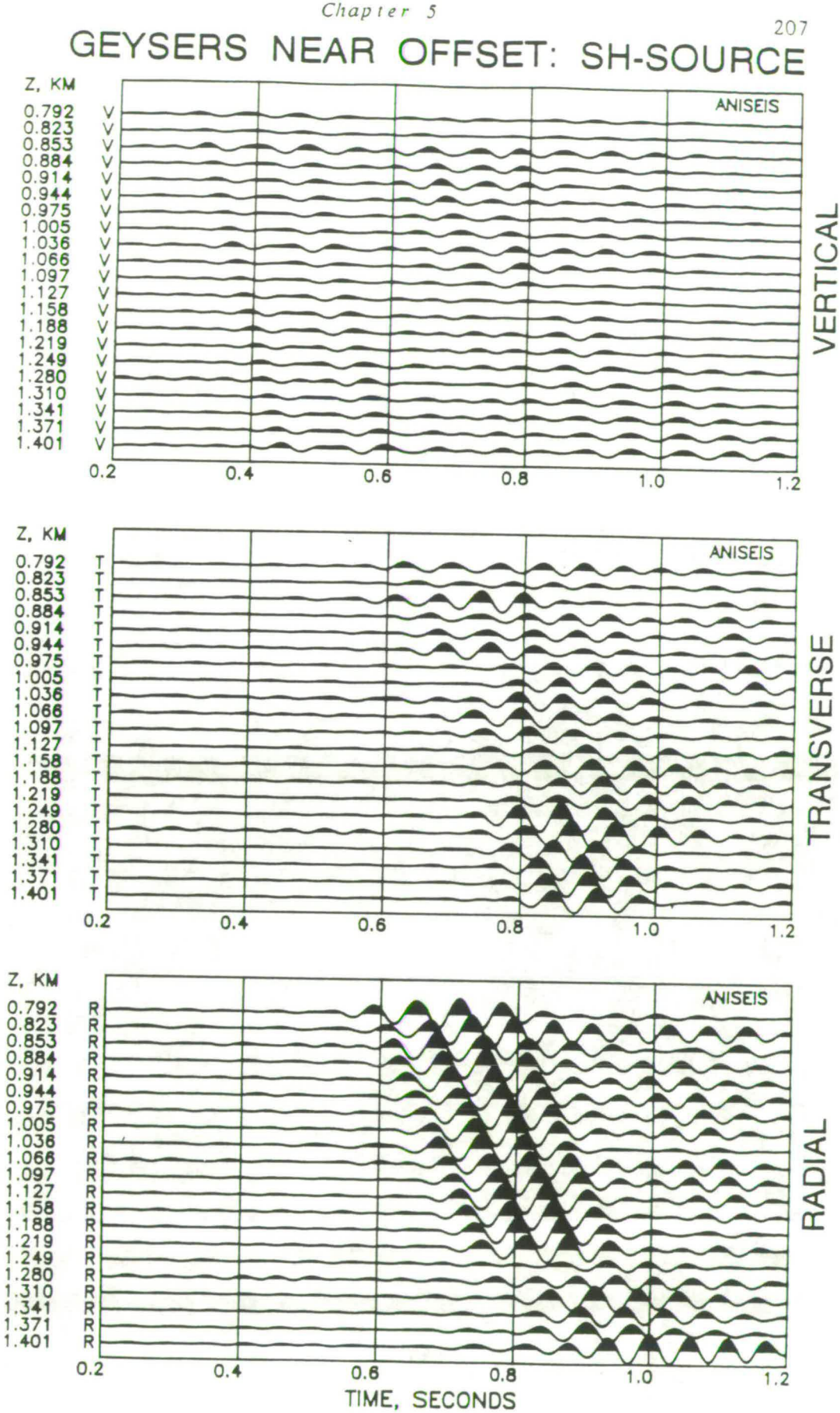

Figure 5.14. Observed seismograms from the near offset *SH*-source. The horizontal components have been rotated to radial and transverse directions using *P*-wave polarizations estimated from the *P*-wave source. Consistent arrivals can be seen on the radial component down to 1.219km, while the transverse component shows less coherency. Considering that the source is supposed to be polarized in the transverse direction, this is a surprising result.

the shear-wave arrival, then most of the attenuation must be above the top geophone position used with the far offset VSP (i.e. above 300m) because the far offset VSP seismograms show similar low frequency arrivals.

Certainly the most surprising observation from the near offset shear-wave data is that most of the shear-wave energy is in the radial direction, orthogonal to the shear-wave vibrator polarization. This can be seen most clearly on the PDs in Figure 5.15a showing the first 100ms of the shear-wave arrivals. Unreliably rotated levels are marked with an asterisk to the left of the box containing the plotted motion. A lot of the PDs are remarkably linear over the first 100ms, including those that have not been rotated correctly. If the time window is extended to 220ms (Figure 5.15b), including the whole shear-wave arrival, the PDs become elliptical with no consistent change throughout the depth range of the geophones. This confirms what was seen at the far offset VSP, that there is little or no observable anisotropy below 300m. It is difficult to believe that the 100ms of linear motion at the begining of the shear-wave arrivals is the polarization of the leading split shear-wave, mainly because if it were, the last 100ms of motion would correspond to the slow shear-wave, with an orthogonal polarization, of which there is no sign. Hence, it must be concluded that the near offset VSP does not exhibit classic shear-wave splitting patterns and that an explanation for the observations will include a complex form of anisotropy and/or some complex structural effects. Furthermore, the near offset observations do not support the estimated crack/fracture strike from the far offset *SV*-source.

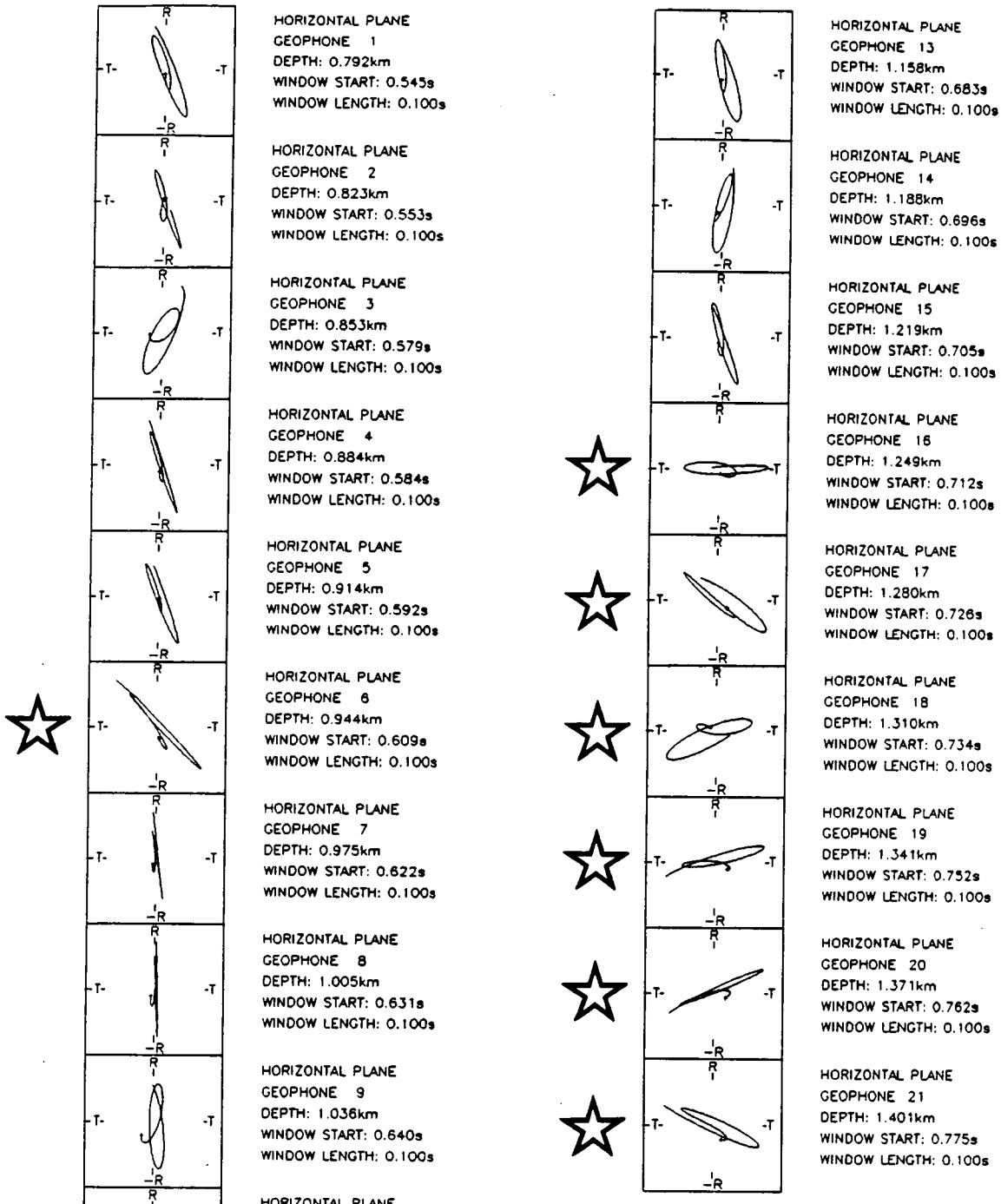

Figure 5.15a

Figure 5.15. Horizontal plane shear-wave PDs from the near offset *SH*-source. A star to the left of a PD indicates that the rotation of horizontal components to radial and transverse should not be trusted. a) Window length of 100ms indicating that this part of the shear-wave motion is linear in the radial direction; b) Window length of 220ms, showing the full shear-wave motion.

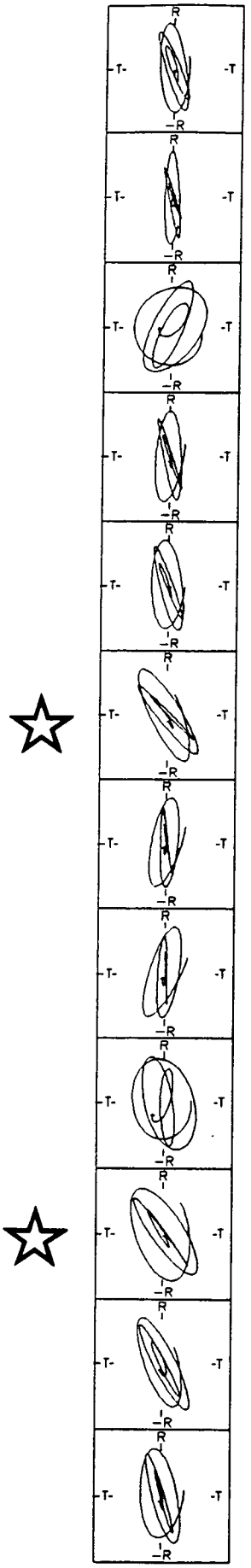

HORIZONTAL PLANE
GEOPHONE 1
DEPTH: 0.792km
WINDOW START: 0.545s
WINDOW LENGTH: 0.220s

HORIZONTAL PLANE
GEOPHONE 2
DEPTH: 0.823km
WINDOW START: 0.553s
WINDOW LENGTH: 0.220s

HORIZONTAL PLANE
GEOPHONE 3
DEPTH: 0.853km
WINDOW START: 0.579s
WINDOW LENGTH: 0.220s

HORIZONTAL PLANE
GEOPHONE 4
DEPTH: 0.884km
WINDOW START: 0.584s
WINDOW LENGTH: 0.220s

HORIZONTAL PLANE
GEOPHONE 5
DEPTH: 0.914km
WINDOW START: 0.592s
WINDOW LENGTH: 0.220s

HORIZONTAL PLANE
GEOPHONE 6
DEPTH: 0.944km
WINDOW START: 0.609s
WINDOW LENGTH: 0.220s

HORIZONTAL PLANE
GEOPHONE 7
DEPTH: 0.975km
WINDOW START: 0.622s
WINDOW LENGTH: 0.220s

HORIZONTAL PLANE
GEOPHONE 8
DEPTH: 1.005km
WINDOW START: 0.631s
WINDOW LENGTH: 0.220s

HORIZONTAL PLANE
GEOPHONE 9
DEPTH: 1.036km
WINDOW START: 0.640s
WINDOW LENGTH: 0.220s

HORIZONTAL PLANE
GEOPHONE 10
DEPTH: 1.066km
WINDOW START: 0.653s
WINDOW LENGTH: 0.220s

HORIZONTAL PLANE
GEOPHONE 11
DEPTH: 1.097km
WINDOW START: 0.666s
WINDOW LENGTH: 0.220s

HORIZONTAL PLANE
GEOPHONE 12
DEPTH: 1.127km
WINDOW START: 0.674s
WINDOW LENGTH: 0.220s

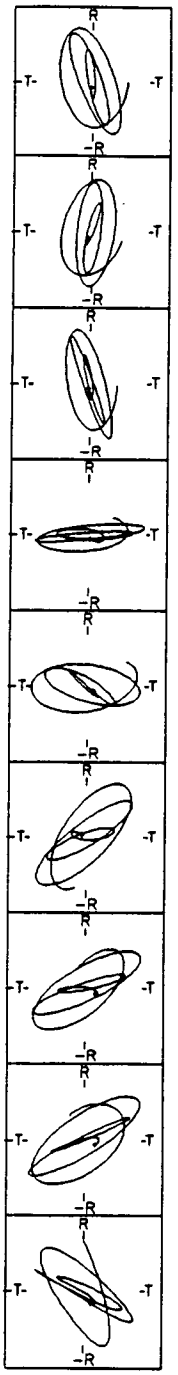

HORIZONTAL PLANE
GEOPHONE 13
DEPTH: 1.158km
WINDOW START: 0.683s
WINDOW LENGTH: 0.220s

HORIZONTAL PLANE
GEOPHONE 14
DEPTH: 1.188km
WINDOW START: 0.696s
WINDOW LENGTH: 0.220s

HORIZONTAL PLANE
GEOPHONE 15
DEPTH: 1.219km
WINDOW START: 0.705s
WINDOW LENGTH: 0.220s

HORIZONTAL PLANE
GEOPHONE 16
DEPTH: 1.249km
WINDOW START: 0.712s
WINDOW LENGTH: 0.220s

HORIZONTAL PLANE
GEOPHONE 17
DEPTH: 1.280km
WINDOW START: 0.726s
WINDOW LENGTH: 0.220s

HORIZONTAL PLANE
GEOPHONE 18
DEPTH: 1.310km
WINDOW START: 0.734s
WINDOW LENGTH: 0.220s

HORIZONTAL PLANE
GEOPHONE 19
DEPTH: 1.341km
WINDOW START: 0.752s
WINDOW LENGTH: 0.220s

HORIZONTAL PLANE
GEOPHONE 20
DEPTH: 1.371km
WINDOW START: 0.762s
WINDOW LENGTH: 0.220s

HORIZONTAL PLANE
GEOPHONE 21
DEPTH: 1.401km
WINDOW START: 0.775s
WINDOW LENGTH: 0.220s

Figure 5.15b

5.4 Anisotropic modelling

The ANISEIS full waveform reflectivity method was used to calculate synthetic seismograms and PDs (Crampin, 1987b). The aim of modelling is to match synthetic seismograms and PDs with those observed. In order to obtain the best match between synthetics and observations, the correct velocity structure and anisotropic structure must be specified in the model along with the correct source characteristics. Estimating the velocity and anisotropic structures is not straightforward, especially when the observed data do not provide clearly defined interpretations. Generally what is done in this situation is to take a velocity structure that correctly matches shear-wave arrival times and then try a number of anisotropic structures until the best model is found. However, with any wide offset VSP the velocity structure plays a very important role in defining how the anisotropic structure affects shear-waves.

Estimating the velocity structure

No *a priori* information was available about the velocity structure at the Geysers, not even to confirm whether plane, horizontal layers could be used with any reliability. A well log providing information about the lithology was available, but this provided very few clues to the velocity structure. Hence, arrival time information available from the seismograms was the only way in which velocities could be calculated, and these gave no ideas about velocity above the top geophone. Because of the lack of information, two basic assumptions were made about the velocity structure above the top geophone:

1. The structure could be defined by plane, horizontal layers;
2. Velocity never decreased as depth increased.

A layer stripping algorithm was used, combined with an isotropic point to point ray tracing program, to estimate interval velocities around each geophone. Shear-wave arrival times were measured from the vertical component *SV*-source seismograms, taking the first trough as the time of arrival and *P*-wave arrival times were taken from the radial component from the *P*-source. With the two assumptions stated above, there are two possible extremes for the velocity structure above the top geophone. Isotropic raypaths for these are given in Figure 5.16 and the actual velocities used are shown in Table 5.1. The first structure, in Figure 5.16a and Table 5.1a, represents a velocity gradient throughout the whole depth range of the VSP. A similar type of structure was used by Shearer (1988) in his modelling.

Layer no.	Layer thickness (km)	*Vp* (km/s)	*Vs* (km/s)	*Vp*/*Vs*
1	0.04	1.28	0.75	1.71
2	0.04	1.45	0.85	1.71
3	0.04	1.62	0.95	1.71
4	0.04	1.79	1.05	1.70
5	0.04	1.96	1.15	1.70
6	0.04	2.13	1.25	1.70
7	0.04	2.30	1.35	1.70
8	0.04	2.70	1.50	1.80
9	0.04	2.74	1.57	1.75
10	0.04	2.82	1.61	1.75
11	0.04	2.86	1.69	1.69
12	0.04	2.95	1.75	1.69
13	0.04	3.09	1.81	1.71
14	0.04	3.13	1.86	1.68
15	0.04	3.24	2.04	1.59
16	Halfspace	3.35	2.17	1.54

Table 5.1a

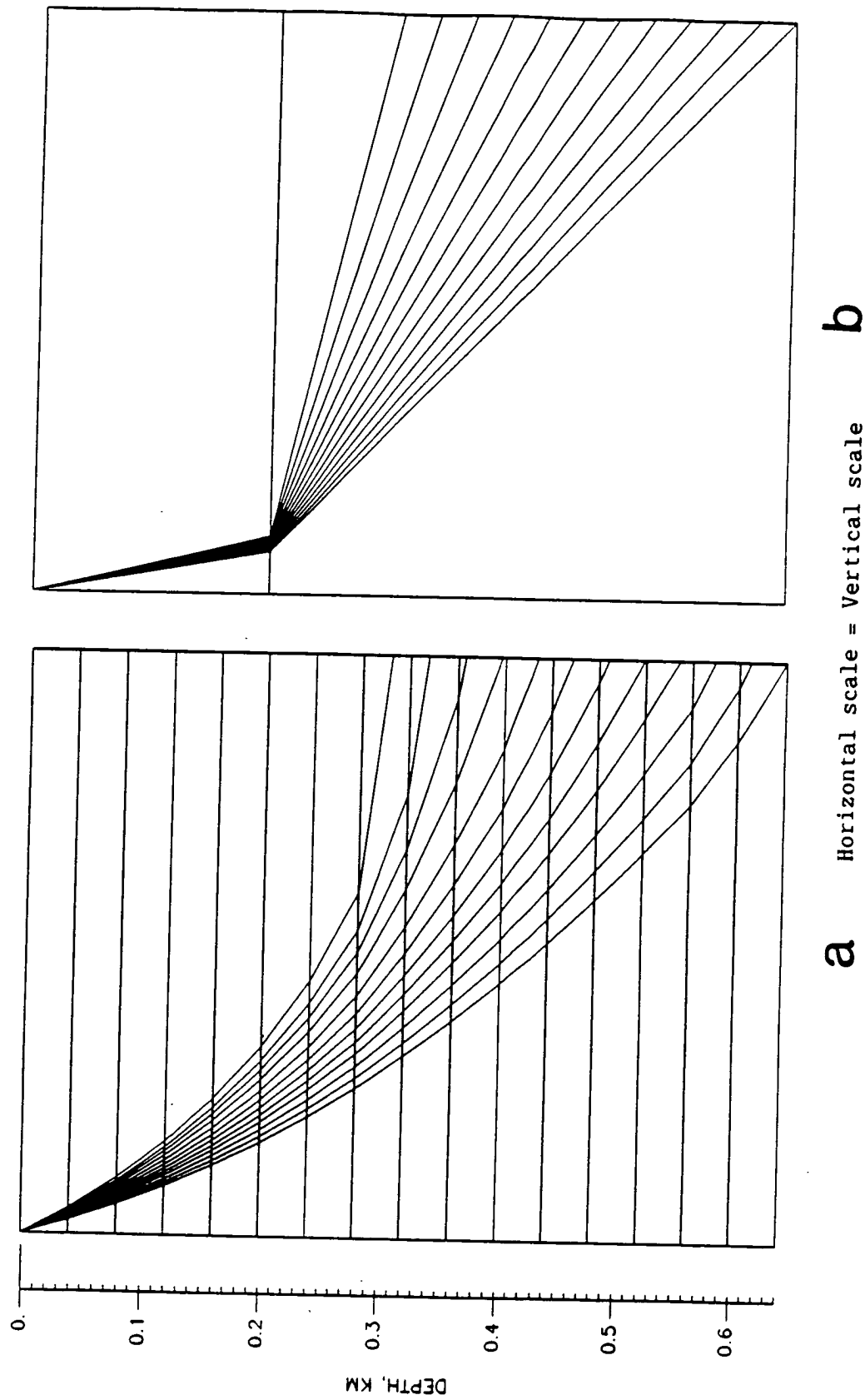

Figure 5.16. Possible shear-wave ray paths for two extreme velocity structures, the parameters of which are given in Table 5.1.
a) Velocity gradient throughout depth range of VSP showing different ray paths to all geophones; **b)** Large velocity contrast at 200m depth, producing common ray paths to all geophones in the top layer.

Layer no.	Layer thickness (km)	Vp (km/s)	Vs (km/s)	Vp/Vs
1	0.2	1.1	0.6	1.83
2	Halfspace	3.75	2.34	1.60

Table 5.1b

The second model, in Figure 5.16b and Table 5.1b, is much simpler in terms of structure, but it contains an enormous velocity contrast at 200m depth, of which there is no sign in the lithology log (it might be expected that such a large velocity change would correspond to a significant change in lithology). The top *P*-wave velocity of 1.1km/s is also very low considering that this layer extends to 200m depth and would suggest a relatively unconsolidated rock with a lower shear-wave velocity than that given in Table 5.1. The Vp/Vs ratio for this upper layer should therefore be much larger, and correspond more closely with values obtained by other workers (e.g. Hamilton, 1979). Overall, this second model is less appealing than the first from a geological point of view.

Estimating the crack geometry

The raypaths in Figure 5.16 give isotropic shear-wave structures which provide an appropriate set of matrix rocks in which to insert cracks. Visually estimating the effects of cracks along the raypaths in both velocity structures is difficult because the large velocity differences between the top and bottom of the models produce raypaths which combine nearly-vertical sections near the source to nearly horizontal sections near the geophones. The behaviour of split shear-waves in cracked structures has been investigated for nearly

vertical raypaths (Crampin, 1985) and for nearly horizontal raypaths (Liu et al., 1989). Paths which combine nearly-vertical and nearly-horizontal sections are difficult to categorize and have not been investigated previously.

Since raypaths to all the geophones in Figure 5.16a are all different, the effects of anisotropy on shear-waves in this velocity structure will be slightly different at each geophone, producing PDs with different shapes. Hence, this velocity structure is unlikely to be able to reproduce the observed shear-wave PDs, which show very little change between the top and bottom geophones. Despite this, numerous models were attempted using this velocity structure, containing many different anisotropic structures, all of which displayed significant changes in the shear-wave PDs over the depth range covered by the geophones.

The second velocity structure offers more hope in terms of obtaining similar PDs at all the geophones. Here, rays to all geophones follow almost identical paths in the top, low velocity, layer. Numerous anisotropic structures were tried with this velocity structure, with the best match between modelled and observed PDs being achieved using thin, parallel, water filled, vertical cracks that rotate from the radial direction at the surface to 36° clockwise from radial (although it could be anticlockwise due to the ambiguity of the polarity of the transverse component) at the bottom of the top layer. This was done by splitting the top layer into 10 separate layers, 20m thick, and adding Hudson cracks to each, giving up to 35% shear-wave anisotropy, decreasing slightly with depth. Similar results can be achieved by rotating the cracks up to 60° from radial, but it was decided to choose the smallest possible rotation to gain

the desired model output. It is assumed that the anisotropy is caused by the presence of cracks/fractures alone, without any complications such as thin layer anisotropy. Table 5.2 specifies the crack parameters and the orientations of the cracks in each layer. The lower halfspace of the model was isotropic.

With a model like this, the *SV*-source excites the fast shear-wave at the surface, which is then rotated as the cracks rotate with increasing depth. The large velocity contrast at 200m depth introduces effects similar to shear-wave splitting (Liu and Crampin, 1990), making the particle motion elliptical. Similarly, the *SH*-source excites the slow shear-wave, which is rotated by the rotating cracks and split by the large velocity contrast. The separate stimulation of the fast and slow shear-waves by the two source types ensures that a time delay will exist between the shear-wave sources.

Orientations of cracks/fractures near the earth's surface are likely to be controlled by surface topography and local stresses in a very complex manner. Rocks already containing fractures created at depth, such as in granite, may be superimposed with a set of inclusions aligned by local stress conditions which are not obvious to the naked eye. This argument may be used to justify the physically unattractive prospect of having vertical cracks, rotating with increasing depth.

A zero phase source pulse was used in the modelling process to represent the source signature. Since the relative phase between the pilot signal and the baseplate velocity of the vibrator was not known, this choice of source signature may not be correct. The SEG

standard has the pilot signal leading the baseplate velocity by 90° so that correlation with geophone records would ideally give a 90° phase pulse. It is not known whether this convention was followed but in hindsight it would have been better to use a 90° phase pulse for the source. The frequency was chosen to match that on the observed seismograms. The calculated, synthetic seismograms and shear-wave PDs from both source polarizations are shown in Figures 5.17 and 5.18 respectively and should be compared with the observed seismograms and PDs in Figures 5.9 and 5.10c.

Model 2 layer no.*	Thickness (km)	*CD*	Crack strike (° from radial)
1	0.02	0.3	0
1	0.02	0.3	4
1	0.02	0.3	8
1	0.02	0.3	12
1	0.02	0.2	16
1	0.02	0.2	20
1	0.02	0.2	24
1	0.02	0.2	28
1	0.02	0.2	32
1	0.02	0.2	36
2	Halfspace	Isotropic	

*These layer numbers correspond to those in Table 5.1b

Table 5.2

Modelled SV-source

Arrival times and amplitudes on the modelled *SV*-source seismograms agree reasonably well with those observed. The main differences are on the vertical component, where an extra, earlier arriving shear-wave can be seen in the model. This results from mode conversion of *P*-waves, direct from the source, to shear-waves at the large velocity contrast at 200m depth. The model also does not reproduce the double shear-wave arrival seen on the observed vertical

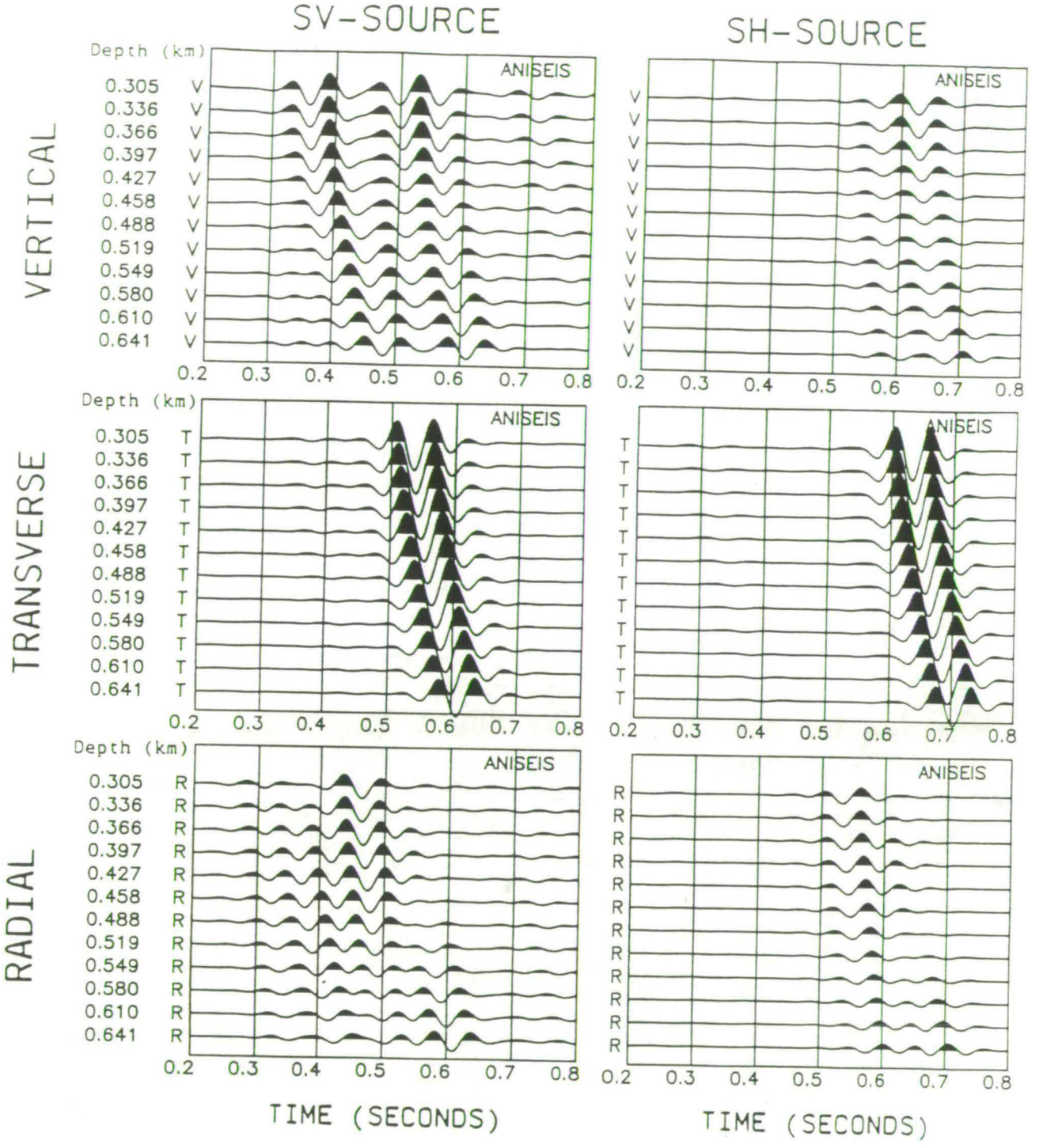

Figure 5.17. Synthetic seismograms using the velocity structure in Figure 5.16b (parameters in Table 5.1b) and the anisotropic structure given in Table 5.2. The observed time delay between the two shear-wave source types is properly modelled and significant amounts of cross component energy is generated.

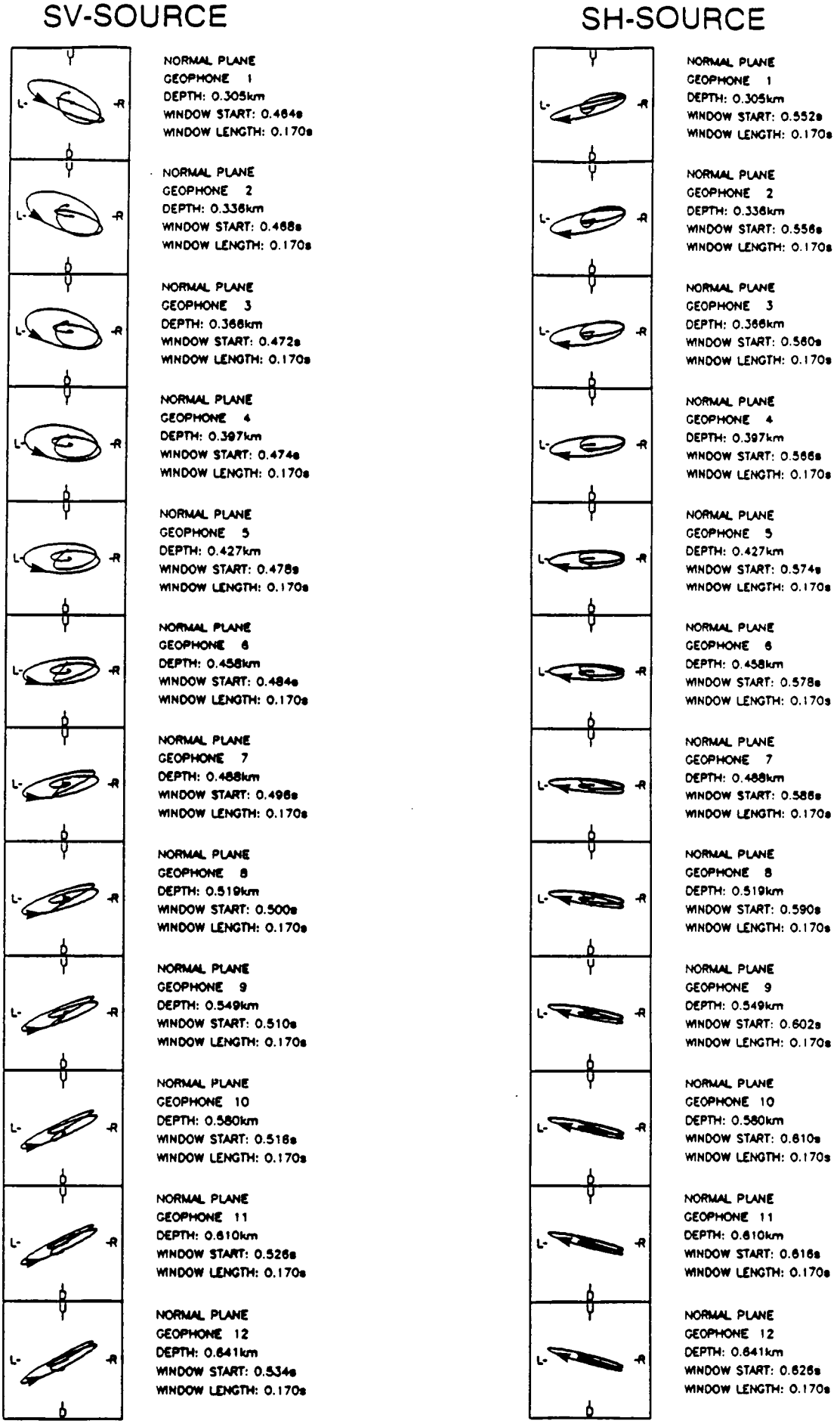

Figure 5.18. Synthetic PDs from the velocity structure in Table 5.1b and the anisotropic structure in Table 5.2. Compared to the observed PDs in Figure 5.10c, these motions are generally less complex in shape.

component. Further, small amplitude arrivals before the main shear-wave arrival can be seen on the observed seismograms, suggesting the presence of velocity boundaries not present in the model.

It is difficult to decide objectively how good a fit is between modelled and observed PDs, than to decide how good a modelled set of seismograms are compared with observations. It is easier with seismograms because there are two readily identifiable criteria that define a good match between theory and observations, these being the arrival times of various seismic phases and the relative amplitudes between these phases. Since PDs are less frequently used by seismic interpreters, they are less well understood than seismograms. This unfamiliarity with PDs is the source of the problem when trying to determine how good a fit is between modelled and observed PDs. In this thesis, three parameters are used in the visual comparison between synthetics and observations. These are the relative amplitudes on the two components, the ellipticity of the motion (bringing in the time delay) and the polarization of the leading split shear-wave.

The modelled shear-wave PDs from the *SV*-source are characterised by a more straightforward elliptical pattern than the observed PDs, which is partly due to the more complex double arrival on the observed vertical component. A gradual change in orientation of the ellipse in the modelled PDs can also be seen that is not present in the observations. The relative amplitudes on the vertical and transverse components agree to a reasonably good extent between the model and observations, although the observations are more elliptical than the model. Initial polarizations are more difficult to compare,

but the direction of rotation of the polarization vector from both source polarizations is reversed between model and observations. This is a relatively important discrepancy between model and observations, and has not been resolved.

Modelled SH-source

Modelled and observed transverse component arrival times are in good agreement from this source, while the modelled vertical component is of much lower amplitude than that observed and the arrival times are slightly too late. The poor match for the vertical component is due to the model not producing the *P*-waves arriving slightly before the shear-waves.

Without these *P*-waves, the match between modelled and observed PDs is not good. The initial, vertical polarization is not present on the model, and the relative amplitudes on the vertical and transverse conmponents are not correctly reproduced by the model. The modelled PDs are also much more linear than the observed PDs. Overall, the *SH*-source produces a poorer fit between model and observations compared to the *SV*-source.

Conclusions on anisotropic modelling

Both the velocity and anisotropic structures had to be estimated in the modelling process for the far offset VSP. This substantially increased the complexity of trying to match modelled seismograms and PDs with those observed because both structures have almost equal importance in influencing the shapes of seismograms and PDs. The anisotropic model presented in this section is, therefore, by no means the only possibility. Without more observations, there must be many more solutions (e.g. Shearer, 1988) with different velocity and

anisotropic structures satisfying the observations. Better fits between synthetics and observations may exist for other models but trying to find these alternative solutions from a forward modelling process, where the number of variables is hundreds, is time consuming in the extreme! The situation is not helped by the unusual PDs from the far offset *SH*-source and the near offset source making interpretation for an appropriate anisotropic structure impossible.

Overall, the model presented here is only a partial solution and there is no reason that it is any better than the model presented by Shearer (1988) or, indeed, any other solution that models the observations to a similar degree.

5.5 Isotropic modelling

During the numerous attempts at finding an appropriate velocity structure for the far offset VSP, one erroneous structure was tried that reproduced the time delay between the *SV*- and *SH*-source types without any anisotropy. This prompted a return to the Geysers VSP site to investigate further.

Near surface velocity structure

In August, 1989, a number of small scale hammer-source seismic refraction experiments were made around the VSP site. This was to determine the shallow velocity structure around the far offset source location, which had not been investigated before. These experiments revealed the presence of a highly attenuating, very low velocity surface layer, about 8m to 10m thick. *P*-wave velocities were measured

in the region of 0.5kms^{-1}. Although no measurements of shear-wave velocity were made, it is likely that *Vp/Vs* ratios would be large, giving shear-wave velocities less than 0.1kms^{-1}. Initial results from this study were published by Campden et al. (1990).

The presence of this low velocity surface layer has a very significant influence on the seismograms from the *SV*-source. What happens is that the *SV*-source generates large amounts of *P*-wave energy at the wide offset. This *P*-wave energy is almost wholly converted into *SV*-waves at the strong velocity contrast at the bottom of the layer. Thus, the first arriving *SV*-wave signal from the *SV*-source starts, not at the source, but at the bottom of the low velocity layer and arrives ahead of the shear-waves that have travelled directly from the source, passing through the very low shear-wave velocity surface layer. Since the *SH*-source does not produce any *P*-wave energy in the sagittal plane (the plane of propagation), the low velocity layer has very little effect on the seismograms from this source. In this case the delay between the two shear-wave source types, previously claimed to be caused by crack induced anisotropy, is principally caused by *P*-to-*S* conversions at the strong velocity contrast at the bottom of the low velocity surface layer.

This new interpretation required that the velocity structure was recalculated, including the low velocity surface layer, and using the arrival times of the transverse component shear-waves from the *SH*-source. Table 5.3 shows the velocity structure that produced the correct arrival times from both source types, and the correct relative amplitudes between the direct arriving shear-waves from the *SV*-source and the *P*-to-*S* converted shear-waves. Synthetic seismograms

from this model are given in Figure 5.19 and show a good match with the observations, except that no cross component energy is present. A zero phase source pulse was used, similar to the anisotropic modelling in the previous section. Note that this model reproduces the double arrival seen on the vertical component from the *SV*-source.

Layer	Thickness (km)	*Vp* (km/s)	*Vs* (km/s)	*Vp*/*Vs*	*Q* *P*-waves	*Q* shear-waves
1	0.01	0.54	0.08	6.75	20	2
2	0.19	1.85	0.97	1.91	25	25
3	0.03	2.20	1.30	1.69	25	25
4	0.04	2.55	1.52	1.68	33	33
5	0.19	2.90	1.77	1.64	50	50
6	0.02	3.10	1.91	1.62	67	67
7	0.03	3.36	2.00	1.68	80	80
8	Halfspace	3.60	2.15	1.67	80	80

Table 5.3

The very high shear-wave attenuation (low *Q*) in the top, low velocity layer is due to the relatively unconsolidated nature of the sediments. Modelled *Vp*/*Vs* ratios are physically plausible, with large values near the surface and a decrease with increasing depth. However, due to the relatively constant value of *Vp*/*Vs* below 200m, modelled incidence angles for both *P*- and shear-wave are similar at all geophones, which is not true on the observed data.

In the previous section, it was found that to obtain similar shear-wave PDs at all geophones, anisotropy causing the significant part of the shear-wave splitting would have to occur in a part of the model where rays to all geophones travelled with almost the same incidence angles. The isotropic shear-wave ray tracing diagram in Figure 5.20 demonstrates that this is not the case for the isotropic model in Table 5.3, except in the top, low velocity layer where all

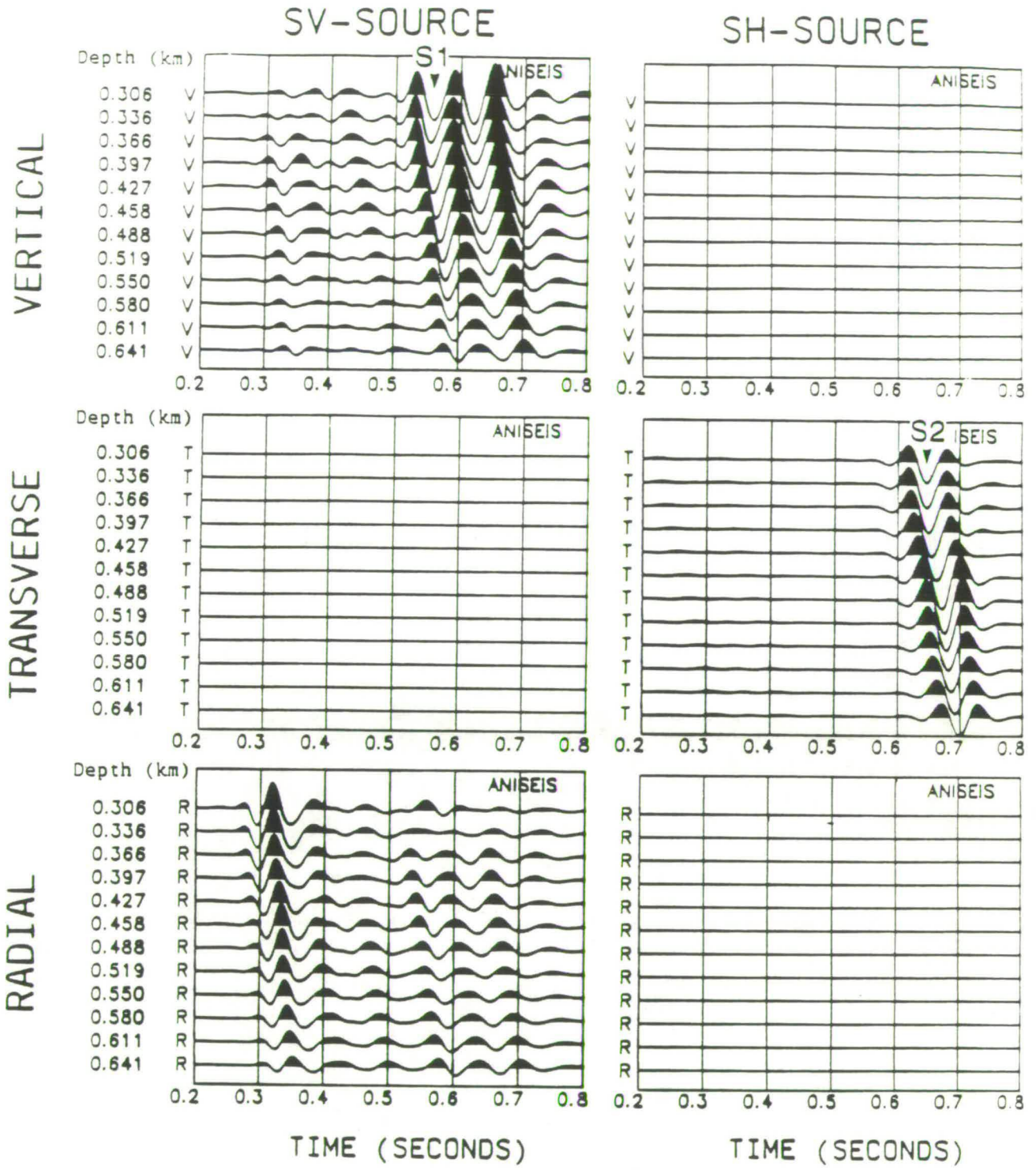

Figure 5.19. Synthetic seismograms using the isotropic velocity structure in Table 5.3. This includes a thin, low velocity layer at the surface, producing mode converted shear-wave from *P*-waves emitted by the *SV*-source, which arrive earlier than the direct shear-wave from the source. Hence, the large time delay between the *SV*- and *SH*-sources is reproduced without anisotropy.

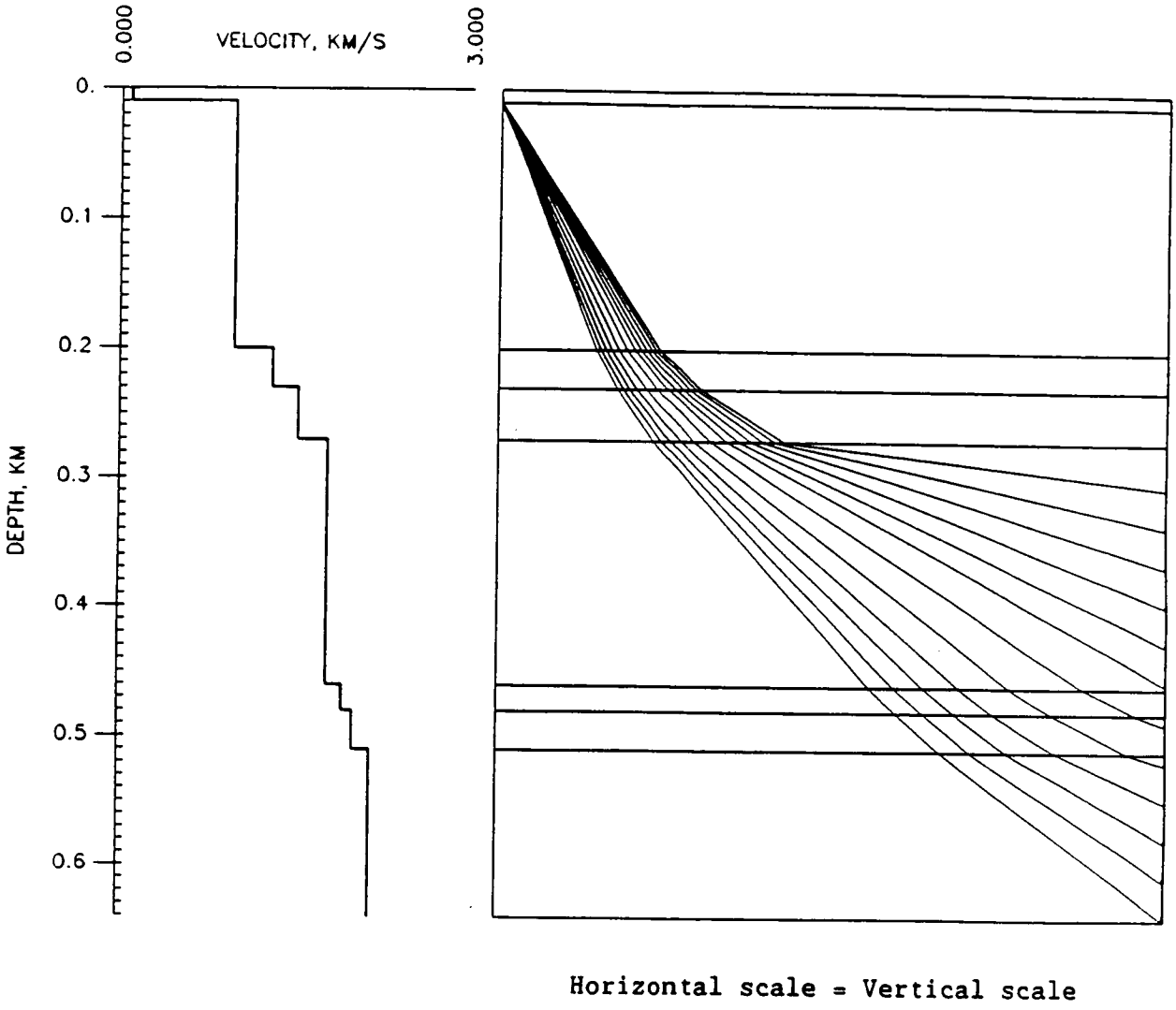

Figure 5.20. Isotropic shear-wave ray tracing using the velocity structure in Table 5.3. No layer contains common ray paths to all geophones, except the top, low velocity layer.

rays are very nearly vertical. Although other velocity models were found that gave similar ray paths in the upper 200m or so, none reproduced simultaneously the relatively large amplitude of the *P*-to-*S* arrival.

Despite the problems mentioned above, a number of anisotropic models were tried. An added complication with this type of velocity structure is how to find an anisotropic structure that will give a single transverse component arrival from the *SV*-source, which effectively produces two shear-wave arrivals on the vertical component. Out of all the anisotropic structures tried, none produced only one shear-wave arrival on the *SV*-source transverse component.

Very large crack densities were still required despite the fact that the delay between source types was now explained by the velocity structure. Without large crack densities, there was little or no cross component energy - i.e. no energy on the transverse component from the *SV*-source. Vertical cracks were tried with a range of (large) crack densities, strike directions and different locations within the velocity structure.

The orientation of near surface, stress aligned inclusions has been proposed by Crampin (1990b). This basically involves horizontally aligned inclusions at the surface, where the minimum compressive stress is vertical, to vertical, parallel inclusions at a depth where the minimum horizontal stress is significantly smaller than the maximum horizontal stress and the vertical stress. At a particular depth, a situation will occur where the vertical and minimum horizontal stresses are equal, giving rise to randomly oriented inclusions with all normals to the inclusions lying in the

plane described by the minimum horizontal and vertical stresses. This type of gradually changing anisotropic structure was tried with the velocity structure above, where the transition from horizontal surface inclusions to parallel, vertical inclusions took place above the top geophone. Various (large) crack densities and orientations of maximum horizontal stress direction were tried with this type of model.

Isotropic model layer no.*	Thickness (km)	*CD*	Crack strike (° from radial)
1	0.01	Isotropic	
2	0.09	Isotropic	
2	0.10	0.07	80
3	0.03	0.10	80
4	0.04	0.16	80
5	0.19	0.20	80
6	0.02	0.20	80
7	0.03	0.20	80
8	Halfspace	0.20	80

*These layer numbers correspond to those in Table 5.3

Table 5.4

Out of all the models tried, the best results were obtained from vertical, fluid filled cracks, striking 80° clockwise from radial. Note that relative to North, the crack strike is N10°E, coinciding with independent measurements of the maximum horizontal stress direction and the fast shear-wave polarization direction from the *SV*-source. Table 5.4 gives the anisotropy parameters of the model. Figures 5.21 and 5.22 show the synthetic seismograms and shear-wave PDs for this model. The modelled *SV*-source seismograms show double shear-wave arrivals on both the transverse and vertical components. The observed *SV*-source seismograms show a double shear-wave arrival only on the vertical component. The amplitude of the modelled

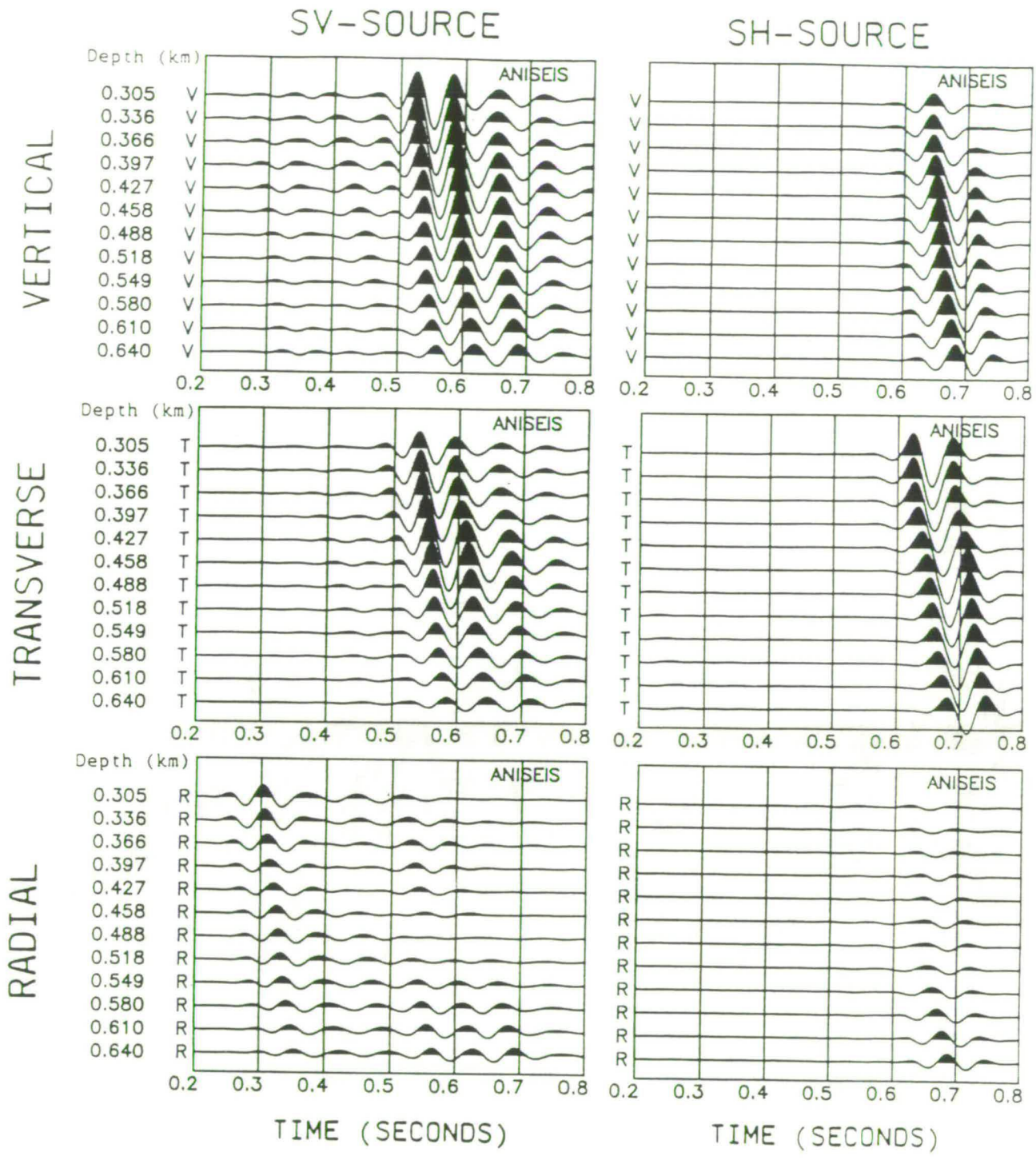

Figure 5.21. Synthetic seismograms using the velocity structure in Table 5.3 and the anisotropic structure in Table 5.4. Compared to the model in Figure 5.17, the cross component amplitudes are not so well modelled and the transverse component from the *SV*-source has a double shear-wave arrival which is not present on the observations.

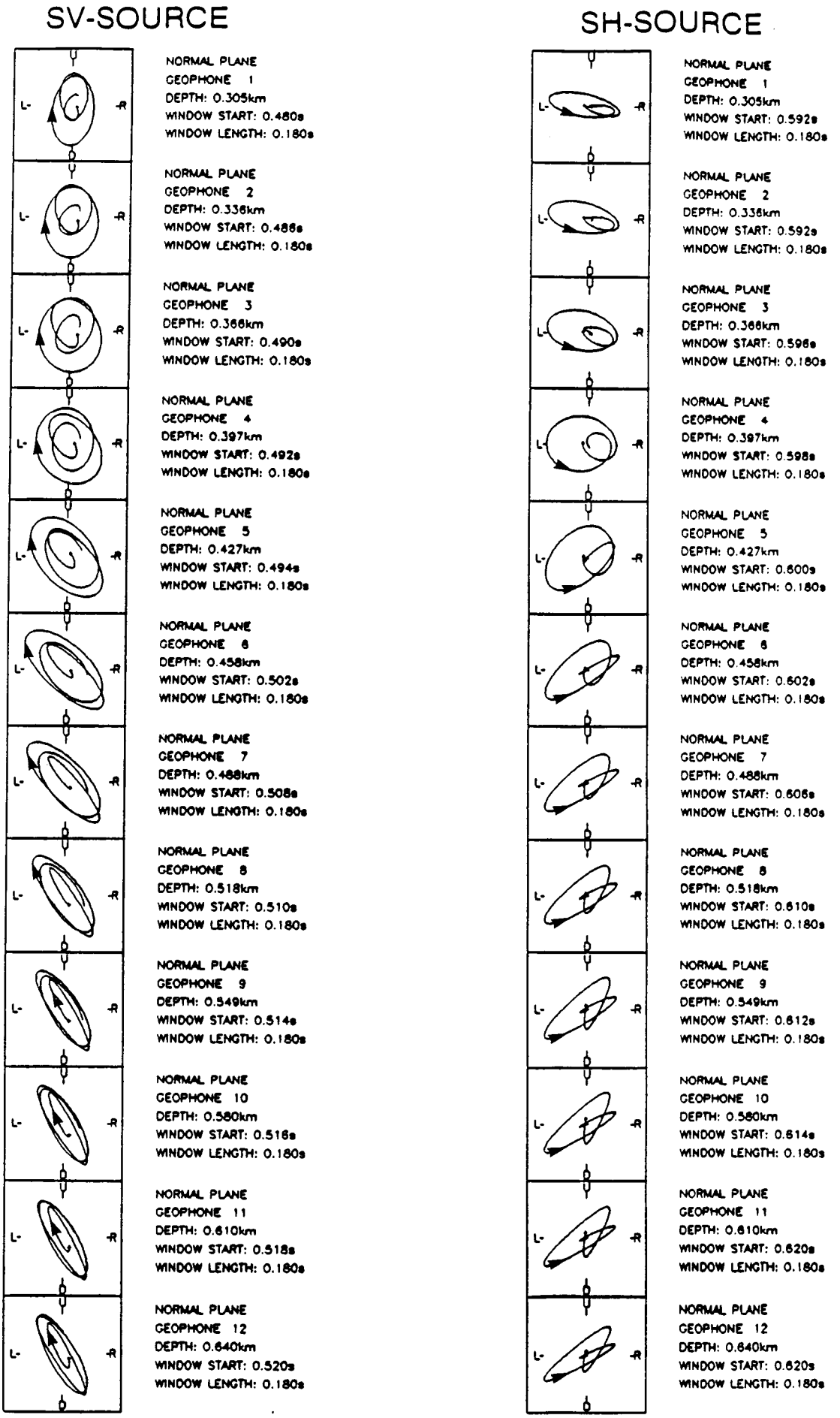

Figure 5.22. Normal plane synthetic PDs from the velocity structure in Table 5.3 and the anisotropic structure in Table 5.4. Since anisotropy is present throughout the depth range of the VSP, shear-wave particle motions show significant differences between the top and bottom geophones.

SV-source transverse component also agrees only poorly with the observations. The main discrepancy between the modelled and observed *SH*-source seismograms is that the synthetic vertical component does not have the early arriving *P*-waves.

As expected with this type of velocity structure, the modelled PDs show significant difference between the top and bottom geophones. The modelled PDs also show much more regular elliptical shapes than the observations, and the orientations of the ellipses are significantly different, especially for the deeper geophones.

Conclusions on isotropic modelling

The large delay in shear-wave arrival times between the far offset *SV*- and *SH*-source types can be explained without the need for anisotropy. A thin, low velocity layer effectively mode converts *P*-waves from the *SV*-source at the bottom of the surface layer, such that they arrive earlier than shear-waves direct from the source.

Energy in the cross components from each shear-wave source can be partially modelled by vertical, fluid filled cracks striking 80° clockwise from vertical, but many differences still exist between the modelled and observed data.

5.6 Discussion

The modelling in sections 5.5 and 5.6 is a good example of how insufficient data make it impossible to distinguish between anisotropic behaviour and that due to strong discontinuities in an

isotropic subsurface. It also shows the importance of knowing the near-source velocity structure for wide offset VSPs. Near offset VSPs are unlikely to be affected by this phenomenon because ray paths are much steeper and less likely to suffer mode conversion.

Although many anisotropic models were attempted with the new velocity structure (i.e. including a low velocity surface layer) none of them satisfactorily modelled the complete waveforms from either shear-wave source. The three main features that could never be modelled were:

1. the single shear-wave arrival on the transverse component and double shear-wave arrival on the vertical component from the *SV*-source;
2. the *P*-waves on the vertical component from the *SH*-source, which arrived slightly before the shear-waves on the transverse component;
3. the correct amplitudes on the cross components

These features suggest that some other interpretation may be required to explain the observations.

Liu and Crampin (1990) have shown that shear-wave splitting phenomena can be created in isotropic media at velocity interfaces. The low velocity at the surface represents a weathered layer, which can be highly irregular in thickness and may dip steeply in some areas. If the large velocity contrast at the base of the weathered layer dips out of the sagittal plane at the point where the rays from the far offset sources penetrate it, possible large amplitude shear-waves in cross component directions may be generated from the *SV*- and *SH*-sources. Furthermore, the *P*-to-*S* mode converted shear-waves from the *SV*-source may be modified substantially by

irregular topography, which could be the cause of the single large amplitude shear-wave arrival on the transverse component from the *SV*-source. Since rays to all geophones from each source pass through almost exactly the same volume of weathered layer, very similar shear-wave patterns would be expected at every geophone.

Unfortunately, it has not been possible to test this alternative interpretation of the Geysers VSP observations, because the relevant software required to model the three-components of shear-wave motion in a model with non planar interfaces was not available. It does, however, seem like an appropriate topic for further investigation.

The near offset VSP provided the only observations of shear-waves within the geothermal reservoir region itself. However, since the horizontal components could not be rotated reliably to known directions, especially in the lower depth range of the VSP, very little interpretable information was available from this experiment. What useful information there was did not help in deciding the type of anisotropic structure present (if any).

5.7 Conclusions

Initial interpretations and anisotropic modelling of the Geysers far offset VSP were effectively invalidated by the discovery of a very low velocity, surface weathered layer in the vicinity of the far offset source location. *P*-waves emitted from the *SV*-source are mode converted to shear-waves at the base of this layer, giving shear-waves from the *SV*-source an apparently earlier arrival time compared to those from the *SH*-source.

Anisotropic modelling using this type of velocity structure has not yielded a satisfactory fit between synthetic and observed seismograms and PDs. Further modelling is hindered by the lack of information from the observations about the type of anisotropic structure present. It should be noted that topography at the base of the weathered may be responsible for many of the observations previously thought to be caused by anisotropy, but due to the inavailability of software, it is not possible to test this possibility.

Overall, nothing can be reliably concluded about crack/fracture orientations within the geothermal reservoir itself, due to the lack of geophone locations within the reservoir.

Chapter 6 - Summary of findings

A number of different aspects of anisotropy have been studied in this thesis, each of which is summarized below, with some suggestions for further related research.

6.1 Attenuation anisotropy

By considering the passage of split shear-waves through a homogeneous, anisotropic medium, it was shown that estimates of attenuation anisotropy from isolated observations of shear-wave splitting require measurement of two differential and two absolute parameters. The differential parameters are the time delay between split shear-waves, and a measure of the apparent attenuation between fast and slow shear-waves, found from spectral interference or spectral ratio methods. The absolute parameters are the travel time of the fast shear-wave from source to receiver, and the attenuation of the fast shear-wave along the ray path from source to receiver. This should be compared to estimating velocity anisotropy, where one differential parameter, the time delay, and one absolute parameter, the travel time of the fast shear-wave, are required. The extra measurements needed in the calculation of attenuation anisotropy will result in larger error bounds compared to those associated with the velocity anisotropy. Hence, attenuation anisotropy is a less reliable quantity than velocity anisotropy.

Which ever method is chosen to calculate attenuation anisotropy, spectral ratios or spectral interference, a large signal bandwidth is essential to enable any chance of success. However, there is likely

to be an increase in the amount of scattered energy present as the frequency increases and the wavelength of the seismic wavelet approaches the size of inhomogeneities in the rockmass. The amount of scattering depends heavily on the size of inhomogeneities and is connected to prevailing geological conditions. Thus, increasing the bandwidth may not necessarily improve estimates of attenuation anisotropy.

Monitoring temporal changes in attenuation anisotropy from repeated observations of shear-wave splitting using identical experiments was also considered. The possibility of calculating changes in attenuation anisotropy from differences between experiments alone was discounted, as knowledge of the initial attenuation anisotropy (or more correctly, the four parameters used in its calculation as mentioned above) is necessary. Once the initial attenuation anisotropy has been found, then only the changes in subsequent observations of shear-wave splitting are necessary in order to calculate changes in attenuation anisotropy. Measuring changes in shear-waves from identical experiments is generally more precise than absolute measurements from individual experiments, making estimates of changes in attenuation anisotropy more reliable than individual estimates.

Due to our present lack of knowledge concerning the mechanisms creating shear-wave attenuation, it is difficult to guess how attenuation anisotropy will be affected by changes in the fluid content of pore space, such as may occur in EOR processes. Changes in both the attenuation and velocity anisotropy may occur, depending on the viscosity of the hydrocarbon making up the reservoir and the type of EOR process chosen (e.g. thermal or chemical flooding). If there

is no change in the shear modulus of the media occupying the pore spaces (if perfect fluid, the shear modulus is zero), then there should be no change in the velocities of the split shear-waves, and hence no change in the velocity anisotropy. There may, however, be a measurable change in the attenuation anisotropy, but without further research into the mechanisms of attenuation it is not possible to say one way or the other.

Further research needs to be done to develop methods for interpreting changes in (attenuation or velocity) anisotropy in terms of movement of the injected gas, chemical or heat flood front. Without being able to display measured changes in anisotropy in a readily interpretable form, the commercial viability of shear-wave splitting as a tool to monitor EOR is in doubt. This view is strengthened by the growing interest and apparent success of *P*-wave tomography, used to image directly the progress of EOR (e.g. see Justice et al., 1989).

The success or failure of any three-component shear-wave experiment to determine anisotropy is very much dependent on the quality of observations and the way in which the anisotropic structure is sampled. If attenuation anisotropy is to be studied, very high quality observations will be required and I suggest that no published observations of shear-waves, to date, are of the required quality.

6.2 Measuring and processing split shear-waves

Two frequency domain methods and one time domain method were developed for automatically determining the time delay between split shear-waves and the polarization of the leading split shear-wave.

These were tested on synthetic VSP data with various amounts of random noise added. The general trend of results indicates that the reliability of the methods decreases as the time delay decreases and (not surprisingly) as the random noise increases.

The automatic methods were also used to show that deterministic source signature deconvolution and F-K filtering can be successfully applied to three-component data without distorting polarization information. For any kind of three-component processing, identical operations must be applied to all three-components, and in the case of F-K filtering (or any other spatial filter), the three components should have the same orientation of axes at all recording locations. F-K filtering appears to be particularly good at removing incoherent noise from observations of shear-wave splitting and thus improving the reliability of time delay and *qSI* polarization estimates.

Processing procedures associated with reflection data are currently being studied for their effect on two-component (horizontal plane) shear-wave recordings by Li (personal communication). The results from this study are of particular importance to the future of shear-wave splitting as a tool for hydrocarbon exploration because if the correct polarization and delay information cannot be preserved in the final, processed sections, no information can be obtained about anisotropic (and in particular fracture) structures at depth. Initial findings have shown that a polarization analysis of CDP gathers is necessary to determine the polarization of the faster split shear-wave, employing similar techniques as those used in the derivation of stacking velocities. Prior to stacking, the two component CDP gather must be rotated, using the angle estimated from polarization analysis, so the fast and slow shear-waves are decoupled

on to separate components. This differs from Alford's approach (Alford, 1986) where the two components were rotated to find the fast and slow shear-wave polarizations after stacking. According to Li's work, this is likely to lead to incorrect results.

Yardley and Crampin (1990b) identify a possible, significant problem with surface recordings of reflected shear-waves: Shear-waves reflected at depth and recorded at the surface will only contain information about the anisotropic structure near the surface. If the near surface anisotropy is different to that at depth, it will not be possible to determine the deeper anisotropic structure from direct analysis of the recorded shear-waves. Winterstein and Meadows (1990) have developed a layer stripping algorithm to compensate for vertical changes in anisotropy. If this type of analysis can be proven reliable, then two component shear-wave reflection seismics could become an important exploration tool in the search for fractured reservoirs.

6.3 Shear-wave VSP studies

The two VSP surveys analysed in this thesis were similar in that they involved wide offset source locations relative to the geophone depths. Neither VSP produced classic observations of shear-wave splitting to which synthetic shear-wave PDs could be matched.

The Vulcan VSPs

Results from the four Vulcan VSPs indicate a crack direction in agreement with the maximum horizontal stress direction found from earthquake focal mechanisms and borehole breakout data. It also appears that one of the offsets was parallel to the dominant crack direction and another was perpendicular to this direction, such that

only from two of the offsets could the crack orientation be identified from shear-wave splitting. The time delay estimates also suggest that all the shear-wave splitting occurs in the cap-rock, with little or no measureable anisotropy in the reservoir rock.

It is an important conclusion from this VSP, that to study shear-wave splitting from mode converted *P*-waves, offsets at about 45° to the estimated maximum horizontal compressive stress direction are desireable, to ensure the prominent excitation of both split shear-waves.

Suggestions that topography at either the top or bottom of the cap-rock may introduce polarization anomalies similar to shear-wave splitting were made, but it is unlikely that the same leading split shear-wave direction would be obtained from two different source azimuths. *P*-wave polarization anomalies were also present at some depths, for which anisotropy cannot be responsible. It would seem plausible that topography at internal interfaces is the cause of these anomalies, and is also the most likely candidate to account for the large amounts of scatter present in the automatic estimates of leading shear-wave polarization. This problem of scattering from non planar interfaces may be common to wide offset VSPs, and at isolated geophones may produce shear-wave motions similar to those caused by shear-wave splitting.

It would be desirable to analyse more marine VSPs in order to obtain an idea of the reliability of shear-waves generated by mode

conversion. The Vulcan VSP is also rather unfortunate to have had all the source to well head directions almost parallel or perpendicular to the crack strike, so there is further interest in studying marine VSP data where better shear-wave splitting is expected.

The Geysers VSP

At the Geysers geothermal zone, geophone positions for the wide offset VSP were relatively shallow, not penetrating the steam reservoir. Hence, no estimate of the *in situ* crack or fracture orientation within the reservoir could be made from these data. Shear-waves were recorded from in-line and cross-line shear-wave sources, with shear-waves from the in-line source arriving about 0.1s earlier than those from the cross-line source. Initial interpretations of the shear-waves suggested the presence of parallel, vertical cracks/fractures striking parallel to the source to well head direction acting to slow down shear-waves from the cross-line source relative to the in-line source.

This initial interpretation was radically altered when a small scale hammer seismic refraction experiment revealed the presence of a thin, very low velocity surface layer at the site of the far offset source. In a structure containing a thin, low velocity surface layer, *P*-waves emitted by the in-line source are mode converted to *SV*-waves at the bottom of the layer, arriving at the geophones earlier than shear-waves travelling directly from the source. Generally, this phenomenon will only be seen in wide offset VSPs using relatively shallow geophones where a strong velocity contrast is present near

the surface. VSPs with steep ray paths will not be so prone to this effect as mode conversion is much less efficient at small incidence angles. Interface dip will also play a part in controlling the amount of mode converted energy.

Shear-waves from both far offset sources exhibited large amounts of cross-component energy; a large transverse component arrival from the in-line source, almost twice the amplitude of the vertical component, and a vertical component arrival of similar amplitude to the transverse component from the cross-line source. No real success was ever achieved in matching the observed shear-wave PDs with synthetics using the ANISEIS full waveform modelling package, suggesting that the near surface anisotropic structure is highly complex around the Geysers VSP and may be laterlally and/or vertically heterogeneous. The lack of observations makes it impossible to tell what the anisotropic structure may be. More source offsets and geophone locations are required.

As an alternative explanation, a non planar interface at the bottom of the surface low velocity layer may introduce significant polarization anomalies into the shear-waves. Since ray paths from source to all geophones take nearly exactly the same route through the surface layer, very similar polarization patterns would be expected at all geophones, fitting in with the observations, which show relatively minor differences in PDs between the top and bottom geophones. However, it is difficult to believe that such large polarization anomalies could result from a non planar interface, even though the velocity contrast across the interface is so extreme.

A near offset VSP with geophones within the steam part of the resevoir could not be reliably interpreted because the orientations of the horizontal component geophones, containing the shear-wave energy, were not known. However, polarization shapes of the recorded shear-waves were generally linear, indicating a lack of shear-wave splitting. This could be caused by isotropy or the source polarization being parallel or perpendicular to a symmetry plane of the anisotropic structure.

The overall solution to the anisotropic structure (if any) at the Geysers is likely to be very complex. The effects of non planar interfaces must be investigated to find how shear-wave polarizations are altered, if only to eliminate this phenomenon from the possible solutions.

6.4 Final remarks

To date, the best published observations of shear-wave splitting have come from VSP surveys (e.g. Bush, 1990; Yardley and Crampin, 1990a). These offer insights to the anisotropy in the near vicinity of the well, and as such provide useful information about the possible movement of fluid in the reservoir immediatly around the well. There is little prospect for mapping out lateral changes in anisotropy over, say, an entire oil reservoir from VSPs. In view of this, shear-wave reflection seismics appear to be the most likely method to give lateral predictions of reservoir anisotropy, and perhaps the most effort should be put into the processing and interpretation of this type of data.

REFERENCES

Alford, R.M., 1986. Shear data in the presence of azimuthal anisotropy: Dilley, Texas, Expanded abstracts, 56th Annual International SEG Meeting, Houston, 476-479.

Angeleri, G.P., Persoglia, S., Poletto, F. and Valenti, G., 1990. Drill-bit noise as seismic source: new solutions for improved results, Technical programme and abstracts, 52nd EAEG Meeting, Copenhagen, 54.

Aronstam, P., Kennedy, B. and Wiggins, W., 1989. Design and performance of a resonant swept-frequency borehole source, Technical programme and abstracts, 51st EAEG Meeting, West Berlin, 162-163.

Backus, G.E., 1962. Long-wave elastic anisotropy produced by horizontal layering, J.Geophys.Res., 67, 4427-4440.

Bifani, R., George, G.T. and Lever, A., 1986. Geological and resevoir characteristics of the Rotliegend sandstones in the Argyll field, in Petroleum Geology of NW europe, J. Brooks and K. Glennie (eds), Graham and Trotman publ., London.

Booth, D.C. and Crampin, S., 1983. The anisotropic reflectivity technique: Theory, Geophys.J.R.astr.Soc., 72, 755-766.

Booth, D.C. and Crampin, S., 1985. Shear-wave polarizations on a curved wavefront at an isotropic free surface, Geophys.J.R.astr.Soc., 83, 31-45.

Booth, D.C., Crampin, S., Evans, R. and Roberts, G., 1985. Shear-wave polarizations near the North Anatolian fault: I, Evidence for anisotropy-induced shear-wave splitting, Geophys.J.R.astr.Soc., 83, 61-73.

Booth, D.C., Crampin, S., Lovell, J.H. and Chiu, J.M., 1990. Temporal changes in shear-wave splitting during an earthquake swarm in Arkansas, J.Geophys.Res., 95, 11151-11164.

Brodov, L.U., Ginodman, A.I., Khudobina, L.N., Kuznetsova, O.N., Levedev, K.A. and Purzyrev, N.N, 1968. Transverse waves and their geological application, Paper presented at the 23rd International Geological Congress Proceedings, Prague.

Bufe, C.G.; Marks, S.M.; Lester, F.W.; Ludwin, R.S. and Stickney, M.C., 1981. Seismicity of the Geysers - Clear Lake region, U.S.Geol.Survey Prof.Paper 1141, 129-137.

Bush, I., 1990. Modelling shear-wave anisotropy in the Paris Basin, Ph.D. thesis, University of Edinburgh.

Bush, I. and Crampin, S., 1987. Observations of EDA and PTL anisotropy in shear-wave VSPs, Expanded abstracts, 57th Annual International SEG Meeting, New Orleans, 476-479.

Campden, D.A., Crampin, S., Majer, E.L. and McEvilly, T.V., 1990. Modeling the Geysers VSP: A progress report, The Leading Edge, 9, 36-39.

Cerveny, V., 1972. Seismic rays and ray intensities in inhomogeneous anisotropic media, Geophys.J.R.astr.Soc., 29, 1-13.

Chapman, C.H. and Shearer, P.M., 1988. Quasi shear-wave coupling in anisotropic media, [abstract] EOS, 69, 1330.

Chen, T.-C., Booth, D.C. and Crampin, S., 1987. Shear-wave propagation near the North Anatolian Fault: III, Observations of temporal changes, Geophys.J.R.astr.Soc., 91, 287-311.

Cherry, J.T. and Waters, K.H., 1968. Shear-wave recording using continuous signal methods, Geophysics, 33, 229-239.

Crampin, S., 1977. A review of the effects of anisotropic layering on the propagation of seismic waves, Geophys.J.R.astr.Soc., 49, 9-27.

Crampin, S., 1978. Seismic wave propagation through a cracked solid: polarization as a possible dilatancy diagnostic, Geophys.J.R.astr.Soc., 53, 467-496.

Crampin, S., 1981. A review of wave motion in anisotropic and cracked elastic media, Wave Motion, 3, 343-391.

Crampin, S., 1985. Evaluation of anisotropy by shear-wave splitting, Geophysics, 50, 142-152.

Crampin, S., 1987a. Geological and industrial implications of extensive dilatancy anisotropy, Nature, 328, 491-496.

Crampin, S., 1987b. Crack porosity and alignments from shear-wave VSPs, in Shear-wave exploration, S.H. Danbom and S.N. Domenico (eds), Geophys.Developments, SEG Special Publication 1, 227-251.

Crampin, S., 1989. Effects of singularities on shear-wave propagation in sedimentary basins, Geophys.J.Int., submitted.

Crampin, S., 1990a. The potential of shear-wave VSPs for monitoring recovery: A letter to management, The Leading Edge, 9, 50-52.

Crampin, S., 1990b. Alignment of near-surface inclusions and appropriate crack geometries for geothermal hot dry rock experiments, Geophys.Prosp., 38, 621-631.

Crampin, S. and Yedlin, M., 1981. Shear-wave singularities of wave propagation in anisotropic media, J.Geophys.Res., 49, 43-46.

Crampin, S., Stephen, R.A. and McGonigle, R., 1982. The polarization of *P*-waves in anisotropic media, Geophys.J.R.astr.Soc., 68, 477-485.

Crampin, S. and Booth, D.B., 1984. Shear-wave polarizations near the North Anatolian fault: II, Interpretation in terms of crack induced anisotropy, Global Seismology report no. 212.

Crampin, S., Evans, R. and Atkinson, B.K., 1984. Earthquake prediction: a new physical basis, Geophys.J.R.astr.Soc., 76, 147-156.

Crampin, S., Evans, R. and Ucer, S.B., 1984. Analysis of records of local earthquakes: The Turkish dilatancy projects (TDP1 and TDP2), Global Seismology report no. 211.

Crampin, S. and Atkinson, B.K., 1985. Evidence for aligned cracks in the Earth's crust, First Break, 3, 12-14.

Crampin, S. and Booth, D.C., 1985. Shear-wave polarizations near the North Anatolian fault: II, Interpretation on terms of crack induced anisotropy, Geophys.J.R.astr.Soc., 83, 75-92.

Crampin, S., Bush, I., Naville, C. and Taylor, D.B., 1986a. Estimating the internal structure of reservoirs with shear-wave VSPs, The Leading Edge, 5, 35-39.

Crampin, S., Booth, D.C., Krasnova, M.S., Chesnokov, E.M., Maximov, A.B. and Tarasov, N.T., 1986b. Shear-wave polarizations in the Peter the First Range indicating crack induced anisotropy in a thrust-fault regime, Geophys.J.R.astr.Soc., 84, 401-412.

Crampin, S., Lynn, H.B. and Booth, D.C., 1989. Shear-wave VSPs: a powerful new tool for fracture and reservoir description, J.Pet.Tech., Paper no. 16866, 3, 283-288.

Conway, A.M., 1986. Geology and petrophysics of the Victor Field, in Habitat of Palaeozoic gas in NW Europe, J. Brooks, J.C. Goff and B. Van Hoorn (eds), Geological Society Special Publication 23, 237-249.

Dankbaar, J.W.M, 1985. Separation of *P*- and *S*-waves, Geophys.Prosp., 33, 970-986.

Dankbaar, J.W.M, 1987. Vertical seismic profiling - separation of *P*- and *S*-waves, Geophys.Prosp., 35, 803-814.

Dieulesaint, E. and Royer, D., 1980. Elastic waves in solids, in French, Masson and Cie (eds), translated by Wiley, New York.

Dillon, P.B., Ahmed, H. and Roberts, T., 1988. Migration of mixed-mode VSP wavefields, Geophys.Prosp., 36, 825-846.

Douma, J., 1988. The effect of the aspect ratio on crack-induced anisotropy, Geophys.Prosp., 36, 614-632.

Duff, G.F.D., 1960. The Cauchy problem for elastic wave propagation in anisotropic media, Phil.Trans.R.Soc., 252, 249-273.

Erickson, E.L., Miller, D.E. and Waters, K.H., 1968. Shear-wave recording using continuous signal methods (Part II), Geophysics, 33, 240-254.

Esmersoy, C., 1990. Inversion of *P* and *SV* waves from multicomponent offset vertical seismic profiles, Geophysics, 55, 39-60.

Evans, J.R., 1984. Effects of the free surface on shear wavetrains, Geophys.J.R.astr.Soc., 76, 165-172.

Fryer, G.J. and Frazer, L.N., 1984. Seismic waves in stratified anisotropic media, Geophys.J.R.astr.Soc, 78, 691-710.

Fryer, G.J. and Frazer, L.N., 1987. Seismic waves in stratified anisotropic media - II. Elastodynamic eigensolutions for some anisotropic systems, Geophys.J.R.astr.Soc., 91, 73-101.

Futterman, W.I., 1962. Dispersive body waves, J.Geophys.Res., 97, 5279-5291.

Ganley, D.C. and Kanasewich, E.R., 1980. Measurement of absorption and dispersion from check shot surveys, J.Geophys.Res., 85, 5219-5226.

Garbin, H.D. and Knopoff, L., 1973. The compressional modulus of a material permeated by a random distribution of free circular cracks, Q.Appl.Math., 30, 453-464.

Garbin, H.D. and Knopoff, L., 1975a. The shear modulus of a material permeated by a random distribution of free circular cracks, Q.Appl.Math., 33, 296-300.

Garbin, H.D. and Knopoff, L., 1975b. Elastic moduli of a medium with liquid filled cracks, Q.Appl.Math., 33, 301-303.

Gledhill, K.R., 1990. Evidence for shallow crustal anisotropy in the Wellington region, New Zealand, paper presented at the Fourth International Workshop on Seismic Anisotropy, held at Heriot-Watt University, Edinburgh.

Glennie, K.W., 1983. Early Permian (Rotliegendes) palaeo winds of the North Sea, Sedimentary Geology, 34, 245-265.

Glennie, K.W., 1986. Development of N.W. Europe's southern Permian gas basin. In Habitat od Palaeozoic gas in N.W. Europe, Brooks, J.; Goff, J.C. and Van Hoorn, B. (eds), Geological Society special publication, 23, 3-22.

Glennie, K.W. and Buller, A.T., 1983. The Permian Weissliegend of N.W. Europe: the partial deformation of aeolian sand dunes caused by the Zechstein transgression. Sedimentary Geology, 35, 43-81.

Goff, F.E., Donnelly, J.M., Thompson, J.M. and Hearn, B.C. Jr., 1977. Geothermal prospecting in the Geysers-Clear Lake area, northern California, Geology, 5, 509-515.

Hamilton, E.L., 1979. *Vp/Vs* and Poisson's ratios in marine sediments and rocks, J.Acous.Soc.Am., 66, 1093-1101.

Hatton, L., Worthington, M.H. and Makin, J., 1986. Seismic data processing: Theory and practice, Blackwell Scientific Publications, Oxford, U.K.

Horowicz, L., 1990. New possibilities for accurate 3-component borehole seismic measurements, presented at the SEG summer research workshop on recording and processing vector wave field data, Snowbird, Utah, 1990.

Hudson, J.A., 1980. Overall properties of a cracked solid, Math.Proc.Camb.Phil.Soc., 88, 371-384.

Hudson, J.A., 1981. Wave speeds and attenuation of elastic waves in material containing cracks, Geophys.J.R.astr.Soc., 64, 133-150.

Hudson, J.A., 1986. A higher order approximation to the wave propagation constants for a cracked solid, Geophys.J.R.astr.Soc., 87, 265-274.

Jolly, R.N., 1956. Investigation of shear-waves, Geophysics, 21, 905-938.

Justice, J.H., Vassiliou, A.A., Singh, S., Logel, J.D., Hansen, P.A., Hall, B.R., Hutt, P.R. and Solanki, J.J., 1989. Acoustic tomography for monitoring enhanced oil recovery, The Leading Edge, 8, 12-19.

Kanasewich, E.R., 1981. Time series analysis in geophysics, The University of Alberta Press, Edmonton, Alberta; 3rd ed.

Kaneshima, S., Ando, M. and Crampin, S., 1987. Shear-wave splitting above small earthquakes in the Kinki district of Japan, Phys.Earth Plan.Int., 45, 45-58.

Kaneshima, S., Ito, H. and Sugihara, M., 1988. Shear-wave splitting above small earthquakes in a geothermal area of Japan, Geophysical Journal, 94, 399-411.

Keith, C.M. and Crampin, S., 1977a. Seismic body waves in anisotropic media: reflection and refraction at a plane interface, Geophys.J.R.astr.Soc., 49, 181-208.

Keith, C.M. and Crampin, S., 1977b. Seismic body waves in anisotropic media: propagation through a layer, Geophys.J.R.astr.Soc., 49, 209-223.

Keith, C.M. and Crampin, S., 1977c. Seismic body waves in anisotropic media: synthetic seismograms, Geophys.J.R.astr.Soc., 49, 225-243.

Klein, R.J. and Barr, M.V., 1986. Regional state of stress in Western Europe, Proceedings of the International Symposium on Rock Stress and Rock Stress Measurements, Stockholm.

Knopoff, L. and MacDonald, G.J.F., 1958. Attenuation of small amplitude stress waves in solids, Revs.Modern Phys., 30, 1178-1192.

Kozlovsky, Y.A., 1984. The world's deepest well, Sci.Am., 251, 6, 98-104.

Kraut, E.A., 1963. Recent advances in the theory of anisotropic elastic wave propagation, Rev.Geophys., 1, 401-448.

Laurent, J., Layotte, P.C., Meynier, P. and Noual, G., 1990. A mechanical wall-clamped borehole source and its use in inverse VSP and cross-hole seismic surveying, Technical programme and abstracts, 52nd EAEG Meeting, Copenhagen, 56-57.

Li, X-Y., 1990. Dynamic and kinematic features of shear-waves in a horizontally stratified anisotropic earth, paper presented at the Fourth International Workshop on Seismic Anisotropy, held at Heriot-Watt University, Edinburgh.

Lighthill, M.J., 1960. Anisotropic wave motions, Phil.Trans.R.Soc., London, 252, 397-470.

Liu, E.; Crampin, S. and Booth, D.C., 1989. Shear-wave splitting in cross-hole surveys: Synthetic modelling, Geophysics, 54, 57-65.

Liu, E. and Crampin, S., 1990. Effects at internal interfaces on shear-wave polarizations: Comparison with anisotropy induced splitting, J.Geophys.Res., 95, 11275-11281.

Liu, E., Crampin, S. and Yardley, G.S., 1990. The polarizations of reflected shear-waves, Geophys.Res.Lett., 17, 1137-1140.

Love, A.E.H., 1944. A treatise on the mathematical theory of elasticity, 4th ed., Dover, New York.

Macbeth, C., 1990. Reservoir characterisation by inversion of shear-wave polarizations, presented at the Fourth International Workshop on Seismic Anisotropy, held at Heriot-Watt University, Edinburgh.

Macbeth, C. and Crampin, S., 1990a. Utility of automatic techniques for estimating the effects of anisotropy in VSP data, Geophys.Prosp., submitted.

Macbeth, C. and Crampin, S., 1990b. Examination of a spectral method for measuring the effects of anisotropy, Geophys.Prosp., submitted.

Majer, E.L. and McEvilly, T.V., 1979. Seismological investigations at the Geysers geothermal field, Geophysics, 44, 246-269.

Majer, E.L., McEvilly, T.V., Eastwood, F.S. and Myer, L.R., 1988. Fracture detection using *P*- and *S*-wave VSPs at the Geysers Geothermal Field, Geophysics, 53, 76-84.

March, D.W. and Bailey, A.D., 1983. A review of the two-dimensional transform and its use in seismic processing, First Break, 1, 9-21.

Marrow, P.C. and Turbitt, T., 1988. Earthquake source mechanisms and principal stress orientations in Britain and N.W. Europe, [abstract] Geophysical Journal, 92.

Mason, W.P., 1959. Physical acoustics and properties of solids, Van Nostrand Publishing, Princeton, N.J.

McLaughlin, R.J., 1981. Tectonic setting of Pre-tertiary rocks and its relation to geothermal resources in the Geysers - Clear Lake area, U.S.Geol.Survey Prof.Paper 1141, 3-23.

Mueller, M., 1990. Prediction of lateral variability in fracture intensity using multicomponent shear-wave surface seismic as a precursor to horizontal drilling, paper presented at the Fourth Internationl Workshop on Seismic Anisotropy, held at Heriot-Watt University, Edinburgh.

Musgrave, M.J.P., 1954. The propagation of elastic waves in crystals and other anisotropic media, Proc.R.Soc., London, 226, 339-355.

Naville, C., 1986. Detection of anisotropy using shear-wave splitting in VSP surveys: requirements and applications, Expanded abstracts, 56th Annual International SEG Meeting, Houston, 391-394.

Nelson, R.A., 1985. Geologic analysis of naturally fractured reservoirs, Gulf Publishing Company, Houston.

Nicoletis, L., Client, C. and Lefeuvre, F., 1988. Shear-wave splitting measurements from multi-shot VSP data, Expanded abstracts, 58th Annual International SEG Meeting, Anaheim, 527-530.

Nishizawa, O., 1982. Seismic velocity anisotropy in a medium containing oriented cracks - transversely anisotropic case, J.Phys.Earth, 30, 331-347.

Noble, M.D., Lambert, R.A., Ahmed, H. and Lyons, J., 1987. The application of three-component VSP data on the interpretation of The Vulcan Gas Field and its impact on future field development (a case history), SSL report, also presented at 49th EAEG Meeting, Belgrade, 1987.

North, F.K., 1985. Petroleum Geology, Allen and Unwin Inc., Winchester, Massachusetts, USA.

Nuttli, O., 1961. The effect of the Earth's surface on the S-wave particle motion, Bull.Seis.Soc.Am., 51, 237-246.

Omnes, G., 1990. The Coupled-Chord downhole seismic source, Technical programme and abstracts, 52nd EAEG Meeting, Copenhagen, 55.

Peacock, S., Crampin, S. and Fletcher, J.B., 1988. Shear-wave polarizations in the Anza seismic gap, southern California: temporal changes at one station - a possible precursor? J.Geophys.Res., 93, 3339-3356.

Postma, G.W., 1955. Wave propagation in a stratified medium, Geophysics, 20, 780-806.

Puzyrev, N.N., Lebedeva, G.N. and Lebedev, K.A., 1966. Generation of transverse seismic waves by explosions, Geol.I.Geofiz., 2.

Safar, M.H., 1990. Compressional and shear-wave energy radiated by a swept frequency downhole dipole seismic source, Technical programme and abstracts, 52nd EAEG Meeting, Copenhagen, 63.

Shearer, P.M., 1988. Synthetic seismogram modelling of shear-wave splitting in VSP data from the Geysers, California, Geophys.Res.Lett., 15, 1085-1088.

Smith, D.B., 1979. Rapid marine transgressions and regressions of the upper Permian Zechstein sea, J.Geol.Soc.London, 136, 155-156.

Taylor, D.B., 1987. Double contour integration for transmissions from point sources through anisotropic layers as used in ROCPAC software, Geophys.J.R.astr.Soc., 91, 373-381.

Taylor, D.B., 1988. ANISEIS manual, Macroc Ltd., 31 Palmerston Place, Edinburgh.

Thomsen, E., Damtoft, K. and Andersen, C., 1986. Hydrocarbon plays in Denmark outside the Central Trough, in Petroleum Geology of NW Europe, J. Brooks and K. Glennie (eds), Graham & Trotman publ., London.

Tinkle, A.R., Watts, D.E., Beitel, J.E. and Cook, G.R., 1990. Analysis of *P* and *S* wave signatures from the Bolt OMNIPULSE, presented at the SEG summer research workshop on recording and processing vector wave field data, Snowbird, Utah, 1990.

Uhrig, L.F. and Melle, V., 1955. Velocity anisotropy in stratified media, Geophysics, 20, 774-779.

Wang, Z. and Nur, A., 1988. Effects of temperature on wave velocities in sands and sandstones with heavy hydrocarbons, SPE reservoir engineering, 3, 158-164.

White, J.E. and Angona, F.A., 1955. Elastic wave velocities in laminated media, J.Acous.Soc.Am., 27, 310-317.

Wild, P. and Crampin, S., 1990. Catalogue of combinations of EDA- and PTL-anisotropy in sedimentary basins, BGS GSRG report WL/90/22.

Willis, H.A., Rethford, G.L. and Bielanski, E., 1987. Azimuthal anisotropy: occurence and effect on shear-wave data quality, Expanded abstracts, 56th Annual International SEG Meeting, Houston, 479-481.

Winterstein, D.F., 1986. Anisotropy effects in *P*-wave and *SH*-wave stacking velocities contain information on lithology, Geophysics, 3, 661-672.

Winterstein, D.F. and Meadows, M.A., 1990. Depth dependence of *S*-wave polarization azimuth near the San Andreas fault, paper presented at the Fourth International Workshop on Seismic Anisotropy, held at Heriot-Watt University, Edinburgh.

Worthington, M.H., 1984. An introduction to geophysical tomography, First Break, 2, 20-26.

Yardley, G.S. and Crampin, S., 1990a. Automatic determination of anisotropic parameters from shear-wave splitting in the Lost Hills VSP, Expanded abstracts, 60th Annual International SEG Meeting, San Francisco, 1424-1426.

Yardley, G.S. and Crampin, S., 1990b. Extensive dilatancy anisotropy: Relative information in VSPs and reflection surveys, Geophys.Prosp., in press.

Yedlin, M.J., 1980. The wavefront in a homogeneous anisotropic medium, Bull.Seis.Soc.Am., 70, 2097-2101.

Ziegler, P.A., 1982. Geological atlas of Western and Central Europe, Elsevier, Amsterdam, 130.

Zoback, M.L. and Zoback, M.D., 1980. State of stress in the conterminous United States, J.Geophys.Res., 85, 6113-6156.

Zoback, M.D.; Zoback, M.L.; Mount, V.S.; Suppe, J.; Eaton, J.P.; Healy, J.H.; Oppenheimer, D.H.; Reasenberg, P.A.; Jones, L.; Raleigh, C.B.; Wong, I.G.; Scotti, O. and Wentworth, C., 1987. New evidence on the state of stress of the San Andreas fault system, Science, **238**, 1105-1111.

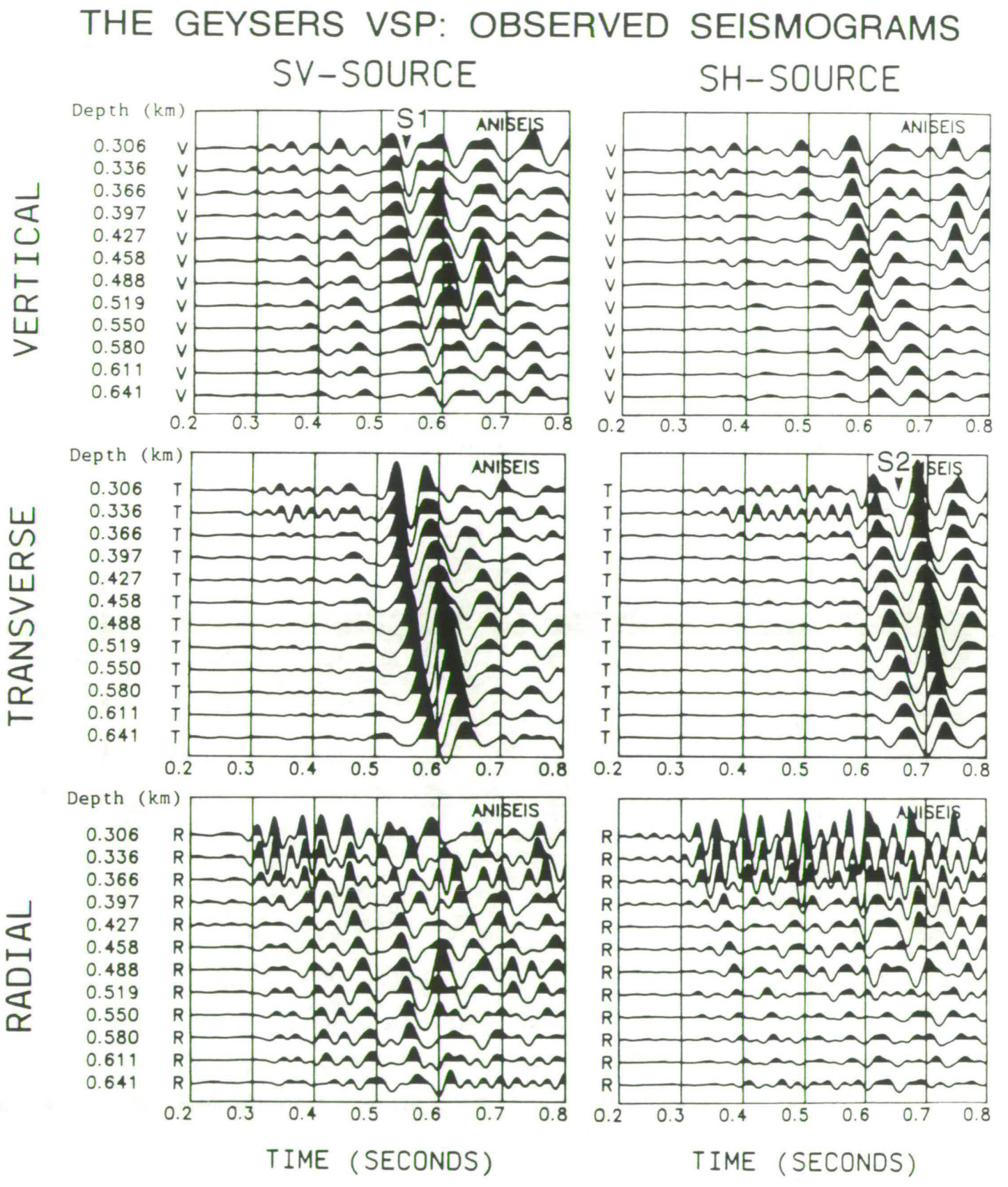

Figure 1. Observed seismograms for a 518 m offset VSP for in-line (*SV*) and cross-line (*SH*) source orientations. Horizontal seismograms have been rotated into horizontal (R)adial and (T)ransverse orientations. S_1 denotes the earlier arriving shear wave from the *SV*-source, and S_2 the later shear wave from the *SH*-source.

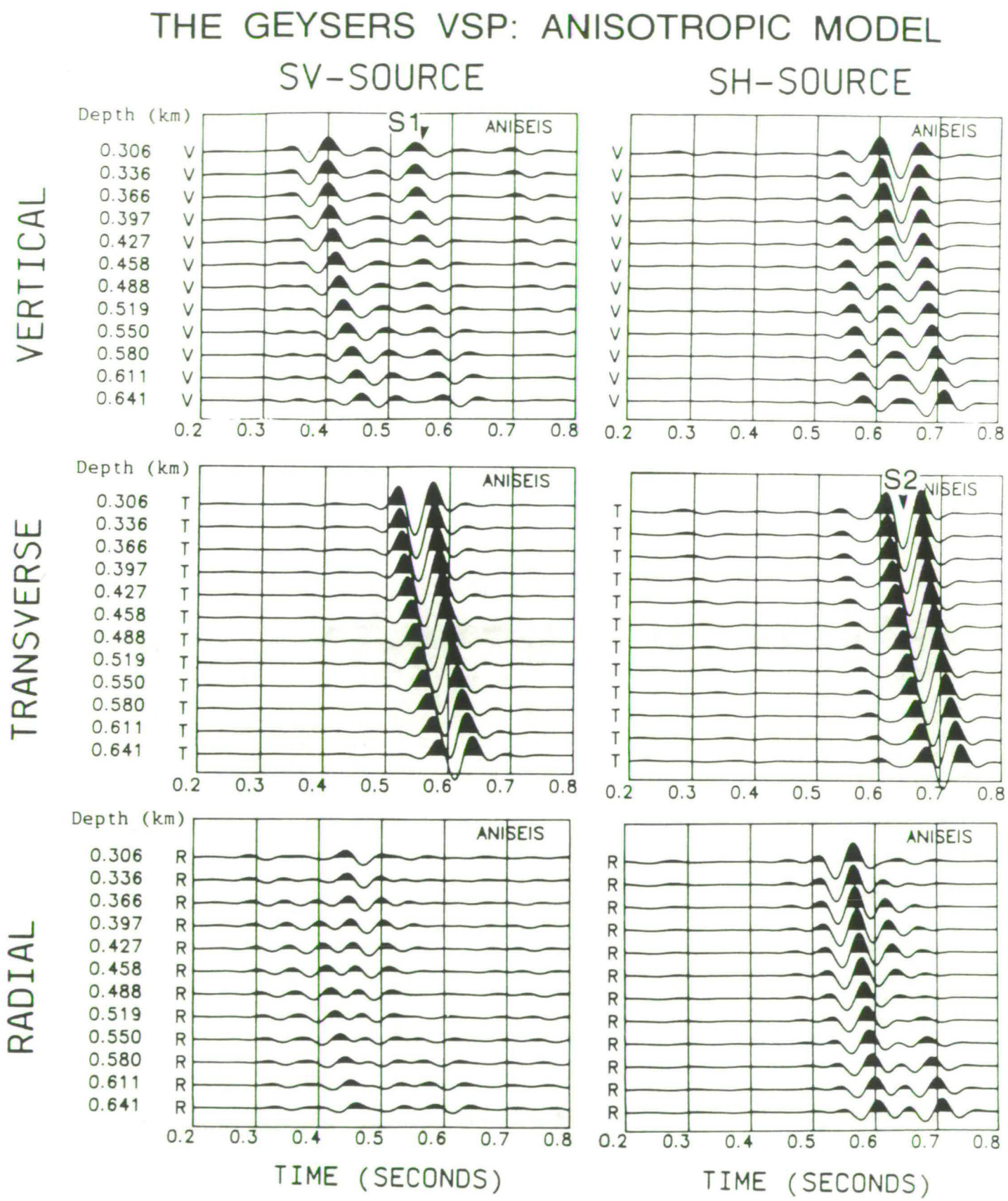

Figure 2. Synthetic seismograms from an anisotropic model reproducing the time delay in shear-wave arrivals from the different source orientations and large amounts of energy on the cross-components. This model uses vertical cracks, striking in the radial direction at the surface, and rotating azimuthally with depth until aligned with the maximum horizontal stress direction (a swing of about 50 degrees).

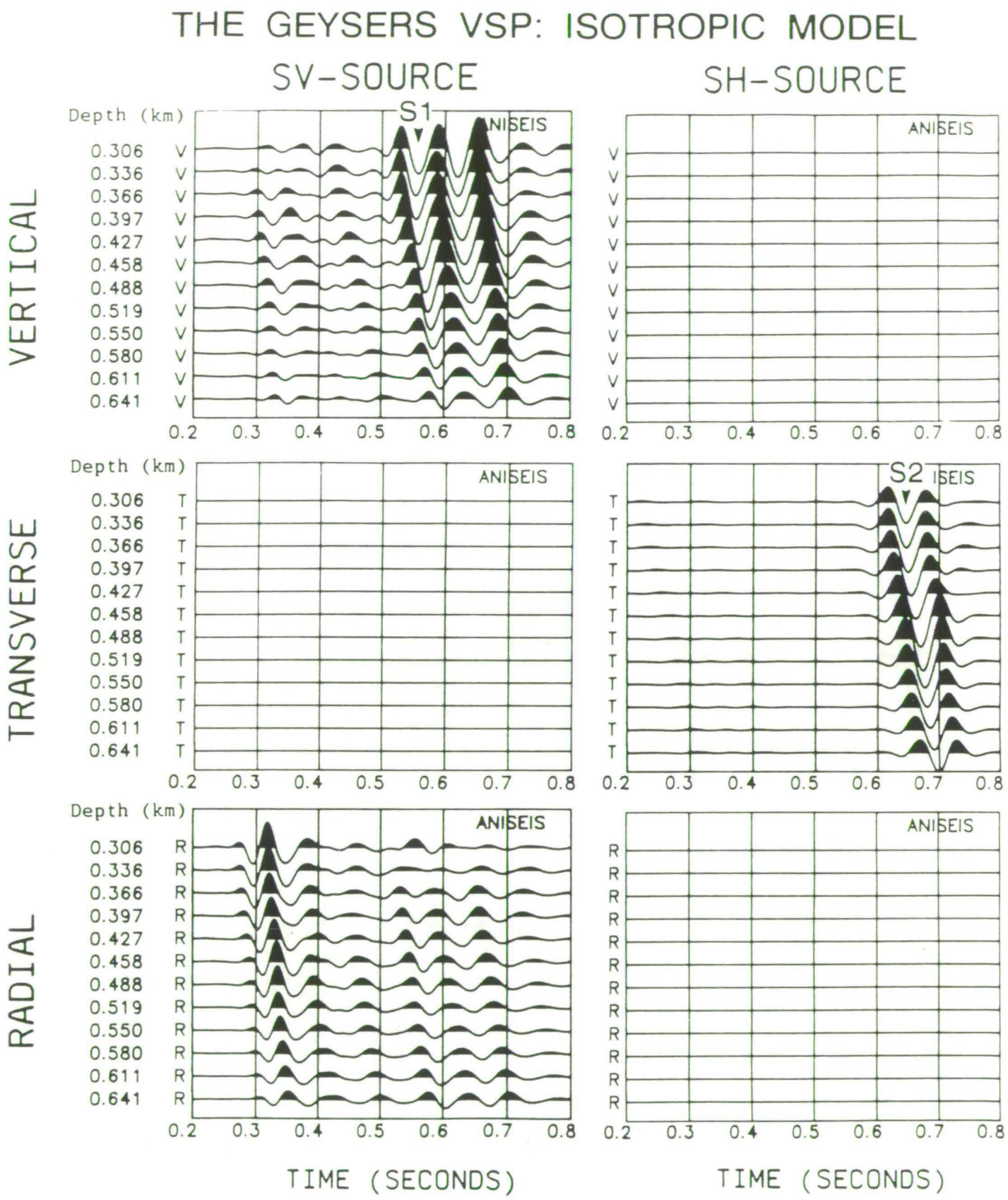

Figure 3. Synthetic seismograms from an isotropic model with a thin very low-velocity surface layer resulting in a 0.1 s time delay between the shear-wave arrivals from the two different source orientations.